FACULTAD DE CIENCIAS

DEPARTAMENTO DE FÍSICA APLICADA

Plataformas sensoras avanzadas basadas en nanohilos de óxidos metálicos y estructuras metálicas plasmónicas

por

Antonio García Marín

Madrid, Octubre 2016

Plataformas sensoras avanzadas basadas en nanohilos de óxidos metálicos y estructuras metálicas plasmónicas

Tesis presentada en el

Departamento de Física Aplicada,

Universidad Autónoma de Madrid

por

Antonio García Marín

para la obtención del grado de doctor

Directores:

Jose Luis Pau Vizcaíno

Encarnación Lorenzo Abad

Madrid, Octubre 2016

Acknowledgements

Me quedo abrumado de la cantidad de agradecimientos que tengo que dar a toda la gente que me ha ayudado, de un modo u otro, en la realización de este trabajo. Da vértigo mirar atrás y ver todo las cosas que han ocurrido estos años. No creo que pueda ser breve. ¡Lo siento!

En primer lugar, sin lugar a dudas, a mis directores de tesis:

José Luis Pau Vizcaíno, del grupo ELySE en el Departamento de Física Aplicada. Ha tenido la tarea titánica de enseñarme desde el principio un sinfín de conceptos de Física a un químico recién salido de un máster sobre Química. Llegué al grupo ELySE sabiendo únicamente que se podían hacer LEDs con semiconductores "p" y "n". Aprendí mucho de él y yo le enseñé también cosas sobre la Química, por supuesto. No olvidaré tampoco los buenos momentos en los congresos y a toda la gente que conocimos.

Encarnación Lorenzo Abad, del grupo SENSOUAM en el Departamento de Química Analítica y Análisis Instrumental. Me ha abierto las puertas a su grupo, permitiendo que no me olvide de mis orígenes. Me ha hecho recordar las cosas más básicas de la Química, una de las ramas más importantes de la Ciencia.

Por supuesto, ha habido otro gran número de personas que han contribuido a ampliar mis conocimientos y que merecen un amplio reconocimiento por ello:

A Juan Piqueras, siempre ayudándome a entender todo tipo de cuestiones teóricas complicadas, como la teoría de bandas y sus desdoblamientos o el amplio mundo de los plasmones superficiales. Recuerdo perfectamente el primer que llegué al laboratorio para hacer la entrevista de trabajo. José Luis a un lado y Juan al otro. ¡Qué miedo sentí en aquel momento! No obstante, cuando salí, de algún modo supe que me acogerían allí.

A José María Abad que me enseñó la química de las nanopartículas en coloides. Pude descubrir lo fácil que se pueden agregar. No obstante, me enseñó muy bien a manejarlas y lograr buenos resultados.

A Carlos García, el compañero que todos queremos tener. Cada vez que necesitaba ayuda para discutir un tema, ahí estaba. Y los dos nos poníamos a hablar sobre ello. Memorables las discusiones sobre los nanohilos de CuO y ZnO hasta altas horas de la tarde-noche, tanto en el laboratorio como de camino a casa en el Cercanías. Y así durante cuatro años de forma intermitente.

A Eduardo Ruiz, un químico entre físicos, que logró crecer los nanohilos de ZnO en un "suspiro" y nos enseñó cómo. Y mucho que suspiramos intentándolos crecer los demás… Edu nos demuestra todos los días lo importante que son los químicos en todo tipo de laboratorios.

A Pedro Rodríguez, nuestro MacGyver, que nos ha fabricado aparatos complejos a partir de chatarra en unas horas y nos ha alegrado, especialmente, los viernes por la mañana. Y yo a él los lunes por la mañana. ¡¡¡¡Yupi, Yuhuu!!!!. Le agradezco también su ayuda en la fabricación de dispositivos electrónicos, entre ellos el aparato de dielectroforesis. También por sus frases, las cuales son lecciones ejemplares sobre la vida diaria, como "todo equipo electrónico funciona mejor si está enchufado" y "el que tiene boca se equivoca".

A Tomás Vallés, José Luis Castaño y a Luis García que me enseñaron que la electrónica no era sólo cosa de gente rara. Tres grandes genios con extensos conocimientos de electrónica. Sus clases de electrónica de "campo" con Arduino han permitido que me quitase una espina que tenía clavada desde cierto examen de Física en primero de licenciatura de Químicas, el cual trató sobre circuitos básicos. Desde entonces, siempre había querido cacharrear con resistencias y LEDs. Ellos me lo pusieron fácil desde el principio.

A Alejandro Braña. Gracias a él he profundizado mucho mis conocimientos en espectrofotometría y, sobre todo, las células solares. Ahora que lo veo todo en conjunto, me doy cuenta que sólo conocía el tema de forma muy básica.

A Manuel Cervera y María Jesús Hernández, por explicarme una y otra vez el funcionamiento del elipsómetro. A base de insistir se me quedaron fijos los conocimientos.

A Andrés Redondo, ¡¡¡Qué no me he olvidado de ti, ehhh!!! Con el que aprendido muchas curiosidades de las Matemáticas y las estadísticas de la vida diaria. Yo a él, por supuesto, le he contado otras tantas de la Química.

A Basilio Javier García y Nair López, que dedicó parte de su tiempo en enseñarme el sistema de crecimiento Chemical Beam Epitaxy (CBE). La primera vez que lo vi, me pareció un equipo sacado de alguna serie de ciencia-ficción.

A todo el grupo de la profesora Encarnación Lorenzo: Félix, Mónica, César, Marta, María, Iria y Emiliano, que me ayudaron en cualquier duda que tuviese a lo largo de estos

años. Mención especial a Tania, conocida formalmente como “la artista del ADN”, capaz de pegar esta biomolécula en las superficies más inhóspitas. También agradecer a mi breve compañero de pádel Abraham, con quien gané el primer torneo interdepartamental de pádel. El trofeo siempre estará visible en mi casa.

A los nueva generación de doctorandos del grupo ELySE, Flavio y Sergio, que espero que aprendan mucho de esta tesis y que disfruten estos años. Solamente podemos obtener el doctorado una vez.

También me gustaría agradecer al Departamento de Física Aplicada por la formación recibida y, en especial, a su secretaria Beatriz Luna por todas las gestiones en las que me ayudado a lo largo de todos estos años.

Al gran equipo del Servicio Interdepartamental de Investigación (SIdI) dentro del cual se han realizado muchas medidas presentadas en esta tesis. Entre ellos, a Isidoro “Isi” Poveda, por las imágenes de SEM. Y, por supuesto, por enseñarme un deporte muy poco conocido, el tiro con arco. A Pascual y a Luis, por las medidas de FTIR y por explicarme la técnica una y otra vez. Y a Noemí, por las medidas de XRD.

Y, como no, a todos aquellos que me acompañaron durante la carrera de Química. A Jaime, Gong, Diego, Sara, Goma… quiero decir Alberto, María Jesús, Sergio, Mario, y Ana. Empezamos la carrera todos siendo como niños y terminamos... ¿igual? Bueno, yo espero que hayamos acabado mejor.

Por supuesto, agradecer a mi familia por el apoyo dado durante estos años, de principio a fin. En especial, a mi madre por aguantarme y motivarme desde hace 29 años de los cuales sólo me acuerdo la mitad. Y por supuesto, por escuchar la presentación de la tesis una y otra vez. A mi hermano que también está siguiendo la eterna senda del doctorado.

También agradecer a la Comunidad de Madrid por el apoyo económico en los proyectos AVANSENS (Ref. S2009/PPQ-1642) y NANOAVANSENS (Ref. S2013/MIT-3029), al Ministerio de Economía y Competitividad por los proyectos CTQ2014-53334-C2-1-R y CTQ2014-53334-C2-2-R, y al Ministerio de Ciencia e Innovación por el proyecto TEC2010-20796, en los que he participado.

Y sin más dilación, aquí están los resultados de este trabajo.

Abstract

The main scope of this thesis comprises the development and characterization of new photodetectors and biosensors. This work can be divided in two parts. The first part deals with the growth and manipulation of two types of metal oxide semiconductor nanowires (NWs) to fabricate photodetectors in different spectral regions. The second part studies the development of ellipsometric biosensors based on the surface plasmon resonance of gold thin films and gallium nanoparticles.

ZnO and CuO NW-based photodetectors. CuO NWs have been grown by direct oxidation of Cu foils under ambient pressure at different temperatures. The oxidized product has been analyzed by different surface characterization techniques. To manipulate and to align the NWs between electrodes, dielectrophoresis (DEP) has been proposed, by applying AC electric fields in these electrodes. DEP has been performed by drop-casting NWs (droplet DEP) on n-type Al-doped ZnO (AZO) electrodes, previously defined on SiO_2/Si substrates. Both, the frequency and effective voltage of the sinusoidal waveform have been optimized in order to align the highest number of NWs. Electro-optical characteristics of CuO NW-based devices have been studied. They have exhibited a responsivity of 9.3 A/W under illumination of the device with a red light emitting diode. Furthermore, fast time responses have been found at 5-20 μs, due to the n-p-n heterojunction formed between the n-type AZO electrodes and the p-type CuO NWs.

On the other hand, ZnO NWs have been grown by vapor-phase transport. NW dispersions have been obtained by sonication of the growth substrate, the same procedure performed for CuO NWs. Besides ZnO NWs, these dispersions contain a large amount of amorphous clusters coming from the growth substrate. In order to remove these clusters, a sedimentation process has been performed by testing different solvents. ZnO NWs have been aligned by DEP between AZO electrodes, defined on glassy substrates. The AZO and the glassy substrate have been used to take advantage of their transparency. In order to simplify and optimize the alignment process, the fabrication of a portable home-made DEP system has been carried out. An optical device has been included in the system to monitor the NW dispersion during DEP. Additionally, an inductance-capacitance-resistance (LCR) meter has been connected to the system, allowing the estimation in the number of aligned NWs and the detection of anomalies in real-time through parallel resistance measurements. The electro-optical characteristics of the ZnO NW-based

devices have been studied. Response times have been obtained in the 5-10 seconds range, whereas a responsivity up to 10^6 A/W has been estimated. The transparent properties of the ZnO NW-based light sensor have enabled its use under front- and back-illumination without any performance loss.

Plasmonic-based ellipsometric biosensors. In this work, two biosensing configurations have been used. The first configuration has consisted of the combination of the Kretschmann approach and spectroscopy ellipsometry, denoted as total internal reflection ellipsometry (TIRE) mode. AZO has been used as an adherent layer between Au and the glassy substrate, taking advantage of its transparent characteristics at the Au resonance energy in the visible spectral region. As a case of study, glutathione (GSH), a low molecular weight biomolecule, has been chosen because of its biological importance in almost all living organisms. An antibody, selective to GSH, has been used as the recognition element in this biosensor. The AZO/Au bilayer has been previously functionalized with a thiolic molecule, the DTSP, in order to immobilize the antibody through the nucleophilic attack of the antibody primary amino groups to the terminal N-succinimidyl esters of the DTSP. To increase the sensitivity of the current biosensor, GSH-capped gold nanoparticle conjugates (GSH-AuNPs) are used as signal amplifiers. Competitive immunoassays have been performed between free GSH and GSH-AuNPs, both of them competing for the antibody active sites. A limit of detection of 6 nM has been estimated.

The second configuration is based on the measurement of the plasmonic resonance of gallium nanoparticles (GaNPs) by external reflection ellipsometry. Close-packed arrays have been directly deposited on silicon substrates by thermal evaporation. The GaNPs plasmonic properties have been studied with the Mie theory and the discrete dipole approximation. The NPs have been characterized by different techniques to determine its structure and composition. The optical behavior of the GaNPs/Si platform has been studied by measuring the pseudodielectric function by spectroscopic ellipsometry. Under certain conditions of photon energy and incidence angle, a reversal of polarization handedness (RPH) has arisen after reflection on the platform surface. This RPH condition has been proved to be sensitive to changes in the refractive index surrounding the NPs, prompting its use for biosensing purposes. The biosensing capabilities of the GaNPs/Si platforms have been demonstrated through the development of both an immunosensor for GSH and a DNA biosensor. For the immunosensor, the NP

surface has been functionalized with the DTSP monolayer to further anchor the antibody. The immunological recognition between the GSH and the antibody has been evaluated, obtaining a limit of detection of 10 nM. On the other hand, a DNA biosensor for the detection of a *H. Pylori* sequence has been developed by using a thiolated capture probe as the recognition element. The capture probe chain has been kept standing with an additional functionalization step with 6-mercapto-1-hexanol, assisting the recognition event. The biosensor has shown a quite low limit of detection of 6.0 pM. Additionally, a good selectivity has been found through two experiments. The first one has comprised the discrimination of single nucleotide polymorphisms (SNPs) in *H. Pylori* sequences with respect to the fully complementary one. The second experiment has been the detection of *H. Pylori* sequences in presence of different concentrations of *E. Coli* DNA strands, acting as a possible interference. Finally, the applicability of the GaNPs/Si platforms for the analysis of real genomic DNA extracted from cells have been shown. As a case of study, the detection of DNA mutated forms that cause the Cystic Fibrosis disease has been accomplished. This has been a particularly relevant result, opening the way to commercialize the platform in the near future.

The research performed in this thesis was funded by the following projects: AVANSENS (S2009/PPQ-1642) and NANOAVANSENS (S2013/MIT-3029) spanish projects from by the Comunidad Autónoma de Madrid; CTQ2014-53334-C2-1-R and CTQ2014-53334-C2-2-R projects from the Ministry of Economy and Competitiveness of Spain; TEC2010-20796 project from the Ministry of Science and Innovation of Spain.

Resumen

El principal objetivo de esta tesis comprende el desarrollo y caracterización de nuevos fotodetectores y biosensores. Este trabajo se puede dividir en dos partes. La primera parte trata sobre el crecimiento y manipulación de dos tipos de nanohilos (NWs) de óxidos metálicos semiconductores para fabricar fotodetectores en diferentes regiones espectrales. La segunda parte estudia el desarrollo de biosensores elipsométricos basados en la resonancia del plasmón superficial de capas finas de oro y nanopartículas de galio.

Fotodetectores basados en nanohilos de ZnO y CuO. Los nanohilos de CuO se han crecido mediante oxidación de láminas de Cu a presión ambiente a diferentes temperaturas. El producto obtenido se ha analizado mediante diferentes técnicas de caracterización superficial. Se ha propuesto la dielectroforesis (DEP) para manipular y alinear los NWs entre electrodos, aplicando campos eléctricos AC. La DEP se ha llevado a cabo mediante depósito por goteo de la dispersión con NWs, sobre electrodos de ZnO dopados con Al (AZO) previamente definidos sobre sustratos Si/SiO_2. Tanto la frecuencia como el voltaje efectivo de la onda sinusoidal aplicada han sido optimizados con el objetivo de alinear el mayor número de NWs. Las características electro-ópticas de los dispositivos de NWs de CuO han sido estudiadas. Estos dispositivos han mostrado una responsividad de 9.3 A/W bajo iluminación con un LED rojo. Además, se han estimado unos tiempos de respuesta rápidos, alrededor de 5-20 μs, debido a la heterounión n-p-n formada entre los electrodos de AZO tipo n y los NWs de CuO tipo p.

Por otra parte, los NWs de ZnO se han crecido mediante transporte en fase vapor. Se han obtenido dispersiones de NWs mediante sonicación del sustrato de crecimiento, con un procedimiento similar al utilizado con los NWs de CuO. Además de los NWs de ZnO, estas dispersiones contienen una gran cantidad de estructuras amorfas, provenientes del sustrato de crecimiento. Se ha llevado a cabo un proceso de sedimentación para eliminar dichas estructuras, probando diferentes disolventes. Los NWs de ZnO se han alineado mediante DEP entre electrodos de AZO, definidos sobre sustratos transparentes. Se han utilizado el AZO y el sustrato transparente para aprovechar sus propiedades transparentes. Se han construido un sistema portable de DEP para simplificar y optimizar el proceso de alineamiento. Se han incluido un dispositivo óptico en este sistema para monitorizar la dispersión durante la DEP. Además, se ha conectado un medidor de inductancia-capacitancia-resistencia (LCR), el cual ha permitido estimar el número de

NWs alineados y detectar anomalías en tiempo real mediante medidas de la resistencia paralela. Se han estudiado las características electro-ópticas de los dispositivos basados en NWs de ZnO. Se han obtenido tiempos de respuesta en el rango de los 5-10 segundos, y una responsividad de hasta 10^6 A/W. Las propiedades transparentes de sensor han permitido su uso bajo iluminación desde ambos lados del dispositivo sin pérdidas significativas entre ambas configuraciones.

Biosensores plasmónicos elipsométricos. En este trabajo se han utilizado dos configuraciones para el biosensado. La primera configuración ha consistido en la combinación de la arquitectura Kretschmann y la elipsometría espectroscópica, denominada elipsometría de reflexión total interna (TIRE). El AZO se ha utilizado como capa adherente entre la capa fina de Au y el sustrato vítreo, aprovechando sus propiedades transparentes en la energía de resonancia del Au situada en la región espectral del visible. Como caso de estudio se ha escogido la detección el glutatión (GSH), una biomolécula de bajo peso molecular, debido a su importancia biológica en casi todos los organismos vivos. Se ha utilizado un anticuerpo, selectivo al GSH, como elemento de reconocimiento en este biosensor. La bicapa AZO/Au se ha modificado químicamente con un tiol, el DTSP, para inmovilizar el anticuerpo mediante ataque nucleofílico de los grupos amino primario del anticuerpo al grupo N-succinimidilester del DTSP. Para aumentar la sensibilidad del biosensor, se han sintetizado conjugados de GSH sobre nanopartículas de oro (GSH-AuNPs), como amplificadores de señal. Se han llevado a cabo immunoensayos competitivos entre el GSH libre y los conjugados GSH-AuNPs, ambos compitiendo por los sitios activos del anticuerpo. Se ha estimado un límite de detección de 6 nM.

La segunda configuración se basa en la medida de la resonancia plasmónica de las nanopartículas de galio (GaNPs) mediante elipsometría de reflexión externa. Arrays de GaNPs se han depositado directamente sobre sustratos de silicio por evaporación térmica. Las propiedades plasmónicas de las GaNPs se han estudiado con la teoría de Mie y la aproximación discreta de dipolos. Estas NPs se han caracterizado por diferentes técnicas para estudiar su estructura y composición. El comportamiento óptico de las plataformas GaNPs/Si han sido estudiadas midiendo la función pseudodieléctrica mediante elipsometría espectróscopica. Bajo ciertas condiciones de energía y ángulo de incidencia, se ha producido una inversión en el sentido de la polarización de la luz (RPH) tras la reflexión sobre la superficie de la plataforma. Esta condición RPH ha mostrado

sensibilidad a los cambios en el índice de refracción que rodea a las NPs, dando lugar a su uso para el biosensado. Las capacidades biosensoras de las plataformas GaNPs/Si se han demostrado mediante el desarrollo de un immunosensor para GSH y un biosensor para ADN. Para el immunosensor, la superficie de las NPs se ha modificado con DTSP para luego anclar el anticuerpo. El reconocimiento entre el GSH y el anticuerpo se ha evaluado, obteniendo un límite de detección de 10 nM. Por otra parte, se ha desarrollado un biosensor de ADN para la detección de una secuencia del patógeno *H. Pylori*, utilizando una sonda tiolada como elemento de reconocimiento. La sonda se ha mantenido erguida mediante una funcionalización adicional de la superficie de las NPs con 6-mercapto-1-hexanol, facilitando el proceso de reconocimiento. El biosensor ha mostrado un límite de detección de 6.0 pM. Además, se ha demostrado una gran selectividad mediante dos experimentos. El primero ha consistido en la discriminación de polimorfismos de nucleótidos simples (SNPs) en secuencias de *H. Pylori*, con respecto a la cadena complementaria. El segundo experimento se ha basado en la detección de secuencias de *H. Pylori*, en presencia de diferentes concentraciones de secuencias de *E. Coli* actuando como posible interferente. Finalmente, se ha demostrado la aplicabilidad de las plataformas para el análisis de ADN genómico extraído de células. Como caso de estudio, se ha llevado a cabo la detección de ADN mutado causante de la enfermedad de la Fibrosis Quística. Este ha sido un resultado particularmente relevante, abriendo el camino a comercializar la plataforma en un futuro próximo.

La investigación llevada a cabo en esta tesis ha sido financiada por los siguientes proyectos: AVANSENS (S2009/PPQ-1642) y NANOAVANSENS (S2013/MIT-3029) de la Comunidad Autónoma de Madrid; CTQ2014-53334-C2-1-R y CTQ2014-53334-C2-2-R del Ministerio de Economía y Competitividad de España; TEC2010-20796 del Ministerio de Ciencia e Innovación de España.

Abbreviations

AC	Alternating current
AL	Aligned out of the site
ALS	Aligned in site
AntiGSH	Antibody specific to GSH
AuNPs	Gold nanoparticles
AZO	Aluminum doped zinc oxide
BE	Binding energy (in XPS)
CE	Counter electrode
CF1-SH	Thiolated probe sequence from the exon 11 of CFTR
$CF2_{WT}$	Complementary wild type sequence from the CFTR
$CF2_{MUT}$	Mutated type sequence from the CFTR
CFTR	Cystic fibrosis transmembrane conductance regulator gene
Cit-AuNPs	Aqueous citrate-stabilized gold nanoparticles
DC	Direct current
DDA	Discrete dipole approximation
DEP	Dielectrophoresis
DMSO	Dimethyl sulfoxide
DNA	Deoxyribonucleic acid
DTSP	3,3′-dithiodipropionic acid di(N-succinimidyl ester)
EDX or EDAX	Energy dispersive x-ray spectroscopy
EMA	Effective medium approximation
FTIR	Fourier-transform infrared spectroscopy
GaNPs	Gallium nanoparticles
GSH	L-reduced glutathione
GSH-AuNPs	Glutathione-gold nanoparticles conjugates
HP1-SH	Thiolated synthetic probe sequence from *Helicobacter Pylori*
$HP2_{C}$	Complementary synthetic sequence from *Helicobacter Pylori*
$HP2_{SNP}$	Single nucleotide polymorphism synthetic sequence from *Helicobacter Pylori*

$HP2_{NC}$	Non-complementary synthetic sequence from *Helicobacter Pylori*
ICDD	International Centre for Diffraction Data
IR	Infrared
ITO	Sn-doped In_2O_3
LCR	Inductance capacitance resistance meter
LED	Light emitting diode
LSPR	Localized surface plasmon resonance
MCH	1-mercaptohexanol
MO	Metal oxide
NAL	Non-aligned
NPs	Nanoparticles
NTSP	N-succinimidyl-3-thiopropionate
NWs	Nanowires
PCR	Polymerase chain reaction
PTFE	Polytetrafluoroethylene
RE	Reference electrode
RSD	Relative standard deviation
SAM	Self-assembled monolayer
SCE	Standard calomel electrode
SCR	Space charge region
SD	Standard deviation
SEM	Scanning electron microscopy
SNP	Single nucleotide polymorphism
SP	Surface plasmons
SPR	Surface plasmon resonance
TCO	Transparent conductive oxides
TEM	Transmission-electron microscopy
TIR	Total internal reflection
TIRE	Total internal reflection ellipsometry
UV	Ultraviolet

VPT	Vapor-phase transport
VLS	Vapor-liquid-solid
VS	Vapor-solid
WE	Working electrode
XRD	X-ray diffraction
XPS	X-ray photoelectron spectroscopy

Index

Acknowledgements I

Abstract V

Resumen IX

Abbreviations XIII

1. Introduction 1

1.1. Semiconductor nanostructures 1

1.1.1. ZnO nanowires 3

1.1.2. CuO nanowires 10

1.2. Al-doped ZnO (AZO) 16

1.3. Plasmon resonance biosensors 19

1.3.1. Non-ellipsometric biosensors 21

1.3.2. Ellipsometric biosensors 25

1.4. Thesis content 28

References 30

2. Materials and methods 39

2.1. Dielectrophoresis physics 39

2.2. Ellipsometry physics 44

2.2.1. Ellipsometric functions definition 44

2.2.1.1. Air/substrate structure 46

2.2.1.2. Air/film/substrate structure 48

2.3. Surface plasmon physics 49

2.4. Localized surface plasmon physics 53

2.4.1. Quasi-static approximation 53

2.4.2. Discrete dipole approximation 56

2.5. Biological recognition elements 58

2.5.1 Antibodies 58

2.5.1.1. IgG antibody structure 58

2.5.1.2. Primary reactions 60

2.5.1.3. Secondary reactions 61

2.5.2. DNA molecules 62

References 65

3. Materials and methods 69

3.1. Materials 69

3.2. ZnO nanowires growth 71
3.3. Gold nanoparticle synthesis 73
3.4. Material deposition 73
3.4.1. Deposition by magnetron sputtering 73
3.4.2. Deposition by Joule-effect thermal evaporation 75
3.5. Photolithography 76
3.6. Optical characterization 78
3.6.1. UV/Visible spectrophotometry 78
3.6.2. Fourier-transform infrared spectroscopy 79
3.7. Surface characterization 80
3.7.1. X-ray photoelectron spectroscopy 80
3.7.2. Cyclic voltammetry 81
3.8. X-ray diffraction 83
3.9. Current-voltage (*I-V*) characterization 84
3.10. Scanning electron microscopy and energy dispersive x-rays spectroscopy 85
3.11. Spectroscopic ellipsometry 86
3.11.1 Ellipsometer 86
3.11.2 External reflection ellipsometry 88
3.11.3 Total internal reflection ellipsometry (TIRE) 89
3.12. Discrete dipole approximation 91
References 93
4. CuO and ZnO nanowire-based light sensors 95
4.1. Cupric oxide nanowires growth and devices 95
4.1.1. Introduction 95
4.1.2. Cupric oxide nanowires growth 97
4.1.3. Structural characterization 98
4.1.4. Alignment by dielectrophoresis 103
4.1.5. Electro-optical characteristics of AZO/CuO NW/AZO heterojunction 106
4.1.6. Time response of AZO/CuO NW/AZO heterojuntions 108
4.1.7. Responsivity 110
4.2. Zinc oxide nanowire devices 111
4.2.1. Introduction 111
4.2.2. Sedimentation study: purification and concentration of zinc oxide nanowire dispersions 111
4.2.2.1. Physics of sedimentation 112

4.2.2.2. Purification of zinc oxide nanowire dispersions 114
4.2.2.3. Concentration of ZnO NW dispersions and calibration 116
4.2.3. Continuous-flow dielectrophoretic system 117
4.2.3.1. Preliminary characterization of the system 119
4.2.3.2. In-situ concentration control 120
4.2.4. Nanowire alignment by dielectrophoresis and real-time monitoring 121
4.2.5. Dark characteristics 125
4.2.6. Optical response 126
4.2.7. Time response and response uniformity 127
4.2.8. Responsivity 129
4.3. Conclusions 131
4.3.1. CuO NW devices 131
4.3.2. ZnO NW devices 131
References 132
5. A glutathione immunosensor based on total internal reflection ellipsometry 135
5.1. Introduction 135
5.2. AuNPs characterization and functionalization 137
5.3. Development and characterization of the biosensing platform 140
5.3.1. Suitability of the Al-doped ZnO layer 140
5.3.2. Surface modification of the biosensing platform 141
5.3.2.1. Formation of the DTSP monolayer 141
5.3.2.2. Formation of the antibody layer 143
5.3.3. Simulation of the ellipsometric response 145
5.4. Immunosensing response 146
5.4.1. Kinetics of GSH-AuNPs conjugates recognition by the antiGSH 146
5.4.2. Optimization of the GSH-AuNPs concentration 147
5.4.3. Competitive immunoassay 149
5.5. Conclusions 151
References 153
6. Ellipsometric biosensing platforms based on gallium nanostructures 157
6.1. Introduction 157
6.2. Plasmonic behavior of gallium nanoparticles: Mie theory and discrete dipole approximation 161
6.2.1. Mie theory calculations 161

6.2.2. Discrete dipole approximation calculations 163
6.3. Characterization of the nanostructured surface 166
6.3.1. GaNP deposition and characterization of size distribution 166
6.3.2. X-ray diffractometry 167
6.3.3. X-ray photoelectron spectroscopy 168
6.3.4. Ellipsometric characterization of GaNPs/Si platforms 169
6.3.4.1. Influence of evaporation time 169
6.3.4.2. Reversal of polarization handedness (RPH) 170
6.4. An immunosensor for glutathione 174
6.4.1. Development of the sensing platform 174
6.4.1.1. FTIR characterization 175
6.4.1.2. Ellipsometric characterization 176
6.4.2. Biosensor response and quantification of glutathione 178
6.5. A DNA biosensor 181
6.5.1. Development of the sensing platform 181
6.5.1.1. X-ray photoelectron spectroscopy characterization 182
6.5.1.2. Ellipsometric characterization 182
6.5.2. Biosensor response and quantification of DNA 185
6.5.3. Detection of single nucleotide polymorphisms 187
6.5.4. Study of interferences 187
6.5.5. Detection of gene mutation in real genomic DNA 188
6.6. Conclusions 191
References 193
7. Conclusions and future work 197
7.1. Nanowire-based light sensors 197
7.1.1. Conclusions 197
7.1.1.1. CuO-based light sensors 197
7.1.1.2. ZnO-based light sensors 198
7.1.2. Future work 199
7.2. An immunosensor for glutathione under total internal reflection ellipsometry 200
7.2.1. Conclusions 200
7.2.2. Future work 201
7.3. Biosensing platforms based on gallium nanostructures 202
7.3.1. Conclusions 202
7.3.2. Future work 204

7. Conclusiones y trabajo futuro 207

7.1. Sensores de luz basados en nanohilos 207

7.1.1. Conclusiones 207

7.1.1.1. Sensores de luz basados en CuO 207

7.1.1.2. Sensores de luz basados en ZnO 208

7.1.2. Trabajo futuro 209

7.2. Inmunosensor para glutatión mediante elipsometría por reflexión total interna 210

7.2.1. Conclusiones 210

7.2.2. Trabajo futuro 211

7.3. Plataformas biosensoras basadas en nanoestructuras de galio 212

7.3.1. Conclusiones 212

7.3.2. Trabajo futuro 215

8. Appendix A 217

1. Introduction

1.1. Semiconductor nanostructures

Great advances in integrated circuit technologies have been done in the last decades that have resulted in electronic devices with lower power consumption and lower costs. For strengthening the interaction between the integrated circuit technologies and the surrounding environment, the search for new ways to enhance integrated sensor characteristics has given rise to the study of one-dimensional structures, such as carbon nanotubes and nanowires (NWs).

NWs have been researched as potential building blocks in micro and nanoelectronics during the last years. NWs can be prepared through reproducible methods in high yield, which is an important feature for the fabrication at a large scale. They have been made of different materials, semiconductor NWs being one of the most abundant in the literature. The good control of the growth process has offered the possibility of synthesizing high crystalline semiconductor NWs out of binary compounds and ternary alloys with different sizes and compositions.[1, 2] This control is particularly relevant taking into account that the NW electrical and optical properties strongly depend on the NW size. The greatest advantages of semiconductor NWs come from their large surface-to-volume ratio, which leads to enhanced biological and chemical sensitivities. This advantage is the main reason why these nanostructures can outperform planar thin films in those particular fields.

There are two basic approaches to produce NWs: top-down and bottom-up. The first one consists in the reduction of the film dimensions to the nanometer size by etching, whereas the second one comprises the assembly of atoms or molecules on a surface to grow a nanostructure. The latter approach is the most common and has been extensively reported in the literature.

Among all bottom-up growth techniques, vapor phase transport (VPT) is one of the most widely employed for producing semiconductor NWs. It comprises the vaporization of a solid source, and its transport in gas phase to a substrate where it condensates. The VPT growth mechanism can be attributed to either vapor-liquid-solid (VLS) or vapor-solid (VS), depending on the presence or not of a liquid phase atop the nanostructure. The first one was proposed by Wagner and Ellis in 1964 for the growth of Si whiskers using Au as a catalyst.[3] The growth was performed by heating Au nanoclusters deposited on a substrate to form liquid metallic droplets. These droplets act as a sink for the Si vapor species, previously vaporized from a solid source, giving rise to the formation of a Au-Si eutectic alloy. The supersaturation of this alloy leads to the nucleation of the solid Si semiconductor. The preferential orientation of the resulting Si NWs is determined by the substrate orientation. This behavior is denoted as epitaxial growth. In the successive years, a wide range of semiconductor NWs have been grown through the VLS mechanism ranging from pure semiconductors, such as Ge,[4] to semiconductor compounds, such as GaAs,[5] InAs,[6] ZnO,[7] etc.

Semiconductor NWs have been used in many applications. Among them, it is remarkable the interest on the fabrication of field-effect transistors (FET) made of Si NWs.[8] The choice of this material has been motivated due to the dominant role of Si in the Industry. Furthermore, recipes for the modification of its electrical properties via extrinsic doping with boron and phosphorus are widely known. In a FET device, the NW is located between two electrodes, the source and the drain, defined on an insulating substrate. A metallic contact, placed on the substrate backside and denoted as gate, allows controlling the electric conductivity of the semiconductor NW.

Another extended application has been the development of photodetectors. Photoconductivity can be defined as the material property in which electrical conductivity increases due to the absorption of electromagnetic radiation. In a light detector, photons of an incident light beam are absorbed by the material, making the electrons transit from a lower to a higher energy state. In the photoconductive operation mode, an external DC

bias is applied and the voltage drop is measured in a reference resistance connected in series under a voltage divider configuration. From the Ohm's law, the photocurrent is calculated. Photoconductivity strongly depends on the surface states. Due to the NW low dimensionality and geometry, NWs contain an extremely high density of those states.[9] Surface states exist due to the termination of lattice periodicity at the surface, surface defects, adsorption of gas molecules from the ambient (like O_2)…, and can notably change the optoelectronic properties of the NW. The above concept represents one of the most important advantages of low dimensional structures for the photodetector technology over higher dimensional sensors, such as thin films.

NW photodetectors have been made of different materials including compounds from group III-V (GaAs, AlGaAs, etc.),[10, 11] group IV (Si and Ge),[12, 13] group VI (Se),[14] group II-VI (CdS, ZnTe, etc.),[15, 16] and metal oxides (ZnO, CuO, etc.).[17, 18] Among all the NW photodetectors, ZnO has been one of the most widely studied in the bibliography.

1.1.1. ZnO nanowires

STRUCTURE

ZnO is semiconductor material with a direct bandgap of around 3.3 eV. ZnO can be found in two crystalline structures: hexagonal wurtzite and cubic zinc blende. Wurtzite is the stable structure under ambient conditions, whereas the zinc blende needs much higher pressure conditions. Its lattice parameters are a = 3.2499 Å, b = 3.2499 Å, c = 5.2066 Å, $\alpha = \beta = 90^{\circ}$ and $\gamma = 120^{\circ}$ (data taken from the powder diffraction file #04-008-8197 of the International Centre for Diffraction Data, ICDD). The c/a ratio of around 1.60 is close to the ideal value for a hexagonal cell (1.633). The u parameter, defined as the length of the anion-cation bond parallel to the c-axis in units of c, is close to 0.383, where the ideal value is 0.375. Wurtzite belongs to the C_{6v}^4 space group, in the Schoenflies notation, and the P63mc space group, in the Hermann-Mauguin notation.[19]

The structure of wurtzite ZnO can be described as a series of alternating planes of Zn^{2+} and O^{2-} atoms tetrahedrally coordinated and stacked along the c-axis (Figure 1.1). The whole crystalline structure is non-centrosymmetric, which confers piezoelectric properties to ZnO.

ZnO can preferentially grow along three directions: $<10\bar{1}0>$, $<1\bar{2}10>$ and $<0001>$. Whereas the growth in the first two directions yields belt-shaped structures, the synthesis along $<0001>$ produces NWs.

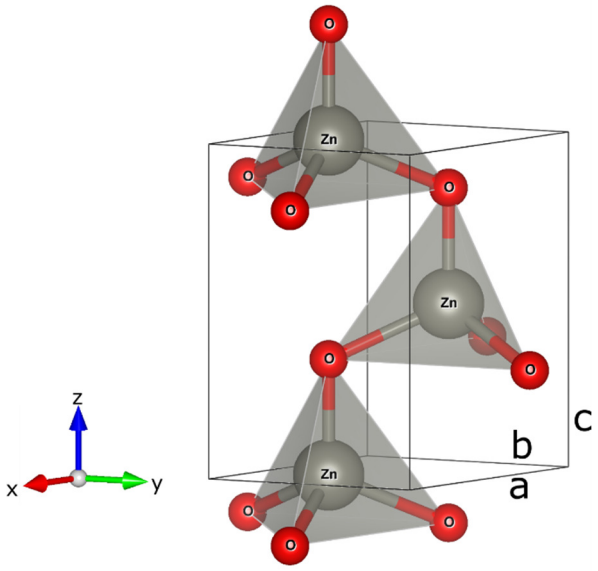

Figure 1.1. ZnO wurtzite crystalline structure.

SYNTHESIS

The growth of ZnO NWs has been performed by a wide range of techniques, such as VPT, pulsed-laser deposition (PLD), hydrothermal methods, chemical vapor deposition, etc. The next sections include the description of each method and the main results achieved.

Pulsed-laser deposition

PLD is a physical deposition growth technique that has been used for the synthesis of thin films and nanostructures. It comprises a high power laser, which emits pulses at a certain frequency on a target located inside a high vacuum chamber (Figure 1.2). This target comprises the pure semiconductor materials, in this case ZnO. The laser pulses vaporize the target atoms (ablation) forming a plasma plume that interacts physically and chemically with the background ambient. Finally, the ablated material condenses on the

growth substrate, forming the NW. The growth substrate often contains a metallic catalyst to assist the NW growth. The advantage of this method is that it does not require any chemical solvent that can left residues and contaminate the NW. However, this method is not scalable and, thus, cannot be used for large scale synthesis.

Vertically aligned ZnO NWs were grown with PLD by Rahm et al.[20] A substrate containing AuNPs was introduced in the growth chamber. After the process, NWs with a length of 1 μm and diameters up to 150 nm were obtained, which depends on the number of laser pulses.

A similar work was performed by Tien et al. on a substrate with a thin film of ZnO evaporated to assist the growth.[21] An improvement of the length was clearly visible from their surface scans. Vertically aligned NWs with 6 μm length and diameters of 50-90 nm were observed.

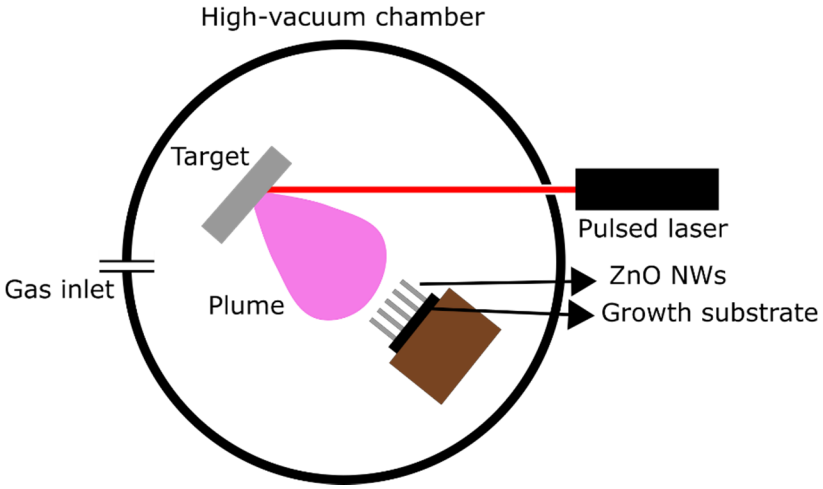

Figure 1.2. Scheme of the PLD process in a vacuum chamber.

Hydrothermal synthesis

This method is quite simple. The reagents are mixed in aqueous solution and introduced in an autoclave to heat up the solution to the reaction temperature. Finally, the product is washed and dried. In some procedures, a substrate with a ZnO layer is introduced within the solution to induce the growth on it. The solution contains a Zn salt ($ZnCl_2$, $Zn(CH_3COO)_2$, etc.) and a base (NaOH, KOH, etc.). The mechanism includes the chemical reaction of the salt with the alkali to form Zn hydroxides. The hydroxide

decomposes at high temperature into ZnO and H_2O. The advantage of this method is that it does not require any expensive vacuum system and that different ZnO nanostructures can be obtained by changing the experimental parameters.

A mixture of ZnO NWs and nanobelts were grown with this method by Hu et al. They reported the use of Na_2CO_3 as the alkali reagent.[22] The nanostructure physical dimensions were controlled by varying the alkali concentration.

Recently, Li et al. synthetized ZnO NWs on a piece of cellulose paper with ZnO NPs, acting as a seed layer. After the growth process, silver contacts were deposited.[23] The ZnO-NW containing paper was used as a UV light and touching sensor.

Vapor-phase transport

As mentioned above, VPT is probably the most widespread method to grow NWs. VPT can be performed through either these two mechanisms: vapor-solid (VS) and vapor-liquid-solid (VLS).

In VLS, an array of metallic nanostructures (Au, Ag, etc) is deposited along the substrate surface by drop-casting of colloidal nanostructure solution or by evaporating metallic thin films. The substrate and Zn source are introduced inside the furnace. During the heating up process, the nanostructures become liquid droplets. These droplets act as a sink for the Zn and O_2 vapor species, reacting inside the droplet to form ZnO (Figure 1.3). When the droplet supersaturates, the nucleation of solid ZnO occurs and the NW starts to grow. As an example, Yang et al. synthesized ZnO NWs with this method.[7] In that work, Au nanoclusters were deposited on a Si substrate and further introduced within the furnace along with the Zn source. A high NW density, whose NW diameter depended on the Au nanocluster size, was obtained. Other catalysts that have been used are Cu,[24] Ge[25] and Zn.[26] However, the drawback of this procedure is that the catalyst can diffuse along the nanostructure at high temperatures changing its composition.[27]

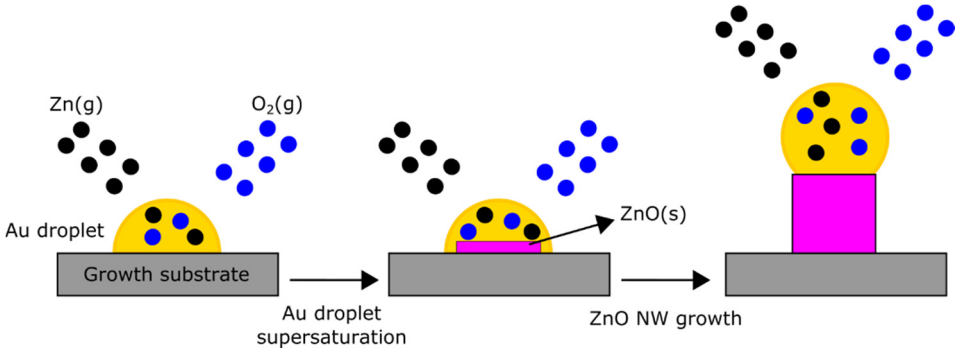

Figure 1.3. Schematic of the VLS mechanism for ZnO NW growth.

In VS, the Zn source and the growth substrate are placed on an alumina boat and introduced in the furnace. Zn and O_2 reacts to form ZnO molecules that crystallizes on the substrate surface (Figure 1.4). In VS growths, a ZnO seed layer can be pre-deposited on the growth substrate to assist the NW growth.[28] This seed layer forms nucleation sites and guides the NW growth along the $<0001>$ direction. The main advantage of this method is that the NWs can grow without the need of a metallic catalyst.

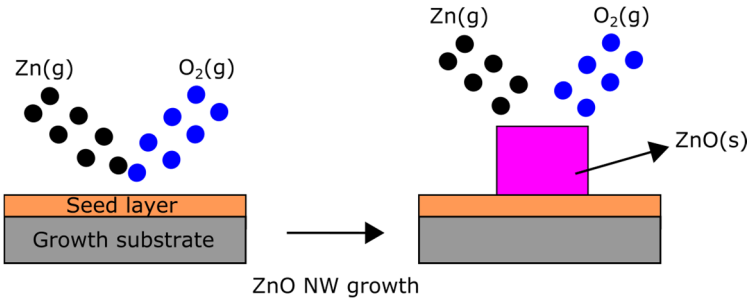

Figure 1.4. Schematic of the VS mechanism for ZnO NW growth.

ELECTRICAL PROPERTIES

ZnO is an n-type semiconductor, whose charge carriers are electrons. Electrical properties of different NWs were estimated by Chang et al. by using the field-effect transistor configuration. Electron mobilities and resistivities were ranged between 20-80 $cm^2/V{\cdot}s$ and 0.12-0.98 $\Omega{\cdot}cm$, for NWs with diameters of 120 and 88 nm, respectively.[29] Goldberger et al. estimated electron mobilities and carrier concentrations of $13{\pm}5$ $cm^2/V{\cdot}s$ and $(5{\pm}2){\cdot}10^{17}$ cm^{-3}, for NWs with diameters up to 200 nm.[30] On the other hand, Soci et al. enhanced the electron mobility up to 270 $cm^2/V{\cdot}s$.[17]

A comparison of those mobilities to that obtained for ZnO thin films (0.2-7.0 $cm^2/V{\cdot}s$)[31, 32] shows that the NWs exhibit higher values due to the absence of grain boundaries, which reduces the electron scattering mechanisms.

MECHANICAL PROPERTIES

The Young's modulus represents one of the most important parameters, describing the mechanical properties of NWs. This modulus was measured by Jiang et al. by compressing a single NW (diameter of 70 nm) with an AFM tip.[33] A value of 140 GPa, similar to that observed in ZnO thin films, was estimated. On the other hand, the dependence of the modulus with the NW diameter was measured by Chen et al.[34] A reduction of this modulus (220 to 140 GPa) was found as the diameter increased from 17 to 550 nm. The high values make ZnO NWs a promising material for the fabrication of nanocantilevers and nanoresonators.

PHOTOLUMINESCENCE PROPERTIES

ZnO NWs exhibit a strong and sharp band at 3.26 eV attributed to the near band-edge UV emission peak.[35] Additionally, they typically present a broad band in the visible spectral region at around 2.5 eV (green band) at a temperature of 10 K, as was observed by Liao et al.[36] By increasing the temperature to ambient values, the green band broadened and more band peaks arose at 2.0 (yellow band) and 2.8 eV (blue band), as a result of different ionized states of the oxygen vacancies.

UV PHOTODETECTORS

There is an extensive bibliography about the development of ZnO NWs photodetectors. One of the earliest reports about these ZnO NW photodetectors was published by Kind et al. in 2002.[37] In that work, the NWs were grown with the VPT method. The conductivity of a single NW was studied in dark and under UV illumination. The oxygen chemisorption role as a regulator of the NW photoconductivity was suggested based on the similar effect observed in ZnO thin films previously.

The transients under UV illumination and the influence of the oxygen concentration in the atmosphere was studied by Li et al. The fundamental role of O_2 readsorption during the recovery transients was demonstrated. The longest times were obtained in vacuum due to the lowest concentration of O_2.[38, 39]

High photogains, up to 10^8, for these NWs were obtained by Soci et al., thanks to the contribution of the O_2 desorption from the surface defects, suggesting a great potential as single-photon photodetectors.[17]

To enhance the optoelectronic properties different approaches have been performed, such as decorating the NWs with metallic NPs, surface functionalization and the formation of Schottky barriers.[40, 41]

Since ZnO photodetectors are developed in this work, a brief explanation of the mechanism of ZnO photodetection is provided.[17, 37] In dark, O_2 molecules are adsorbed on the ZnO surface capturing free electrons from the NW according to the following reaction:

$$O_2(g) + e^- \rightarrow O_2^-(ad) \tag{1.1}$$

and immobilizing them on surface states (electron traps). Those filled states yield a depletion layer near the surface with a strong impact on the optoelectronic properties.

Under illumination, above the ZnO bandgap, electron-hole pairs are photogenerated in the NW volume (Equation 1.2). In that scenario, the photogenerated holes migrate to the surface along the potential slope produced by the band bending, and recombine with the trapped electrons provoking the desorption of O_2 from the surface (Equation 1.3).

$$h\upsilon \rightarrow e^- + h^+ \tag{1.2}$$

$$h^+ + O_2^-(ad) \rightarrow O_2(g) + e^- \tag{1.3}$$

This process gives rise to an effective enhancement of the electron concentration in the NW and thus, the NW conductivity.

The response can be separated into several zones before and after the illumination event. These curves can be optimally fitted by using sums of exponential functions. Fast components are related to photogenerated electron-hole pairs, with short time constants,

whereas slow ones are caused by the O_2 desorption and re-adsorption processes, as described above.[17] The re-adsorption process is particularly slow, giving rise to relaxation times of several minutes and hindering its use in many applications.

OTHER APPLICATIONS

ZnO NWs have been proved to be suitable for different applications. Taking advantage of their piezoelectricity, ZnO NWs has also opened the way to the fabrication of nanogenerators to produce electricity through physical deformation of vertically aligned NWs.[42]

Another application is the development of gas sensors. Ahn et al. measured the concentration of NO_2 up to 0.5 ppm at an optimized working temperature of 225 ºC.[43] Furthermore, Wang et al. demonstrated the applicability to detect H_2.[44] A maximum sensitivity was found with a working temperature of 250 ºC, estimating a limit of detection of 20 ppm.

The use of ZnO NWs for the development of biosensors was also shown. Glucose was measured by Pradhan et al. by immobilizing the enzyme glucose oxidase on the NW surface.[45] A detection limit of 50 μM and a response time of less than 5 s were obtained.

Other typical applications, non-related to the fabrication of sensors, can be found in the literature, such as the development of solar cells[46] and UV lasers.[47]

1.1.2. CuO nanowires

STRUCTURE

CuO is a semiconductor material with a direct bandgap of around 1.2 eV, which crystallizes in a monoclinic structure. The CuO mineral is known as the tenorite. Its lattice parameters are a = 4.683 Å, b = 3.421 Å, c = 5.129 Å, α = γ = 90º and β = 99.57º. CuO belongs to the C_{2h}^6 space group in the Schoenflies notation and the C2/c space group in the Hermann-Mauguin notation (data taken from the powder diffraction file #04-008-8209 of the International Centre for Diffraction Data, ICDD).

In CuO, each Cu atom is coordinated to four coplanar O atoms forming a parallelogram, whereas each O atom is coordinated to four Cu atoms yielding a distorted tetrahedron (Figure 1.5).[48]

CuO NWs preferentially grow along two directions: $<111>$ and $<\bar{1}11>$. These two crystalline structures can be found in a single NW separated by a (111) twin plane.

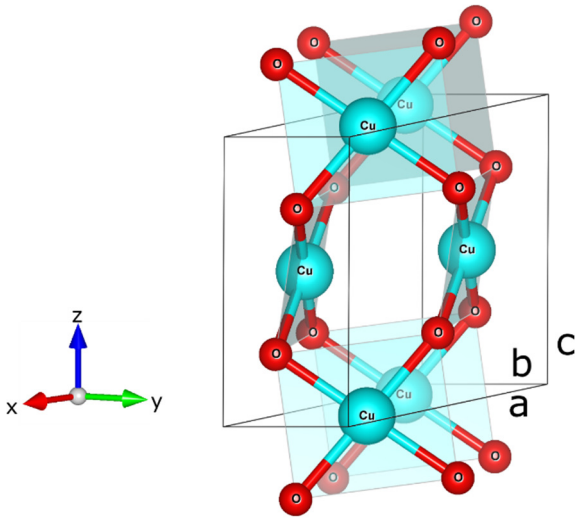

Figure 1.5. CuO tenorite crystalline structure.

SYNTHESIS

Metallic Cu has two stoichiometric oxides: cupreous oxide (Cu_2O) and cupric oxide (CuO). Both are p-type semiconductors with bandgaps of 2.0 and 1.2 eV, respectively. Their bandgaps, lying in the visible-IR spectral region, make them suitable for a wide range of photo-applications. The growth of copper oxide NWs has been mainly performed following different approaches:

Template-assisted electrodeposition

This technique describes the use of electrochemical cells (with two or three electrodes), in which porous templates are immersed within a chemical solution containing copper salts. The application of a potential to the template (working electrode) gives rise to the deposition of copper oxides on the working electrode following the

template pattern (Figure 1.6). This procedure has been mostly used for the growth of Cu_2O NWs.

Daltin et al. synthetized Cu_2O NWs on a polycarbonate membrane with nanometric pores (diameter = 90 nm and thickness = 16 μm) on a stainless steel substrate.[49] To enhance the electrochemical deposition, the template was covered with 50 nm of Au in order to increase its conductivity. The chemical solution contained Cu(II) lactate, obtained from cupric sulfate and lactic acid. Other templates and solutions can be used. Hong et al. reported the use of anodic aluminum oxide templates (pore diameter and thickness around 200 nm and 60 μm, respectively).[50] The main components of the precursor solution were $CuCl_2$ and HCl. However, poly(vinyl pyrrolidone) was included in the solution enabling the synthesis of ultra-thin NWs with diameters below 10 nm.

CuO NWs can be also obtained from this procedure. However, it requires an additional step. Hsieh et al. performed a similar procedure than that reported by Daltin et al. by using the polycarbonate membrane on a Cu foil.[51] In this case, the chemical solution was composed of $CuSO_4$ in H_2SO_4. After the application of a DC voltage to the foil, and the subsequent removal of the template, Cu nuclei were found on the substrate. The posterior oxidation at 500 ºC in an O_2 atmosphere yielded single-crystalline and long CuO NWs.

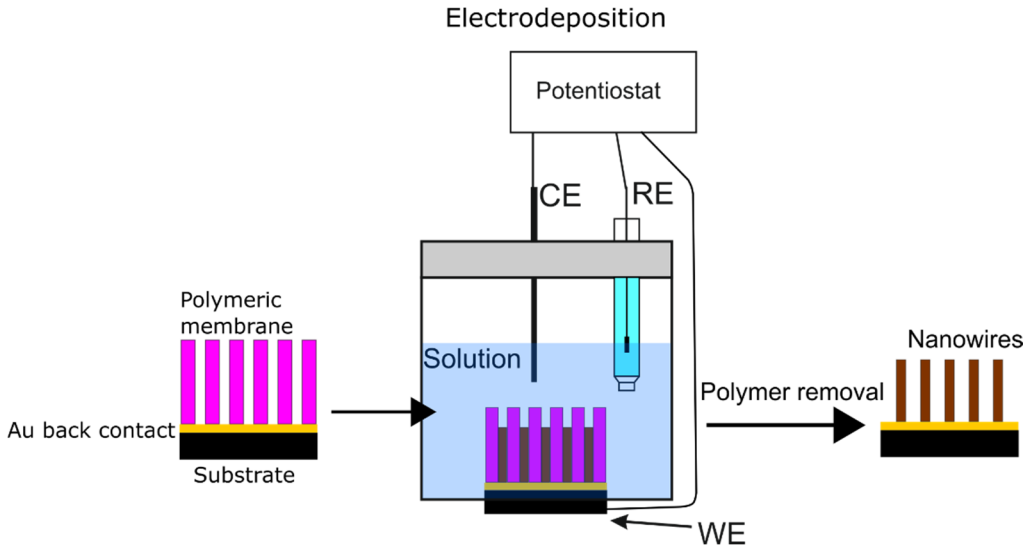

Figure 1.6. Scheme of the template-assisted electrodeposition.

Hydrothermal synthesis

This procedure comprises the heating of a solution in order to form the necessary precursor, Cu hydroxide NWs. These precursors are annealed to transform the hydroxide into CuO NWs.

Zhu et al. prepared the precursor from an aqueous solution of $CuCl_2$ and NaOH at 65 ºC.[52] After washing, filtering and drying the suspension, a calcination process was performed in air at 300 ºC. X-ray measurements confirmed the complete transformation of the precursor to CuO. SEM images showed NWs of diameters of 20-30 nm. The drawback was obtaining a certain number of broken NWs forming bundles after the calcination. A similar procedure was carried out by Li et al.[53] In that work, a more complex solution was used to form the hydroxide precursor, including the surfactant hexadecyl trimethyl ammonium bromide (CTAB). The precursor was washed and dried before being further calcinated at 400 ºC for 2 hours. An interesting study about the influence of the surfactant molar concentration was reported. By increasing its concentration, the morphology of the nanostructure changed from spheres to NWs.

The main drawback of hydrothermal synthesis is the long time and numerous steps needed to grow the NWs.

Thermal oxidation

Thermal oxidation comprises a different approach to grow CuO NWs compared to the previous methods. The NW growth process only requires heating Cu substrates, without the need of using artificial oxidizing atmospheres, chemical reagents or surface pretreatments.

One of the first publications and, probably, the most relevant describing this procedure was the work performed by Jiang et al. in 2002.[54] Cu substrates were heated in air for 4 hours. A surface scan revealed the presence of a high density of CuO NWs that grow at temperatures between 400 and 700 ºC. NW diameters were in the 30-100 nm range with lengths up to 15 μm. TEM microscopy analysis demonstrated that NWs crystalized in the monoclinic structure. Some NWs were found to be bicrystals due to the formation of a twin plane along the NW long axis. However, the growth mechanism remained unclear at that point.

A few years later, a relationship between the growth temperature and time with the NW physical dimensions was found by Xu et al. and Chen et al.[55, 56] The fact that NWs grow on a Cu_2O/CuO bilayer was also elucidated. A mechanism was proposed based on the diffusion of Cu ions from the foil to the surface through the oxidized layers.

The influence of the oxidizing atmospheres was studied by Xu et al. No NWs grew under N_2 atmospheres, whereas an increase of the partial pressure of O_2 leaded to higher density of NWs. The role of wet and dry atmospheres was studied, suggesting that H_2O might affect the nucleation of NWs although its role was unclear.[57]

On the other hand, the impact of using two Cu substrates with different purities was studied by Hansen et al. used. There were only slight variations in the NW orientation, although both substrates exhibited a high density of NWs.[58]

The ease of growth and the high NW density obtained under this procedure has made thermal oxidation the most attractive approach to obtain CuO NWs nowadays.

ELECTRICAL PROPERTIES

A p-type behavior is found in both copper oxides due to the formation of Cu vacancies.[59, 60] For a single CuO NW, the hole mobility has been estimated to vary between 2-5 $cm^2/V{\cdot}s$ by using the field-effect transistor configuration.[61] Recently, average mobilities around 0.58 $cm^2/V{\cdot}s$ and hole concentrations of $1.13{\cdot}10^{18}$ cm^{-3} have been also found by a different group.[62] Both measurements were performed for thermally grown CuO NWs.

A comparison of these mobilities to that obtained for CuO thin films (0.01 $cm^2/V{\cdot}s$) shows that the NWs exhibited higher values due to the absence of grain boundaries that reduces the hole scattering mechanisms.

MECHANICAL PROPERTIES

The Young's modulus was measured by Tan et al. by using the three-point bending test in single CuO NWs.[63] A range of 70-300 GPa was found for diameters between 80-180 nm. This decreasing behavior of the modulus with the increasing NW diameter is similar to that found in other NWs, such as ZnO NWs.

PHOTOLUMINESCENCE PROPERTIES

CuO NWs can exhibit photoluminescence at 520 nm, mainly due to surface defects or impurities that appeared during NW growth. Some NWs can present a weak band at 820 nm attributed to a mixed Cu_2O/CuO phase at the NW base.[64]

PHOTODETECTOR APPLICATIONS

The optoelectronic properties of CuO NWs are not extensively studied in comparison to other metal oxide NWs, which makes its research very appealing. Since its bandgap lies in the infrared region, CuO NWs have been proposed for full visible spectrum detection in the last few years. Hansen et al. measured responsivities of 1-8 A/W, for a single NW of 225 nm in diameter deposited between Ag electrodes, by illuminating with a white light source (power densities ranged between 1 and 45 mW/cm^2). The recovery time was estimated to be around 36 s due to the slow molecular adsorption. The fast component, limited by the RC time constant, was found to be 240 ms.

A different configuration was used by Wang et al. In that work, a 0.1 mm Cu wire was thermally oxidized to cover it with CuO NWs and immobilized it with Ag paste. Time responses in the 15-20 second range were obtained by illuminating with a laser diode (808 nm) at a power density of 0.8 mW/cm^2.[18]

OTHER APPLICATIONS

CuO NWs have received a great deal of attention because of their high performance as part of gas sensing devices. These gas sensors typically operate at high temperatures to promote the adsorption of the analyte onto the NW surface. Kim et al. measured NO_2 and CO at temperatures above 200 ºC, in the tail pipe from gasoline and diesel engines.[65] Liao et al. reported sensitivity to CO in the range of 5-1200 ppm at an operating temperature of 200 ºC.[61] In 2012, a H_2S sensor was developed by Li et al., by thermally oxidizing a Cu NW into CuO. A limit of detection in the ppb range was estimated, at an operating temperature of 180 ºC.[66]

Interesting catalytic properties have been also reported for CuO, showing potential to substitute noble metal catalysts.[67, 68] In this field, Feng et al. and Yan et al. have demonstrated the good catalytic performance of CuO NWs to transform CO into CO_2.[69, 70]

1.2. Al-doped ZnO

Transparent conductive oxides (TCOs) are semiconductor oxides that have emerged as potential transparent materials for optoelectronic applications, such as solar cells, electrodes, flat-panel displays, etc.[71] These TCOs are typically polycrystalline materials deposited on a substrate by sputtering, PLD, spray pyrolysis, etc. The idea behind a TCO is the use of wide bandgap oxides (more than 3.0 eV) beyond the visible spectral region. The problem associated to these oxides is their low conductivity. The introduction of doping impurities can considerably enhance their electrical conductivity.

The discovery of the first TCO was attributed to K. Badeker in 1907, a CdO thin film. Little use was found for this material due to the high toxicity of Cd. It was not until the 1970s when conductive oxides based on In_2O_3 were used.[72] Since then, other TCOs have been developed (based on SnO_2 or ZnO) and nowadays some of them are commercially available, being Sn-doped In_2O_3 (ITO) the most widespread.

Alternatives based on ZnO have strongly emerged due to the high toxicity and the increasing value of In. In this regard, the most attractive alternative is the n-type Al-doped ZnO (AZO) with the advantage of the low toxicity and high abundance of Al and ZnO.

SYNTHESIS AND MEASURED PROPERTIES

The fabrication and optical properties of AZO were reported by Minami et al. in the 1980s. A good transparency up to 80% in the visible region was measured for thin films with thicknesses of 400-600 nm obtained by sputtering, being opaque in the UV and the IR regions. Nevertheless, the cut-off wavelength in the IR region strongly depends on the amount of Al doping. A higher amount of Al leaded to a redshift of this cut-off wavelength due to the increasing carrier concentration. The electrical resistivities between $3.0 \cdot 10^{-4}$ and $9.0 \cdot 10^{-4}$ $\Omega \cdot cm$ were found along with carrier concentrations

between, $3 \cdot 10^{20}$ and $15 \cdot 10^{20}$ cm^{-3}, and mobilities between 10 and 30 $cm^2/V \cdot s$ for those thicknesses.

Since then, the research was focused on the improvement of its electro-optical characteristics. Several years later, Minami et al. demonstrated the influence of the substrate temperature during the deposition of AZO by sputtering.[73] An enhancement of the electrical properties was clearly measured for temperatures of at least 300 ºC due to larger migration of the sputtered ions and the improvement of the thin film crystallinity. On the other hand, Suzuki et al. improved the resistivity of AZO up to $1.4 \cdot 10^{-4}$ Ω·cm by growing thin films with PLD.[74] However, these growth techniques require expensive vacuum systems. For this reason, other authors such as Lee et al. and Pandey et al. grew AZO by using spray pyrolysis, a quite cost-effective and scalable approach.[75, 76] In this technique, the liquid precursors (acetates, nitrates or chlorates of Al and Zn) are sprayed on a heated substrate, reacting between them to form the oxidized material. The drawback is the high resistivity values obtained up-to-date ($>10^{-3}$ Ω·cm) compared to the previously shown methods. A more recent work describes the use of the sol-gel coating method, another interesting scalable technique.[77] Similar to the spray pyrolysis, the same liquid precursors were deposited on a glassy substrate by spin coating and, then, heated at 300 ºC for several minutes. After several repetitions, an additional thermal treatment was performed at 650 ºC during 1.5 hours. A resistivity in the range of $2.0 \cdot 10^{-4}$-$4.0 \cdot 10^{-4}$ Ω·cm was measured, improving the results obtained by spray pyrolisis.

CHEMICAL ETCHING

Similarly to ZnO, AZO can be etched by using acidic solutions.[78] A good review of the etching mechanism for different acids was thoroughly described by Hüpkes et al.[79] Briefly, in a polycrystalline film, the etching solution tends to initiate the attack on the grain boundaries, due to their high surface energy, forming characteristic craters at locations where the surface energy reaches the highest values. The crater depth and width was found to depend on the physical and chemical properties of the etching agent, concentration and solution temperature. The last two typically showed an increasing number of craters and, thus, high etching rates.

One of the most commonly used etching agents is HCl, whose reaction is: $ZnO(s) + 2H_3O^+(l) \rightarrow Zn^{2+}(l) + 3H_2O(l)$. The H_3O^+ ions comes from the dissociation of HCl into H^+ and Cl^- in water: $HCl + H_2O \rightarrow H_3O^+ + Cl^-$. This strong inorganic acid easily removes AZO from the substrate. Fast etching rates as well as high lateral etchings were observed for HCl, which complicate its use for patterning purposes. One interesting point was that the number of etching points could be controlled with HCl concentration. A similar situation occurred when acetic acid was studied but with a lower etching rate.

On the other hand, to reduce the lateral etching, the use of phosphoric acid was proposed due to the increase of the viscosity in the etching solution. Lee et al. observed that this acid assisted to obtain quite steep ZnO sidewalls in contrast to HCl.[80] Since then, diluted mixtures of phosphoric and acetic acids in water have been suggested for AZO.[81, 82]

APPLICATIONS

AZO has been used for several applications as transparent electric contacts, substituting ITO, such as solar cells,[83] light emitting diodes[84] and displays.[85] Thin films of AZO have also showed potential applicability for the development of gas sensors. Hjiri et al. measured CO molecules at the sub-ppm levels with AZO obtained with the sol-gel technique.[86] On the other hand, Sahay et al. deposited AZO by spray pyrolysis and measured methanol in air in the 100-500 ppm range.[87]

One special application, recently found in the bibliography, is its use as an intermediate layer between Au and glassy substrates, being an alternative to Cr and Ti, for the development of plasmonic sensors. Chang et al. studied its potential use in 2010 by fabricating an immunosensor.[88] Briefly, in plasmonic sensors, the visible light must go through the substrate and the intermediate film in order to reach the Au thin film and excite the surface plasmon resonance. The advantage of AZO over metallic Cr or Ti is its high transparency at the resonance energies of Au thin films.

1.3. Plasmon resonance biosensors

The first observation of the surface plasmon resonance (SPR) started at the beginning of 20th century in 1902, when Wood observed a patterned of anomalous dark and light bands on the reflected light during the illumination of a mirror with a diffraction grating on its surface.[89] A physical explanation was not provided but Wood reported that these singularities only appeared when the incident light was p-polarized (electrical vector parallel to the incident plane). The interpretation to this phenomenon was initiated by Rayleigh,[90] which was useful in predicting the band position but not their shape or intensity. It was further refined by Ugo Fano who explained the discrepancy between the theoretical predictions by Rayleigh and the experimental data by Wood.[91]

In 1952, Pines and Bohm discussed the behavior of electrons in a dense electron gas.[92, 93] An energy loss associated to an organized oscillation of the entire system, the so-called plasma oscillation, was found. Later, in 1957, Ritchie reported a new energy loss during fast electron impacts on metal films boundary, whose frequency is given by $\omega = \omega_p/\sqrt{2}$ where ω_p is the plasma frequency of the corresponding material under study.[94] This loss, which appears due to the finiteness of a metallic thin film, was accordingly referred as surface plasmon (SP). During those decades, the excitation of the SPs required the use of expensive and complex equipment.

It was not possible until 1968 when Otto, Kretschmann and Raether reported a new approach through more cost-effective optical methods.[95, 96] Both papers explained the use of prisms to optically induce the formation of plasmons on Au thin films. Whereas Otto introduced a distance between the prism and the metal film, Kretschmann and Raether positioned directly the prism on the metal. Their approaches enable the coupling between the incident photon and the characteristic SP wavevectors. In both cases, the polariton wave propagates along a metal/air interface (Figure 1.7A).

On the other hand, the SPR phenomenon is not only restricted to thin films. The term localized surface plasmon resonance (LSPR) defines the non-propagating polariton waves produced in nanostructures with average sizes comparable to the light wavelength, contrary to the propagating wave nature occurred in thin film SPR (Figure 1.7B). In this case, the polariton wave is confined around the nanostructure. The optical features of the LSPR have been observed centuries ago. The most prominent examples are the Lycurgus Cup, from the 4th century, or stained glasses, from the Middle Age, such as the South

Rose window at Notre Dame Cathedral. Both examples comprise the inclusion of noble metal structures at the nanometer scale embedded in glass, giving them the strong colored appearance during illumination with visible light.

The main difference with the SPR phenomenon in thin films is that the experimental conditions to excite SPs relax due to the nanostructure geometry finiteness and, thus, no optical couplers are needed.[97] In summary, the excitation of the LSPR only requires the right photon energy and polarization. The most prominent benefit provided by LSPR is that this phenomenon generates a very intense electric field surrounding the nanostructure.[98] This is a very interesting feature that makes LSPR attractive for the development of sensors.[99] In the past few years, this type of resonance has been found to play a critical role in Surface-Enhanced Raman Spectroscopy (SERS) applications, a technique that mostly relies on the electric field generated by the nanostructures during their adequate illumination with a laser.[100]

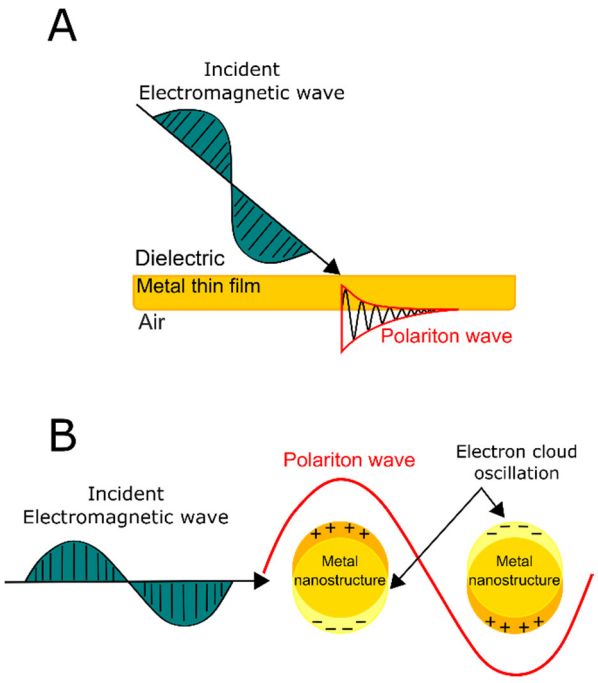

Figure 1.7. Representation of the polariton waves produced on (A) thin films and (B) nanostructures.

1.3.1. Non-ellipsometric biosensors

SPR BIOSENSORS

As it was mentioned above, SPR detection methods measure changes in the intensity of a reflected beam as a function of the incidence angle. The most common noble metal for the fabrication of SPR sensors is Au. Despite being more expensive than Ag and Cu, Au is found to be quite stable under ambient conditions and presents a very extensive functionalization chemistry.

The first sensor based on the prism approach was demonstrated in 1982 by Nylander and Liedberg.[101, 102] In this sensor, the Kretschmann configuration was well suited for gas and biomolecular sensing purposes. Since then, there has been an extensive literature concerning this approach to analyze samples within different matrices, proving its great versatility. Examples of recent applications are shown below, such as that developed by Enrico et al. In their biosensor, the *Legionella pneumophila* bacterium was detected in water samples by immobilizing an antibody, selective to the microorganism, on a Au film.[103] A special attention has been focused on urine matrices since an extensive information can be obtained from this liquid medium. In that respect, Vega et al. analyzed urine to detect chemokines, proinflammatory cytokines that regulate leukocyte trafficking in inflammatory processes.[104] Recently, Lechuga et al. have developed a biosensor to detect the α-gliadin 33-mer peptide (biomarker for gluten) in urine, from celiac patients.[105] Milk matrices are also important. Early detection of different diseases can be diagnosed from milk samples produced by the cattle, as was demonstrated by Ashley et al. In this case, the presence of bovine catalase, a possible bio indicator of mastitis disease, was detected by using an aptamer (a single DNA strand) as the recognition element. A limit of detection of 20.5 nM was estimated.[106] Milk, as other foods, are susceptible of being falsified through the addition of illegal compounds. As an example, Lu et al. performed analysis to detect melamine, a synthetic chemical used to illegally alter its protein levels.[107]

During the last decade, the coupling systems for bioanalysis based on optical prisms have been upgraded to improve its performance. Homola et al. developed new SPR systems to extract information from multiple analysis points or different regions of the same point (channels). The resonance information of these channels was codified in different spectral regions of a polychromatic light beam. To perform such approach, part

of Au thin film was coated with a thin dielectric layer, yielding two resonance energies due to the two different surrounding media. This approach was denoted as wavelength division multiplexing (WDM).[108] Another way to perform the WDM was the use of an irregular trapezoidal prism, impinging the channels with different incidence angles.[109] Thanks to this method, a more accurate information of biomolecular interaction was obtained. Additionally, this method was also used for multiple analyte measurements.[110]

Besides the use of the prism-coupling approach, other configurations arose during the development of SPR biosensors, such as the use of grating and optical fibers. Homola et al provided a good review about this topic.[111]

The principle of the optical fiber approach is similar to the prism configuration. A high refractive index core is surrounded by a metallic film in one point of the fiber after removing its commercial cladding. The light travels along the fiber through the multiple reflections due to the total internal reflection phenomenon. The surface functionalization of the metallic cladding yields energy shifts in the resonance, which can be monitored at the fiber end. This approach has been attractive because of the possibility to miniaturize the optical fiber and to fabricate portable devices, such as lab-on-a-chips.

Rajan et al. provided a good example of this method to measure the pesticide chlorphyrifos.[112] After removing the commercial cladding of one part of the optical fiber, an Ag thin film was deposited. This film was functionalized with acetylcholinesterase, an enzyme selective to acetylcholine, for which the pesticide acts as an inhibitor. The pesticide concentration was determined by using a competitive assay against the acetylthiocholine iodide for the acetylcholinesterase binding sites. Different optimizations have been performed to improve the performance of this approach. Suzuki et al. studied the influence of the metallic thin film thickness.[113] The highest sensitivity was achieved for a film thickness of 65 nm during the measurement of different refractive index solutions. Another improvement has been performed recently by Liu et al. by using a multiplexing approach, similar to that proposed by Homola et al. for the prism-coupling method, but applied to optical fibers.[114]

Nowadays, some efforts are being performed to couple the optical fiber approach to daily-use devices. Liu et al. used an optical fiber to connect the white light LED and the camera from a smartphone, as the light source and the detector respectively.[115] A smartphone application reads the intensity of the light detected by the camera and shown

in the phone. In the middle part of the fiber, the cladding was removed and a 50-nm Au thin film was deposited. A very small flow cell surrounding the Au thin film was used to introduce the sample solutions. The Au thin film was functionalized with a protein A, which can capture antibodies IgG. A limit of detection of around 50 nM of bovine IgG was estimated.

On the other hand, the grating method comprises the definition of a periodic pattern on a metallic thin film by photo or electron beam lithography. Under this approach, the resonance wavelength strongly depends on the period and fill factors of the pattern. Despite the need of this additional step, the advantage of this method is that the excitation of plasmons does not require any optical coupler. Nevertheless, the drawback of this method is lower theoretical sensitivity values compared to the previous approaches.[111] For this reason, publications reporting the use of grating are very scarce. An example was proposed by Cullen et al. who studied antibody-antigen immunological recognitions by using Au gratings.[116, 117] A method to enhance the sensitivity of this approach was proposed by Cai et al. This improvement, denoted as doubled-dips method, was based on the measurement of the separation of two sharp dips from different diffraction orders.[118]

A similar approach related to the definition of gratings is that based on patterning nanoholes on a metallic film. One of the first authors reporting the optical properties of these nanoholes was Ebbesen et al.[119] The physical explanation was further reviewed in the literature.[120, 121] The fabrication of nanoholes was mainly carried out on Au thin films deposited on glassy substrates, as that performed by Ji et al.[122] In that work, glutathione S-transferase was immobilized on the film in order to detect an antibody specific to this molecule, in the range of 10-300 nM. A step further was performed by Angulo et al. They demonstrated the use of Al nanoholes for biosensing, taking advantage of its cost-effectiveness compared to noble metals, such as Au and Ag.[123] These Al nanohole arrays have been fabricated on flexible substrates and compact disks.[124, 125] For the latter, a competitive immunoassay was performed between biotin-dextran-lipase conjugates, immobilized on the array surface, and biotin present in the sample solution for an antibody selective to biotin.

Among all these approaches, the use of the prism configuration for the fabrication of sensors is the most widespread. Pharmacia Biosensor AB became interested in using this technology to study interaction between biomolecules. In 1990, the company

launched the BIAcore, which has been capable to be used for real specific interaction analysis without the use of labels.

Nowadays, the biosensing research field based on SPR techniques is significantly extended. A simple search in the "Web of Science" (see Figure 1.8) leads a steady trend in the number of publications since 2008-2009, which demonstrates that research on SPR-based transduction methods have reached a mature level and opened new possibilities for the industrial development of related products.

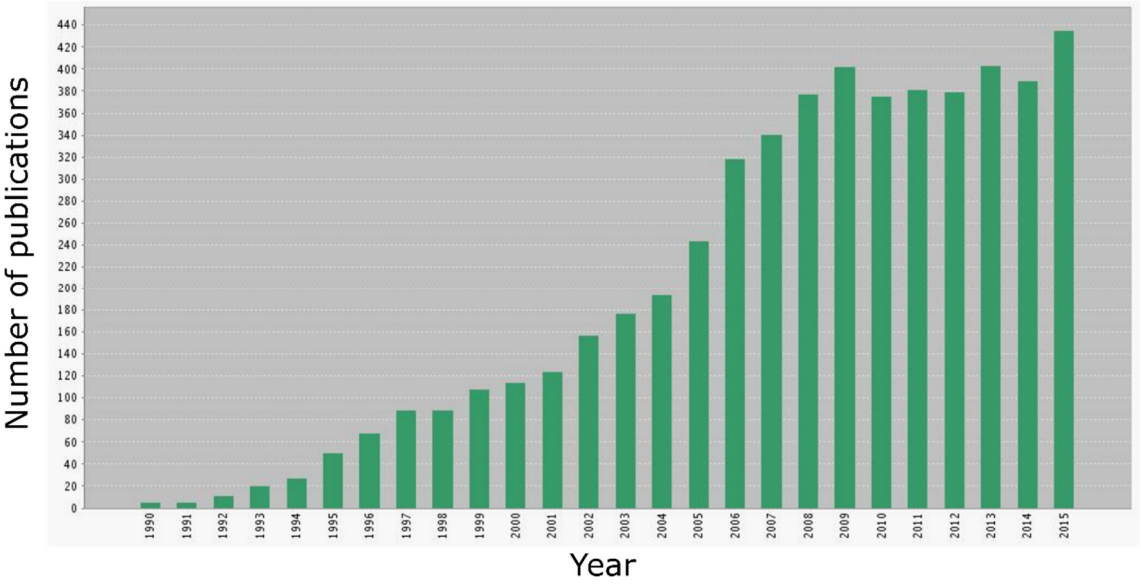

Figure 1.8. Results from a search in the Web of Science by typing *SPR AND biosensors* in the topic field.

LSPR BIOSENSORS

As it was mentioned, the LSPR describes non-propagating plasma waves confined in nanostructures with sizes below the visible wavelength. The most commonly metals used to synthesize these nanostructures are Au and Ag, which have attracted considerable attention recently because of their multiple interesting properties. Among them, the formation of air-stable colloids, resonance frequency lying in the IR-visible part of the spectrum, and the small imaginary part of the dielectric constant at the resonance frequency, can be highlighted.[98, 126-128]

In the biosensing field, metal nanostructures have shown a broad versatility to fabricate different biosensors. El-Sayed et al. presented AuNPs conjugated to an antibody

that specifically recognized malignant cells from an oral cancer with a high sensitivity.[129] By using an optical microscopy, noticeable differences were observed when non-malignant and malignant cells were incubated with the functionalized NPs. This result was corroborated with absorption measurements after the recognition event.

Van Duyne et al. contributed in the development of LSPR biosensors. They obtained arrays of Ag nanoprisms on glassy substrates by photolithography. These nanoprisms were functionalized with different biomolecules in order to study and quantify a wide range of biological interactions, such as the biotin-antibiotin immunological recognition, or the mannose (a sugar) and Concanavalin A interaction.[130, 131] Furthermore, a biosensor to detect ADDLs (amyloid-beta-derived diffusible ligands), a protein found at elevated levels in human brains with Alzheimer's disease, was developed.[132] In that work, analysis in human brain extracts were also performed, proving the viability of LSPR-based sensors.

More recently, an immunosensor to detect HIV-1 virus particles was developed by Lee et al. reaching a limit of detection of 200 fg/mL.[133] Likewise, a biosensor for early diagnosis of colorectal cancer was fabricated by Lechuga et al. by using an array of Au nanodisks on glass substrates.[134]

Metallic NPs have been also used to develop DNA biosensors. A limit of detection in the nanomolar level was estimated by Spadavecchia et al., for 40 base pairs synthetic DNA strands.[135] On the other hand, Soares et al. studied the recognition event and performed analysis with DNA amplicons from human saliva.[136]

Nowadays, the Industry have shown interest in LSPR biosensors. LamdaGen Corporation has become famous for its commercial LSPR chips, which has been used to detect cytokines extracted from blood samples, among other analytes.[137]

1.3.2. Ellipsometric biosensors

SPECTROSCOPIC ELLIPSOMETRY

One of the main topics in this work is the use of spectroscopic ellipsometry. This technique has been mainly used to detect any surface change on an arbitrary substrate. The high sensitivity to these surface changes at the nanoscale has provided the scientific community with a great tool for surface analysis.

There are many definitions for ellipsometry in the literature. Two of the most known authors in modern ellipsometry, Azzam and Bashara, define ellipsometry as an optical technique for the characterization of events on a thin film, based on the exploitation of the polarization change that occurs to the incident beam after reflection or transmission through the sample.[138] As stated in this definition, ellipsometry can work under different configurations. However, reflection ellipsometry is the most widespread for the analysis of surfaces.

The history of ellipsometry can go back to the characterization of the electromagnetic nature of light waves by Maxwell in the 1860s. After that, the most important advance was done by Paul Drude, providing a strong background in the optics field. In his book, entitled "Theory of Optics" and published in English in 1902, he depicted the necessary components to fabricate the ellipsometer predecessor. It was not until 1945 when Rothen coined the term ellipsometer.[139] The use of this instrument was not very extended in the next decades. With the development of computers in the 1960-70s, ellipsometry underwent a large expansion due to the possibility to automatize the measurements and to perform the calculations with the corresponding software. A wide range of different configurations has been developed for these automated ellipsometers depending on the components and their position inside the ellipsometer. Muller provided an extensive review about this issue in 1976.[140]

The spectroscopic ellipsometer used in this work is a phase-modulated instrument. This approach has been developed by Jasperson et al., and further by Drevillon et al.[141, 142] This ellipsometer includes a component, denoted as modulator, made of a material that exhibits birefringence when it is subjected to certain conditions. Thanks to this property, the modulator makes the light travel slower when the beam is polarized in certain directions, giving rise to a known phase change in the incident light beam. The advantage of this approach is the possibility to obtain very high sensitivity measurements with low noise in a short-time range. Nowadays, this type of ellipsometer is mainly commercially available from HORIBA and Wollam Companies.

SPR ELLIPSOMETRIC BIOSENSORS

Thanks to the high sensitivity of spectroscopic ellipsometry to surface changes, this technique is particularly interesting as a transduction method for plasmonic biosensor

developing. A plasmonic sensor relies on the refractive index change undergone around a metallic thin film or nanostructure. The combination of the ellipsometer and the SPR was denoted as total internal reflection ellipsometry (TIRE).

E. Bortchagovsky was the first one to discuss the possibility of using TIRE for the development of sensors.[143] Westphal et al. demonstrated the capabilities of TIRE in 2002.[144] A step further was performed by Poksinski and Arwin, who designed a flow cell to measure the protein binding in real-time TIRE in a Au thin film deposited on a glass slide.[145] In the subsequent years, the binding of different proteins with the same configuration was studied.[146, 147]

A great advance in the development of TIRE biosensors was carried out by Nabok et al. In their first work, an immunosensor for the detection of environmental toxins was developed.[148] The use of TIRE was extended to analyze DNA recognition events.[149] A wide range of mycotoxins (fungus metabolism products that appear because of inappropriate food storing) were also detected by them in the next years, such as Aflatoxin B1, T-2 and Zearalenone.[150, 151] DNA strands were also detected by Le et al.[152] An ultra-thin film of poly(methyl methacrylate) was prepared on the Au substrate by spin coating. After exposition to UV/O_3, the film was activated with carboxyl groups to further anchor a DNA strand. A limit of detection for the subsequent recognition event with the complementary chain was found to be 10 pM.

In the last few years, the efforts are being focused on the combination of TIRE and other different analysis techniques. In 2014, Liu and Li et al. were able to combine TIRE to electrochemical detection methods in the same cell.[153, 154] The formation of polyaniline, a polymer sensitive to O_2, on a Au layer was proposed to measure the O_2 dissolved in a solution.

Ellipsometry has been also combined to the quartz crystal microbalance technique. Examples of this procedure have been recently performed by Rodenhausen et al. and Meulen et al. to determine surface modifications with a very high sensitivity.[155, 156] It should be noted that this approach is of great interest since commercial platforms are being supplied by companies, such as Biolin Scientific, proving the interest of the Industry in ellipsometric biosensors.

On the other hand, there has been some efforts to use the resonance of metallic nanostructures, the LSPR, to develop ellipsometric sensors. Lodewijks et al. confirmed

that measuring the Δ function, related to the phase shift, can lead to very sensitive measurements in the refractive index of the surrounding medium of an array of plasmonic nanostructures, increasing the figure of merit (ratio between the sensitivity and the width of the resonance band).[157]

In this line, a few works were performed by Moirangthem et al. with AuNPs deposited on a glassy substrate.[158] The immunological recognition was measured in real time between the bovine serum albumin (BSA) protein, adsorbed on the NP surface, and an antibody selective to the BSA (antiBSA). A higher sensitivity was claimed by measuring the Δ function in ellipsometry, compared to monitoring the Ψ function, related to the ratio of the intensity of the reflected and incident light. Later, the same NPs were partially embedded on the glass substrate, yielding a better performance compared to simply NPs deposited on the substrate.[159] Additionally, LSPR nanostructures can be also combined to tune the SPR band of thin films. Its applicability was demonstrated by studying the same BSA-antiBSA recognition event.[160]

The high sensitivity of LSPR to changes in the refractive index of the surrounding medium motivates us to develop biosensors by using spectroscopic ellipsometry as the transduction method.

1.4. Thesis content

This thesis is divided in 7 chapters and 1 appendix. The content of the next chapters is described below:

Chapter 2 provides insights about the most relevant physical phenomena and biological interactions dealt in this thesis: dielectrophoresis, ellipsometry physics, surface plasmons, localized surface plasmons, antibody structure and its immunological interaction with the antigen, and DNA structure.

Chapter 3 enumerates the materials used in this work and their suppliers. Additionally, the preparation of different nanostructures and thin films by VPT, colloidal synthesis, thermal evaporation, sputtering are presented. The procedure followed to fabricate electrodes by photolithography is shown gradually. The optical, electrical and surface characterization techniques used in this work are explained briefly. The Chapter

finalizes with a description of the discrete dipole approximation method to simulate the plasmonic resonance of nanostructures.

Chapter 4 describes the growth, characterization, alignment and optoelectronic properties of CuO and ZnO NWs-based photodetectors. The first part presents the results for the growth study of the CuO NWs, the structural characterization and the NW manipulation by DEP between AZO electrodes. The potential advantages of the AZO/CuO NW/AZO heterojunction as a photodetector are studied. The second part contains the development of a procedure to improve the NW dispersion quality based on particle sedimentation. The Section continues with the presentation of a continuous-flow DEP system to improve the NW alignment procedure. A monitoring process based parallel resistance measurements is proposed to estimate the number of aligned NWs and to detect possible anomalies during DEP. The NW alignment by DEP is performed on AZO electrodes defined on glassy substrates in order to obtain transparent photodetectors. Finally, the electro-optical characterization of the developed photodetector is presented.

Chapter 5 describes the development of a glutathione (GSH) immunosensor based on the total internal reflection ellipsometry approach. The procedure to fabricate and characterize the biosensing platform based on an AZO/Au bilayer. The use of AZO instead of conventional Cr and Ti intermediate layers is motivated by the high transparency of this material at the Au thin film resonance energy. The immunoassay is based on the competition between free GSH and GSH-AuNPs conjugates to increase the ellipsometric response. The kinetics of immunological recognition between the GSH-AuNPs conjugates and antibody layer, the optimization of the conjugate concentration and the results of the competitive immunoassay are presented.

Chapter 6 is focused on the development of ellipsometric biosensing platforms based on Ga nanostructures deposited on Si substrates. The first parts of the Chapter deals with the theoretical analysis of the GaNPs plasmonics with the Mie theory and DDA. The fabrication of GaNPs/Si platforms and their surface characterization by XPS and XRD are shown. A deep study of the platform by ellipsometry under external reflection mode is presented, including the description of the RPH condition used for biosensing purposes. The fabrication of biosensors for GSH and DNA strands from the *H. Pylori* pathogen by using the ellipsometer as the transduction method is shown. For both cases, the characterization of the functionalization steps is studied by different techniques. The

applicability of the current platform to the detection of mutations in real genomic DNA is demonstrated.

Chapter 7 summarizes the general conclusions of the whole thesis about the development of metal oxide NW-based photodetectors and ellipsometric biosensors. This chapter also proposes new ideas to continue or to open novel research lines.

Appendix A presents the publication list, conference contributions, book chapters and a patent resulting from this work.

REFERENCES

1. K. Ziemelis. The future of microelectronics. *Nature* **2000**, 406, 1021.
2. Y. N. Xia; P. D. Yang; Y. G. Sun; Y. Y. Wu; B. Mayers; B. Gates; Y. D. Yin; F. Kim; Y. Q. Yan. One-dimensional nanostructures: Synthesis, characterization, and applications. *Adv. Mater.* **2003**, 15, 353-389.
3. S. Wagner; W. C. Ellis. Vapor-Liquid-Solid mechanism of single crystal growth. *Appl. Phys. Lett.* **1964**, 4, 89-90.
4. J. H. Woodruff; J. B. Ratchford; I. A. Goldthorpe; P. C. McIntyre; Chidsey. Vertically Oriented Germanium Nanowires Grown from Gold Colloids on Silicon Substrates and Subsequent Gold Removal. *Nano Lett.* **2007**, 7, 1637-1642.
5. X. Duan; J. Wang; C. M. Lieber. Synthesis and optical properties of gallium arsenide nanowires. *Appl. Phys. Lett.* **2000**, 76, 1116-1118.
6. K. Tomioka; J. Motohisa; S. Hara; T. Fukui. Control of InAs Nanowire Growth Directions on Si. *Nano. Lett.* **2008**, 8, 3475-3480.
7. P. Yang; H. Yan; S. Mao; R. Russo; J. Johnson; R. Saykally; N. Morris; J. Pham; R. He; H. J. Choi. Controlled Growth of ZnO Nanowires and Their Optical Properties. *Adv. Funct. Mater.* **2002**, 12, 323-331.
8. Y. Cui; Z. Zhong; D. Wang; W. U. Wang; C. M. Lieber. High Performance Silicon Nanowire Field Effect Transistors. *Nano. Lett.* **2003**, 3, 149-152.
9. Z. Zhang; J. T. Yates. Band Bending in Semiconductors: Chemical and Physical Consequences at Surfaces and Interfaces. *Chem. Rev.* **2012**, 112, 5520-5551.
10. H. Wang. High gain single GaAs nanowire photodetector. *Appl. Phys. Lett.* **2013**, 103, 093101.
11. X. Dai; S. Zhang; Z. Wang; G. Adamo; H. Liu; Y. Huang; C. Couteau; C. Soci. GaAs/AlGaAs Nanowire Photodetector. *Nano Lett.* **2014**, 14, 2688-2693.
12. Y. H. Ahn; J. Park. Efficient visible light detection using individual germanium nanowire field effect transistors. *Appl. Phys. Lett.* **2007**, 91, 162102.
13. A. Zhang; S. You; C. Soci; Y. Liu; D. Wang; Y.-H. Lo. Silicon nanowire detectors showing phototransistive gain. *Appl. Phys. Lett.* **2008**, 93, 121110.
14. L. B. Luo; J. S. Jie; Z. H. Chen; X. J. Zhang; X. Fan; G. D. Yuan; Z. B. He; W. F. Zhang; W. J. Zhang; S. T. Lee. Photoconductive properties of selenium nanowire photodetectors. *J. Nanosci. Nanotechnol.* **2009**, 9, 6292-6298.
15. G. Li; Y. Jiang; Y. Zhang; X. Lan; T. Zhai; G.-C. Yi. High-performance photodetectors and enhanced field-emission of CdS nanowire arrays on CdSe single-crystalline sheets. *J. Mater. Chem. C* **2014**, 2, 8252-8258.

16. Z. Liu; G. Chen; B. Liang; G. Yu; H. Huang; D. Chen; G. Shen. Fabrication of high-quality ZnTe nanowires toward high-performance rigid/flexible visible-light photodetectors. *Opt. Express* **2013**, 21, 7799-7810.
17. C. Soci; A. Zhang; B. Xiang; S. A. Dayeh; D. P. R. Aplin; J. Park; X. Y. Bao; Y. H. Lo; D. Wang. ZnO nanowire UV photodetectors with high internal gain. *Nano. Lett.* **2007**, 7, 1003-1009.
18. S. B. Wang; C. H. Hsiao; S. J. Chang; K. T. Lam; K. H. Wen; S. C. Hung; S. J. Young; B. R. Huang. A CuO nanowire infrared photodetector. *Sens. Actuators A Phys.* **2011**, 171.
19. H. Morkoç; Ü. Özgür. *Zinc Oxide: Fundamentals, Materials and Device Technology*. Wiley: 2008.
20. A. Rahm; M. Lorenz; T. Nobis; G. Zimmermann; M. Grundmann; B. Fuhrmann; F. Syrowatka. Pulsed-laser deposition and characterization of ZnO nanowires with regular lateral arrangement. *Appl. Phys. A* **2007**, 88, 31-34.
21. L. C. Tien; S. J. Pearton; D. P. Norton; F. Ren. Synthesis and microstructure of vertically aligned ZnO nanowires grown by high-pressure-assisted pulsed-laser deposition. *J. Mater. Sci.* **2008**, 43, 6925-6932.
22. H. Hu; X. Huang; C. Deng; X. Chen; Y. Qian. Hydrothermal synthesis of ZnO nanowires and nanobelts on a large scale. *Mater. Chem. Phys.* **2007**, 106, 58-62.
23. X. Li; Y. H. Wang; A. Lu; X. Liu. Controllable Hydrothermal Growth of ZnO Nanowires on Cellulose Paper for Flexible Sensors and Electronics. *IEEE Sens. J.* **2015**, 15, 6100-6107.
24. S. Y. Li; C. Y. Lee; T. Y. Tseng. Copper-catalyzed ZnO nanowires on silicon (100) grown by vapor–liquid–solid process. *J. Cryst. Growth* **2003**, 247, 357-362.
25. Z. W. Pan; S. Dai; C. M. Rouleau; D. H. Lowndes. Germanium-Catalyzed growth of zinc oxide nanowires: a semiconductor catalyst for nanowire synthesis. *Angew. Chem. Int. Ed.* **2005**, 44, 274-278.
26. M. Wei; D. Zhi; J. L. MacManus-Driscoll. Self-catalysed growth of zinc oxide nanowires. *Nanotechnology* **2005**, 16, 1364-1368.
27. S. M. Kim; G. Shen; D. S. Wilbert; W. Baughman; N. Dawahre; M. M. Murphy; M. York; J. Kim; P. Kung. In *Synthesis and optical properties of ZnO nanowires for nanophotonics*, Nanotechnology (IEEE-NANO), 10th IEEE Conference on, 2010; pp 285-288.
28. J. J. F. Conley; L. Stecker; Y. Ono. Directed assembly of ZnO nanowires on a Si substrate without a metal catalyst using a patterned ZnO seed layer. *Nanotech.* **2005**, 16, 292.
29. P.-C. Chang; Z. Fan; D. Wang; W.-Y. Tseng; W.-A. Chiou; J. Hong; J. G. Lu. ZnO Nanowires Synthesized by Vapor Trapping CVD Method. *Chem. Mater.* **2004**, 16, 5133-5137.
30. J. Goldberger; D. J. Sirbuly; M. Law; P. Yang. ZnO Nanowire Transistors. *J. Phys. Chem. B* **2005**, 109, 9-14.
31. N. Junya; M. H. Faruque; T. Shingo; A. Tetsuya; S. Koji; O. Yuji; O. Isao; K. Shuya; O. Akira; F. Tomoteru; M. Fumihiro; O. Yuzo; K. Hideomi; O. Hideo; K. Masashi. High Mobility Thin Film Transistors with Transparent ZnO Channels. *Jpn. J. Appl. Phys.* **2003**, 42, L347.
32. R. L. Hoffman; B. J. Norris; J. F. Wager. ZnO-based transparent thin-film transistors. *Appl. Phys. Lett.* **2003**, 82, 733-735.
33. D. Jiang; C. Tian; Q. Liu; M. Zhao; J. Qin; J. Hou; S. Gao; Q. Liang; J. Zhao. Young′s modulus of individual ZnO nanowires. *Mat. Sci. Eng. A-Struct.* **2014**, 610, 1-4.

34. C. Q. Chen; Y. Shi; Y. S. Zhang; J. Zhu; Y. J. Yan. Size Dependence of Young's Modulus in ZnO Nanowires. *Phys. Rev. Lett.* **2006**, 96, 075505.
35. M. H. Huang; Y. Wu; H. Feick; N. Tran; E. Weber; P. Yang. Catalytic Growth of Zinc Oxide Nanowires by Vapor Transport. *Adv. Mater.* **2001**, 13, 113-116.
36. Z.-M. Liao; H.-Z. Zhang; Y.-B. Zhou; J. Xu; J.-M. Zhang; D.-P. Yu. Surface effects on photoluminescence of single ZnO nanowires. *Phys. Lett. A* **2008**, 372, 4505-4509.
37. H. Kind; H. Yan; B. Messer; M. Law; P. Yang. Nanowire Ultraviolet Photodetectors and Optical Switches. *Adv. Mater.* **2002**, 14, 158-160.
38. Q. H. Li; T. Gao; Y. G. Wang; T. H. Wang. Adsorption and desorption of oxygen probed from ZnO nanowire films by photocurrent measurements. *Appl. Phys. Lett.* **2005**, 86, 123117.
39. Q. H. Li; Q. Wan; Y. X. Liang; T. H. Wang. Electronic transport through individual ZnO nanowires. *Appl. Phys. Lett.* **2004**, 84, 4556-4558.
40. J. Zhou; Y. Gu; Y. Hu; W. Mai; P.-H. Yeh; G. Bao; A. K. Sood; D. L. Polla; Z. L. Wang. Gigantic enhancement in response and reset time of ZnO UV nanosensor by utilizing Schottky contact and surface functionalization. *Appl. Phys. Lett* **2009**, 94.
41. D. Lin; H. Wu; W. Zhang; H. Li; W. Pan. Enhanced UV photoresponse from heterostructured Ag–ZnO nanowires. *Appl. Phys. Lett.* **2009**, 94, 172103.
42. Z. L. Wang; J. Song. Piezoelectric Nanogenerators Based on Zinc Oxide Nanowire Arrays. *Science* **2006**, 312, 242-246.
43. M. W. Ahn; K. S. Park; J. H. Heo; D. W. Kim; K. J. Choi; J. G. Park. On-chip fabrication of ZnO-nanowire gas sensor with high gas sensitivity. *Sensor. Actuat. B-Chem.* **2009**, 138, 168-173.
44. J. X. Wang; X. W. Sun; Y. Yang; H. Huang; Y. C. Lee; O. K. Tan; L. Vayssieres. Hydrothermally grown oriented ZnO nanorod arrays for gas sensing applications. *Nanotech.* **2006**, 17, 4995.
45. D. Pradhan; F. Niroui; K. T. Leung. High-Performance, Flexible Enzymatic Glucose Biosensor Based on ZnO Nanowires Supported on a Gold-Coated Polyester Substrate. *ACS Appl. Mater. Interfaces* **2010**, 2, 2409-2412.
46. M.-L. Zhang; F. Jin; M.-L. Zheng; J. Liu; Z.-S. Zhao; X.-M. Duan. High efficiency solar cell based on ZnO nanowire array prepared by different growth methods. *RSC Adv.* **2014**, 4, 10462-10466.
47. D. Vanmaekelbergh; L. K. van Vugt. ZnO nanowire lasers. *Nanoscale* **2011**, 3, 2783-2800.
48. Cupric oxide (CuO) crystal structure, lattice parameters. In *Non-Tetrahedrally Bonded Elements and Binary Compounds I*, Madelung, O.; Rössler, U.; Schulz, M., Eds. Springer Berlin Heidelberg: Berlin, Heidelberg, 1998; pp 1-3.
49. A.-L. Daltin; A. Addad; J.-P. Chopart. Potentiostatic deposition and characterization of cuprous oxide films and nanowires. *J. Cryst. Growth* **2005**, 282, 414-420.
50. X. Hong; G. Wang; W. Zhu; X. Shen; Y. Wang. Synthesis of sub-10 nm Cu_2O Nanowires by Poly(vinyl pyrrolidone)-Assisted Electrodeposition. *J. Phys. Chem. C* **2009**, 113, 14172-14175.
51. C.-T. Hsieh; J.-M. Chen; H.-H. Lin; H.-C. Shih. Synthesis of well-ordered CuO nanofibers by a self-catalytic growth mechanism. *Appl. Phys. Lett.* **2003**, 82, 3316-3318.
52. L. Zhu; Y. Chen; Y. Zheng; N. Li; J. Zhao; Y. Sun. Ultrasound assisted template-free synthesis of Cu(OH)2 and hierarchical CuO nanowires from Cu7Cl4(OH)10·H2O. *Mater. Lett.* **2010**, 64, 976-979.

53. C. Li; Y. Yin; H. Hou; N. Fan; F. Yuan; Y. Shi; Q. Meng. Preparation and characterization of $Cu(OH)_2$ and CuO nanowires by the coupling route of microemulsion with homogenous precipitation. *Solid State Commun.* **2010**, 150, 585-589.
54. X. Jiang; T. Herricks; Y. Xia. CuO nanowires can be synthesized by heating copper substrates in air. *Nano Lett* **2002**, 2, 1333–1338.
55. C. H. Xu; C. H. Woo; S. Q. Shi. Formation of CuO nanowires on Cu foil. *Chem. Phys. Lett.* **2004**, 399, 62-66.
56. J. T. Chen; F. Zhang; J. Wang; G. A. Zhang; B. B. Miao; X. Y. Fan; D. Yan; P. X. Yan. CuO nanowires synthesized by thermal oxidation route. *J. All.Comp.* **2008**, 454.
57. C. H. Xu; C. H. Woo; S. Q. Shi. The effects of oxidative environments on the synthesis of CuO nanowires on Cu substrates. *Superlattices Microstruct.* **2004**, 36, 31-38.
58. B. J. Hansen; G. Lu; J. Chen. Direct Oxidation Growth of CuO Nanowires from Copper-Containing Substrates. *J. Nanomater.* **2008**, 2008, 7.
59. D. Wu; Q. Zhang; M. Tao. LSDA + U study of cupric oxide: Electronic structure and native point defects. *Phys. Rev. B* **2006**, 73, 235206.
60. A. O. Musa; T. Akomolafe; M. J. Carter. Production of cuprous oxide, a solar cell material, by thermal oxidation and a study of its physical and electrical properties. *Sol. Energ. Mat. Sol. Cells* **1998**, 51, 305-316.
61. L. Liao; Z. Zhang; B. Yan; Z. Zheng; Q. L. Bao; T. Wu; C. M. Li; Z. X. Shen; J. X. Zhang; H. Gong; J. C. Li; T. Yu. Multifunctional CuO nanowire devices: p-type field effect transistors and CO gas sensors. *Nanotechnology* **2009**, 20, 085203.
62. L.-B. Luo; X.-H. Wang; C. Xie; Z.-J. Li; R. Lu; X.-B. Yang; J. Lu. One-dimensional CuO nanowire: synthesis, electrical, and optoelectronic devices application. *Nanoscale Res. Lett.* **2014**, 9, 1-8.
63. E. P. S. Tan; Y. Zhu; T. Yu; L. Dai; C. H. Sow; V. B. C. Tan; C. T. Lim. Crystallinity and surface effects on Young's modulus of CuO nanowires. *Appl. Phys. Lett.* **2007**, 90, 163112.
64. C. Y. Huang; A. Chatterjee; S. B. Liu; S. Y. Wu; C. L. Cheng. Photoluminescence properties of a single tapered CuO nanowire. *Appl. Surf. Sci.* **2010**, 256, 3688-3692.
65. Y.-S. Kim; I.-S. Hwang; S.-J. Kim; C.-Y. Lee; J.-H. Lee. CuO nanowire gas sensors for air quality control in automotive cabin. *Sens. Actuators B Chem.* **2008**, 135, 298-303.
66. X. Li; Y. Wang; Y. Lei; Z. Gu. Highly sensitive H_2S sensor based on template-synthesized CuO nanowires. *RSC. Adv.* **2012**, 2.
67. V. D. Kumari; M. Subrahmanyam; A. Ratnamala; D. Venugopal; B. Srinivas; M. V. P. Sharma; S. S. Madhavendra; B. Bikshapathi; K. Venkateswarlu; T. Krishnudu; K. B. S. Prasad; K. V. Raghavan. Correlation of activity and stability of CuO/ZnO/Al2O3 methanol steam reforming catalysts with Cu/Zn composition obtained by SEM–EDAX analysis. *Catal. Commun.* **2002**, 3, 417-424.
68. K. Zhou; R. Wang; B. Xu; Y. Li. Synthesis, characterization and catalytic properties of CuO nanocrystals with various shapes. *Nanotechnology* **2006**, 17, 3939-3943.
69. Y. Z. Feng; X. L. Zheng. Plasma-enhanced catalytic CuO nanowires for CO oxidation. *Nano Lett.* **2010**, 10, 4762–4766.
70. H. Yan; X. Liu; R. Xu; P. lv; P. Zhao. Synthesis, characterization, electrical and catalytic properties of CuO nanowires. *Mater. Res. Bull.* **2013**, 48, 2102-2105.
71. A. Stadler. Transparent Conducting Oxides—An Up-To-Date Overview. *Materials* **2012**, 5, 661.

72. D. B. Fraser; H. D. Cook. Highly Conductive, Transparent Films of Sputtered $In_{2-x}Sn_xO_{3-y}$. *J. Electrochem. Soc.* **1972**, 119, 1368-1374.
73. T. Minami; H. Sato; H. Imamoto; S. Takata. Substrate Temperature Dependence of Transparent Conducting Al-Doped ZnO Thin Films Prepared by Magnetron Sputtering. *Jpn. J. Appl. Phys.* **1992**, 31, L257.
74. Akio Suzuki; Tatsuhiko Matsushita; Naoki Wada; Yoshiaki Sakamoto; Masahiro Okuda. Transparent Conducting Al-Doped ZnO Thin Films Prepared by Pulsed Laser Deposition. *Jpn. J. Appl. Phys.* **1996**, 35, L56.
75. R. Pandey; S. Yuldashev; H. D. Nguyen; H. C. Jeon; T. W. Kang. Fabrication of aluminium doped zinc oxide (AZO) transparent conductive oxide by ultrasonic spray pyrolysis. *Curr. Appl. Phys.* **2012**, 12, Supplement 4, S56-S58.
76. J.-H. Lee; B.-O. Park. Characteristics of Al-doped ZnO thin films obtained by ultrasonic spray pyrolysis: effects of Al doping and an annealing treatment. *Mat. Sci. Eng. B-Solid* **2004**, 106, 242-245.
77. M.-C. Jun; J.-H. Koh. Optical and Structural Properties of Al-Doped ZnO Thin Films by Sol Gel Process. *J. Nanosci. Nanotechnol.* **2013**, 13, 3403-3407.
78. J. I. Owen. *Growth, Etching, and Stability of Sputtered ZnO:AI for Thin-film Silicon Solar Cells*. Forschungszentrum Jülich: 2011.
79. J. Hüpkes; J. I. Owen; S. E. Pust; E. Bunte. Chemical Etching of Zinc Oxide for Thin-Film Silicon Solar Cells. *Chemphyschem* **2012**, 13, 66-73.
80. J.-M. Lee; K.-K. Kim; C.-K. Hyun; H. Tampo; S. Niki. Microstructural Evolution of ZnO by Wet-Etching Using Acidic Solutions. *J. Nanosci. Nanotechnol.* **2006**, 6, 3364-3368.
81. M. Mehta; C. Meier. Controlled Etching Behavior of O-Polar and Zn-Polar ZnO Single Crystals. *J. Electrochem. Soc.* **2011**, 158, H119-H123.
82. C. C. Hsiao; Y. C. Hu; R. C. Chang. Some design considerations on the electrode layout of ZnO pyroelectric sensors. *Sens. Mater.* **2010**, 22, 417-425.
83. A. Crossay; S. Buecheler; L. Kranz; J. Perrenoud; C. M. Fella; Y. E. Romanyuk; A. N. Tiwari. Spray-deposited Al-doped ZnO transparent contacts for CdTe solar cells. *Sol. Energ. Mat. Sol. Cells* **2012**, 101, 283-288.
84. J. Meyer; P. Görrn; S. Hamwi; H.-H. Johannes; T. Riedl; W. Kowalsky. Indium-free transparent organic light emitting diodes with Al doped ZnO electrodes grown by atomic layer and pulsed laser deposition. *Appl. Phys. Lett.* **2008**, 93, 073308.
85. B.-Y. Oh; M.-C. Jeong; T.-H. Moon; W. Lee; J.-M. Myoung; J.-Y. Hwang; D.-S. Seo. Transparent conductive Al-doped ZnO films for liquid crystal displays. *J. Appl. Phys.* **2006**, 99, 124505.
86. M. Hjiri; L. El Mir; S. G. Leonardi; A. Pistone; L. Mavilia; G. Neri. Al-doped ZnO for highly sensitive CO gas sensors. *Sens. Actuators B Chem.* **2014**, 196, 413-420.
87. P. P. Sahay; R. K. Nath. Al-doped ZnO thin films as methanol sensors. *Sens. Actuators B Chem.* **2008**, 133, 222-227.
88. C.-C. Chang; N.-F. Chiu; D. S. Lin; Y. Chu-Su; Y.-H. Liang; C.-W. Lin. High-sensitivity detection of carbohydrate antigen 15-3 using a gold/zinc oxide thin film surface plasmon resonance-based biosensor. *Anal. Chem.* **2010**, 82, 1207-1212.
89. R. W. Wood. On a Remarkable Case of Uneven Distribution of Light in a Diffraction Grating Spectrum. *Proc. Phys. Soc. London* **1902**, 18, 269-275.
90. J. W. S. L. Rayleigh). On the Dynamical Theory of Gratings. *Proc. R. Soc. Lond. A* **1907**, 79, 399-416.
91. U. Fano. The Theory of Anomalous Diffraction Gratings and of Quasi-Stationary Waves on Metallic Surfaces (Sommerfeld's Waves). *J. Opt. Soc. Am.* **1941**, 31, 213-222.
92. D. Pines. Collective energy losses in solids. *Rev. Mod. Phys.* **1956**, 28, 184-198.

93. D. Pines; D. Bohm. A Collective Description of Electron Interactions: II. Collective vs Individual Particle Aspects of the Interactions. *Phys. Rev.* **1952**, 85, 338-353.
94. R. H. Ritchie. Plasma losses by fast electrons in thin films. *Phys. Rev.* **1957**, 106, 874-881.
95. A. Otto. Exitation of nonradiative surface plasma waves in silver by the method of frustrated total reflection. *Z. Phys.* **1968**, 216, 398-410.
96. E. Kretschmann; H. Reather. Radiative decay of nonradiative surface plasmon excited by light. *Z. Naturf.* **1968**, 23A, 2135-2136.
97. S. A. Maier. *Plasmonics: Fundamentals and Applications*. Springer: 2007.
98. K. A. Willets; R. P. V. Duyne. Localized surface plasmon resonance spectroscopy and sensing. *Annu. Rev. Phys. Chem.* **2007**, 58, 267-297.
99. K. M. Mayer; J. H. Hafner. Localized Surface Plasmon Resonance Sensors. *Chem. Rev.* **2011**, 111, 3828-3857.
100. B. Sharma; R. R. Frontiera; A.-I. Henry; E. Ringe; R. P. Van Duyne. SERS: Materials, applications, and the future. *Mater. Today* **2012**, 15, 16-25.
101. C. Nylander; B. Liedberg; T. Lind. Gas detection by means of surface plasmons resonance. *Sens. Actuators* **1982**, 3, 79-88.
102. B. Liedberg; C. Nylander; I. Lundström. Surface plasmons resonance for gas detection and biosensing. *Sens. Actuators* **1983**, 4, 299-304.
103. D. L. Enrico; M. G. Manera; G. Montagna; F. Cimaglia; M. Chiesa; P. Poltronieri; A. Santino; R. Rella. SPR based immunosensor for detection of Legionella pneumophila in water samples. *Opt. Commun.* **2013**, 294, 420-426.
104. B. Vega; A. Calle; A. Sánchez; L. M. Lechuga; A. M. Ortiz; G. Armelles; J. M. Rodríguez-Frade; M. Mellado. Real-time detection of the chemokine CXCL12 in urine samples by surface plasmon resonance. *Talanta* **2013**, 109, 209-215.
105. M. Soler; M. C. Estevez; M. d. L. Moreno; A. Cebolla; L. M. Lechuga. Label-free SPR detection of gluten peptides in urine for non-invasive celiac disease follow-up. *Biosens. Bioelectron.* **2016**, 79, 158-164.
106. J. Ashley; S. F. Y. Li. An aptamer based surface plasmon resonance biosensor for the detection of bovine catalase in milk. *Biosens. Bioelectron.* **2013**, 48, 126-131.
107. Y. Lu; Y. Xia; M. Pan; X. Wang; S. Wang. Development of a surface plasmon resonance immunosensor for detecting melamine in milk products and pet foods. *J. Agric. Food Chem.* **2014**, 62, 12471-12476.
108. J. Homola; H. B. Lu; G. G. Nenninger; J. Dostálek; S. S. Yee. A novel multichannel surface plasmon resonance biosensor. *Sens. Actuators B Chem.* **2001**, 76, 403-410.
109. J. Dostálek; H. Vaisocherová; J. Homola. Multichannel surface plasmon resonance biosensor with wavelength division multiplexing. *Sens. Actuators B Chem.* **2005**, 108, 758-764.
110. J. Homola; H. Vaisocherová; J. Dostálek; M. Piliarik. Multi-analyte surface plasmon resonance biosensing. *Methods* **2005**, 37, 26-36.
111. J. Homola; S. S. Yee; G. Gauglitz. Surface plasmon resonance sensors: review. *Sens. Actuators B Chem.* **1999**, 54, 3-15.
112. Rajan; S. Chand; B. D. Gupta. Surface plasmon resonance based fiber-optic sensor for the detection of pesticide. *Sens. Actuators B Chem.* **2007**, 123, 661-666.
113. H. Suzuki; M. Sugimoto; Y. Matsui; J. Kondoh. Effects of gold film thickness on spectrum profile and sensitivity of a multimode-optical-fiber SPR sensor. *Sens. Actuators B Chem.* **2008**, 132, 26-33.

114. Z. Liu; Y. Wei; Y. Zhang; Y. Wang; E. Zhao; Y. Zhang; J. Yang; C. Liu; L. Yuan. A multi-channel fiber SPR sensor based on TDM technology. *Sens. Actuators B Chem.* **2016**, 226, 326-331.
115. Y. Liu; Q. Liu; S. Chen; F. Cheng; H. Wang; W. Peng. Surface Plasmon Resonance Biosensor Based on Smart Phone Platforms. *Sci. Rep.* **2015**, 5, 12864.
116. D. C. Cullen; R. G. W. Brown; C. R. Lowe. Detection of immuno-complex formation via surface plasmon resonance on gold-coated diffraction gratings. *Biosensors* **1987**, 3, 211-225.
117. D. C. Cullen; C. R. Lowe. A direct surface plasmon—polariton immunosensor: Preliminary investigation of the non-specific adsorption of serum components to the sensor interface. *Sens. Actuators B Chem.* **1990**, 1, 576-579.
118. D. Cai; Y. Lu; K. Lin; P. Wang; H. Ming. Improving the sensitivity of SPR sensors based on gratings by double-dips method (DDM). *Opt. Express* **2008**, 16, 14597-14602.
119. T. W. Ebbesen; H. J. Lezec; H. F. Ghaemi; T. Thio; P. A. Wolff. Extraordinary optical transmission through sub-wavelength hole arrays. *Nature* **1998**, 391, 667-669.
120. H. F. Ghaemi; T. Thio; D. E. Grupp; T. W. Ebbesen; H. J. Lezec. Surface plasmons enhance optical transmission through subwavelength holes. *Phys. Rev. B* **1998**, 58, 6779-6782.
121. S.-H. Chang; S. K. Gray; G. C. Schatz. Surface plasmon generation and light transmission by isolated nanoholes and arrays of nanoholes in thin metal films. *Opt. Express* **2005**, 13, 3150-3165.
122. J. Ji; J. G. O'Connell; D. J. D. Carter; D. N. Larson. High-Throughput Nanohole Array Based System To Monitor Multiple Binding Events in Real Time. *Anal. Chem.* **2008**, 80, 2491-2498.
123. C. A. Barrios; V. Canalejas-Tejero; S. Herranz; J. Urraca; M. C. Moreno-Bondi; M. Avella-Oliver; Á. Maquieira; R. Puchades. Aluminum Nanoholes for Optical Biosensing. *Biosensors* **2015**, 5, 417-431.
124. C. A. Barrios; V. Canalejas-Tejero; S. Herranz; M. C. Moreno-Bondi; M. Avella-Oliver; R. Puchades; A. Maquieira. Aluminum Nanohole Arrays Fabricated on Polycarbonate for Compact Disc-Based Label-Free Optical Biosensing. *Plasmonics* **2014**, 9, 645-649.
125. C. A. Barrios; V. Canalejas-Tejero. Compact discs as versatile cost-effective substrates for releasable nanopatterned aluminium films. *Nanoscale* **2015**, 7, 3435-3439.
126. S. Eustis; M. A. El-Sayed. Why gold nanoparticles are more precious than pretty gold: Noble metal surface plasmon resonance and its enhancement of the radiative and nonradiative properties of nanocrystals of different shapes. *Chem. Soc. Rev.* **2006**, 35, 209-217.
127. R. Viswambari Devi; M. Doble; R. S. Verma. Nanomaterials for early detection of cancer biomarker with special emphasis on gold nanoparticles in immunoassays/sensors. *Biosens. Bioelectron.* **2015**, 68, 688-698.
128. M.-C. Daniel; D. Astruc. Gold Nanoparticles: Assembly, Supramolecular Chemistry, Quantum-Size-Related Properties, and Applications toward Biology, Catalysis, and Nanotechnology. *Chem. Rev.* **2004**, 104, 294-346.
129. I. H. El-Sayed; X. Huang; M. A. El-Sayed. Surface Plasmon Resonance Scattering and Absorption of anti-EGFR Antibody Conjugated Gold Nanoparticles in Cancer Diagnostics: Applications in Oral Cancer. *Nano Lett.* **2005**, 5, 829-834.
130. C. R. Yonzon; E. Jeoung; S. Zou; G. C. Schatz; M. Mrksich; R. P. V. Duyne. A Comparative Analysis of Localized and Propagating Surface Plasmon Resonance Sensors: The Binding of Concanavalin A to a Monosaccharide Functionalized Self-Assembled Monolayer. *J. Am. Chem. Soc.* **2004**, 126, 12669-12676.

131. W. P. Hall; S. N. Ngatia; R. P. Van Duyne. LSPR Biosensor Signal Enhancement Using Nanoparticle−Antibody Conjugates. *J. Phys. Chem. C* **2011**, 115, 1410-1414.
132. A. J. Haes; L. Chang; W. L. Klein; R. P. Van Duyne. Detection of a Biomarker for Alzheimer's Disease from Synthetic and Clinical Samples Using a Nanoscale Optical Biosensor. *J. Am. Chem. Soc.* **2005**, 127, 2264-2271.
133. J.-H. Lee; B.-C. Kim; B.-K. Oh; J.-W. Choi. Highly sensitive localized surface plasmon resonance immunosensor for label-free detection of HIV-1. *Nanomedicine* **2013**, 9, 1018-1026.
134. M. Soler; M. C. Estevez; R. Villar-Vazquez; J. I. Casal; L. M. Lechuga. Label-free nanoplasmonic sensing of tumor-associate autoantibodies for early diagnosis of colorectal cancer. *Anal. Chim. Acta* **2016**, 930, 31-38.
135. J. Spadavecchia; A. Barras; J. Lyskawa; P. Woisel; W. Laure; C.-M. Pradier; R. Boukherroub; S. Szunerits. Approach for Plasmonic Based DNA Sensing: Amplification of the Wavelength Shift and Simultaneous Detection of the Plasmon Modes of Gold Nanostructures. *Anal. Chem.* **2013**, 85, 3288-3296.
136. L. Soares; A. Csaki; J. Jatschka; W. Fritzsche; O. Flores; R. Franco; E. Pereira. Localized surface plasmon resonance (LSPR) biosensing using gold nanotriangles: detection of DNA hybridization events at room temperature. *Analyst* **2014**, 139, 4964-4973.
137. B.-R. Oh; N.-T. Huang; W. Chen; J. H. Seo; P. Chen; T. T. Cornell; T. P. Shanley; J. Fu; K. Kurabayashi. Integrated Nanoplasmonic Sensing for Cellular Functional Immunoanalysis Using Human Blood. *ACS Nano* **2014**, 8, 2667-2676.
138. R. M. A. Azzam; N. M. Bashara. *Ellipsometry and polarized light*. North-Holland Pub. Co.: 1977.
139. A. Rothen. The Ellipsometer, an Apparatus to Measure Thicknesses of Thin Surface Films. *Rev. Sci. Instrum.* **1945**, 16, 26-30.
140. R. H. Muller. Present status of automatic ellipsometers. *Surf. Sci.* **1976**, 56, 19-36.
141. B. Drevillon; J. Perrin; R. Marbot; A. Violet; J. L. Dalby. Fast polarization modulated ellipsometer using a microprocessor system for digital Fourier analysis. *Rev. Sci. Instrum.* **1982**, 53, 969-977.
142. S. N. Jasperson; S. E. Schnatterly. An Improved Method for High Reflectivity Ellipsometry Based on a New Polarization Modulation Technique. *Rev. Sci. Instrum.* **1969**, 40, 761-767.
143. E. G. Bortchagovsky. In *Possibilities of ellipsometry with surface plasmon excitation in the investigation of thin films in comparison to separated ellipsometry and surface plasmon spectroscopy*, Proc. SPIE Polarimetry and Ellipsometry, 1997; pp 239-249.
144. P. Westphal; A. Bornmann. Biomolecular detection by surface plasmon enhanced ellipsometry. *Sensor. Actuat. B-Chem.* **2002**, 84, 278-282.
145. M. Poksinski; H. Arwin. Protein monolayers monitored by internal reflection ellipsometry. *Thin Solid Films* **2004**, 455-456, 716-721.
146. M. Poksinski; H. Arwin. Total internal reflection ellipsometry: ultrahigh sensitivity for protein adsorption on metal surfaces. *Opt. Lett.* **2007**, 32, 1308-1310.
147. H. Arwin; M. Poksinski; K. Johansen. Total internal reflection ellipsometry: principles and applications. *Appl. Optics* **2004**, 3028-3036.
148. A. Nabok; A. Tsargorodskaya; A. Hassan; N. Starodub. Total internal reflection ellipsometry and SPR detection of low molecular weight environmental toxins. *Appl. Surf. Sci.* **2005**, 246, 381-386.

149. A. Nabok; A. Tsargorodskaya; F. Davis; S. P. J. Higson. The study of genomic DNA adsorption and subsequent interactions using total internal reflection ellipsometry. *Biosens. Bioelectron.* **2007**, 23, 377-383.
150. A. Nabok; A. Tsargorodskaya; M. K. Mustafa; I. Székács; N. F. Starodub; A. Székács. Detection of low molecular weight toxins using an optical phase method of ellipsometry. *Sensor. Actuat. B-Chem.* **2011**, 154, 232–237.
151. A. V. Nabok; M. K. Mustafa; A. Tsargorodskaya; N. F. Starodub. Detection of Aflatoxin B1 with a Label-Free Ellipsometry Immunosensor. *BioNanoScience* **2011**, 1, 38-45.
152. N. C. H. Le; V. Gubala; E. Clancy; T. Barry; T. J. Smith; D. E. Williams. Ultrathin and smoothpoly (methylmethacrylate) (PMMA) films for label-free biomolecule detection with total internal reflection ellipsometry (TIRE). *Biosens. Bioelectron.* **2012**, 36, 250-256.
153. W. Liu; M. Li; Z. Luo; G. Jin. Using Electrochemistry - Total Internal Reflection Ellipsometry Technique to Observe the Dissolved Oxygen Reduction on Clark Electrode. *Electrochim. Acta* **2014**, 142, 371-377.
154. M. Li; W. Liu; J. P.Correia; A. C. Mourato; A. S. Viana; G. Jin. Optical and Electrochemical Combination Sensor with Poly-Aniline Film Modified Gold Surface and Its Application for Dissolved Oxygen Detection. *Electroanal.* **2014**, 26, 374-381.
155. K. B. Rodenhausen; T. Kasputis; A. K. Pannier; J. Y. Gerasimov; R. Y. Lai; M. Solinsky; T. E. Tiwald; H. Wang; A. Sarkar; T. Hofmann; N. Ianno; M. Schubert. Combined optical and acoustical method for determination of thickness and porosity of transparent organic layers below the ultra-thin film limit. *Rev. Sci. Instrum.* **2011**, 82, 103111.
156. S. A. J. van der Meulen; G. V. Dubacheva; M. Dogterom; R. P. Richter; M. E. Leunissen. Quartz Crystal Microbalance with Dissipation Monitoring and Spectroscopic Ellipsometry Measurements of the Phospholipid Bilayer Anchoring Stability and Kinetics of Hydrophobically Modified DNA Oligonucleotides. *Langmuir* **2014**, 30, 6525-6533.
157. K. Lodewijks; W. V. Roy; G. Borghs; L. Lagae; P. V. Dorpe. Boosting the figure-of-merit of LSPR-based refractive index sensing by phase-sensitive measurements. *Nano Lett.* **2012**, 12, 1655-1659.
158. R. S. Moirangthem; Y.-C. Chang; P.-K. Wei. Investigation of surface plasmon biosensing using gold nanoparticles enhanced ellipsometry. *Opt. Lett.* **2011**, 36, 775-777.
159. R. S. Moirangthem; M. T. Yaseen; P.-K. Wei; J.-Y. Cheng; Y.-C. Chang. Enhanced localized plasmonic detections using partially-embedded gold nanoparticles and ellipsometric measurements. *Biomed. Opt. Express* **2012**, 3, 899-910.
160. R. S. Moirangthem; Y.-C. Chang; P.-K. Wei. Ellipsometry study on gold-nanoparticle-coated gold thin film for biosensing application. *Biomed. Opt. Express* **2011**, 2, 2569-2576.

2. Background

2.1. Dielectrophoresis physics

In this section, a summary of the dielectrophoresis (DEP) physics is shown aiming at describing the properties that lead to manipulate particles in a liquid medium. The analysis begins with the study of a spherical particle under the action of an electric field. In that scenario, the charges inside the particle and the medium are redistributed forming effective dipoles in the vicinity of the particle-medium interface whose strength depends on the polarizability of the particle and the liquid medium.

Figure 2.1 shows the electric field lines surrounding a dielectric particle within a liquid medium for: a) a uniform electric field, created by an infinite parallel plane capacitor (Figure 2.1A), and b) a non-uniform electric field, created by a parallel plane capacitor formed by an infinite (left, Figure 2.1B) electrode and a finite electrode (right, Figure 2.1B). In both cases, it is assumed as a common case that the dielectric constant of the particle is larger than the one in the liquid medium, thus bending the electric field lines towards the inner volume of the particle. In the non-uniform electric field case, the electric field strength on the right part of the particle is greater than in the left part due to the finiteness of the right electrode. This produces an inhomogeneous dipole distribution along the particle surface. The force exerted on the surface of the particle by the non-uniform electric field is equal to $\vec{m} \cdot \nabla \vec{E}$ where $\vec{m}$ is the dipole moment vector, and $\nabla \vec{E}$ is the electric field gradient. In case the effective $\vec{m}$ across the particle surface points out towards the medium, the force points out in the direction of increasing electric field

(positive DEP). If, on the other hand, the effective $\vec{m}$ across the particle surface points out towards the inner volume of the particle, the force points out in the direction of decreasing electric field (negative DEP).

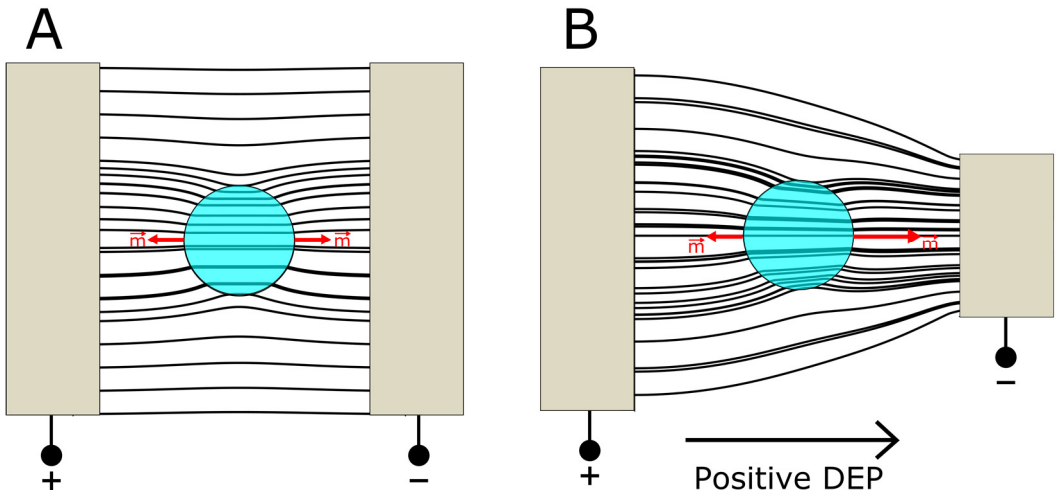

Figure 2.1. Representation of the electric field lines in a plane parallel capacitor for a dielectric particle embedded in a liquid medium under a (A) uniform or (B) non-uniform electric field. It is assumed that the dielectric constant of the particle is larger than the dielectric constant of the medium so the dipole moment vector at the interface points out towards the surrounding medium.

Taking into account the different polarizabilities of the particle and medium, the net dielectrophoretic force (F_{DEP}) acting on a homogeneous spheroid particle suspended in a homogeneous medium can be expressed as:

$$F_{DEP} = c\varepsilon_m \,\mathrm{Re}\{f_{cm}\}\nabla E^2, \qquad (2.1)$$

where c is a factor related to the particle volume, ε_m is the dielectric constant of the medium, ∇E^2 is the gradient of the squared electric field and $Re\{f_{cm}\}$ is the real part of the Clausius-Mossotti factor.

The expression for f_{cm} was given by the physicists O. Mossotti[1] and R. Clausius,[2] and can be understood as the strength of the effective dipole in the particle immersed in an electric field, after taking into account the screening of the surrounding dipoles. For a spherical particle, the factor is given by:

$$f_{cm} = \frac{\varepsilon_p^* - \varepsilon_m^*}{\varepsilon_p^* + 2\varepsilon_m^*}, \tag{2.2}$$

where ε_p^* and ε_m^* are the complex dielectric constants of the particle and the medium, respectively, defined as $\varepsilon^* = \varepsilon - i\,(\sigma/\omega)$. σ and ω are the electrical conductivity and the angular frequency, respectively. As can be seen in this equation, when the dielectric constant of the particle is larger than the dielectric constant of the medium, f_{cm} is positive and particles move towards the regions with the highest electric field (positive DEP). Otherwise, particles move to the regions with the lowest electric field (negative DEP).

Although further information about the influence of different shaped-particles to the DEP force can be found in the bibliography,[3] it is here considered the case of NWs that can be approximated by ellipsoids with a high aspect ratio.[4] In that case, a depolarization factor L_t is introduced in the *t* direction and f_{cm} is redefined as:

$$f_{cm} = \frac{\varepsilon_p^* - \varepsilon_m^*}{3\left(\varepsilon_m^* + L_t\left(\varepsilon_p^* - \varepsilon_m^*\right)\right)} \tag{2.3}$$

$$L_t = \frac{r_1 r_2 r_3}{2}\int_0^\infty \frac{ds}{\left(s + r_t^2\right)\sqrt{\left(s + r_1^2\right)\left(s + r_2^2\right)\left(s + r_3^2\right)}}, \tag{2.4}$$

where the subindices 1, 2 and 3 in L_t represent the ellipsoid's principal axis.

Equations 2.3 and 2.4 denote that f_{cm} strongly depends on the NW dimensions (NW radius, r_{NW}, and length, L_{NW}) and the relative orientation of the NW with respect to the electric field direction. For NWs, Equation 2.4 can be rewritten as:

$$L_t = \frac{r_{NW}^2\left(L_{NW}/2\right)}{2}\int_0^\infty \frac{ds}{\left(s + r_t^2\right)\sqrt{\left(s + r_{NW}^2\right)^2\left(s + \left(L_{NW}/2\right)^2\right)}}, \tag{2.5}$$

where r_t is equal to r_{NW}, when the electric field is perpendicular to the NW long axis, and equal to $L_{NW}/2$, when the electric field is parallel to the NW.[3]

Previous studies in our laboratory have analyzed the influence of the different parameters in Equation 2.1 on the DEP force exerted on a ZnO NW (ε_{ZnO} = 10ε_0, σ_{ZnO} = 1 S/m), through the application of an external AC bias between two coplanar electrodes deposited on an insulating substrate and separated 4 μm.[5-7] The ZnO NW has been

assumed to be an ellipsoid of average radius and length of 50 nm and 10 μm, respectively. The main conclusions of these studies are included here:

- **Gradient of the squared electric field (∇E^2):** this parameter strongly depends on the electrode geometry and the effective voltage, V_{RMS}. Approximating the coplanar electrode geometry by a parallel plate capacitor, the electric field between electrodes can be calculated from: $E_{RMS} = V_{RMS}/d$, where d is the distance between electrodes. This value represents the maximum electric field in the region between electrodes near the substrate surface. For a V_{RMS} = 10 V and a d = 4 μm, the electric field takes a value of 2.5×10^4 V/cm. As the distance from the surface increases, the value of the electric field decays. In the far-field region, the squared electric field drops proportionally to $\left(V_{RMS}/\pi z\right)^2$ along the midpoint line between electrodes, where z is the distance to the substrate plane (Figure 2.2). It is worth noticing that the electric field value at those distances is weakly dependent on the width of the gap between electrodes, as shown in Figure 2.2 for three gaps: 2, 4 and 6 μm. Taking into account that $F_{DEP,z} \propto \nabla E_{RMS}^2$, the force decreases as z^{-3} as the distance of the NW to the substrate plane increases. To give and idea of the magnitude of the DEP force, a numerical calculation can be done for a particular case of a NW located at a distance of 10 μm above the interelectrode gap under an AC bias of 10 V and a frequency of 100 kHz. The attracting DEP force on the NW would be about 30 pN at the position z = 1 μm. To intensify the electric field strength in specific parts of the host substrate, coplanar electrodes are typically defined by optical lithography on a thin film of a conductive material. Those electrodes are connected to an external voltage source to generate the AC signal.

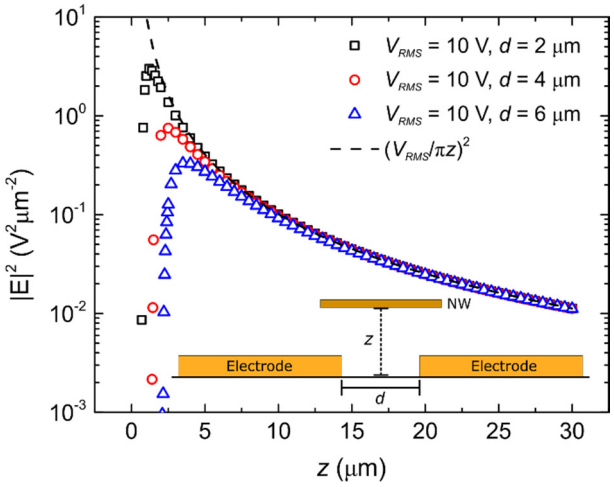

Figure 2.2. Electric field squared calculated as a function of the height *z* for gap widths of 2 µm, 4 µm and 6 µm. The inset of this Figure illustrates the scheme followed to calculate the electric field squared, for two coplanar electrodes separated an interelectrode gap *d*, and a NW located at a distance *z* from the substrate surface.

- **Frequency:** the frequency of the applied alternating voltage has a strong influence on the Clausius-Mossotti factor, which is related to the effective dipole moment formed in the NW. This factor depends on the nanostructure material and the NW orientation with respect to the electric field. Typically, f_{cm} is fairly constant at very low frequencies (< 1 kHz). As the frequency increases, the polarizability of the structure reduces and the f_{cm} experiments a decrease of a factor of 100 per decade.

- **NW orientation:** Equations 2.3-2.5 indicate how the orientation of the NW affects the f_{cm} value through the depolarization factor L_t. For a NW located at 10 µm above the interelectrode gap and under an AC bias of V_{RMS} = 7.5 V and a frequency of 10 kHz, the strongest force exerted on the NW is found when the NW largest axis is aligned parallel to the field, being in the order of 20 pN. However, this force decreases rapidly up to a steady level of around 0.02 pN when the NW forms an angle of 40º with the direction of the electric field.

Whilst reading this section, one should note the importance of taking into account all the experimental conditions. The change from one nanostructure or medium to other ones with different physical and chemical properties will probably lead to different experimental parameters for optimum NW trapping and alignment.

2.2. Ellipsometry physics

2.2.1. Ellipsometric functions

Ellipsometry is a non-destructive optical technique for studying surfaces and thin films.[8, 9] It has been extensively used in semiconductor and electronics development due to its high sensitivity for the determination of thin film thicknesses and optical parameters. To assist in the understanding of the results included in further Chapters with this powerful technique for surface characterization, a brief explanation of its physics is provided in the next lines.

Light is an electromagnetic wave, whose nature can be fully described by four vectors: electric field, electric displacement density, magnetic field and magnetic flux density, all of which are related through the Maxwell's equations. Historically, the electric field ($\vec{E}$) has been the vector chosen to study the polarization state of light. $\vec{E}$ can be decomposed, at a fixed point of the space, into three orthogonal components in the Cartesian coordinate system (*x*, *y* and *z*):

$$\vec{E}(t) = \vec{E}_x \vec{u}_x + \vec{E}_y \vec{u}_y + \vec{E}_z \vec{u}_z \tag{2.6}$$

where $\vec{u}_x$, $\vec{u}_y$ and $\vec{u}_z$ are the unit vectors along the coordinate axes. Since the time variation of $\vec{E}$ for a monochromatic plane wave takes a sinusoidal form. Therefore, each one of these components can be represented by its amplitude (E_i) and phase (δ_i) along the *i* coordinate as:

$$\vec{E}_i(t) = E_i \cos\left(\omega t + \delta_i\right) \tag{2.7}$$

where ω and *t* are the angular frequency and time, respectively.

It is useful to transform the previous sinusoidal function into a complex number by using the Euler's formula. Since the electromagnetic waves keep the same frequency when they are reflected or transmitted at an interface, it is possible to drop the time-varying component and adopt the phasorial representation. Thus, the *i* component of the electric field yields:

$$\vec{E}_i(t) = \mathrm{Re}\left\{E_i e^{j\delta_i} e^{j\omega t}\right\} \tag{2.8}$$

$$\hat{E}_i = E_i e^{j\delta_i} \tag{2.9}$$

where $\hat{E}_i$ is the phasor of the *i* component. To understand what happens to an arbitrary incident electromagnetic wave when it reflects onto an interface, it is adequate to represent the amplitude and phase in terms of the orthogonal p- and s-polarizations ($\vec{E}_P$, $\vec{E}_S$). The first term accounts for an electric field parallel to the incident plane, whereas in the second term the electric field is perpendicular to that plane, as shown in Figure 2.3. In this Figure, φ_i represents the incidence angle of the light beam with respect to the surface normal.

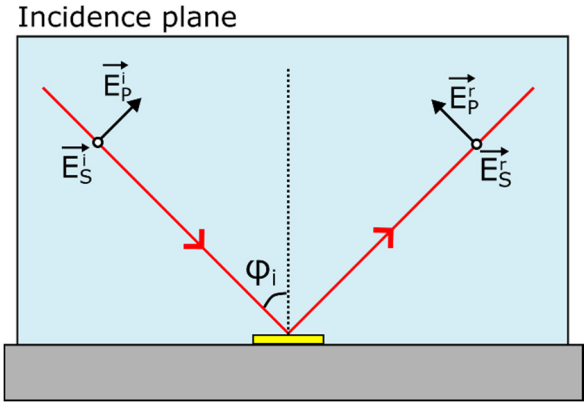

Figure 2.3. A scheme of a light beam impinging a sample surface where the orthogonal components of the electric field, $\vec{E}_P$ and $\vec{E}_S$ are represented. The incidence angle is measured with respect to the surface normal.

$\vec{E}_P$ and $\vec{E}_S$ before and after the reflection are related through the Fresnel reflection coefficients, as given by the following expressions:

$$E_P^r e^{j\delta_{r,P}} = r_P E_P^i e^{j\delta_{i,P}} \tag{2.10}$$

$$E_S^r e^{j\delta_{r,S}} = r_S E_S^i e^{j\delta_{i,S}} \tag{2.11}$$

where "*i*" and "*r*" refer to the incident and reflected light beams, respectively. The Fresnel reflection coefficients evaluate the change induced on the amplitude and phase of the incident light. To examine this change in more detail, the coefficients are shown in their phasorial representation:

$$r_P = |r_P| e^{j\delta_P} \tag{2.12}$$

$$r_S = |r_S| e^{j\delta_S} \tag{2.13}$$

where $|r_P| = E_P^r / E_P^i$ and $|r_S| = E_S^r / E_S^i$ are the ratio of the amplitudes of the electric field vectors of the reflected waves with respect to the incident one, for each polarization. On the other hand, $\delta_P = \delta_{r,P} - \delta_{i,P}$ and $\delta_S = \delta_{r,S} - \delta_{i,S}$ represent the phase shifts upon reflection.

Reflection ellipsometry can measure the states of polarization induced on the incident wave upon reflection. This technique gives the Ψ and Δ parameters, expressed in degrees, which are known as ellipsometric functions or ellipsometric angles. These functions are related to the Fresnel coefficients ratio (ρ) through:

$$\rho = \frac{r_P}{r_S} = \tan(\Psi) e^{(j\Delta)} \tag{2.14}$$

$$\tan(\Psi) = \frac{|r_P|}{|r_S|}, \qquad \Delta = \delta_P - \delta_S \tag{2.15}$$

The tangent of Ψ is typically denoted as the amplitude ratio between p- and s-polarization components of the reflected beam. Δ is the difference between the phase shifts for both polarization components.

2.2.1.1. Air/substrate structure

The simplest structure to analyze under reflection ellipsometry is the air/substrate system. This system comprises two semi-infinite isotropic media, whose refractive indices are considered to undergo an abrupt change at the interface. When an incident light beam, whose direction of propagation lies on the incidence plane, impinges on the sample surface, part of this beam is reflected and the other part is transmitted (see Figure 2.4). In this model, the incidence (φ_1) and refraction (φ_2) angles are related by the Snell's law: $\tilde{N}_1 \sin(\varphi_1) = \tilde{N}_2 \sin(\varphi_2)$, whereas the incidence and reflected angles must be the same. $\tilde{N}_1$ and $\tilde{N}_2$ are the complex refractive indices ($\tilde{N} = n + i\kappa$) of media 1 and 2. The reflected part of the beam undergoes changes in its amplitude and phase, which are not

the same for both electrical vector components. The magnitude of these changes depends on the optical properties of both media, and is quantified through the Fresnel reflection coefficients.

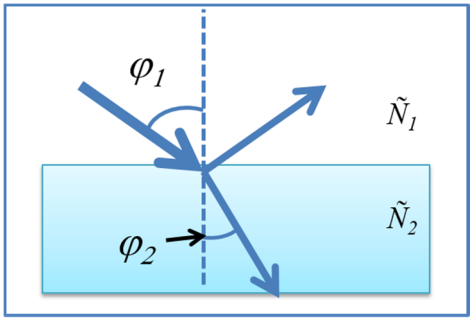

Figure 2.4. Scheme of the reflections and transmissions at a single interface.

These coefficients for a single layer interface, r_{12}^P and r_{12}^S, are defined as:

$$r_{12}^P = \frac{\tilde{N}_2 \cos\varphi_1 - \tilde{N}_1 \cos\varphi_2}{\tilde{N}_2 \cos\varphi_1 + \tilde{N}_1 \cos\varphi_2} \tag{2.16}$$

$$r_{12}^S = \frac{\tilde{N}_1 \cos\varphi_1 - \tilde{N}_2 \cos\varphi_2}{\tilde{N}_1 \cos\varphi_1 + \tilde{N}_2 \cos\varphi_2}, \tag{2.17}$$

where φ_1 and φ_2 are the beam angles represented in Figure 2.4. Subscripts refer to media 1 and 2.

In the air/substrate system, it is possible to determine the complex dielectric function (ε) of the medium 2 from the Fresnel ratio and the incidence angle as:

$$\varepsilon = \varepsilon_r + i\varepsilon_i = \sin^2(\varphi_1) \cdot \left(1 + \tan^2(\varphi_1) \cdot \frac{(1-\rho)^2}{(1+\rho)^2} \right) \tag{2.18}$$

Since the Fresnel coefficient ratio and ellipsometric angles are related through Equation 2.14, the following expression for the real and imaginary parts of the dielectric function are obtained:

$$\varepsilon_r = n^2 - \kappa^2 = \sin^2(\varphi_1)\cdot\left(1+\frac{\tan^2(\varphi_1)\cdot\left(\cos^2(2\Psi)-\sin^2(\Delta)\cdot\sin^2(2\Psi)\right)}{\left(1+\sin(2\Psi)\cdot\cos(\Delta)\right)^2}\right) \quad (2.19)$$

$$\varepsilon_i = 2n\kappa = \frac{\sin^2(\varphi_1)\cdot\tan^2(\varphi_1)\cdot\sin(4\Psi)\cdot\sin(\Delta)}{\left(1+\sin(2\Psi)\cdot\cos(\Delta)\right)^2} \quad (2.20)$$

Thus, the calculation of the optical properties of a flat substrate with infinite thickness is quite straightforward from the ellipsometric functions. However, there are only a few cases where this simple model can be applied. In general, Ψ and Δ are measured in more complex systems that depart from this ideal structure due to effects of roughness or inhomogeneities on the surface. The use of Equations 2.18-2.20 yields a complex dielectric function that accounts for the optical properties of the whole multi-layered system. In this case, the calculated values of the dielectric function are commonly written between brackets ($<\varepsilon>$) and named with the prefix "pseudo".

2.2.1.2. Air/film/substrate structure

The addition of a thin film on the substrate gives rise to more complicated Fresnel equations. In this case, the resultant reflected wave to medium 1 comprises the light reflected directly from the first interface plus all the refracted beams from medium 2 obtained from the multiple reflections at the substrate surface (see Figure 2.5). From Figure 2.5, the first reflected wave only depends on the reflection produced at the 1-2 interface. The next reflected wave to medium 1 will depend on the first reflection produced at the 2-3 interface and twice the transmission along the medium 2, and so forth. The addition of all the partial reflection waves to medium 1 yields an infinite geometric series, whose summation gives rise to the following Fresnel reflection coefficients:

$$r_{13}^P = \frac{r_{12}^P + r_{23}^P e^{-j2\beta}}{1 + r_{12}^P r_{23}^P e^{-j2\beta}} \quad (2.21)$$

$$r_{13}^S = \frac{r_{12}^S + r_{23}^S e^{-j2\beta}}{1 + r_{12}^S r_{23}^S e^{-j2\beta}}, \quad (2.22)$$

where β is given by:

$$\beta = 2\pi \frac{d_{film}}{\lambda} \tilde{N}_2 \cos\varphi_2 , \qquad (2.23)$$

and where d_{film} is the thin film thickness.

The dielectric properties of the thin film can be calculated from Ψ and Δ by using Equations 2.18-2.20. However, the ellipsometric functions contain information of the whole air/film/substrate system. Therefore, the dielectric functions are pseudodielectric, as discussed in the previous Section.

From Equations 2.14 and 2.21-2.23, the thickness of the analyzed layer can be estimated from the ellipsometric spectra, if the complex refractive index of each medium is known, by using the ellipsometer software to match the simulated and experimental spectra. The veracity of the fitting depends on whether the layer/substrate model assumed is correct. For this aim, it is important to know qualitatively the layer structure under analysis through other surface characterization techniques.

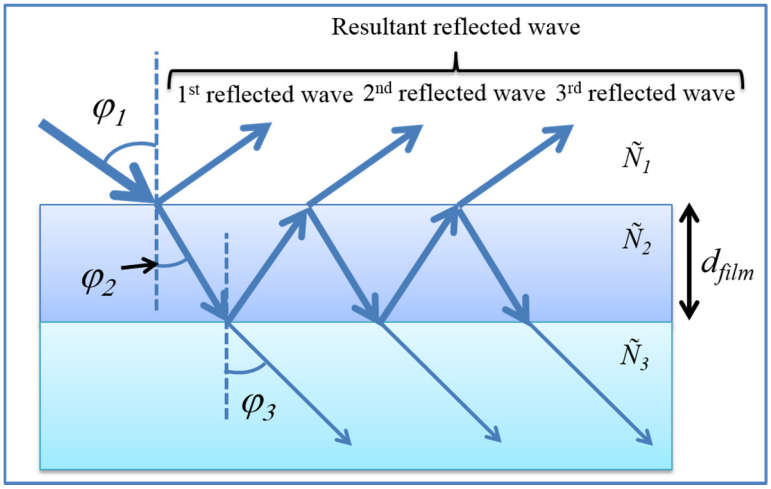

Figure 2.5. Scheme of the reflections and transmissions undergone within the air/film/substrate structure.

2.3. Surface plasmon physics

The surface plasmon resonance can be defined as the longitudinal collective oscillation of free electrons at the interface between a positive and a negative dielectric constant material. When this happens, there is an energy and momentum transfer from photons of the incidence light to the material electrons. This objective is fulfilled by

coupling the p-polarized component of the light (also called transverse magnetic, TM) to the metallic thin film. On the contrary, the s-polarized light (transverse electric, TE) cannot excite the thin film polariton. It is evident that spectroscopic ellipsometry is a very powerful tool to analyze plasmonic structures since the ellipsometric functions give information about the amplitude and phase for both types of polarization. Figure 2.6 represents one of the most common optical coupling systems based on the Kretschmann configuration: a high refractive index prism attached to an Au thin film.

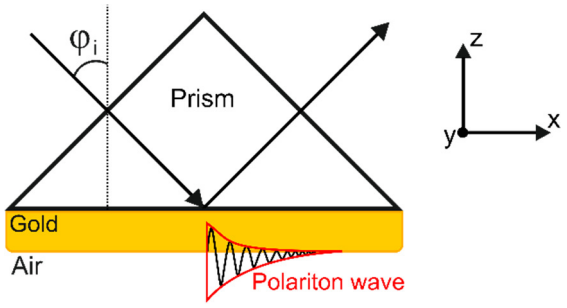

Figure 2.6. Scheme of the prism-based coupling system, where φ_i is the incidence angle of the light beam with respect to the surface normal. The polariton wave produced in the metal and the dielectric media is represented in red.

In the rest of the Section, we analyze the conditions that lead to the excitation of the surface plasmon (SP) at the gold-air interface for the setup and coordinate system sketched in Figure 2.6. The SP excitement requires satisfying the wavevector conservation equation between the incidence light wavevector in the direction of propagation (k_x^{light}) should be equal to the real part of the SP wavevector ($k_{x,r}^{SP}$):

$$k_x^{light} = k_{x,r}^{SP}. \tag{2.24}$$

For light travelling inside the prism (dielectric constant of the prism = ε_{prism}) to the metallic film at an incidence angle, φ_i, the x component of the light beam wavevector is:

$$k_x^{light} = \frac{\omega}{c}\sqrt{\varepsilon_{prism}}\sin(\varphi_i). \tag{2.25}$$

On the other hand, the $k_{x,r}^{SP}$ parameter is given by the optical properties of the metal and the dielectric material (in this case air) forming the lower interface.[10] Since this

parameter must satisfy the Maxwell's equations, it can be demonstrated that the real part of $k_{x,r}^{SP}$ is given by the following expression:

$$k_{x,r}^{SP} = \frac{\omega}{c}\left(\frac{\varepsilon_{m,r}\varepsilon_d}{\varepsilon_{m,r}+\varepsilon_d}\right)^{1/2}, \tag{2.26}$$

where $\varepsilon_{m,r}$, ε_d, ω and c are the real part of the metal dielectric constant, the dielectric constant of air, the angular frequency and the speed of light in vacuum, respectively.

The imaginary part of the SP wavevector is related to the energy loss through absorption in the metal and gives information about the attenuation of the SPs in the direction of propagation. From the Maxwell's equations, it can be also demonstrated that the imaginary part is given by:

$$k_{x,i}^{SP} = \frac{\omega}{c}\left(\frac{\varepsilon_{m,r}\varepsilon_d}{\varepsilon_{m,r}+\varepsilon_d}\right)^{3/2}\frac{\varepsilon_{m,i}}{2\left(\varepsilon_{m,r}\right)^2}. \tag{2.27}$$

The propagation length in the *x* direction can be estimated from $(2k_{x,i}^{SP})^{-1}$. In the gold/air system, this propagation length can reach up to 10 μm at 2.0 eV.

To get a surface propagating wave confined in the gold/air interface along the *x* direction, a real value of k_x^{SP} and an imaginary value of the SP wavevector in the *z* direction $\left(k_z^{SP}\right)$ are needed. This situation occurs when $\varepsilon_{m,r} < 0$ and $\left|\varepsilon_{m,r}\right| > \varepsilon_d$. Most metals fulfill these requirements in a wide spectral range.[11, 12]

As mentioned above, k_z^{SP} must be purely imaginary. In that case, the k_z^{SP} function provides information about the polariton wave (Figure 2.6) in metal and dielectric regions:

$$k_{z,m}^{SP} = \frac{\omega}{c}\left(\frac{\varepsilon_{m,r}^2}{\varepsilon_{m,r}+\varepsilon_d}\right)^{1/2} \tag{2.28}$$

$$k_{z,d}^{SP} = \frac{\omega}{c}\left(\frac{\varepsilon_d^2}{\varepsilon_{m,r}+\varepsilon_d}\right)^{1/2}. \tag{2.29}$$

From these parameters, the skin depth (Z) into each medium is defined as the value at which the field decays an e factor in the transverse direction. It can be calculated from:

$$Z = \frac{1}{\left|k_z^{SP}\right|}. \tag{2.30}$$

An estimation of the skin depth for the Au/air system within the metal and dielectric media yields values of 30 and 300 nm at 2.0 eV, respectively.

The representation of $k_x^{light} \cdot c/\omega$ and $k_{x,r}^{SP} \cdot c/\omega$, from Equations 2.25 and 2.26 is illustrated in Figure 2.7 for the Au/air system. $k_{x,r}^{SP} \cdot c/\omega$ (black solid curve) is a function that monotonously increases with energy. For Au, whose dielectric constants resemble the Drude model, $\varepsilon_{m,r}$ becomes more negative at lower energies. At these low energies, the absolute value of $\varepsilon_{m,r}$ is much larger than ε_d $\left(\left|\varepsilon_{m,r}\right| \gg \varepsilon_d\right)$ and the value of $k_{x,r}^{SP} \cdot c/\omega$ tends asymptotically to $\sqrt{\varepsilon_d}$. As the plasmon energy increases, $\left|\varepsilon_{m,r}\right|$ decreases approaching the condition $\varepsilon_{m,r} = -\varepsilon_d$. That condition occurs at 2.6 eV, producing and asymptotic growth in $k_{x,r}^{SP} \cdot c/\omega$.

From the described behavior, it is possible to conclude that Equation 2.24 is not going to be satisfied when light impinges directly on the Au/air interface from the air medium without the use of an optical coupler. The reason is that, according to Equation 2.25, the maximum value of $k_x^{light} \cdot c/\omega$ in that case is 1 when φ_i = 90º, represented as a red dashed curve (note that $\sqrt{\varepsilon_{prism}} = \sqrt{\varepsilon_{air}}$ in the absence of a prism). Thus, $k_x^{light} \cdot c/\omega$ will be lower than $k_{x,r}^{SP} \cdot c/\omega$, impeding the SP excitation. This conclusion can be generalized to any situation.

Therefore, to allow an optical excitation, the wavevector of the incident light must be increased. This can be accomplished by passing the light beam through a medium with higher refractive index, such as prisms (glass, BK7, fused silica or quartz). The refractive index of those materials used for commercial prisms is higher than the refractive index of air, mostly in the 1.46-1.54 range in the UV-Visible-IR spectral region, allowing to

increase the value of k_x^{light}, through Equation 2.25. At an arbitrary incidence angle of 45º, k_x^{light} (pink dashed curve) takes a constant value of 1.06 for a $\sqrt{\varepsilon_{prism}} = 1.50$. The energy in which both curves coincide (in this case, around 2.2 eV or 560 nm) is the energy required to excite the SPR.

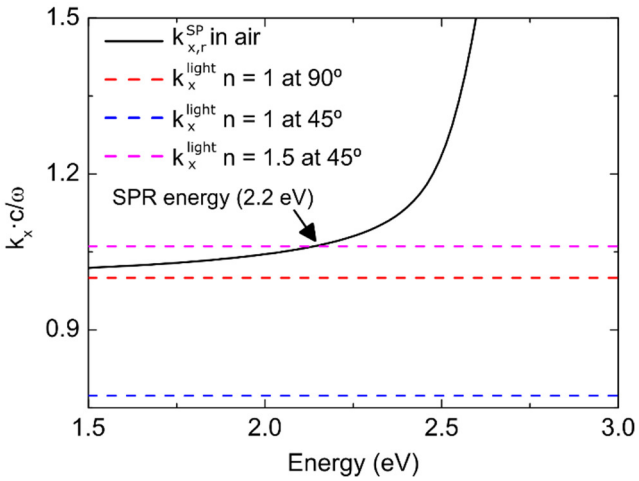

Figure 2.7. Real part of the SP wavevector ($k_{x,r}^{SP}$) in air obtained from the optical constants of Au,[13] compared to the light electromagnetic wavevector in the direction of plasmon propagation (k_x^{light}). Red and blue dashed lines represent k_x^{light} for an incidence through air medium (n = 1) at incidence angles of 90º and 45º, respectively. Pink dashed line represents k_x^{light} for an incidence through a transparent medium with an incidence angle of 45º and a refractive index of 1.5. It is worth noting that $n = \sqrt{\varepsilon}$ for a non-absorbing material. The SPR excitation occurs when both $k_{x,r}^{SP}$ and k_x^{light} wavevectors match.

2.4. Localized surface plasmon physics

2.4.1. Quasi-static approximation

The simplest theory to describe the optical behavior of nanostructures was developed by Rayleigh in 1871. This theory is only valid for very small spheres, and does not include retardation effects, typical of large nanostructures. It can be derived from an isotropic and homogeneous sphere inside an electromagnetic field with a constant amplitude. Several books address this topic, but a good one without involving quite complex formalism is the one written by Maier.[14] The approach is based on the polarization induced ($\vec{P}$) on an isotropic sphere, embedded in a dielectric medium, in the presence of an electric field $\overrightarrow{E_0}$:

$$\vec{P} = \varepsilon_m \alpha \vec{E_0}\,, \tag{2.31}$$

where α is the polarizability, which depends on the complex dielectric constants $\left(\varepsilon^* = \varepsilon_r - j\varepsilon_i\right)$ of the particle $\left(\varepsilon_p^*\right)$ and medium $\left(\varepsilon_m^*\right)$, and is defined as:

$$\alpha = 4\pi r_{sp}^3 \frac{\varepsilon_p^* - \varepsilon_m^*}{\varepsilon_p^* + 2\varepsilon_m^*}\,, \tag{2.32}$$

where r_{sp} is the sphere radius.

The real part of the polarizability can be obtained from Equation 2.32 for a non-absorbing medium $\left(\varepsilon_{m,i} = 0\right)$:

$$\mathrm{Re}\{\alpha\} = 4\pi r_{sp}^3 \frac{\varepsilon_{p,r}^2 - 2\varepsilon_{m,r}^2 + \varepsilon_{p,i}^2 - \varepsilon_{p,r}\varepsilon_{m.r}}{\left(\varepsilon_{p,r} + 2\varepsilon_{m,r}\right)^2 + \varepsilon_{p,i}^2}\,, \tag{2.33}$$

Subindices *r* and *i* refers to the real and imaginary part, respectively. It is evident that Equations 2.33 yields an infinite polarizability at the energy at which $\varepsilon_{p,r} = -2\varepsilon_m$, for $\varepsilon_{p,i} = 0$. This is the so-called Fröhlich's condition, which allows to predict the resonance energy in the presence of an electric field, whose oscillation energy $\left(E = \hbar\omega\right)$ yields these values for ε_p^* and ε_m^*. Therefore, the resonance energy depends, not only on the particle material, but also on the surrounding medium. From Equation 2.33, when $\varepsilon_{p,i} = 0$, an increase in $\varepsilon_{m,r}$ requires a more negative $\varepsilon_{p,r}$ in order to nullify the denominator. For most metals, the dielectric constants resemble the Drude model and $\varepsilon_{p,r}$ becomes more negative at longer wavelengths. Therefore, a redshift in the resonance is expected as the dielectric constant of the medium increases.

The main assumption of this approach is that the electric field amplitude inside the sphere is uniform during the excitation of the particle with the incident electromagnetic wave. Actually, this only happens for very small particles. Therefore, the theoretical analysis is also named the *electrostatic approximation*. Within this approximation, the absorption, scattering and extinction cross-sections can be extracted. They are defined following the below premise. If an imaginary sphere is constructed around an arbitrary particle (Figure 2.8), the cross-section can be defined as the net rate of electromagnetic

energy (W) that crosses through the surface A of this sphere divided by the incident irradiance (I_i):

$$C_{abs} = \frac{W_{abs}}{I_i} = k\,\mathrm{Im}\{\alpha\} = 4\pi k r_{sp}^3\,\mathrm{Im}\left\{\frac{\varepsilon_p^* - \varepsilon_m^*}{\varepsilon_p^* + 2\varepsilon_m^*}\right\} \tag{2.34}$$

$$C_{sca} = \frac{W_{sca}}{I_i} = \frac{k^4}{6\pi}|\alpha|^2 = \frac{8}{3}\pi k^4 r_{sp}^6 \left|\frac{\varepsilon_p^* - \varepsilon_m^*}{\varepsilon_p^* + 2\varepsilon_m^*}\right|^2 . \tag{2.35}$$

$$C_{ext} = C_{sca} + C_{abs} \tag{2.36}$$

where k is the modulus of the electromagnetic wave ($k = 2\pi/\lambda$), and the subscripts *sca*, *ext* and *abs* denote scattering, extinction and absorption, respectively. These equations arise from the integration of the time-averaged Poynting vector $\left(\vec{S}\right)$ along the $\vec{u}_n$ unit vector over the entire sphere surface (A): $W = -\int_A \vec{S}\cdot\vec{u}_n \cdot dA$, where $\vec{S} = \frac{1}{2}\mathrm{Re}\left\{\vec{E}\times\vec{H}^*\right\}$. $\vec{E}\times\vec{H}^*$ is the vector product between the electric field vector and the conjugate of the magnetic field vector. The full mathematical deduction can be found in the bibliography.[15] As can be observed in Equations 2.34-2.36, the cross-sections become infinite at the Fröhlich's condition.

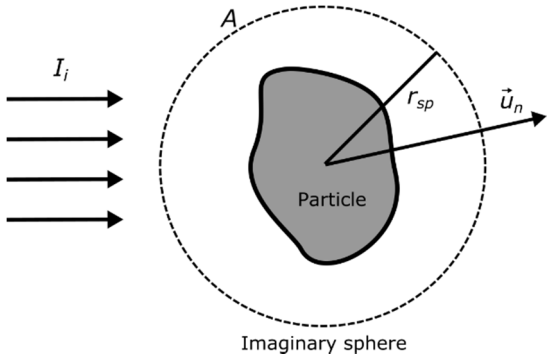

Figure 2.8. Representation of an imaginary sphere of radius r_{sp} surrounding the particle under the illumination of a plane wave.

The corresponding efficiencies (Q_{sca}, Q_{abs} and Q_{ext}) can be found dividing these cross-sections by the geometrical cross-section of the particle. For a sphere, the

geometrical cross-section becomes πr_{sp}^2. According to Bohren and Huffman, efficiencies are not limited to the unity. They demonstrated that small particles are well-known to exhibit this behavior and can be interpreted as if they are perturbing the electromagnetic field of an area larger than its cross-section.[15]

This quasi-static approximation can be extended to ellipsoidal particles. The introduction of a depolarizing factor (L_t) in the *t* direction allows expressing the polarizability in this non-spherical structure. The polarizability can be redefined as:

$$\alpha_t = 4\pi r_1 r_2 r_3 \frac{\varepsilon_p^* - \varepsilon_m^*}{3\left(\varepsilon_m^* + L_t\left(\varepsilon_p^* - \varepsilon_m^*\right)\right)}, \tag{2.37}$$

In this Equation, L_t takes the form of:

$$L_t = \frac{r_1 r_2 r_3}{2}\int_0^\infty \frac{ds}{\left(s + r_t^2\right)\sqrt{\left(s + r_1^2\right)\left(s + r_2^2\right)\left(s + r_3^2\right)}}, \tag{2.38}$$

where the subindices 1, 2 and 3 in L_t represent the ellipsoid's principal axis. In this Equation, r_t is the ellipsoidal particle dimension oriented parallel to the electric field direction. Thus, its value will strongly depend on this orientation.

According to the previous Equation, for an ellipsoid with arbitrary dimensions, L_t exhibits lower values as r_t becomes larger. Thus, the L_t takes a minimum value when the long ellipsoid axis becomes more aligned parallel to the electric field. With the introduction of L_t, the Fröhlich's condition now becomes $L_t\varepsilon_{p,r} = -\varepsilon_m$, when $\varepsilon_{p,i} = 0$. Two conclusions arise from this redefined Equation: first, different oscillatory modes arise depending on the orientation of the particle with respect to the electric field direction and, thus, a resonance splitting for the ellipsoidal case becomes possible; second, the resonance of the particle will redshift if the spherical particle is elongated in the direction of the electric field. It is worth noting that this theory is quantitatively valid for particles smaller than the excitation wavelength.

2.4.2. Discrete dipole approximation

The discrete dipole approximation (DDA) is a method to solve the Maxwell's equations for particles of arbitrary shape with complex refractive index. The basic idea

was introduced by DeVoe,[16, 17] and later by Purcell and Pennypacker.[18] It was not until Draine and Flatau research that this idea was implemented into an open-source program named DDSCAT.[19]

DDA is based on the discretization of the whole nanostructure (target) into an array of N-point dipoles located on a cubic lattice at positions r_i with polarizabilities α_i. After exposure to an incident electric field, the polarization of each dipole $\vec{P}_i$ is given by:

$$\vec{P}_i = \alpha_i \cdot \vec{E}(r_i) \tag{2.39}$$

where $\vec{E}(r_i)$ is the electric field in the dipole site. The total electric field in each site can be obtained from the summation of the incident plane contribution ($\vec{E}_{inc,i}$):[19, 20]

$$\vec{E}_{inc,i} = \vec{E}_0 e^{j\vec{k}\vec{r}_i - j\omega t} \tag{2.40}$$

and the contribution from the rest of dipoles:

$$E_{other,i} = -\sum_{j \neq i} A_{ij} P_j \,. \tag{2.41}$$

In Equation 2.40, $\vec{k}$ represents the electromagnetic wave wavevector, ω is the angular frequency and t is the time. In Equation 2.41, A_{ij} is a 3×3 tensor that represents the interaction between dipoles i and j. From the previous equations, $\vec{P}_i$ can be obtained by solving the following system of linear equations:

$$\vec{P}_i = \overline{\alpha_i}\left(\vec{E_0} e^{j\vec{k}\vec{r}_i - j\omega t} - \sum_{j \neq i} A_{ij} \vec{P}_j \right) \tag{2.42}$$

There is a controversy regarding the choice of a good formalism for α_i to reproduce the dielectric behavior of the target. A review of the different formalisms can be found in the literature.[19, 21] As mentioned above, the analyzed target is discretized into an array of point dipoles with a particular interdipole distance (*ID*). The first formalism to describe the polarizability in DDA was based on the Clausius-Mossotti factor that relates the macroscopic property of the dielectric function with the microscopic property of the molecular polarizability. This formalism is exact when $k \cdot ID \to 0$, being k the modulus of the incident light wavevector. Different corrections were introduced in the subsequent years in order to extend the DDA for $k \cdot ID \neq 0$. The one used in this thesis is based on

the lattice dispersion relation (GKDLDR), developed by Draine and Goodman and refined by Gutkowicz-Krusin and Draine, whose complete formulation is found in the literature.[22, 23] This formalism was developed for wave propagation along polarizable points located on a cubic lattice and has been found quite versatile, being recommended by Draine and Flatau as the first option for the simulations.

Once the linear equations (Equation 2.42) are solved in the whole system, the extinction, absorption and scattering cross-sections can be obtained.[24] All these features demonstrate that DDA can be a promising approach to study the LSPR, as will be shown in further Chapters.

2.5. Biological recognition elements

Biological recognition elements are the key component in the fabrication of biosensors. They have the characteristic of being highly specific to a certain analyte. Among all the recognition elements present in the bibliography, antibodies and single DNA strands are employed for biosensor development.

In biosensors, these recognition elements are typically attached on a substrate surface. For this aim, a wide variety of approaches is available in the literature for the immobilization of the element on the corresponding surface. These reactions generally rely on a chemisorption, covalent bonds, or a simple physisorption. Once they are immobilized, the biological recognition event can be performed through the exposure to the analyte. In the next Sections, the chemical structure of the elements used in this work (antibodies and DNA strands) is reviewed along with the chemical bonds formed during the recognition event.

2.5.1. Antibodies

2.5.1.1. IgG antibody structure

Antibodies or immunoglobulins (Ig) are glycoproteins that are part of the immune system.[25-27] The term glycoprotein means that the protein includes an oligosaccharide in its structure, covalently attached during a post-translational process (glycosylation).

In general, proteins are biomolecules (polypeptides) composed of a high number of smaller blocks named aminoacids. Among all the possible aminoacids, only 20 are the most abundant in proteins. These aminoacids are small molecules containing an amine and a carboxyl functional groups, typically bonded to the same carbon (named α-carbon). The main difference between aminoacids is the nature of the side chain, denoted as an "R" in Figure 2.9. Two aminoacids are bonded between each other through the peptide bond. This bond is formed when the carboxyl group of one aminoacid molecule reacts with the amino group of the other aminoacid, causing the release of water.

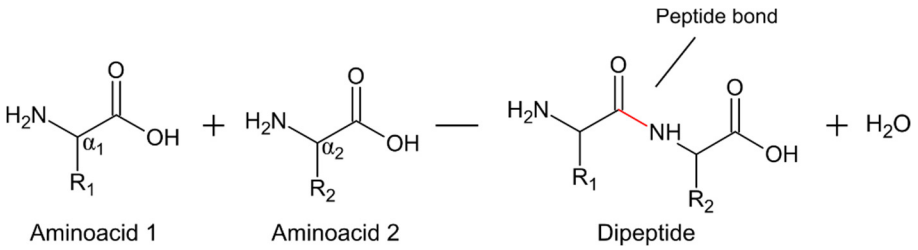

Figure 2.9. Chemical reaction of two aminoacids in order to form a dipeptide. The peptide bond formed is represented in red.

The general structure of a protein can be organized in four basic levels: the primary level is defined by the aminoacids sequence itself; the secondary level is caused by the local arrangement of adjacent aminoacids due to a variety of forces, such as hydrogen bonding, into more complex structures, such as α-helix or β-sheet; the tertiary level is considered the 3D structure of the entire polypeptide chain; and the quaternary level refers to the union of different polypeptide chains into a larger proteins, such as the hemoglobin.

Antibodies are secreted by the B cells as a part of the immunological response against any external agent (denoted as antigen) invading a living being. There is a wide family of antibodies depending on its function in the immune system. In human beings, there are five types (IgG, IgM, IgD, IgA and IgE). The most common subclass is the IgG, whose main function involves the targeting of pathogens to promote their killing by the immune cells.

The IgG structure (see Figure 2.10) comprises two heavy chain (50-80 kDa) joined by disulfide bonds. At the same time, each heavy chain is bonded to a light chain (around 25 kDa) through disulfide bonds as well. The whole structure resembles a "Y" shape with

a width and height of in the order of 14.5 and 8.5 nm, respectively.[28] The antigen-binding site, also denoted as paratope, is located around the upper tips of the Y-shaped structure (Fab region). This region contains the variable domains with specific spatial and charge distributions depending on the target antigen. This region recognizes a specific part of the antigen, denoted as epitope. The other part of the antibody is the Fc region, which differs from different antibody subclasses. This region is the one that undergoes the glycosylation previously mentioned.

The following Sections will provide further information about the chemical reactions undergone during the immunological recognition of antigen.

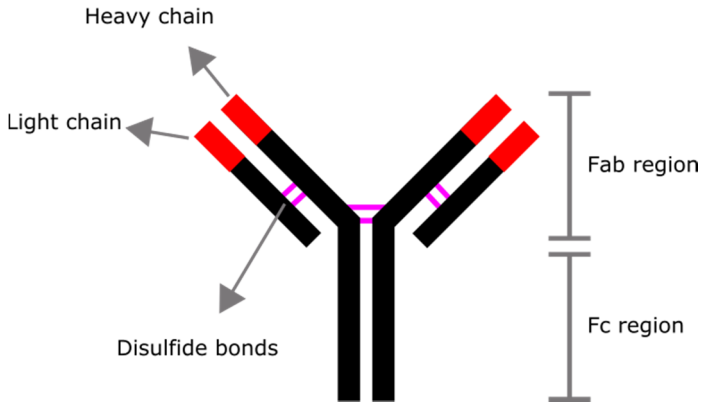

Figure 2.10. Representation of the IgG antibody structure. The variable and constant domains are shown in red and in black, respectively.

2.5.1.2. Primary reactions

The primary reactions comprise the antibody-antigen immunological recognition itself. These reactions are reversible and fast, where the molecules are bonded by non-covalent bonds. Individually, non-covalent bonds are not strong enough compared to the covalent bond. However, many of them are formed during the recognition forging a resulting strong bond.

Non-covalent bonds formed during the immunological recognition include:

- Hydrogen bonding: this type of interaction arises when a hydrogen atom bonded to an electronegative atom, yielding a strong dipole moment, share the charge with other electronegative atom from the same or different molecule. This is considered a strong interaction within the non-covalent bonds group. There are several

aminoacids in proteins that have carboxyl, hydroxyl or amine groups, especially susceptible to form these bonds (aspartate, serine, lysine, etc.)

- Electrostatic force: this force arises from the interaction between charged molecules with opposite polarities. Some aminoacids residues are easily charged negatively or positively at the corresponding solution pH (aspartate, glutamate, etc.).
- Hydrophobic force: this force comes from the interaction between non-polar parts of a molecule. A typical example of a non-polar part, susceptible to this force, are those aminoacids with a long chain of carbons or with aromatic groups (phenylalanine, valine, leucine, etc.). In the aqueous solutions in which the antibodies are held, water molecules force the hydrophobic groups to curl up in order to minimize the non-polar surface in contact with water.
- Van der Waals forces: these forces have their origins in the dipole or induced-dipole interactions. All molecules give rise to these forces in a greater or lesser extent. This list of forces include: 1) permanent dipoles interaction, also denoted as Keesom force; 2) permanent and induced dipole interaction, named as Debye force; and 3) induced dipoles interaction that is known as London forces.

Each of these forces will contribute in different extensions in the immunological recognition depending on the nature and location of the functional groups of both the aminoacid and the antigen. Besides the non-covalent bonds, the conformation of the antigen-recognition site plays a critical role in the immunological reaction. It is important that the site can accommodate the antigen to increase the number of non-covalent interactions, resulting in stronger overall bindings. This consideration resembles what is called in the bibliography as the lock-and-key or the hand-in-glove analogies.

2.5.1.3. Secondary reactions

Despite the primary reaction, the next part of the immunological response comprises a series of secondary antigen-antibody reactions. These reactions involve the combination of different antibodies-antigen complexes resulting in their precipitation. Opposite to the primary ones, the precipitation usually requires longer times from several minutes to a few hours.

The mechanism of these complexes precipitation was proposed by J. R. Marrack in 1934. He stated that the aggregates comprise a large network of antibody and antigen molecules into the formation of a lattice. This theory required both molecules to be multivalent, that is, each antigen or antibody can be bonded to two or more antigens or antibodies.

The antibody-antigen precipitation dynamic curve was studied by J. Danysz in 1902, being denoted as the Zone Phenomenon or Danysz Phenomenon in his honor. This precipitation has a reversible nature and comprises three zones depending on the antibody/antigen ratio. In the first zone (prozone), an increase of the antigen concentration results in a higher and larger number of agglomerations. All the antigens are located in the precipitate whereas there are still free antibodies in the supernatant. In the second zone (equivalence zone), all the antibodies and antigens are part of the precipitate. From this point, higher concentrations of the antigen increase the solubility of the agglomerate, resulting in the third zone. In this last zone (post-zone), the antigen starts to be present in the supernatant, whereas all the antibody is part of the precipitate.

These secondary reactions play a critical role during certain immunoassay configurations because the precipitate can change the optical properties of the solution. For those biosensing configurations, in which the antibody is immobilized on a surface, these reactions do not need to be considered.

2.5.2. DNA strands

The deoxyribonucleic acid (DNA) is a very large biomolecule that carries the necessary genetic instructions for the growth, development and functioning of all living organisms.

A recent publication provides a good historical background of the DNA research in the 20th century.[29] Briefly, the increasing attention for genetics started in 1865 with Mendel through his experiments about the inheritance with pea plants. In 1869, F. Miescher isolated the genetic biomolecule, giving the name of nuclein. Later, this molecule was renamed into nucleic acid by R. Altmann. The building blocks of DNA (adenine, thymine guanine and cytosine) were identified by P. Levene in 1929. In 1949, E. Chargaff conducted experiments to study the DNA molecules in different species. He

discovered, within any species, the almost 1:1 ratio between some bases (adenine = thymine and guanine = cytosine), in what is called Chargaff's rules. A few years later, in 1953, the DNA was studied through x-ray diffraction analysis by R. Franklin and M. Wilkins. They discovered that DNA exhibited a repetitive helicoidal structure. The same year, Watson and Crick proposed the double helix structure for the DNA, comprising two strands linked through small rungs. These rungs were the nucleotides, in which a nucleotide of one of the strands was joined by hydrogen bonds to the complementary nucleotide of the other strand.

Nowadays, the DNA biomolecule structure can be defined as a right-handed helix formed by two long polynucleotide strands or chains bonded through hydrogen bonds.[30] The diameter of the double helix is estimated around 2.0 nm. Figure 2.11 shows a complete representation of two complementary polynucleotide strands. A single DNA strand is composed of three major parts:

1) Nitrogenous bases (atoms highlighted in purple in Figure 2.11): two different bases appear in the DNA, the purines that form a double ring structure (adenine and guanine) and the pyrimidines with a single ring structure (thymine and cytosine). These bases are directed into the center of the double helix and stack together in order to increase the stability of the DNA thanks to the non-covalent forces between the rings.

2) Sugar (atoms highlighted in black in Figure 2.11): this molecule connects the base to the external part of the DNA backbone. In DNA, this sugar is the 2-deoxyribose, a pentose with 5 carbon atoms. The sugar has a defined numeration, from 1 to 5, to identify each carbon in its structure. The bond formed between the base and the sugar is called N-glycosidic bond, where glycosidic refers to any bond formed with a sugar and "N" indicates the atom to which this sugar is bonded, in this case nitrogen. The combination of the sugar and the nitrogenous base is named nucleoside. Before taking part of the DNA structure, the nucleoside must be bonded to a phosphate molecule.

3) Phosphate (atoms highlighted in red in Figure 2.11): these molecules (one phosphor and four oxygens atoms) act as linkers between the different sugar molecules. These molecules are located at the external part of the DNA, providing a negatively charged backbone to the DNA strands. This charged

backbone plays a major role in the DNA packaging, coiling around positively charged proteins denoted as histones, which contain a high concentration of positive aminoacids: arginine, lysine, etc. This comprises the first step of DNA packaging, whose most packed form is the chromosome.

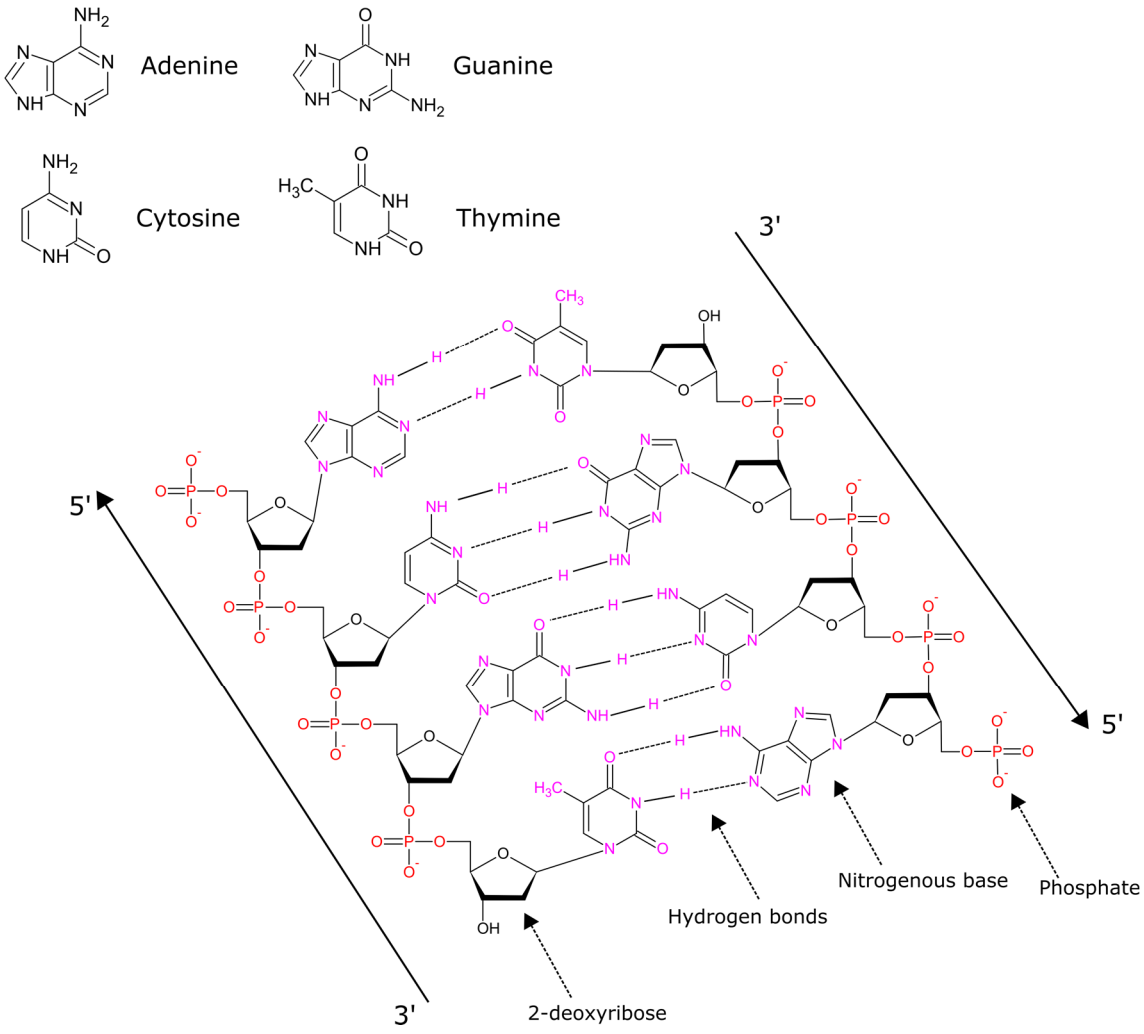

Figure 2.11. Representation of the DNA double chain structure. Atoms of the nitrogenous bases, sugars and phosphates are highlighted in purple, black and red, respectively.

The nitrogenous base, sugar and phosphate combination is named nucleotide. Nucleotides are bonded together through the 3'-5' phosphodiester bond. Under this bond configuration, a phosphate molecule of one nucleotide, bonded to the 3rd carbon atom of the corresponding sugar, is linked to the subsequent nucleotide with another phosphate through the 5th carbon atom of the same sugar. Figure 2.12 shows a schematic representation of the phosphodiester bond. An important point to take into account is that

the strand ends have a different nature. One end comprises a hydroxyl group in the 3rd carbon atom of the sugar. This end is denoted as 3'. The opposite end of the polynucleotide has a phosphate molecule bonded to the 5th carbon atom of the last sugar. In this case, this end is named 5' (see Figure 2.11).

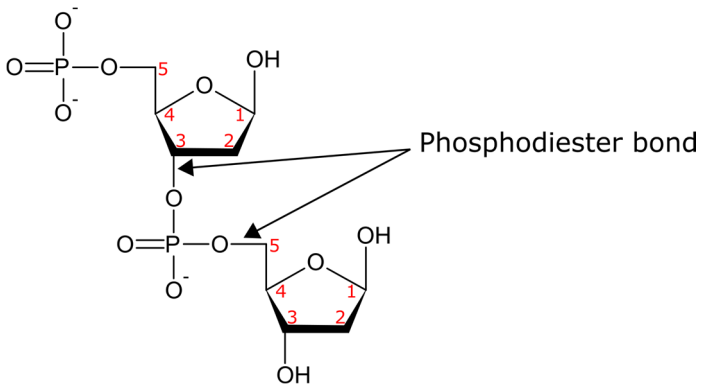

Figure 2.12. Representation of the 3'-5' phosphodiester bond between the 3rd and 5th carbon atoms of the same sugar. The carbon numeration in the sugar is highlighted in red.

As mentioned above, the full structure of the DNA includes two antiparallel-oriented polynucleotides chains. This means that the direction of one strand is 3'-5' oriented, whereas the complementary strand is oriented 5'-3'. The connection between both chains is produced through the non-covalent hydrogen bonds with a complete distance of around 0.3 nm. Adenine and thymine are bonded through 2 of these bonds, whereas the guanine and cytosine joint is composed of 3 bonds. These hydrogen bonds have a key role in DNA biosensing assays since they are the main participants during the recognition between two complementary strands. In case of a non-fully complementary sequence is used during an assay, the recognition becomes hindered and a distorted double helix will likely arise.

REFERENCES

1. O. F. Mossotti. *Mem. di mathem. e fisica in Modena* **1850**, 24, 49.
2. R. Clausius. *Die Mechanische Wärmetheorie* **1879**, 2, 62.
3. H. Morgan; N. G. Green. *AC Electrokinetics: colloids and nanoparticles*. Research Studies Press Ltd.: Philadelphia, 2003.
4. J. Venermo; A. Sihvola. Dielectric polarizability of circular cylinder. *J. Electrost.* **2005**, 63, 101-117.

5. C. García Núñez. Contribution to the Development of Electronic Devices Based on Zn_3N_2 Thin Films, and ZnO Nanowires and GaAs Nanowires. Universidad Autónoma de Madrid, Madrid (Spain), 2015.
6. C. G. Núñez; A. G. Marín; P. Nanterne; J. Piqueras; P. Kung; J. L. Pau. Conducting properties of nearly depleted ZnO nanowire UV sensors fabricated by dielectrophoresis. *Nanotechnology* **2013**, 24, 415702.
7. J. L. Pau; C. García Núñez; A. García Marín; C. Guerrero; P. Rodríguez; S. Borromeo; J. Piqueras. In *Contact properties and surface reaction kinetics of single ZnO nanowire devices fabricated by dielectrophoresis*, 2014; pp 89871Q-89871Q-11.
8. H. G. Tompkins. *A User's Guide to Ellipsometry*. Academic Press: 1993.
9. H. G. Tompkins; E. A. Irene. *Handbook of Ellipsometry*. William Andrew Pub.: 2005.
10. H. Raether. *Surface plasmons on smooth and rough surfaces and on gratings*. Springer: 1988.
11. M. A. Ordal; L. L. Long; R. J. Bell; S. E. Bell; R. R. Bell; R. W. Alexander; C. A. Ward. Optical properties of metals Al, Co, Cu, Au, Fe, Pb, Ni, Pd, Pt, Ag, Ti, and W in the infrared and far infrared. *Appl. Optics* **1983**, 11, 1099-1119.
12. R. B. M. Schasfoort; A. J. Tudos. *Handbook of surface plasmon resonance*. RSC Publishing, Cambridge: 2008.
13. D. E. Aspnes; E. Kinsbron; D. D. Bacon. Optical properties of Au: sample effects. *Phys. Rev. B* **1980**, 21, 3290-3299.
14. S. A. Maier. *Plasmonics: Fundamentals and Applications*. Springer: 2007.
15. C. F. Bohren; D. R. Huffman. *Absorption and scattering of light by small particles*. Wiley: 1983.
16. H. DeVoe. Optical Properties of Molecular Aggregates. I. Classical Model of Electronic Absorption and Refraction. *J. Chem. Phys.* **1964**, 41, 393-400.
17. H. DeVoe. Optical Properties of Molecular Aggregates. II. Classical Theory of the Refraction, Absorption, and Optical Activity of Solutions and Crystals. *J. Chem. Phys.* **1965**, 43, 3199-3208.
18. E. M. Purcell; C. R. Pennypacker. Scattering and absorption of light by nonspherical dielectric grains. *Astrophys. J.* **1976**, 186, 705–714.
19. B. T. Draine; P. J. Flatau. Discrete-Dipole Approximation For Scattering Calculations. *J. Opt. Soc. Am. A* **1994**, 11, 1491-1499.
20. E. Bichoutskaia. *Computational Nanoscience*. RSC Publishing: 2011.
21. F. D. Sala; S. D'Agostino. *Handbook of Molecular Plasmonics*. Taylor & Francis: 2013.
22. D. Gutkowicz-Krusin; B. T. Draine. Propagation of Electromagnetic Waves on a Rectangular Lattice of Polarizable Points. *http://arXiv.org/abs/astro-ph/0403082* **2004**.
23. B. T. Draine; J. Goodman. Beyond Clausius-Mossotti - Wave Propagation on a Polarizable Point Lattice and the Discrete Dipole Approximation. *Astrophys. J.* **1993**, 405, 685-697.
24. B. T. Draine. The Discrete-Dipole Approximation and its Application to Interstellar Graphite Grains. *Astrophys. J.* **1988**, 333, 848-872.
25. L. Å. Hanson; H. Wigzell. *Immunology*. Elsevier Science: 2014.
26. K. D. Elgert. *Immunology: Understanding The Immune System*. Wiley: 2009.
27. T. W. Mak; M. E. Saunders; M. R. Chaddah. *The Immune Response: Basic and Clinical Principles*. Elsevier Science: 2005.
28. M. E. Browning-Kelley; K. Wadu-Mesthrige; V. Hari; G. Y. Liu. Atomic Force Microscopic Study of Specific Antigen/Antibody Binding. *Langmuir* **1997**, 13, 343-350.

29. R. Dahm. Friedrich Miescher and the discovery of DNA. *Dev. Biol.* **2005**, 278, 274-288.
30. R. R. Sinden. *DNA Structure and Function*. Elsevier Science: 2012.

3. Materials and methods

3.1. Materials

The following materials have been used during this thesis without further purification:

- Sigma-Aldrich (St. Louis): L-reduced glutathione (GSH), 3 3′-dithiodipropionic acid di(N-succinimidyl ester) (DTSP), dimethyl sulfoxide (DMSO), potassium chloride (KCl), gold (III) chloride trihydrate, trisodium citrate dihydrate, 99.9995% pure Zn micrometer-sized powder, 99.98% pure Cu 0.25-mm thick foils, and the following DNA sequences:
  - 12 nucleotides synthetic sequence from Helicobacter Pylori: thiolated probe sequence (HP1-SH), complementary sequence ($HP2_C$), single nucleotide polymorphism sequence ($HP2_{SNP}$) and non-complementary sequence ($HP2_{NC}$).
  - 25 nucleotides synthetic sequence from *Escherichia Coli.*
  - 100 nucleotides synthetic 5'-end hexamethylthiol modified sequence from the exon 11 of cystic fibrosis transmembrane conductance regulator gene (CFTR). This sequence is denoted as CF1-SH, is as follows:

  The nucleotide sequences are shown in Table 3.1.

Table 3.1. DNA sequences used in this work.

Synthetic oligonucleotides	
HP1-SH	5'-SH $(CH_2)_6$–CAAAGGGCAGGA
HP2$_C$	5'-TCCTGCCCTTTG
HP2$_{SNP}$	5'-TCCTACCCTTTG
HP2$_{NC}$	5'-CAAGTAAAGGGC
E. Coli sequence	5'-TGCCGCTCATCCGCCACATATCCTG
CF1-SH	5'-SH $(CH_2)_6$– TCTCAGTTTTCCTGGATTATGCCTGGCACCATTAAAGAA AATATCATCTTTGGTGTTTCCTATGATGAATATAGATAC AGAAGCGTCATCAAAGCATGCC.

- Medical and Molecular Genetics Institute (INGEMM) of Madrid (Spain): 373 base-pairs wild type or complementary ($CF2_{WT}$) and 370 base-pairs mutated ($CF2_{MUT}$) sequences (see Table 3.2), extracted from peripheral blood leukocites. The procedure used by the INGEMM was described elsewhere.[1] For all patients, informed consent was obtained.

Table 3.2. Sequences amplified by PCR of the genomic DNA samples used in this work.

Synthetic oligonucleotides	
CF2$_{WT}$	5'- AACCGATTGAATATGGAGCCAAATATATAATTTGGGTA GTGTGAAGGGTTCATATGCATAATCAAAAAGTTTTCAC ATAGTTTCTTACCTCTTCTAGTTGGCATGCTTTGATGAC GCTTCTGTATCTATATTCATCATAGGAAACACCAAAGA TGATATTTTCTTTAATGGTGCCAGGCATAATCCAGGAA AACTGAGAACAGAATGAAATTCTTCCACTGTGCTTAAT TTTACCCTCTGAAGGCTCCAGTTCTCCCATAATCACCAT TAGAAGTGAAGTCTGGAAATAAAACCCATCATTATTAG GTCATTATCAAATCACGCTCAGGATTCACTTGCCTCCA ATTATCATCCTAAGCAGAAGTGTATATTC
CF2$_{MUT}$	5'- AACCGATTGAATATGGAGCCAAATATATAATTTGGGTA GTGTGAAGGGTTCATATGCATAATCAAAAAGTTTTCAC ATAGTTTCTTACCTCTTCTAGTTGGCATGCTTTGATGAC GCTTCTGTATCTATATTCATCATAGGAAACACCA_____A TGATATTTTCTTTAATGGTGCCAGGCATAATCCAGGAA AACTGAGAACAGAATGAAATTCTTCCACTGTGCTTAAT TTTACCCTCTGAAGGCTCCAGTTCTCCCATAATCACCAT TAGAAGTGAAGTCTGGAAATAAAACCCATCATTATTAG GTCATTATCAAATCACGCTCAGGATTCACTTGCCTCCA ATTATCATCCTAAGCAGAAGTGTATATTC

- Panreac (Spain): ethanol (EtOH), acetone and trichloroethylene ($CHCCl_3$).
- Goodfellow (England): 99.9999% pure Ga pellets and 99.99% pure Au wires.
- Abcam (United Kingdom): GSH polyclonal antibody from rabbits.
- UQG Optics (United Kingdom): 20 × 20 mm quartz plates.
- Lesker (United Kingdom): sputtering targets of 99.999% pure ZnO w/2% Al_2O_3 (Al-doped ZnO or AZO) and 99.995% pure Zn.
- Materion (USA): sputtering target of 99.999% pure Al.
- Praxair (USA): 99.999% pure Ar, N_2 and O_2 gases.
- Thorlabs (Germany): matching index fluid and equilateral fused-silica prisms.
- Institute of Electronic Materials Technology (Poland): p-type silicon wafers (6.33 Ω·cm).

Ultrapure deionized water is produced by Ultramatic Wasserlab and Direct-Q 3 UV Millipore purification systems (18 MΩ·cm). For the DNA biosensing experiments, the deionized water is further sterilized with a Nüve OT 012 small steam autoclave.

3.2. ZnO nanowires growth

Zinc oxide nanowires (ZnO NWs) are grown on Si(100) substrates by vapor phase transport (VPT) in a 1-m length quartz tube placed inside a furnace. The gas entrance and the rotatory pump are located on each side of the tube. Prior to each growth, the tube is cleaned using an HCl solution and annealed at 200 ºC under Ar atmosphere during 1 h in order to desorb water molecules from the tube. Figure 3.1 represents a scheme and a picture of the VPT system. Many of the ZnO NWs used in this work have been synthetized in our laboratory using that system following the procedure widely reported in the literature.[2, 3]

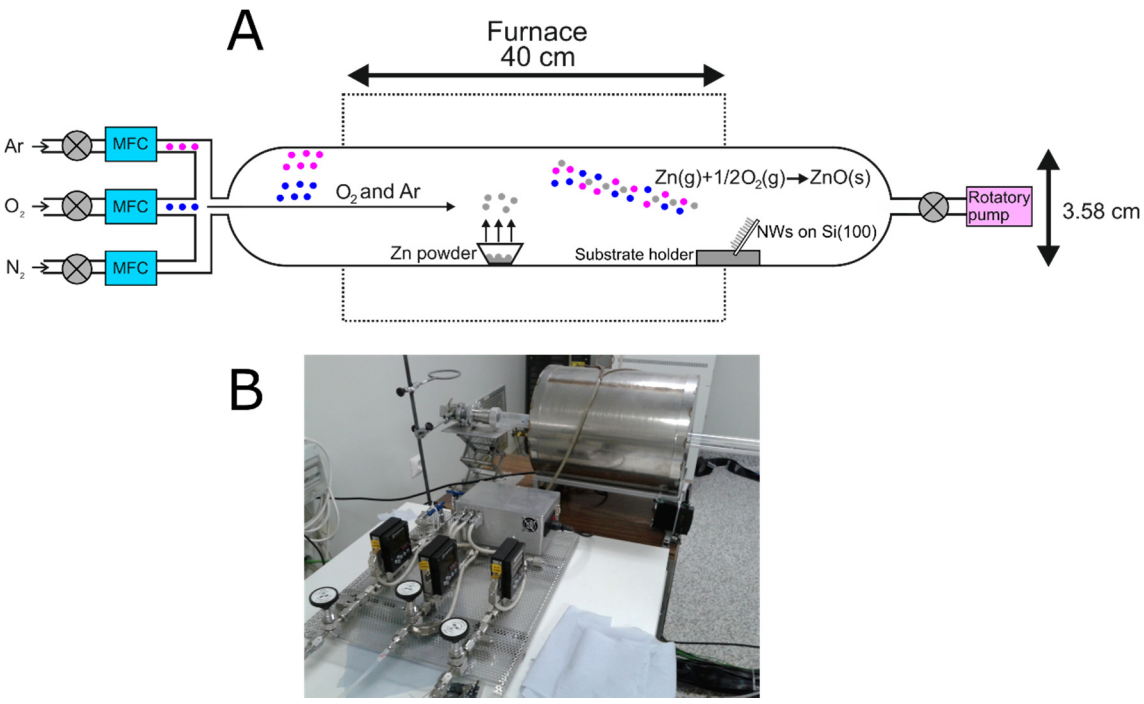

Figure 3.1. (A) scheme of the quartz tube furnace used to grow ZnO NWs; (B) picture of the growth system.

The temperature of the furnace is increased up to 900 °C under a 100-sccm Ar flux, controlled with a mass flow controller (MFC), in order to vaporize Zn powder and avoid its oxidation. After that temperature is reached, the O_2 valve is opened. During the growth process, O_2(g) reacts with the Zn(g), which is transported by the carrier gas. The product of the reaction (ZnO) grows preferentially on the Si substrate, forming vertically aligned NWs.

The growth substrate is a Si(100) piece of wafer deoxidized in HF–EtOH (10% in volume) for 5 min, rinsed in EtOH and dried with N_2 gas. A 7-nm thick Zn layer is grown by sputtering on the substrate. This layer has an important role, acting as a seed layer and self-catalyzing the NW growth. In each process, 0.5 g of Zn powder is spread on a ceramic crucible and loaded in the middle of the furnace. The substrate is placed on a substrate holder nearly perpendicular to the gas flow in order to obtain a homogeneous deposition of ZnO NWs. Finally, the holder is placed near the rotatory pump inlet.

It is worth noticing that some of the ZnO NWs, used in Chapter 4 have been grown at the Department of Electrical and Computer Engineering of the University of Alabama.[4] They have been synthesized by VPT on sapphire c-plane (0001) substrates following a similar procedure to the one described above.

3.3. Gold nanoparticle synthesis

Aqueous citrate-stabilized gold nanoparticles (Cit-AuNPs) are synthetized following the well-known reduction method.[5, 6] According to this procedure, the ratio between chloroauric acid and sodium citrate can be set to obtain NPs with a particular average diameter. In the present work, an average diameter of around 14 nm has been chosen for glutathione sensing in the ellipsometric setup. To obtain that NP diameter, a solution of 18 mg of $HAuCl_4 \cdot 3H_2O$ in 40 mL of deionized H_2O is prepared in a round-bottom flask. The flask, coupled to a condenser, is heated up to ebullition and, then, a solution of 44 mg of trisodium citrate dihydrate in 10 mL of deionized H_2O is gently added while stirring the mixture with a magnetic stirrer. The final concentration in this solution (50 mL) is 0.90 mM for Au and 3.00 mM for the citrate (citrate/Au ratio of 3.3). After 10 minutes, the hot plate is turned off and the mixture is left to cool down. The solution is put into a flask, previously cleaned with deionized H_2O and acetone to remove the left-overs that can aggregate to the synthetized NPs. The experimental setup is shown in Figure 3.2.

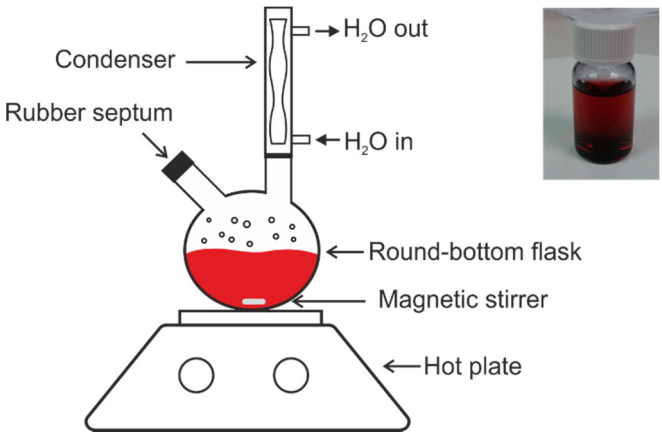

Figure 3.2. Cit-AuNPs synthesis experimental setup. The photograph shows the final colloidal solution within a vial.

3.4. Material deposition

3.4.1. Deposition by magnetron sputtering

Sputtering is a process that allows depositing a wide variety of thin films on a substrate. Briefly, the deposition method relies on the ejection of atoms from a solid target material due to bombardment of the target by ions coming from an electrically-generated

plasma. This plasma is produced when the sputtering gas (inert gases, such as Ar or Ne, or more reactive ones, such as O_2 or N_2) is subjected to a strong electromagnetic field. In many systems, the plasma activation is triggered by the emission of hot electrons from a tungsten filament to initiate the Townsend avalanche, which creates more ions and electrons from the neutral gas atoms and molecules by impact ionization. The ions from the plasma hit the target atoms with an energy greater than the binding energy, producing their ejection from the target. Since the target atoms acquire a high kinetic energy, they tend to deposit on the walls of the chamber and, in particular, on the substrate placed in front of the target. This process typically takes place in high vacuum conditions under the assistance of a turbomolecular pump, and leads to the formation of a thin film whose thickness is proportional to the span of the process. The use of a magnetron allows to trap gas electrons through a closed magnetic field to increase the sputtering rate at lower gas pressures. This consists of an array of magnets placed beneath the target. Figure 3.3 shows a basic scheme of the magnetron sputtering process.

The power source for the deposition of AZO in our Alcatel A450 system is a radio frequency source. Prior to the material deposition, a pre-sputtering process is performed for a few minutes with an Ar plasma to remove possible left-overs or native oxides on the target and substrate surfaces. For the AZO deposition, the substrate temperature is set up to 300ºC to improve the thin film crystallinity and conductivity.[7]

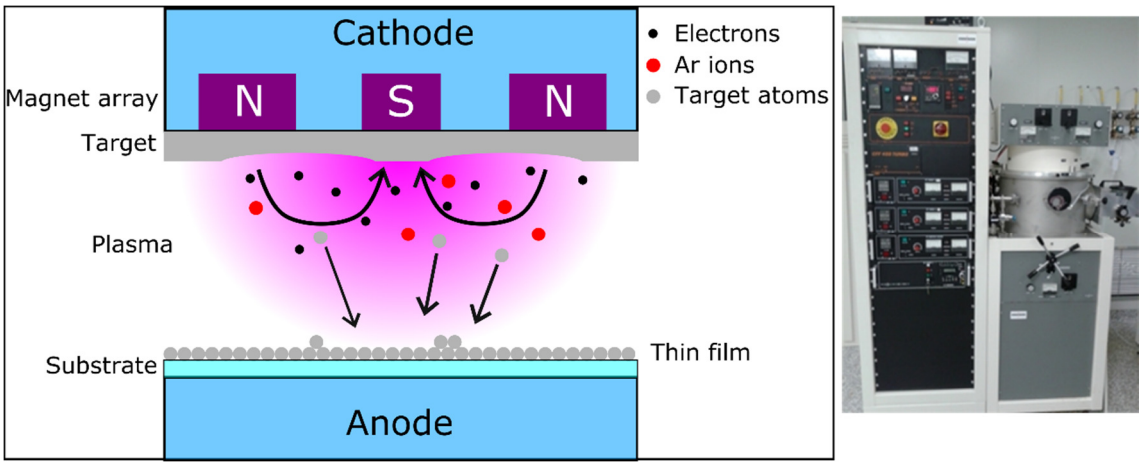

Figure 3.3. Scheme of the magnetron sputtering process in a vacuum chamber (left image) and a picture of the Alcatel A450 sputtering system used in this work (right image).

The thickness of the sputtered films depends on plasma power, deposition time, pressure, gas composition, gas flow and target material. The calibration data for AZO obtained in our system are presented in Figure 3.4. It represents the layer thickness as a function of the growth time, under the conditions detailed in the inset. A deposition rate of 30 nm/min is extracted from the linear fitting.

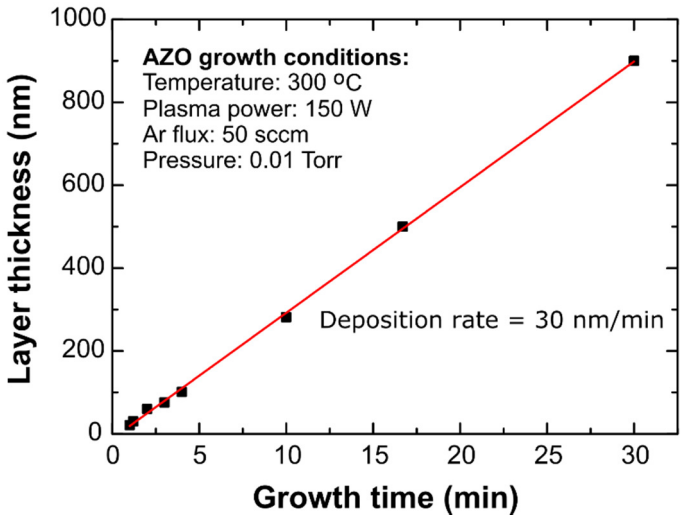

Figure 3.4. Calibration curve for the sputtered film.

3.4.2. Deposition by Joule-effect termal evaporation

Thermal evaporation is another very common method for thin film deposition. In a high vacuum chamber, the source material (wires, pellets, etc.) is placed on a boat consisting of a tungsten resistive wire (99.90% purity) that is connected to an AC power supply. Prior to the evaporation, the chamber reaches a base pressure of $2 \cdot 10^{-6}$ Torr with a turbomolecular pump. A metallic shutter, externally controlled by the user, is placed between the substrate and the boat. The material evaporation begins when a large electric current is driven through the wire. When the power reaches 50 W, the user opens the shutter to start depositing the film on the substrate. The work pressure during the evaporation reaches a value of $2 \cdot 10^{-4}$ Torr. Before sample extraction, a cooling-down step is usually carried out by leaving the sample in the vacuum chamber for a couple of hours. This step helps to extend the lifetime of the filament and to limit the surface oxidation of the thin film by ensuring that the samples are in thermal equilibrium before entering in contact with the air ambient.

In our laboratory, this method is performed with a Joule-effect thermal evaporator (Edwards E306) to deposit Au thin films and GaNPs on different substrates during the development of ellipsometric optical sensors. The scheme is represented below (Figure 3.5). For Ga evaporation, a heat sink is included within the evaporator where the substrate is attached. The heat sink comprises a stainless steel L-shape and ice-cooled structure connected to an ice supplier. The distance between the substrate and the filament is 20 cm. Since the substrate temperature has an important influence on the NP size distribution, the ice supplier contributes to keep the substrate temperature near zero degrees Celsius during the evaporation.

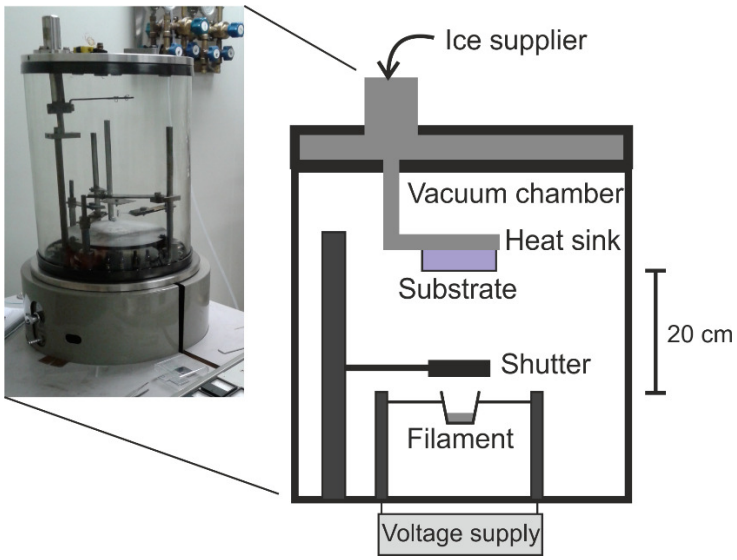

Figure 3.5. Scheme of the Joule-effect thermal evaporator with a picture of the Edwards E306 system.

3.5. Photolithography

Photolithography is a standard technique massively used to produce integrated circuits in the Industry. In this work, this technique has been employed to define Al-doped ZnO electrodes on different surfaces (glassy substrates or Si wafers) for the dielectrophoretic alignment of ZnO and CuO nanowires. The procedure includes the following steps, which are also represented in Figure 3.6:

- Coating with a photoresist: several droplets of a positive photoresist are spin-coated on the surface, followed by a soft-bake process in an oven to dry the photoresist. The thickness of the photoresist is typically 1 μm. The photoresist

is based on Novolac polymers. Chemically, they consist of phenol-formaldehyde polymers with a small amount of diazonaphthaquinone.

- UV exposure: the surface is exposed to UV light from a xenon lamp through a quartz mask that contains the desired pattern. This mask is previously aligned on the surface with the assistance of an optical microscope. The mask aligner works in the contact mode. The UV exposure produces different photoreactions that lead to a chemical rearrangement in this irradiated area.
- Development: the photoresist in the irradiated area is washed away (positive photolithography) by using a basic (OH^- containing) developer solution. After this step, the surface should be always inspected through an optical microscope to ensure the complete photoresist removal in the irradiated area. After checking, a post-baking step is performed to harden the remaining resist and enhance its resistance to the etchants.
- AZO etching: the sample is dipped into a phosphoric acid: acetic acid: water (1:1:75) solution. After this step, the surface is rinsed with deionized water to get rid of the acidic agents.
- Cleaning: finally, the surface is soaked in acetone to eliminate the remaining resist. If the resist is not stripped away easily, sonication is used.

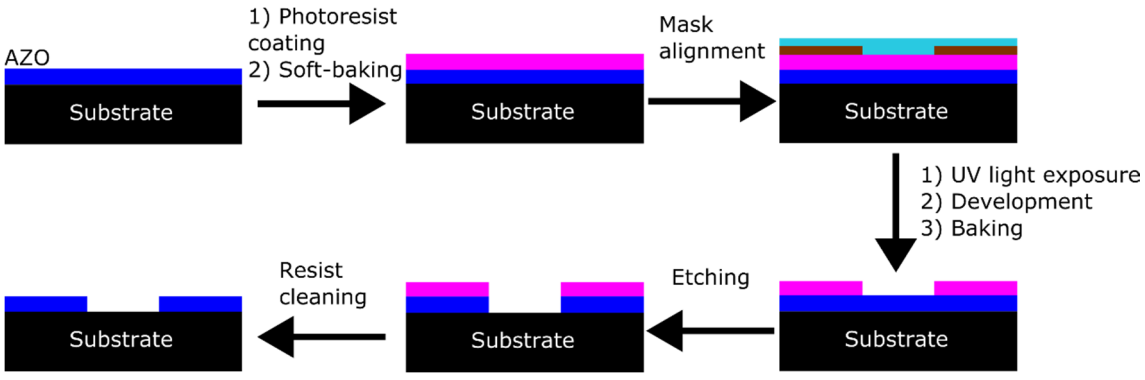

Figure 3.6. Scheme of the photolithographic process

3.6. Optical characterization

3.6.1. UV/Visible spectrophotometry

UV/visible spectrophotometry is an optical technique that measures the light intensity emitted by a light source after passing through a sample (I_L), and compares it with the intensity emitted from the source (I_O). The typical configuration of a spectrophotometer requires the use of a UV (deuterium lamp) and visible (halogen lamp) light sources, a monochromator to select the incident wavelength and the detector (silicon photodiode, photomultiplier tubes, etc). Most systems have the double-beam configuration in order to measure the sample and the reference at the same time. A basic scheme of such spectrophotometer is shown in Figure 3.7. The transmitted light intensity through a sample follows the Lambert-Beer's law (Equations 3.1 and 3.2):[8]

$$I_L = I_O \cdot e^{-\sigma \cdot l \cdot c}, \tag{3.1}$$

$$A = \sigma \cdot l \cdot c, \tag{3.2}$$

where A, σ, l and c are the absorbance, extinction coefficient, the path length and the concentration, respectively. The physical processes that contribute to the light attenuation before reaching the detector are absorption, reflection and scattering. All those processes contribute to enlarge the value of σ.

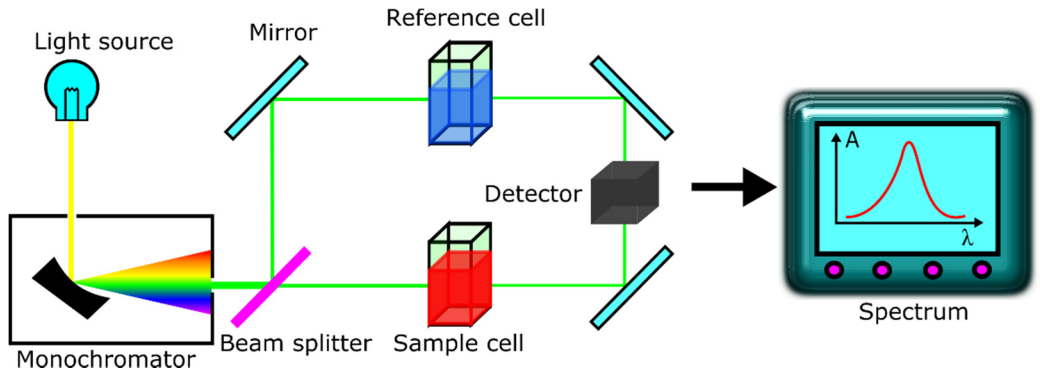

Figure 3.7. Basic scheme of a double-beam spectrophotometer.

In this work, two spectrophotometers are used. The first one is a double beam PharmaSpec UV-1700 series from Shimadzu Corporation, which is used to study the effectiveness of AuNPs functionalization. The other spectrophotometer is a double beam

UV/Cary 100 from Agilent, which is used to monitor the sedimentation of ZnO NWs in liquid mediums. Spectra acquisitions are taken at 1 nm resolution.

3.6.2. Fourier-transform infrared spectroscopy

Fourier-transform infrared spectroscopy (FTIR) is another optical technique used to characterize materials through the interaction of IR light with the vibrational and rotational modes of the molecules that constitute the material. In contrast to UV-Visible spectrophotometry (a dispersive technique), FTIR does not require the use of a monochromator and, thus, the complete light source spectrum reaches the sample at the same time.

The main part of the FTIR equipment is the Michelson interferometer.[9] It comprises a beam-splitter, a fixed mirror and a moving mirror, as shown in the scheme below (Figure 3.8). The IR beam is divided into two halves in the beam splitter. Half of the beam reaches the fixed mirror, while the remaining half goes toward the moving mirror. These two beams are reflected in the fixed and moving mirrors, respectively, and come back to the beam splitter, where they recombine into a new beam that passes through the sample and finally reaches the detector. During the measurement, the moving mirror is displaced away from the beam-splitter in order to obtain an interference pattern between both beams as a function of distance (interferogram). By using the Fourier-transformation, a spectrum versus the incident wavenumber is obtained from the interferogram.

In this thesis, IFS60v and IFS66v spectrophotometers from Bruker are used to study the presence of molecules chemically attached to nanostructures. The first one is employed to characterize functionalized AuNPs with a variable angle specular reflectance accessory, by drop-casting the NPs on a BaF_2 window and leaving them to dry. Specular spectra acquisitions are obtained at 4 cm^{-1} resolution after 250 scans. The other one is used to measure functionalized GaNPs with a diffuse reflection accessory. Under this configuration, the acquisitions are obtained at 4 cm^{-1} resolution after 1000 scans.

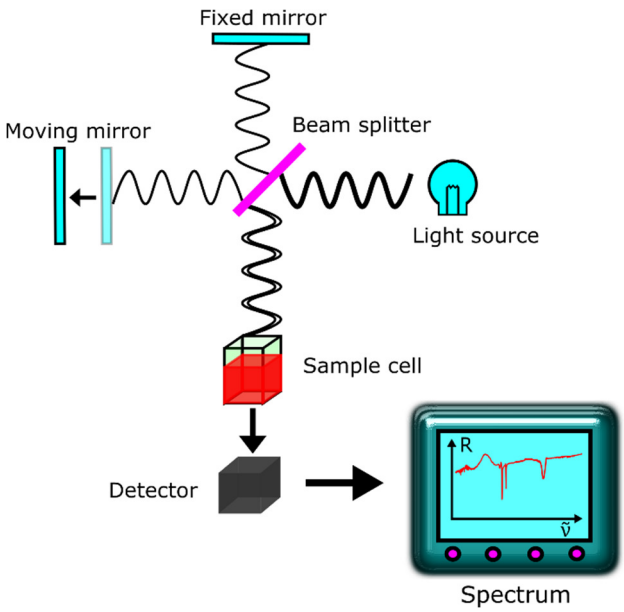

Figure 3.8. Scheme of a Michelson interferometer within a FTIR spectrophotometer.

3.7. Surface characterization

3.7.1. X-ray photoelectron spectroscopy

XPS is a surface characterization technique that measures the elemental composition and electronic state of a material. The technique is based on the irradiation of the target with x-rays and the measurement of the kinetic energy (*KE*) of the emitted electrons from the material surface (Figure 3.9A).

XPS spectra typically shows the number of electrons versus their binding energy (*BE*) for the corresponding chemical bond in the analyzed material.[10] The basic equation is defined through Equation 3.3:

$$BE = E_{photon} - \left(KE + \phi\right) \tag{3.3}$$

where E_{photon} and ϕ are the photon energy of the x-ray source and the material work function, respectively.

In this work, XPS measurements are performed on as-deposited GaNPs in an ultrahigh vacuum system (UHV, with a base pressure of $5 \cdot 10^{-10}$ mbar) equipped with a monochromatic Al K-alpha line as exciting photon source (E_{photon} = 1486.7 eV) and a SPECS PHOIBOS 150 hemispherical analyzer with a 9 MCD detector. A takeoff angle of 60° relative to the surface normal is chosen. Scans are measured with a step energy of 50 meV, except the survey scan that is obtained with a step energy of 75 meV.

The other equipment used to assess the GaNPs functionalization is also in ultrahigh vacuum conditions (UHV, with a base pressure of $5x10^{-10}$ mbar), and is equipped with an Al K-alpha line x-ray source, and a SPHERA-U7 hemispherical energy analyzer. The step energy is set to 50 meV. In order to compensate the built-up positive charge on the sample surface during the measurements, it was necessary the use of a Flood Gun (FG-500, Specs) to neutralize the surface with low energy electrons (3 eV and 40 μA).

A basic scheme of a XPS equipment is shown in Figure 3.9B. For analysis, the raw data are visualized by using the software CasaXPS provided by SPECS GmbH (Berlin, Germany).

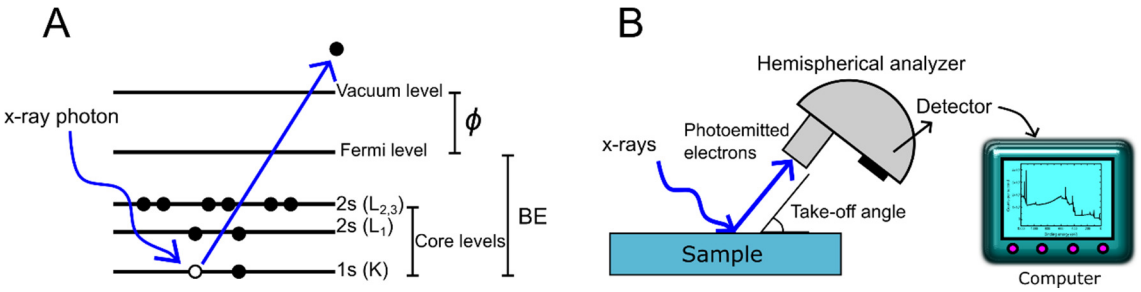

Figure 3.9. (A) Schematic of the photoelectric effect induced by x-rays; (B) basic scheme of the XPS equipment.

3.7.2. Cyclic voltammetry

Cyclic voltammetry is an electrochemical technique used for the study of the electrochemical properties of an analyte in solution or confined on an electrode surface.[11] It is extensively used in many fields, such as electrochemistry, biochemistry, organic chemistry, etc. It is often the first experiment carried out to study the electrochemical behavior of a compound in solution or the conductivity of a working electrode. Its effectiveness comes from the ease of use and the capability for rapidly observing the redox reactions at the working electrode surface.

Cyclic voltammetry consists of linearly cycling the potential applied to an electrode (working electrode) immersed in a solution and measuring the resulting current. One of the advantages of the technique for surface characterization is that it is possible to study the adsorption/desorption of electroactive species as the potential is being cycled. This property allows the quantification of the species adsorbed or desorbed from the surface

of the working electrode. The potential is applied between the working electrode and the reference electrode. One of the most used reference electrodes is the saturated calomel electrode (SCE). Cyclic voltammetry is usually employed in the three-electrode configuration, including a counter electrode (also known as auxiliary electrode), made of a conductive material like platinum, supplies the current to the working electrode surface. The area of this electrode should be larger than the working electrode. This three-electrode arrangement prevents large currents from passing through the reference electrode that could change its potential.

In this work, this technique is used to prove the presence of the DTSP monolayer onto the Au surface (working electrode, WE). The experiment is performed at room temperature with an Autolab potentiostat (PGSTAT 30, Eco Chemie), in a three-electrode cell. Platinum gauze is used as counter electrode (CE) and the potentials are measured respect to saturated calomel reference electrode (RE). All solutions are deoxygenated in order to avoid the interference caused by dissolved oxygen in the aqueous solution by bubbling nitrogen for 30 minutes before the measurements. The scan rate used is 100 mV/s. Figure 3.10 shows the experimental setup described above.

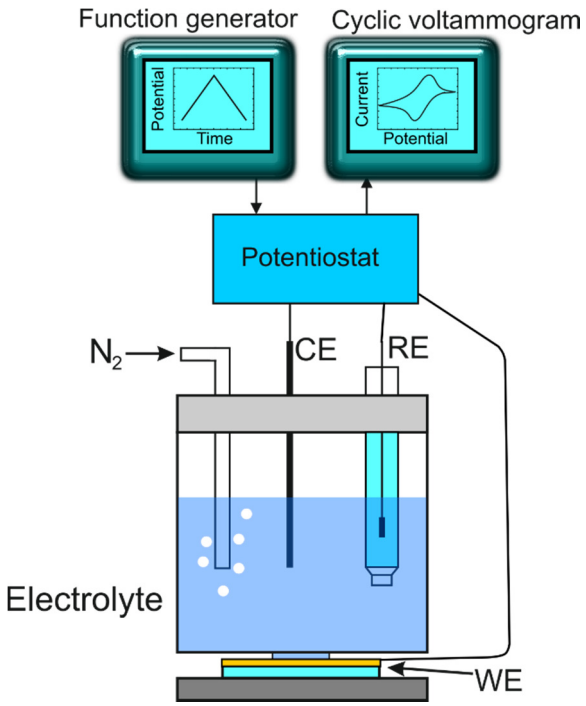

Figure 3.10. Scheme of the experimental setup for voltammetric measurements.

3.8. X-ray diffraction

X-ray diffraction (XRD) analysis is a characterization technique that provides information about the composition, the crystal structure of the sample and its periodicity.[12] A monochromatic x-ray beam impinges on the sample, interacting with the atoms. As a result of the interaction, scattered beams get out from the sample. The scattered beams interfere constructively if the optical path difference between them is a multiple integer (n) of the beam wavelength (λ), giving rise to a diffracted beam. Taking into accound the discrete nature of the matter and the lattice periodicity, that situation will happen when the Bragg's law is satisfied:

$$2d_{hkl}\sin\theta = n\lambda \tag{3.4}$$

where d_{hkl} is the distance between crystal planes (identified with the Miller indices: hkl) that produces the diffraction, and θ the incidence angle between the incident and diffracted beams (see Figure 3.11).

Each crystal structure has its own pattern of diffracted peaks, which makes this technique useful for identification of unknown samples.

In this work, the X'Pert PRO diffractometer from Panalytical is used. This technique is used to analyze the composition and crystal structure of the Cu foil after thermal oxidation in Chapter 3, and the GaNPs/Si platforms in Chapter 6 after the evaporation of metallic Ga on Si substrates.

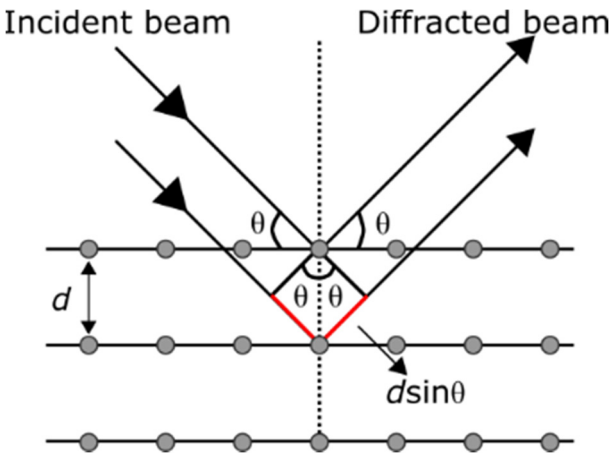

Figure 3.11. Schematic of the Bragg's law.

3.9. Current-voltage *(I-V)* characterization

Current-voltage measurements are generally used as a tool to study the electrical behavior of an electronic device and to extract its basic parameters. The characteristics of the resulting curve can be sometimes reproduced using equivalent circuit models that include resistors, capacitors, inductances, and power sources.

A resistor exhibits the simplest *I-V* characteristic, which according to Ohm's Law ($V = I \cdot R$), shows a linear relationship between the applied voltage and the electric current driven through the resistor. The resistance of the device can be estimated from the slope of that curve. However, there are many electronic components and devices, which have non-linear characteristics, that is, their *I-V* ratio is not constant. Semiconductor devices such as diodes or transistors comprise PN junctions connected together and exhibit non-linear *I-V* curves.

In the present work, the electrical characterization is performed with a HP 4145B semiconductor parameter analyzer. Figure 3.12 shows a schematic of the whole characterization system. The device is connected to the HP 4145B analyzer by using steel probes that can smoothly contact the electrodes using micropositioners under the assistance of an optical microscope. All those components are hosted inside a Faraday cage to shield the device from external electric noise. The analyzer applies a DC voltage and measures the current. Results are recorded and read through a remote computer.

I-V characterization has been used to study the optoelectronic properties of ZnO and CuO NWs. Prior to the measurement, the NWs have been aligned by dielectrophoresis between electrodes, pre-patterned by photolithography. The dielectrophoretic process has been performed by applying sinusoidal waveforms with a function generator connected to the electrodes.

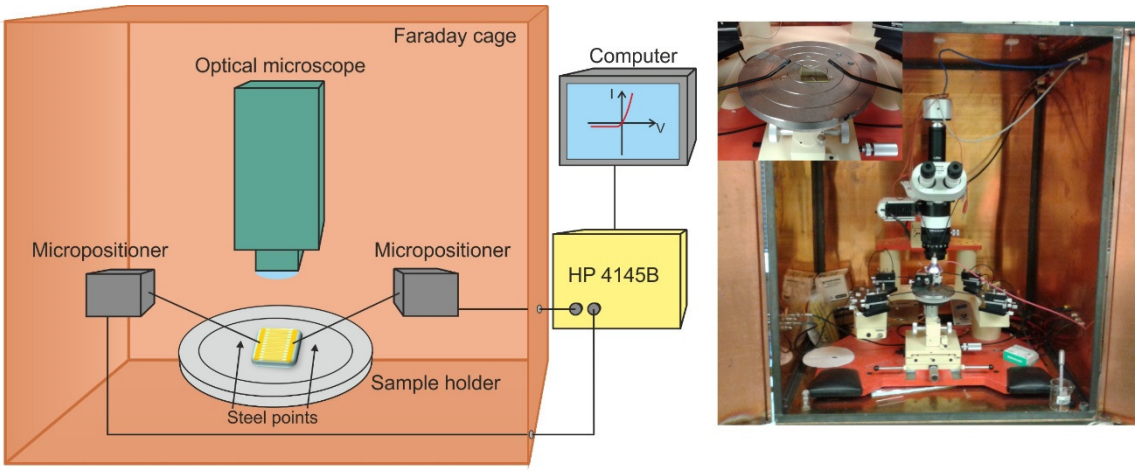

Figure 3.12. Probe station used to measure the *I-V* characteristics of the NW-based devices.

3.10. Scanning electron microscopy and energy dispersive x-rays spectroscopy

This technique is a type of electron microscopy in which a focused electron beam coming from an electron gun is directed to a sample (see Figure 3.13A).[13] These electrons (primary electrons) interact with the sample (interaction volume), dislodging its electrons and emitting X-rays that are collected by the corresponding detector (Figure 3.13B). A wide range of information can be collected depending on the electrons or X-rays detected:

- Secondary electrons: these are low energy electrons coming from the sample and excited by the incident electron beam. They escape from the most superficial layers of the sample and their detection provides information about the sample morphology.

- Backscattered electrons: these are primary electrons suffering elastic collisions with the sample atoms. The backscattered electron energy depends on the sample element and its determination provides information about the chemical composition of the sample.

- X-rays: these photons are released during relaxation of a sample atom, previously excited with the primary electron beam. The energy of the X-rays strongly depends on the atom nature and their analysis is the basis of the EDX or EDAX technique. The mechanism for the emission of these photons comprises the ejection of an inner-shell electron after imping the sample with the primary beam. An electron from an outer-shell fills the hole, releasing those high-energy photons (Figure 3.13C).

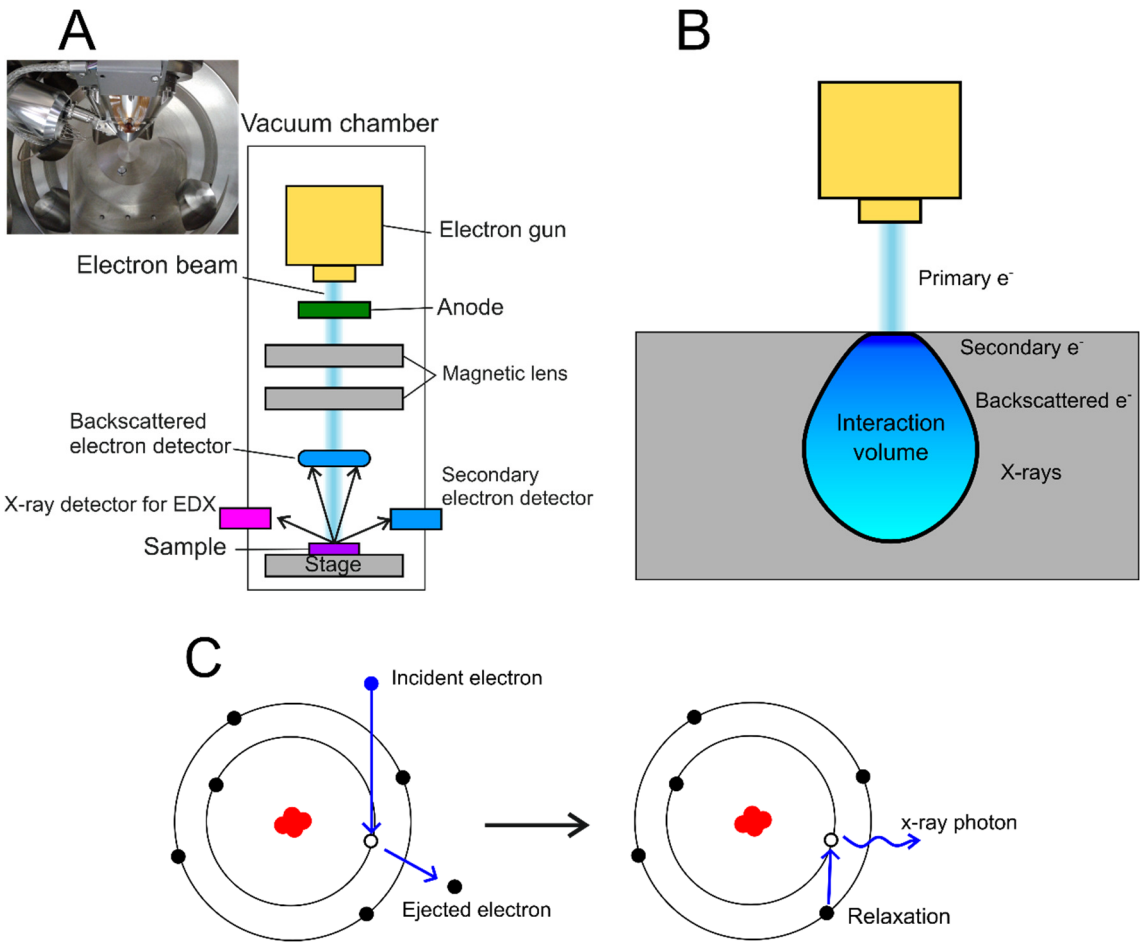

Figure 3.13. (A) Scheme of a SEM-EDX equipment. The inset of this figure shows the vacuum chamber of the Philips XL30 S-FEG microscope; (B) typical electron-sample interactions for the sample characterization; (C) schematic of the EDX principle.

In this work, two field emission-scanning electron microscopes (FE-SEM) are used: a FEI Nova NANOSEM 230 with a backscatter electron detector to scan the sensor surface after AuNPs adsorption in Chapter 5 and a Philips XL30 S-FEG with a secondary electron detector (Everhart-Thornley) to scan NWs and GaNPs in Chapters 4 and 6. The inset of Figure 3.13A shows the inner vacuum chamber of the microscope.

3.11. Spectroscopic ellipsometry

3.11.1. Ellipsometer

Spectroscopic ellipsometry has constituted a very powerful technique to analyze the optical properties of thin films and determine their thicknesses with high accuracy. Moreover, in reflection mode, its high sensitivity to the surface properties allows the

development of gas and biological sensors. The ellipsometer used in this thesis is a UVISEL Jobin-Yvon photoelastic modulator ellipsometer (Figure 3.14) and comprises the following components:

- Light source: Xenon lamp for the UV-Visible wavelength range. The light from this source is unpolarized.
- Polarizer: two calcite prisms with an extinction coefficient lower than 10^{-5}. After passing through this component, the incident light beam becomes linearly polarized.
- Photoelastic modulator: comprises a birefringent material made of fused silica which modules the incident light phase before reaching the sample. The introduced phase change follows the expression $\delta(t) = a * sen(\omega t)$, where "$a$" represents the modulation amplitude, as a function of the wavelength and the applied voltage, and ω is the resonant frequency of the photoelastic material (50 kHz). After passing through the modulator, the light is elliptically polarized.
- Sample holder: a planar surface with several micropositioners to adjust the position and the holder tilt and achieve the highest signal level.
- Analyzer: similar to the polarizer. The output beam is linearly polarized.
- Monochromator: Jobin-Yvon HR-250 model. It includes a diffraction grating with 1200 grooves/mm and a functional range of 240-850 nm (1.45-5.20 eV). The monochromator has two filters at the entrance: one used for the UV range (240-340 nm) and the other one used in the visible range for wavelengths larger than 500 nm.
- Detector: photomultiplier tube, Hamamatsu R928S model.

The ellipsometric components are connected through optical fibers and attached to a motorized goniometer. The incidence angle can be varied between 90° and 30°. The electric signal from the detector is recorded and the spectrum is shown in the computer. The ellipsometer software can be used to show the spectrum and build models to simulate the values obtained for the ellipsometric functions and the pseudodielectric functions.

The configuration used for all the acquired spectra is M = 0º, A = +45º and P-M = +45º, where "P", "M" and "A" are the angles of the polarizer, modulator and analyzer respect to the plane of incidence.

Two different configurations have been used in this work, external reflection and total internal reflection.

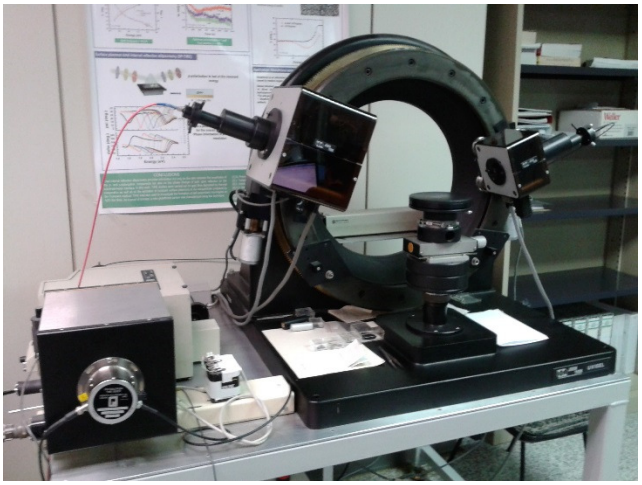

Figure 3.14. Spectroscopic ellipsometer used in the Microelectronics Laboratory at UAM.

3.11.2. External reflection ellipsometry

This external reflection mode is mainly used in this work to measure the plasmonic resonance of GaNPs and to estimate the thickness of a thin film, typically AZO and SiO_2, deposited on a substrate.

The procedure to carry out the measurements is simple. First of all, the sample is directly placed on the sample holder and the incidence angle is set in the software. Before the measurement, the position and tilt are adjusted with the holder micropositioners, until the sample is completely horizontal and the reflected beam is centered on the analyzer. Finally, the energy range and the energy step are set in the software before launching the measurement. A scheme is included in Figure 3.15, where φ_i represents the incidence angle.

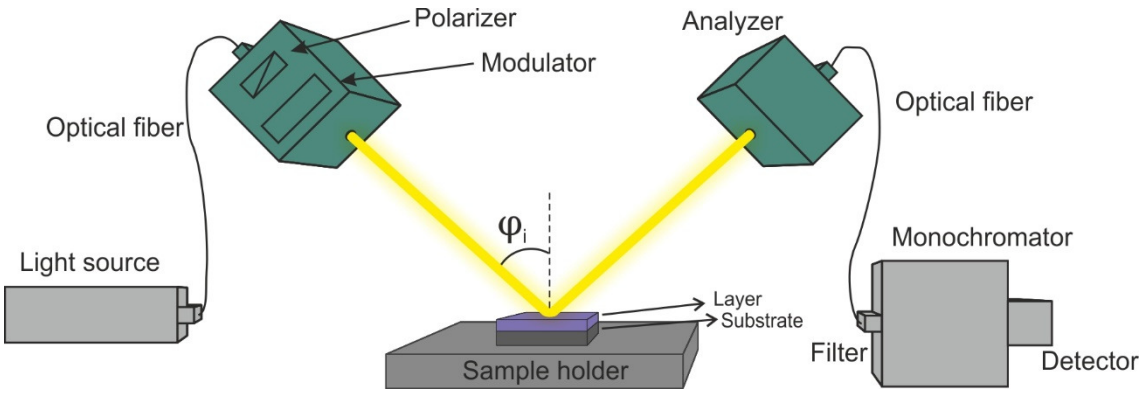

Figure 3.15. Scheme of the spectroscopic ellipsometer and its components. The sample holder contains a sample under analysis in external reflection mode.

3.11.3. Total internal reflection ellipsometry

This configuration is used to measure the plasmonic response of metallic thin films. If the incidence light wavevector couples to the surface plasmon wavevector, the resonance of the surface plasmons (SPR) occurs.[14, 15] The most common optical components to enable coupling between the incident electromagnetic radiation and plasmon polaritons are prisms, gratings and optical waveguides. Most widespread instruments use the prism coupling approach, also known as the attenuated total reflection approach. The prism and the sample containing the metal surface can be attached following two different configurations, the Kretschmann and the Otto configuration. In this work, we focus on the Kretschmann approach because of its wide use in SPR experiments and its lower impact on the surface properties during the development of optical biosensors.

The optical excitation of the SPR is accompanied by the transfer of the incident light beam energy into the surface plasmons and its dissipation in the metal film. In common SPR, this process is measured as an intensity reduction of the reflected light when the incident beam is p-polarized. In addition to the reduction of the light intensity of the p-component, spectroscopic ellipsometry can measure the phase change of the outgoing beam with respect to the incident one. The coupling between the incident radiation and the plasmon polariton is strongly revealed through a significant phase change, as discussed below.

The experimental setup used in this work follows the Kretschmann configuration with the spectroscopic ellipsometer to measure the intensity and the phase changes. The

samples are attached to a right-angle fused silica prism using a matching index fluid on the backside of the substrate in order to minimize reflections at the prism/substrate interface. The prism, hosting the sample underneath, is directly put on a polyvinyl chloride homemade flow cell, sealed with a rubber O-ring, and connected to a peristaltic pump to inject the as-prepared solutions from the inlet tubing. During the functionalization process, the solution is kept motionless. Solutions waste is recovered from the outlet tubing after the process. The experimental setup is represented in Figure 3.16A. In this Figure, $\varphi_{i,2}$ is the incidence angle after entering the high refractive medium. If the external incidence angle (φ_i) is normal to the prism surface, then $\varphi_{i,2} = \varphi_i$.

The SPR resonance in the TIRE spectra presents a characteristic reduction of the Ψ function due to the extinction of the p-polarized light component of the light beam, and a strong angle shift of the Δ function. The resonance energy can be determined by the position of the Ψ function minimum ($E_{\Psi min}$). A strong variation of the Δ function is also observed at that energy (Figure 3.16B).

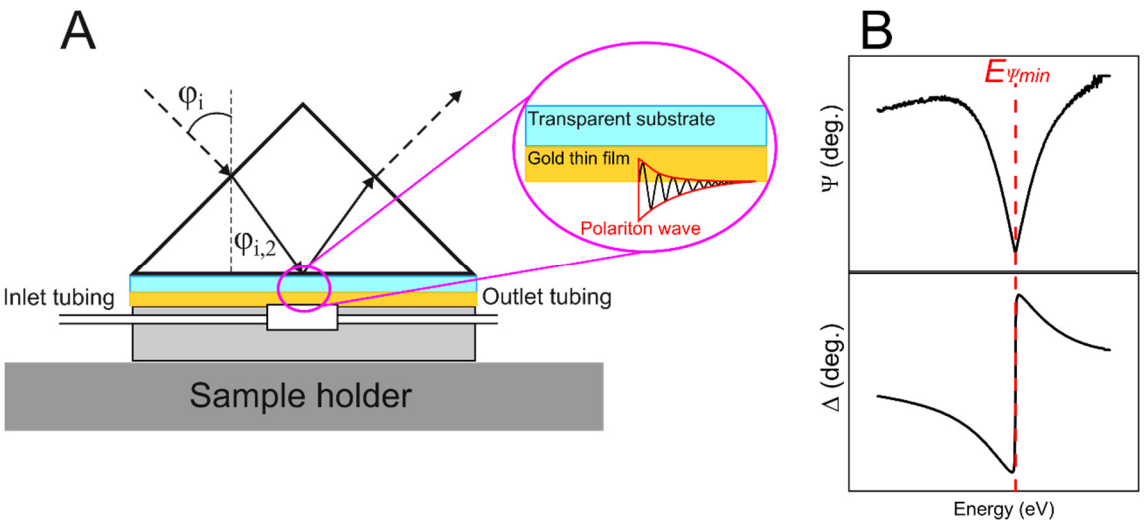

Figure 3.16. Scheme of the system used for TIRE measurements based on the Kretschmann configuration. The inset shows typical shapes of Ψ and Δ functions around the surface plasmon resonance.

3.12. Discrete dipole approximation

The discrete dipole approximation (DDA) is a method used to solve the Maxwell's equations for particles of arbitrary shape with complex refractive index. It is useful to study the LSPR of nanostructures, and the influence of the surrounding medium and the substrate.

To perform the simulations with the DDA method, the software DDSCAT 7.3.0 is used. This program has been developed in FORTRAN and is freely available on the Internet together with a user guide and many practical examples.[16, 17] After downloading the source code, the program is compiled with MinGW for Windows 7 64 bits in order to obtain the executable.

To run the software, the following issue should be kept in mind. Two folders must be created. The first one contains the dielectric properties of each material, one file per material. For simulating structures with different dielectric behaviors, i.e. multiple or anisotropic materials, one file for each behavior in the corresponding direction is required. As an example, an anisotropic material with different properties in all the Cartesian directions requires three files. In the second folder, the executable (ddscat.exe) and the parameter file (ddscat.par) have to be present. Pressing double click in the executable initiates the program. Results are stored in different output files, but the cross-sections are located in the qtable file.

The parameter file includes all the input parameters. Below, we include the most important used. Interested readers are referred to the user's guide for further information.

- Target shape definition: a user typically takes the previously defined targets, which are defined by the variable CSHAPE, such as ellipsoids, blocks, etc. The next lines in the ddscat.par file include the SHPAR variables, which define the number of dipoles along the "x", "y" and "z" directions. It is worth noting that the higher is this number, the better is the accuracy of the simulation. However, it can increase exponentially the computational cost. An interdipole spacing of around 2 nm gives accurate enough results. If the target geometry has not been predefined previously, CSHAPE is set to FROM_FILE, and a shape.dat file, which contains the dipole positions of the custom target, must be included. The user guide provides an extensive information about this topic.

- Dielectric properties: the number of components are specified by the NCOMP variable. In the next lines, the file direction in the hard drive should be provided.

- Size: the real size of the target is introduced by the parameter named "effective radius" which is defined as the radius of an equal volume sphere expressed in microns. It is defined through the equation $a_{eff} = (3 \cdot V / 4 \cdot \pi)^{1/3}$, where V is the volume of the target.

- Wavelength: the range of wavelengths used along with the interval, expressed in microns.

- Light polarization: the polarization state of the incident wave can be set in any direction by defining the e01 vector in the parameter file. The software assumes that the incident radiation is propagating along the "x" axis.

- Target orientation: the orientation of the target with respect to the light can be changed, if needed, with three angles (beta, theta and phi).

The DDSCAT software also enables the calculation of the near-field around the target following the procedure explained by Flatau and Draine.[18] For this calculation, the software runs twice. The first time, it calculates the induced polarization for the total target and stores the result in .polx files. The second run, DDSCAT takes the stored values and proceeds to calculate the electric field at the lattice points in an extended rectangular volume, storing the results in .Ex files. To carry out such calculations, the ddscat.par should be modified, setting the NRFLD variable to 1. In the next line, the extended volume is specified in all directions where the electric field is calculated.

To visualize the near-field, a post-process is necessary in order to obtain suitable data for its use with an external visualization software. DDSCAT includes an executable, ddpostprocess.exe, which reads the parameter file ddpostprocess.par. In this file, the near-field calculation can be performed in the whole area (IVTR = 1) or in a single line (ILINE = 1). In the first case, the executable transforms the .Ex file into the VTK format. Open-source programs, i.e. Paraview, MayaVi2, etc., allows the 3D visualization of these files. The DDSCAT userguide provides some basic steps for this software. For the second case, the coordinates of the line in physical units must be included in the parameter file. After the simulation, the electric field in all directions is stored in an output file (ddpostprocess.out). From these results, the electric field modulus can be calculated.

REFERENCES

1. T. García-Mendiola; T. Barreiro Martínez; F. Pariente; J. Molano; E. Lorenzo. Screening of Specific Gene Mutations Associated with Cystic Fibrosis. *Electroanal.* **2014**, 26, 1362-1372.
2. C. G. Núñez; J. L. Pau; E. Ruíz; A. G. Marín; B. J. García; J. Piqueras; G. Shen; D. S. Wilbert; S. M. Kim; P. Kung. Enhanced fabrication process of zinc oxide nanowires for optoelectronics. *Thin Solid Films* **2014**, 555, 42-47.
3. M. Wei; D. Zhi; J. L. MacManus-Driscoll. Self-catalysed growth of zinc oxide nanowires. *Nanotechnology* **2005**, 16, 1364-1368.
4. G. Shen; N. Dawahre; J. Waters; S. M. Kim; P. Kung. Growth, doping, and characterization of ZnO nanowire arrays. *J. Vac. Sci. Technol. B* **2013**, 31, 041803.
5. J. Turkevich; P. C. Stevenson; J. Hillier. A study of the nucleation and growth processes in the synthesis of colloidal gold. *Discuss. Faraday Soc* **1951**, 11, 55-75.
6. G. Frens. Controlled nucleation for the regulation of the particle size in monodisperse gold suspensions. *Nat. Phys. Sci* **1973**, 241, 20-22.
7. J. L. Pau; J. M. Abad; M. J. Hernández; M. Cervera; E. Ruiz; C. G. Nuñez; E. Lorenzo; J. Piqueras. In *Investigation of surface plasmon resonance in Au nanoparticles deposited on ZnO:Al thin films*, Proceedings of the 8th Spanish Conference on Electron Devices, CDE'2011, 2011.
8. J. G. Solé; L. E. Bausá; D. Jaque. *An Introduction to the Optical Spectroscopy of Inorganic Solids*. 1st ed.; John Wiley & Sons: New Jersey, 2005.
9. P. R. Griffiths; J. A. De Haseth; J. D. Winefordner. *Fourier Transform Infrared Spectrometry*. Wiley: 2007.
10. C. D. Wagner; W. M. Riggs; L. E. Davis; J. F. Moulder. *Handbook of x-ray photoelectron spectroscopy: a reference book of standard data for use in x-ray photoelectron spectroscopy*. Physical Electronics Division, Perkin-Elmer Corp.: 1979.
11. J. M. P. Carrazón; P. S. Batanero. *Química electroanalítica: fundamentos y aplicaciones*. Síntesis: 1999.
12. C. Kittel. *Introduction to Solid State Physics*. Wiley: 2004.
13. C. E. Lyman; D. E. Newbury; J. Goldstein; D. B. Williams; A. D. Romig; J. Armstrong; P. Echlin; C. Fiori; D. C. Joy; E. Lifshin. *Scanning Electron Microscopy, X-Ray Microanalysis, and Analytical Electron Microscopy: A Laboratory Workbook*. Springer US: 2012.
14. R. B. M. Schasfoort; A. J. Tudos. *Handbook of surface plasmon resonance*. RSC Publishing, Cambridge: 2008.
15. J. L. Pau; A. G. Marín; M. J. Hernández; M. Cervera; J. Piqueras. Analysis of Plasmonic Structures by Spectroscopic Ellipsometry. In *Research Perspectives on Functional Micro- and Nanoscale Coatings*, Ana, Z.; Maria Carmen, M.-M., Eds. IGI Global: Hershey, PA, USA, 2016; pp 208-239.
16. B. T. Draine; P. J. Flatau. Discrete-Dipole Approximation For Scattering Calculations. *J. Opt. Soc. Am. A* **1994**, 11, 1491-1499.
17. DDSCAT 7.3. http://ddscat.wikidot.com/ (accessed February, 2015).
18. P. J. Flatau; B. T. Draine. Fast near field calculations in the discrete dipole approximation for regular rectilinear grids. *Opt. Express* **2012**, 20, 1247-1252.

4. CuO and ZnO nanowire-based light sensors

4.1. Cupric oxide nanowires growth and devices

4.1.1. Introduction

Metal oxides (MO) are attractive compounds for industrial purposes since high-quality crystal nanowires (NWs) can be obtained by cost-effective methods that do not require expensive vacuum systems or environmentally unfriendly chemical reactants. A few examples of MO for building NWs are SnO_2, In_2O_3, ZnO and CuO. The latter is a p-type semiconductor, which is a less common material and not widely studied in comparison to n-type structures. Its optical bandgap lies in the infrared region (E_g = 1.2-1.4 eV, 1030-890 nm) which allows developing light sensors in the full-visible wavelength range.[1]

CuO NWs can be grown by using different methods, such as chemical,[2] template-assisted techniques,[3] or direct oxidation of regular Cu foils.[4] The latter has been demonstrated to be an easy and cost-effective method where no catalysts or expensive equipment is needed. This method is carried out by placing a Cu foil on a hot source (hot plates, furnaces, etc.) in an oxidizing atmosphere.

The NW growth occurs from the diffusion of Cu ions from the metal, as shown in Figure 4.1. This diffusion predominantly takes place through grain boundaries (grain

boundary diffusion) in the intermediate oxidized layers at temperature in the 300-800 ºC range.[5-7] Once the Cu ions are on the surface, they diffuse through the NW base to the tip (surface diffusion) driven by the concentration gradient. For higher temperatures, NWs do not grow since the ions start to diffuse along the crystal lattice of the oxidized layers, a mechanism that requires higher activation energies. Grain boundaries are regions with low degree of order and packing density and, thus, subject to strong stresses, i.e. thermal, mechanical… Ions in those regions tend to flow to the surface in order to minimize their surface energy.[8] These NWs obtained by this method grow mostly vertically and present a highly crystalline monoclinic structure. These NWs often present a twin plane along the longitudinal axis when they are scanned by electron microscopy.[4]

Due to interfacial stresses induced by the large differences in crystal structure and thermal expansion coefficients between the Cu_2O and the substrate, this layer tends to peel off from the substrate after cooling down, releasing a self-standing layer which contains the NWs.[9]

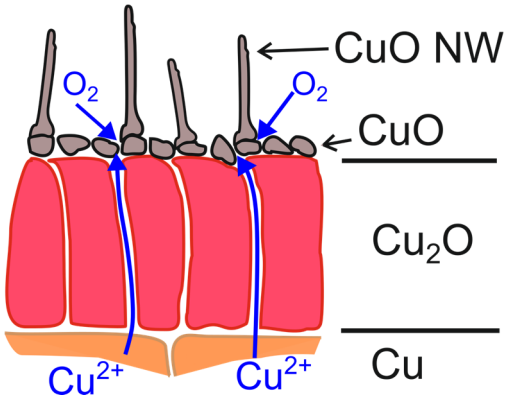

Figure 4.1. Scheme of CuO NWs growth mechanism. Three different layers can be observed: Cu foil (bottom-most layer), Cu_2O (middle one) and CuO (top-most one, where NWs grow).

In this Section, the main objective is to synthetize p-type CuO NWs, by direct oxidation of copper, and align between n-type Al-doped ZnO (AZO) electrodes by dielectrophoresis. The heterostructure is electro-optically characterized showing fast recovery times in the microsecond range, mainly limited by the resistance-capacitance product of the equivalent circuit, without signs of persistent effects. The fast response is attributed to short transit times across space charge regions built between CuO and AZO materials and fast carrier recombination at neutral regions.[10]

4.1.2. Cupric oxide nanowires growth

CuO NWs can be obtained by thermal oxidation of Cu in ambient air. First experiments are performed using a hot plate at a constant heating power for a fast process to obtain quite thin NWs. To better study the influence of the temperature, the NWs are grown inside a furnace. For both growth processes, 99.98% pure Cu foils of 1.0×1.0 cm^2 area are pre-treated by dipping the foil in EtOH, sonicating for 2 min to remove adsorbed impurities, and blowing with dry N_2.

For NWs grown on the hot plate, Cu foils are placed on the surface (previously covered with aluminum paper to distribute the temperature homogeneously) at a temperature range of 390-410ºC during 1 h, leaving the sample on the unheated plate overnight for cooling down. This temperature range is estimated by using a thermocouple. After a few seconds on the hot plate, the Cu foil changes its color from light brown to dark red, and then, to black. A few Cu foils are oxidized on the hot plate at that temperature range, removed from it at the corresponding oxidation stages, and shown in Figure 4.2. All these colors are attributed to the successive oxidation states of metallic Cu; dark red is the Cu_2O (Cu^+) whereas the black colored surface corresponds to CuO (Cu^{2+}), the most oxidized state of Cu.[11, 12]

For the furnace experiments (see Figure 4.3A), Cu foils are placed on a 10 cm quartz boat and introduced close to the quartz tube center, around 20 cm far from the loading end of the tube, where the temperature is more uniform. The influence of the temperature is studied using different oxidation temperatures ranged between 200 and 750 ºC at a constant oxidation time of 4 h. A measurement carried out with a thermocouple shows good temperature uniformity along the furnace. The cooling-down process is carried out by leaving the sample inside the furnace until reaching ambient temperature. As shown in Figure 4.3B, all the resulting surfaces are black-colored after the 4-hour growth except the 200 and 350 ºC batches which are red-violet and grey, respectively.

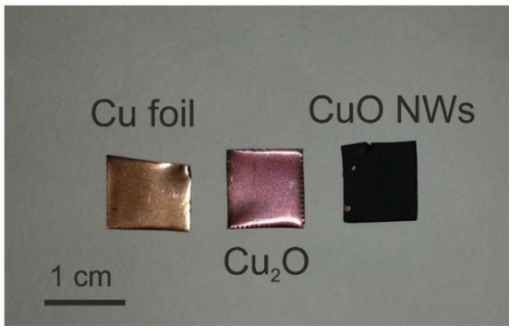

Figure 4.2. Image of the different oxidation stages of the Cu foil.

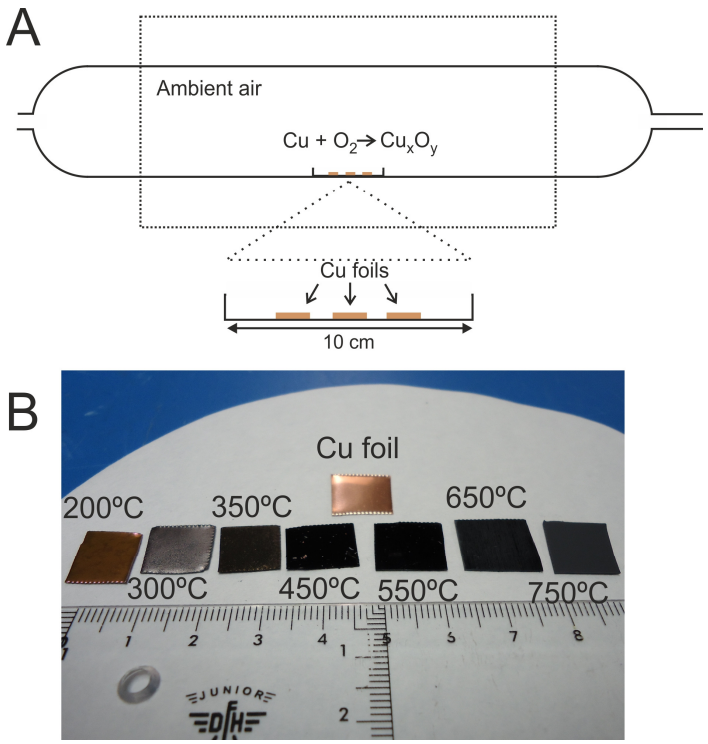

Figure 4.3. (A) Scheme of the furnace where an aluminum boat is placed in the middle. This boat contains several Cu foils to grow NWs; (B) Image of Cu foils after 4-hour treatments at temperatures ranged between 200 and 750 ºC.

4.1.3. Structural characterization

Foil surfaces are characterized by using SEM, X-ray diffraction and energy dispersive X-ray spectroscopy (EDX) techniques.

X-ray diffractograms of an oxidized sample and an as-received Cu foil are obtained in θ-2θ mode (Figure 4.4). Diffraction peaks corresponding to the Cu, Cu_2O, and CuO phases are identified from the powder diffraction files (#04-009-2090, #04-007-9767, and #04-008-8209, respectively) of the International Centre for Diffraction Data (ICDD). As

can be seen, the original Cu foil presents a polycrystalline structure showing preferential orientation along (111) and (200) plane directions. After oxidation, the strongest peak, indexed using the Pn-3m space group, corresponds to the Cu_2O (111) plane whose origin is related to the layer built on top of the foil at the early stages of the process. This layer is also polycrystalline as suggested by other Cu_2O phase reflections present in the diffractogram. On the other hand, all CuO peaks can be indexed using the C2/c space group of the monoclinic structure. Those CuO peaks (110, 111 and -111), which are not completely overlapped with other peaks, are shown in Figure 4.4. Cu is still observable on the oxidized surface because x-rays can penetrate several micrometers through the surface.

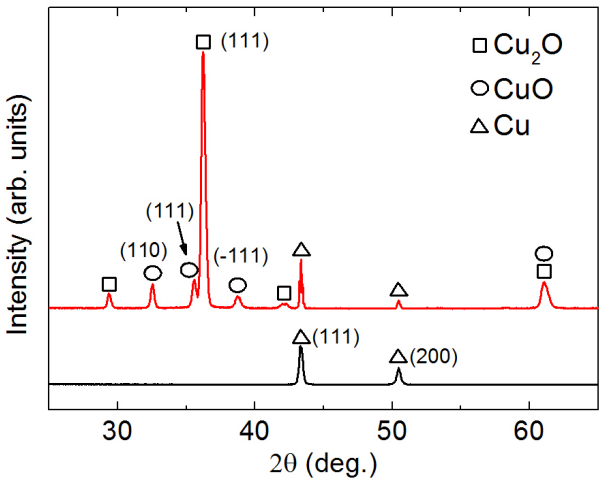

Figure 4.4. X-ray diffractograms obtained before (bottom scan) and after thermal oxidation (top scan) of the Cu foil.

SEM scans of the oxidized surfaces in the furnace, obtained at a 10 kV operating voltage, reveal high NW densities for growth temperatures ranged between 350-650ºC. Figure 4.5 shows samples grown at 350 and 650 ºC. It is worth noticing that the 750ºC sample does not present NWs. The presence of a two-layer structure is observed in the cross-section images (Figure 4.5, third column). The thinnest one acts as a template layer for NW growth and corresponds to CuO.

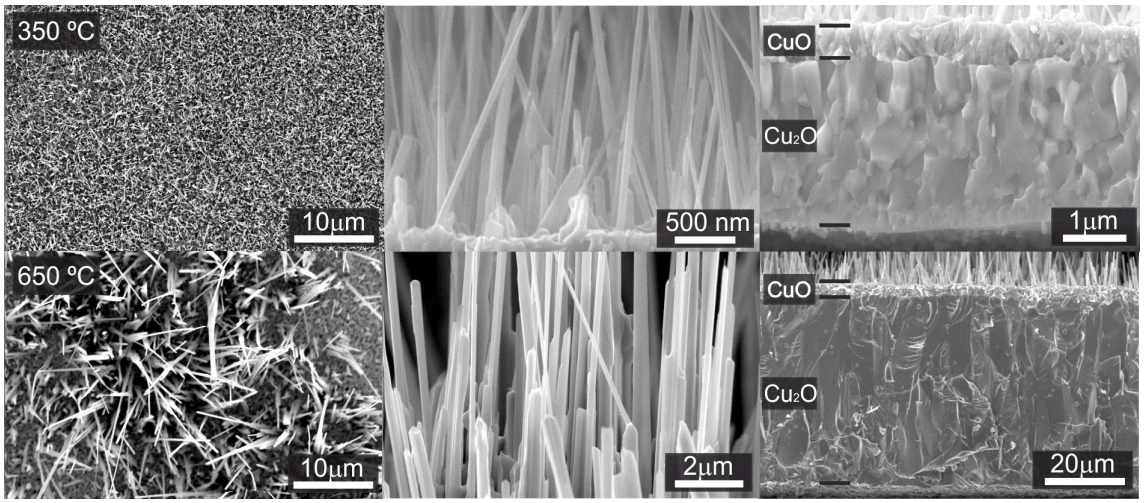

Figure 4.5. SEM images of the NWs for two different growth temperatures (350 and 650ºC). The first column is a plane view of the samples at a 5000x magnification. Second and third columns represent cross-sectional images of NWs and copper oxide layers, respectively.

Chemical composition of these layers is analyzed through EDX spectroscopy (Figure 4.6). The thickest structure gives rise to Cu and O concentrations of 67% and 33%, respectively, matching the stoichiometry of the Cu_2O phase. The thinnest layer and the NWs yield a higher concentration of oxygen. However, it is difficult to quantify the concentration due to the wide interaction volume of the primary electrons that carries information of the other layers.

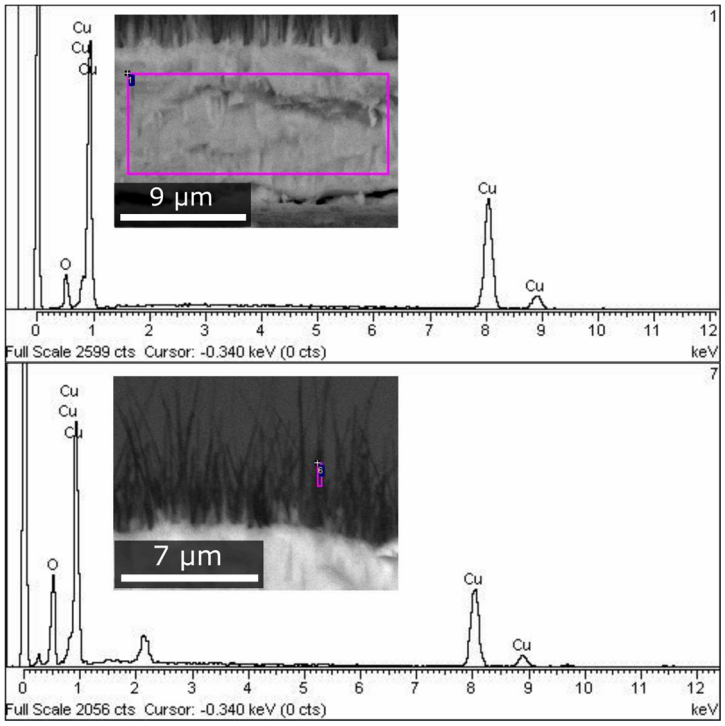

Figure 4.6. EDX spectra of an oxidized Cu surface.

The estimation of the Cu_2O and CuO layers thicknesses shows an increasing variation with the growth temperature (Figure 4.7A). The thickness of the CuO layer increases strongly for temperatures between 350 and 450 ºC and remains fairly constant around 2.60 µm at higher temperatures. On the other hand, the thickness of the Cu_2O layer is quite constant at temperatures lower than 450 ºC and increases significantly at high temperatures. At 750 ºC, the whole surface is black colored and the interface between these two layers cannot be distinguished by SEM. For that reason, thicknesses for this temperature are not included in Figure 4.7A.

The dimensions of NWs also exhibit increasing trends with the growth temperature. The NW length presents a linear relationship with the oxidation temperature in the 350-650 ºC range (Figure 4.7B) due to the large ion mobilities at these temperatures. It is interesting to notice that, under the same growth time (4 hours in this study), the average NW length is around 100 nm longer per temperature degree. The curve fitting yields with correlation coefficient of $R^2 = 0.9717$. Likewise, NW diameters are not constant along the length. Base and tip diameters, estimated as a function of growth temperature, are shown in Figure 4.7C. The strong increase of both diameters with the temperature can be explained from the formation of polycrystalline NWs that comprises several crystals separated by twin planes.[4] This effect can be observed in the SEM image

in Figure 4.7D. In this Figure, the twin plane is remarked as a dotted line. However, at 350 ºC, this effect is not observed suggesting that the temperature is not high enough to produce the polycrystalline structure.

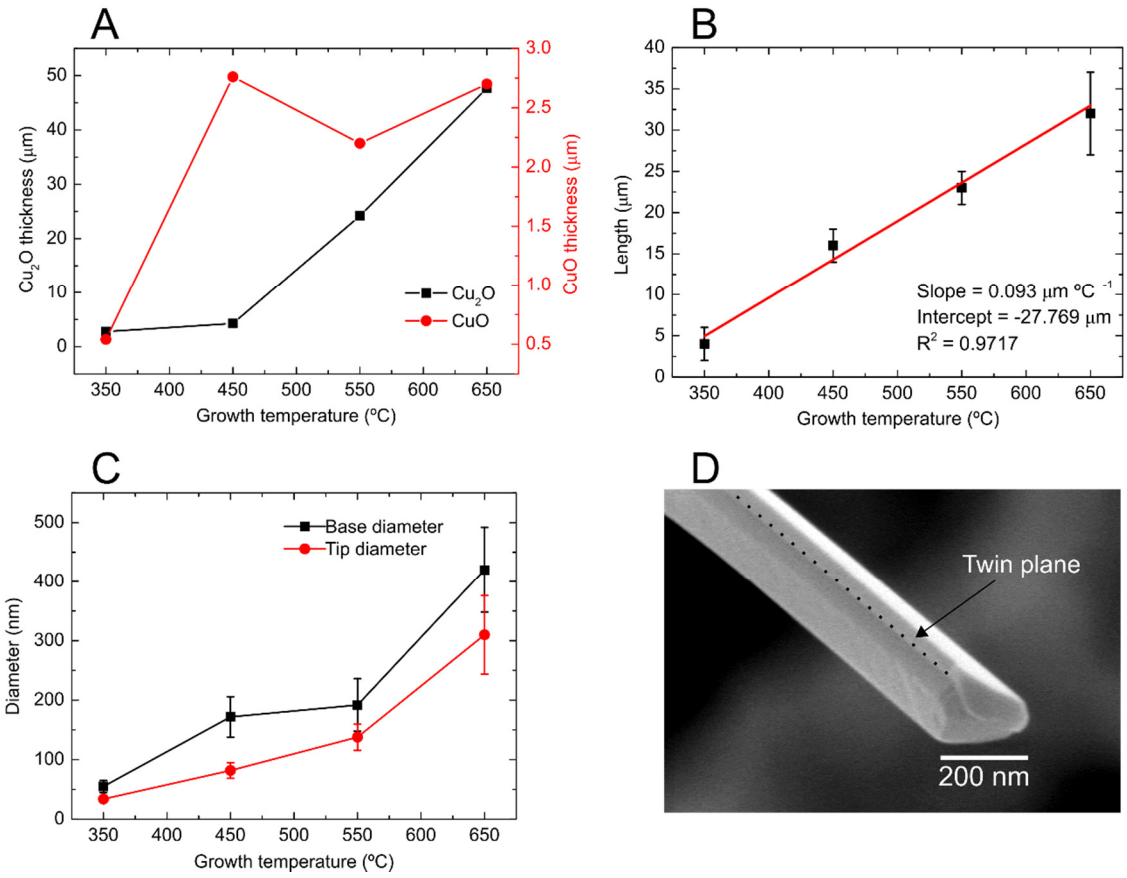

Figure 4.7. (A) Thicknesses of the copper oxide Cu layers measured in cross-sectional SEM images; (B) NW length; (C) base and tip diameters; (D) SEM image of a NW tip. Error bars in (B,C) represent the standard deviation of three measurements.

To find out the doping type of the CuO NW, the following experiment is performed based on the surface chemisorption of H_2O molecules.[13] A sample is prepared using CuO NWs dispersed on pre-patterned AZO interdigitated electrodes with 250-µm spacing. For the sake of comparison, another sample is prepared by drop-casting ZnO NWs on a pattern with the same geometry and material. Both samples are biased at 5 V using an external power supply to measure the current variations between electrodes when the samples are exposed to the water vapor supplied by an ultrasonic humidifier (Figure 4.8).

As the humidity rises up after turning the apparatus on (vertical dashed line in Figure 4.8), the current from the ZnO NWs suddenly increases, whereas the signal from the CuO NWs decreases. According to Han et al., the adsorbed O^- ions on the NW surface interact with the H_2O molecules, releasing O_2 to the ambient and electrons to the NW volume. As a result, the electrical conductivity of n-type semiconductors is enhanced, whereas p-type materials suffer a reduction of their conductivity. Therefore, the experiment corroborates that the CuO NW behaves as a p-type semiconductor material.

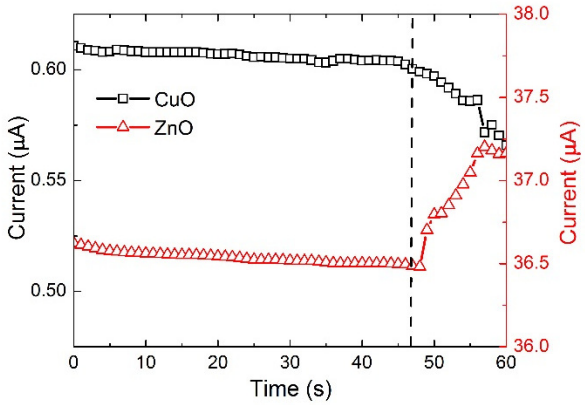

Figure 4.8. Electrical current through coplanar electrodes covered by CuO (black squares) and ZnO (red triangles) NWs. The vertical dashed line indicates the turn-on moment of the humidifier.

4.1.4. Alignment by dielectrophoresis

The first objective is to design an electrode geometry to enhance ∇E^2 in certain regions (alignment sites) in order to increase the number of trapped NWs. For this aim, coplanar Au electrodes with a castellated geometry are chosen to produce an array of alignment sites. The electrodes are 100-nm thick, fabricated using optical lithography and chemical etching. They are connected to two bus bars separated 50 μm and contain a set of 160 alignment sites. Each alignment site is defined by two opposite squares of around 20×20 μm^2 with a minimum distance of 10 μm between them (Figure 4.9A).

The sinusoidal waveform for alignment purposes is applied by using a 1-MHz function generator with frequencies ranged between 0.01 to 1000 kHz and either effective voltages (V_{RMS}) of 7 or 14 V. Prior to the alignment, a NW dispersion is prepared by sonication of the NW sample in EtOH. Typical NW concentration achieved by this means

ranges between 100 and 1000 NWs/µL. A few microliter drop of this solution is casted on the electrodes while AC bias is applied. Since the solvent used is EtOH, the sample gets dried in a few seconds.

After the process, the surface is observed by optical microscope. A certain number of NWs are spotted, most of them aligned and in physical contact with the electrodes. Optimal NW contact between both electrodes is labelled as an "aligned in site" (ALS) event; NWs in contact with one electrode are named "aligned out of the site" (AL); NWs located far from the alignment site belong to the "non-aligned" (NAL) group. Examples of the different groups in Figure 4.9A.

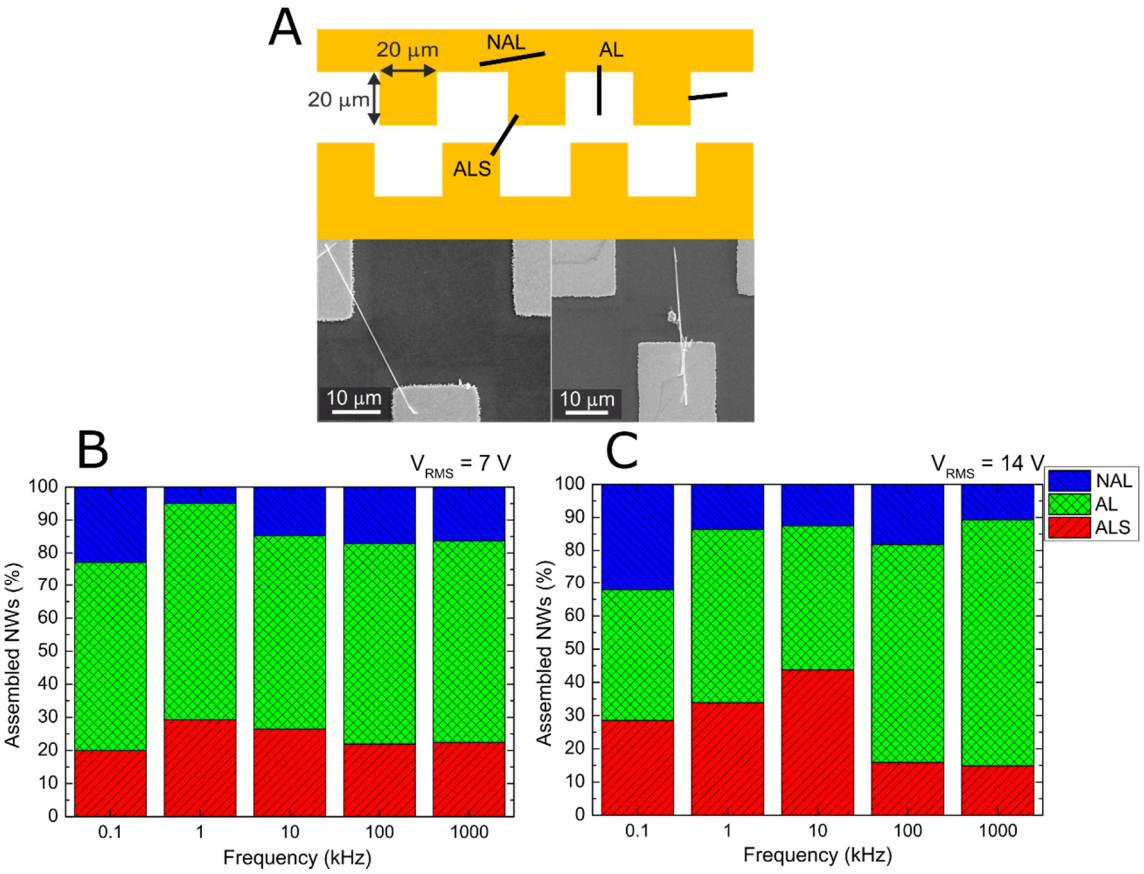

Figure 4.9. (A) Scheme of the gold castellated electrodes and SEM images of some NWs found after the DEP process. NAL means "non-aligned", AL means "aligned out of the site", and ALS means "aligned in site"; (B) alignment results for CuO NWs at 7 V and at (C) 14 V and at different applied frequencies.

Statistical results are summarized in Figure 4.9B,C revealing several interesting points. On one hand, an increasing number of ALS NWs is usually obtained at higher

voltages. In terms of DEP force (F_{DEP}), there is a strong dependence with the bias effective voltage squared explaining this effect and predicting a larger number of NWs aligned between electrodes.

On the other hand, the DEP efficiency increases with frequency until reaching a maximum value of ALS NWs in the range of 1-10 kHz. Then, a downwards trend occurs when the highest frequencies are applied. As described in Chapter 2, the real part of the Claussius-Mossotti factor (Re[f_{cm}]) gives information about the polarization of the structure and depends on the electrical properties of the nanostructure and the solvent, helping us to predict the optimal frequencies for alignment purposes. Figure 4.10A shows a representation of Re[f_{cm}] versus frequency for a single NW in EtOH under two relative orientations with respect to the electric field. The solvent and CuO physical parameters used in the calculation are $\varepsilon_{CuO} = 25 \cdot \varepsilon_0$, for the NW; $\sigma_{EtOH} = 1.00 \cdot 10^{-7}$ S/m and $\varepsilon_{EtOH} = 24.3 \cdot \varepsilon_0$, where ε_0 is the vacuum permittivity. The conductivity of a single CuO NW is estimated by trapping a single NW between AZO electrodes. In order to improve the electrical contact and avoid voltage drops between NW and electrode, a second lithographic step is carried out to cover the NW tips with a 100-nm thick Al film by room-temperature sputtering, followed by a lift-off process. From its electrical characteristics, a conductivity value (σ_{CuO}) of $1.9 \cdot 10^{-3}$ S/m is estimated.

A sudden decrease in Re[f_{cm}] is clearly observed at high frequencies, especially for those NWs oriented parallel to the electric field (0º in this Figure), which reduces the number of attracted NWs on alignment sites. This effect agrees with the experimental results in Figure 4.9B,C. On the other hand, despite the fact that the Re[f_{cm}] curve predicts higher F_{DEP} at low frequencies, experimental results show that these conditions are not suitable for NW trapping, leading to an increase of NAL NWs in comparison to ALS and AL NWs. It was reported before that the application of very low frequencies or high voltages may give rise to unexpected effects, such as electrode damage or bubble formation because of the solvent electrolysis.[14, 15] The observation of the surface by using an optical microscopy during DEP reveals a continuous bubble formation that greatly hinders NW trapping on the electrode gap.

The diameter distribution of CuO NWs dispersed on a piece of Si wafer (reference curve in Figure 4.10B) is compared with those distributions of ALS NWs assembled by

DEP carried out at a V_{RMS} of 14 V and different frequencies ranged between 0.1 to 1000 kHz. These curves follow a Gaussian function, whose center is shifted toward lower average diameters as the frequency decreases. The most common diameter value found in the NW reference dispersion is around 450 nm, whereas the other distributions show that DEP tends to trap NWs with lower diameters. The shortest diameters obtained are ranged between 230 and 300 nm at 1 kHz.

This is an important conclusion since DEP can help to discriminate between NWs with different sizes. Additionally, NWs with lower diameter are usually more desirable for sensor developing because of the higher surface-to-volume ratio.

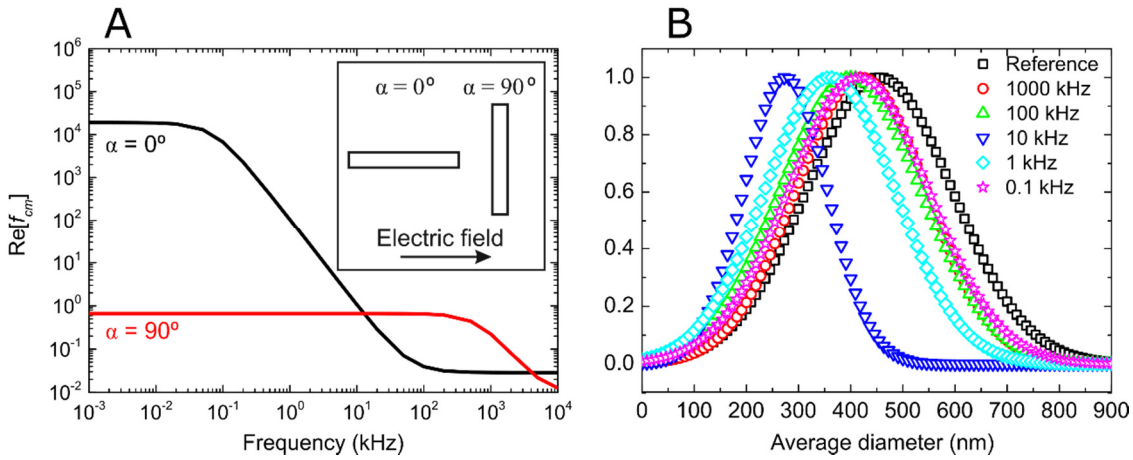

Figure 4.10. (A) Real part of the Clausius-Mossotti factor for two NW orientations, 0° (parallel to the electric field) and 90° (perpendicular to the electric field), as represented in the inset of this figure; (B) ALS diameter distributions found at different DEP frequencies and a V_{RMS} of 14 V, compared to the as-dispersed CuO NWs (reference).

4.1.5. Electro-optical characteristics of AZO/CuO NW/AZO heterojunction

To investigate the electro-optical characteristics of CuO NWs, a AZO/CuO/AZO heterojunction is fabricated by means of dielectrophoretic alignment. For this aim, a 50 nm thick AZO film is deposited on a SiO_2(200 nm)/Si substrate by rf-magnetron sputtering. Besides its high n-type conductivity, the interest of using AZO in these devices is based on its better mechanical resistance and adherence to the substrate in comparison to typical metallic electrodes. In addition, one can take advantage of the AZO high transparency in the visible spectral range for the precise alignment of NWs in transparent electronic.

Parallel electrodes with 4-µm spacing are defined by optical lithography and chemical etching to provide a large area for multiple NW alignment. DEP is performed by applying a sinusoidal waveform of V_{RMS} = 6 V and f = 100 kHz with a function generator. The scheme of the final light sensing device can be observed in Figure 4.11. As shown in the previous Section, NWs follow the electric field gradient and are attracted to the gap between electrodes.

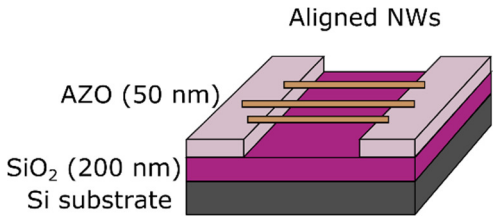

Figure 4.11. Scheme of the light sensing device.

Resultant NW density on the parallel electrodes is about 65–80 NWs per millimeter length. After DEP process, the structure shows high stability in liquid mediums. Finally, samples are annealed at 170 ºC for 30 s in air ambient to improve the electrical contact of the junctions between the NWs and the AZO electrodes.

I-V characteristics are measured after device processing. The curves present a rectifying behavior likely induced by the n-p-n double junction between AZO and the CuO NW (Figure 4.12A). In fact, if CuO NWs are replaced by ZnO NWs, the device exhibits non-rectifying behavior due to the n-type doping type of ZnO NWs.

The current delivered by the AZO/CuO NW/AZO structure noticeably increases when it is illuminated with a halogen lamp of 4.54 mW/cm^2 power density. Furthermore, the response obtained at constant bias voltages (Figure 4.12B) shows fast transients except for the erratic behavior of the dark current at 4.5 V caused by the noise level of the setup. Due to the different doping type, a space charge region (SCR) is expected to be built at the junctions between the NW and the AZO electrodes maximizing the electric field strength and contributing to promptly separate carriers upon photogeneration.

In semiconductor photodetector theory, time response in p-n structures is predicted to be limited by transit time across SCRs and by diffusion times in the neutral regions around the junction.[16] However, in practice, these theoretical times are usually shorter

than the charge and discharge times of the parasitic capacitances.[17] On the other hand, in detectors with uniform electric field profiles, i.e. photoconductive-type detectors, time response is limited by the generation-recombination times of the photocarriers which, in the presence of trapping centers, can become very long.[18] Thus, the fast response found in the structure under study may be related to the alignment of p-type NWs between n-type electrodes, which yields series-opposing photodiodes capable of minimizing the effect of trapping centers. Another complementary explanation of the fast response is that, unlike other metal oxide NWs, surface states in CuO may act as recombination centers, helping to speed up charge recombination after illumination at neutral regions. Femtosecond transient absorption spectroscopy studies have also demonstrated relaxation times in the picosecond range in p-type CuO NWs, which somehow proves the fast dynamic behavior of photocarriers in this material.[19]

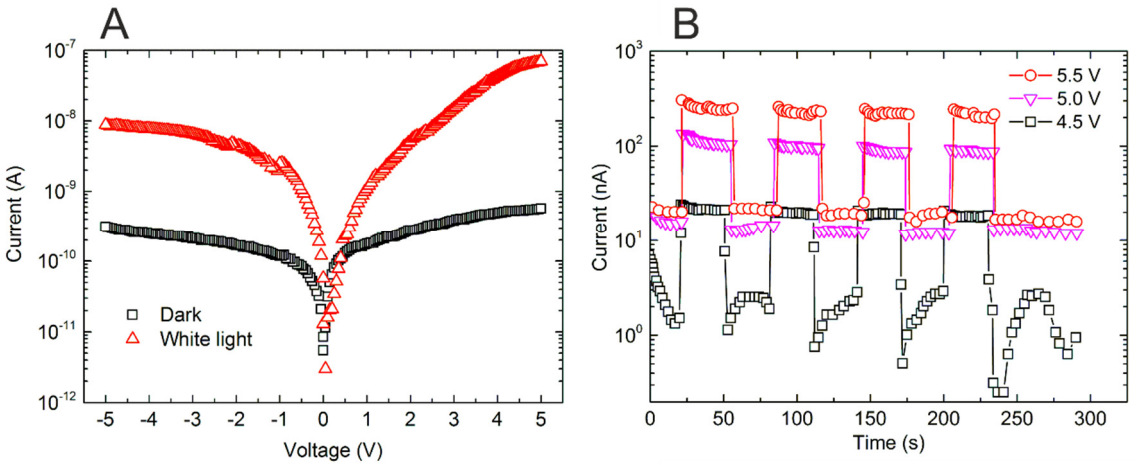

Figure 4.12. (A) *I-V* characteristics of the assembled CuO NWs in darkness and under white light illumination; (B) current transients obtained under pulsed illumination taken at bias voltages of 4.5, 5.0, and 5.5 V.

4.1.6. Time response of AZO/CuO NW/AZO heterojunctions

One important parameter to characterize the photodetector is the time response of the device to the light stimulus. To further investigate this time response, the structure is illuminated with 100 μs pulses from a red (peak wavelength = 630 nm, power density = 0.76 mW/cm^2) light emitting diode (LED) at a repetition rate of 1 kHz by using a function generator. The device is connected to a 5 V external power supply and a load resistance

(R_L) to measure the photocurrent pulses in a Tektronix TDS210 oscilloscope. The response pulses followed first-order exponentials for rise and decay portions of the curve with time constants in the few microsecond level. An example is shown in the inset of Figure 4.13A, for a R_L of 510 kΩ.

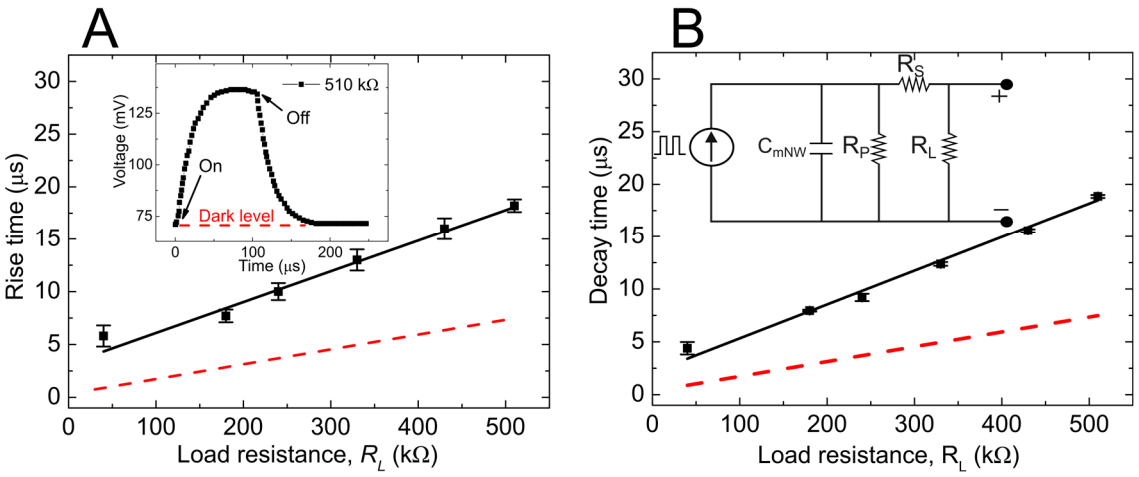

Figure 4.13. (A) Rise time as a function of R_L. Inset: a registered pulse obtained at R_L = 510 kΩ; (B) decay time as a function of load resistance. Inset: equivalent circuit. The red dashed lines in both figures represent the RC product calculated from the equivalent circuit model.

The time constants, represented in Figure 4.13, are estimated using exponential growth and decay fittings for pulses obtained with different R_L. The value of the time constants reduces as R_L diminishes, indicating that the device response is limited by the resistance-capacitance (RC) product of the equivalent circuit. To confirm this, a LCR meter is used at a V_{RMS} of 50 mV and 1 kHz under a DC bias of 5 V. Parallel (R_P) and series (R_S) resistances are estimated to be 60 MΩ and 0.024 MΩ, respectively. Since R_S is significantly lower than R_P, the effect of the latter can be neglected to calculate the RC constant of the circuit according to the diode model shown in the inset of Figure 4.13B.

The R_S value has its origin in the AZO electrode resistivity and it hardly changes after NW deposition. Differential capacitance between both electrodes before and after NW alignment allows to determine the contribution of the NWs to the total capacitance (C_{mNW}) resulting in C_{mNW} =14 pF. This capacitance is attributed to the sum of capacitors

formed at the contact points between NWs and DEP electrodes. Dividing by the total number of NWs in the device (around 500 NWs observed by optical microscopy), one can estimate the capacitance per each aligned NW in 28 fF. This value is close to 21 fF, a value previously reported for a single CuO NW.[20]

The RC product, calculated from $(R_S + R_L)\cdot C_{mNW}$, is represented against R_L in red dashed lines in Figures 4.13, showing a fairly good correlation between the model and the experimental data. This means that, unlike other metal oxide NW photodetectors, the time response is mainly limited by the RC product without traces of surface persistent effects. The small misfit between the model curve and the experimental data is attributed to parasitic capacitances between the AZO electrodes and the floating substrate through the dielectric layer.

The capacitance between the Si substrate and the AZO electrodes has been measured in different devices using a backside contact. Values between 20 and 55 pF are respectively found in depletion and accumulation biasing conditions for the 200-nm thick SiO_2 intermediate layer. Despite vertical conduction through the oxide is measured to be null, these capacitors associated to the AZO electrodes may slow down the response speed since their capacitance is comparable or even larger than C_{mNW}.

4.1.7. Responsivity

The spectral responsivity of the device, defined as the ratio between the photocurrent and the power absorbed by the NWs, is estimated from the pulse obtained with a R_L of 510 kΩ (inset of Figure 4.13A). The photocurrent can be obtained from the increase of the voltage drop in the load resistance during the illumination. From the Ohm's law, the photocurrent is calculated, being 140 nA. On the other hand, the power absorbed by the NWs is estimated from the LED power density multiplied by the NW sensor area: $P_{LED}\cdot A_{sensor}$, where $P_{LED} = 0.76\ mW/cm^2$ and $A_{sensor} = 2\cdot 10^{-5} cm^2$. Thus, the absorbed power is $1.5\cdot 10^{-5}$ mW and the responsivity is 9.3 A/W.

4.2. Zinc oxide nanowire devices

4.2.1. Introduction

In this Section, we provide insights on the integration of ZnO NWs on transparent substrates by DEP for the fabrication of UV photodetectors. Typically, to integrate the NWs between electrodes, the nanostructures are separated from the substrate by sonication and dispersed in a liquid medium, as has been shown in the previous Section for CuO NWs. To enhance the NW concentration and get rid of possible impurities, a sedimentation step is followed prior to the DEP process. A calibration curve is performed to estimate the NW concentration in further experiments by using transmittance monitoring.

We also study new modifications of the dielectrophoretic process, leading to develop a new home-made DEP system in order to optimize the whole process and to increase the NW trapping probability. A monitoring system is included in this work to estimate the number of trapped NWs for the assessment of the alignment quality in real time. As a case of study, we choose ZnO NWs to take advantage of their interesting electro-optical characteristics and to fabricate UV light sensing elements. The DEP electrodes are made of AZO, a transparent conductive oxide, giving rise to chips with fully transparent characteristics. The uniformity, speed, and spectral responsivity are measured in the fabricated sensors. The transparency of the substrate and the electrodes allows the device operation under front- and back-illumination, a useful property for flip-chip bonding integration.[21]

4.2.2. Sedimentation study: purification and concentration of zinc oxide nanowire dispersions

ZnO NWs are obtained by vapor phase transport, as described in Chapter 3. The NW powder is weighed and immersed in a liquid medium and further sonicated in an ultrasonic bath for times between 30 and 180 s to homogenize the dispersion. Despite being an easy procedure, this approach produces large amounts of ZnO clusters coming from the seed layer, which may influence negatively on the DEP process by short-circuiting the electrodes. For this reason, a purification step is developed in order to improve the quality of the dispersions. Simple sedimentation and continuous

transmittance monitoring are proposed in this work to allow accurate control for the production of uniform and purified NW dispersions.

4.2.2.1. Physics of sedimentation

The sedimentation rate of particles depends on the balance of different forces.[22] The net force on each particle comprises gravitational force (F_g), which is directed downwards; and buoyancy (F_b) and drag (F_d) forces, which are oriented upwards, as shown in Figure 4.14A. They are defined as:

$$F_b = V \cdot \rho_m \cdot g \tag{4.1}$$

$$F_g = m \cdot g \tag{4.2}$$

$$F_d = f_0 \cdot v_t = 6 \cdot \pi \cdot \mu \cdot v_t \tag{4.3}$$

where m, V, g, ρ_m, ρ_{ZnO}, v_t and μ represent the particle mass, particle volume, gravity constant, medium and ZnO particle densities, terminal velocity and medium viscosity. The constant f_0 is known as the frictional coefficient. According to the Stokes's law, these equations allow estimating v_t, which represents the speed of a falling sphere when the net force is zero (constant speed). Thus, this parameter can be obtained from the following equation:

$$v_t = \frac{V_{sp} \cdot g \cdot (\rho_{ZnO} - \rho_m)}{f_0} \tag{4.4}$$

where V_{sp} is the volume of the sphere. According to hydrodynamics, f_0 is dependent on the particle morphology. For the long-rod case, F_d is redefined as $F_d = f \cdot v_t$ where f becomes:

$$f = \frac{\left(2/3\right)^{1/3} A^{2/3}}{\ln(2 \cdot A)} \cdot f_0 \tag{4.5}$$

and A represents the aspect ratio between the length of the NW and its diameter. It is important to notice that f_0 is the frictional coefficient for a sphere of an equal volume. Taking into account the other two forces, F_b and F_g, v_t for NWs can be redefined as:

$$v_t = \frac{V_{NW} \cdot g \cdot (\rho_{ZnO} - \rho_m)}{f} \tag{4.6}$$

where V_{NW} is the volume of the NW. For equal NW and sphere volumes, differences in v_t for spheres and NWs are determined by the ratio between frictional coefficients (f/f_0). This ratio is always larger than 1 and accounts for the faster sedimentation of spheres.[22] The physical origin of this is related to the lower friction of the flowing spheres in the liquid solution.

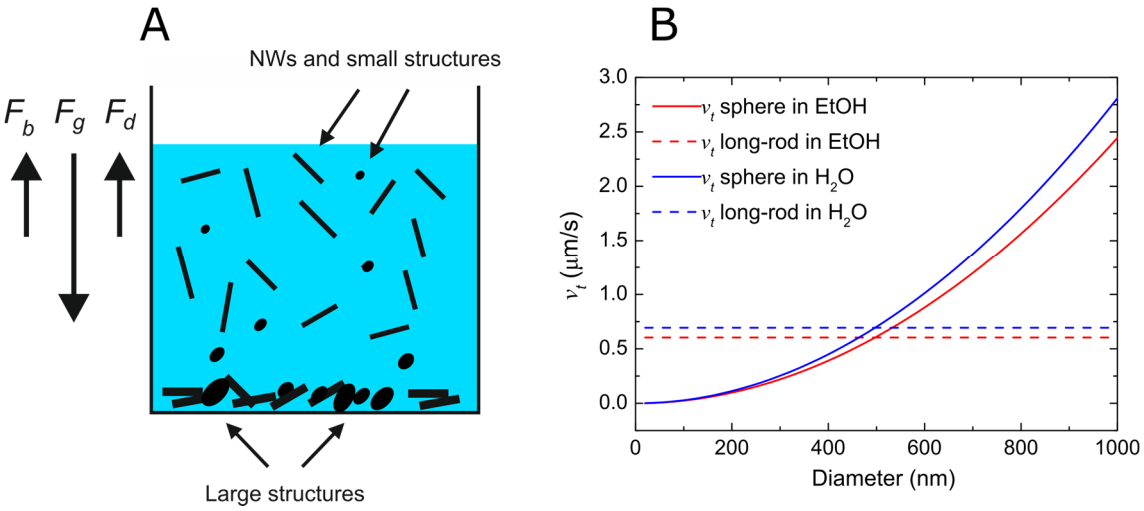

Figure 4.14. (A) Scheme of the forces involved during sedimentation, where NWs and other small structures remain in suspension; (B) terminal velocities for a sphere with different radii and a long-rod (ρ_{ZnO} = 5610 kg/m^3), with a length of 14 μm and a diameter of 190 nm, in EtOH (ρ = 790 kg/m^3 and μ = 10.7×10^{-4} Pa·s) and in H_2O (ρ = 990 kg/m^3 and μ = 8.90×10^{-4} Pa·s).

To apply this model to the prepared dispersions, an estimation of the average size of the ZnO NWs is previously made using SEM images of drop-casted NWs on a Si substrate. The dispersion under study shows average length and diameter of 14 ± 5 μm and 190 ± 30 nm, respectively. Thus, the average aspect ratio of those NWs is approximately 75 which yields an f/f_0 ratio equals to 3.3. This means that spheres with equal (equivalent diameter = 900 nm) or larger volume are expected to fall down at least

3.3 times faster than NWs. As an example, spherical particles with a diameter of 2 μm will sediment 16 times faster than the NW. In Figure 4.14B, we plot v_t for spherical particles (solid lines) of different diameters in two solvents, H_2O and EtOH, and compare with v_t for the average NW (dashed lines). From those graphs, it is concluded that spherical particles with diameters larger than 500 nm are expected to suffer a faster sedimentation process than the NWs. This fact has been used to eliminate impurities coming out of the substrate during the sonication process (purification step). In an ideal dispersion in which all the impurities were spherical, 500 nm would be the critical diameter that one may expect to filter out. It is important to notice that the alternative use of membrane filters with similar porous sizes would yield very low NW concentrations in the purified dispersions caused by the accumulation of NWs in the sidewalls of the pores which may end up clogging them. Therefore, although real dispersions usually contain impurities with random morphologies, this filtration process is seen as an effective method to remove impurities up to a submicron level while keeping large NW concentrations available for DEP processes.

Despite the different physical properties of EtOH and H_2O, i.e. viscosity and density, Figure 4.14B shows that both solvents give rise to similar terminal velocities. However, in practice, NWs can show different velocities in both solvents due to the surface interactions among them.

4.2.2.2. Purification of zinc oxide nanowire dispersions

ZnO NW dispersions are prepared in H_2O and EtOH to validate the use of sedimentation for the preparation of homogeneous NW dispersions. To compare the sedimentation rates, an aliquot of each dispersion is introduced in quartz cuvettes, monitoring changes in the absorbance (*Abs*) for 1 hour in a UV/visible spectrophotometer at a constant wavelength of 400 nm. Figure 4.15A represents different kinetic curves after baseline subtraction (EtOH or H_2O) for dispersions with different concentrations ranging from 80 to 380 mg/L. As expected, the measured *Abs* increases with concentration due to the increasing number of scattering centers. Interestingly, the initial values show larger *Abs* in EtOH than in H_2O, even at the first data points. It is hypothesized that this happens as a result of the stronger interaction between NWs in H_2O, which tend to form larger aggregates, yielding a faster sedimentation rate compared to EtOH. In both solvents, the

time-dependent absorbance curves can be optimally fitted with bi-exponential functions indicating the presence of structures inside the dispersion with different characteristic sizes. The shorter time constant ranges from 210 to 420 s and is related to the sedimentation of large particles, either particles coming from the nucleation layer in the substrate or NW aggregates formed during the dispersion preparation. The longer time constant of the fitting is attributed to the sedimentation of single NWs and ranges from 1300 to 4000 s.

From the analysis of the absorbance at the end of the 1 h process, it is found that the concentration of NWs in EtOH is higher than in H_2O. As a larger concentration increases the trapping probability in the DEP process, the NW integration is only performed on dispersions prepared from EtOH solvent. Besides, the final NW concentrations are quite stable over the time needed to perform the DEP alignment (around 1 min), ensuring the homogeneity of the NW dispersion during the whole DEP process.

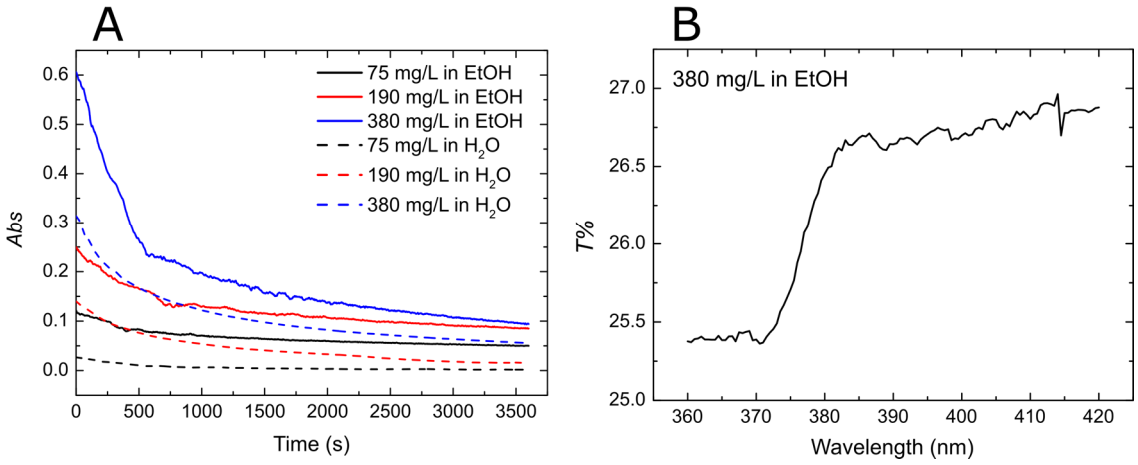

Figure 4.15. (A) Kinetic measurement of the absorbance for as-sonicated dispersions with different concentrations between 75 and 380 mg/L for EtOH and H_2O; (B) transmission measurement of the as-sonicated ZnO dispersion in EtOH with a concentration of 380 mg/L in ZnO. The scan rate is set at 300 nm/min.

The spectral characteristic of the optical transmittances (*T%*) is analyzed using a UV/visible spectrophotometer. A fast scan (300 nm/min) from 420 to 360 nm is performed in the NW/EtOH dispersion with a ZnO concentration of 380 mg/L. As shown in Figure 4.15B, *T%* presents a fairly constant value around 27% above the bandgap

wavelength of ZnO (λ = 380 nm), as a result of the optical losses caused by scattering phenomena. Below that wavelength, ZnO absorption contributes to reduce the *T%* down to 25.5%, a loss that is significantly smaller than those caused by scattering. Thus, both UV and visible light extinctions seem to be dominated by the scattering phenomena, a point that it is also confirmed by analyzing dispersions with different concentrations.

4.2.2.3. Concentration of ZnO NW dispersions and calibration

After the sedimentation step described above, the supernatant is transferred to another container and heated up near the EtOH boiling point in order to evaporate part of the solvent and increase the concentration. A highly concentrated dispersion with a final *Abs* of 0.29 is obtained at a wavelength of 400 nm. The number of NWs within a 1-µL volume is estimated from microscopic images to calculate the NW concentration, yielding a value of 790 NWs/µL. Successive dilutions of this concentrated dispersion are performed and characterized over 1 h. An estimation of the number of NWs in these aliquots obtained from microscopic analysis is represented as a function of absorbance (Figure 4.16). This counting process is repeated three times for each sample in order to reduce the statistical error in the number of NWs. The calibration curve obtained from those experimental data follows a linear relationship between *Abs* and concentration with a coefficient of determination (R^2) of 0.9985. This behavior follows the Lambert-Beer's law which predicts that *Abs* is equal to $\sigma \cdot c \cdot l$ where σ, c and l are the extinction coefficient, the NW concentration, and the optical path length (1 cm), respectively.[23] From the slope of the linear fitting, a σ value of 3.26×10^{-4} $\mu L \cdot NW^{-1} \cdot cm^{-1}$ is obtained. Taking into account the average size of the NWs showed above (length and diameter of 14 ± 5 µm and 190 ± 30 nm, respectively), this σ corresponds to a value of 12300 $L \cdot mol^{-1} \cdot cm^{-1}$. It is important to notice that, although NW extinction coefficient accounts for all optical losses,[24] it is dominated by scattering, as explained before.

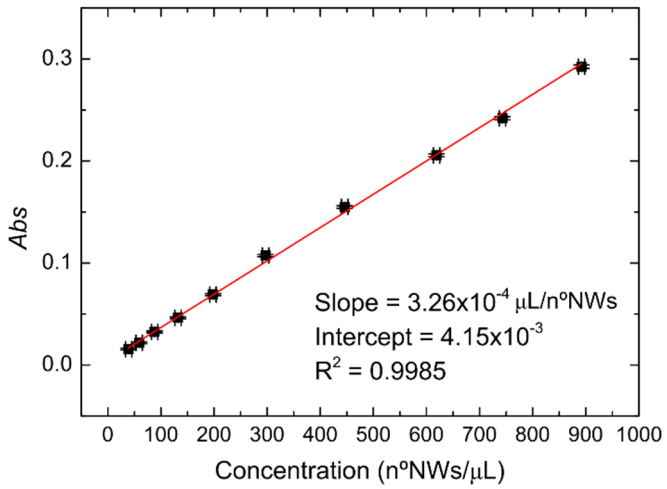

Figure 4.16. Calibration curve obtained from different purified dispersions. Concentration error is calculated as the standard deviation obtained from three samples of the same dispersion and plotted as horizontal error bars. Vertical error bars are calculated from 3 measurements for each sample.

4.2.3. Continuous-flow dielectrophoretic system

A continuous-flow dielectrophoretic system is developed in our laboratory to trap NWs between coplanar electrodes and improve the results obtained by the drop-casting method.

In this home-made system (Figure 4.17), the receptor chips are mounted onto a polytetrafluoroethylene- (PTFE) made cell. This includes an O-ring where the chip is attached downwards. The inner diameter of the O-ring is about 5 mm. Total volume of the microfluidic cell is 20 µL. NW dispersions are loaded into a syringe cartridge (around 7 mL) and pumped into the system by a peristaltic pump at a speed of 6 mL/min. Prior to reaching the DEP cell, nanostructures pass through a filter (200 µm pore size) to remove possible dust particles which may block the tubing.

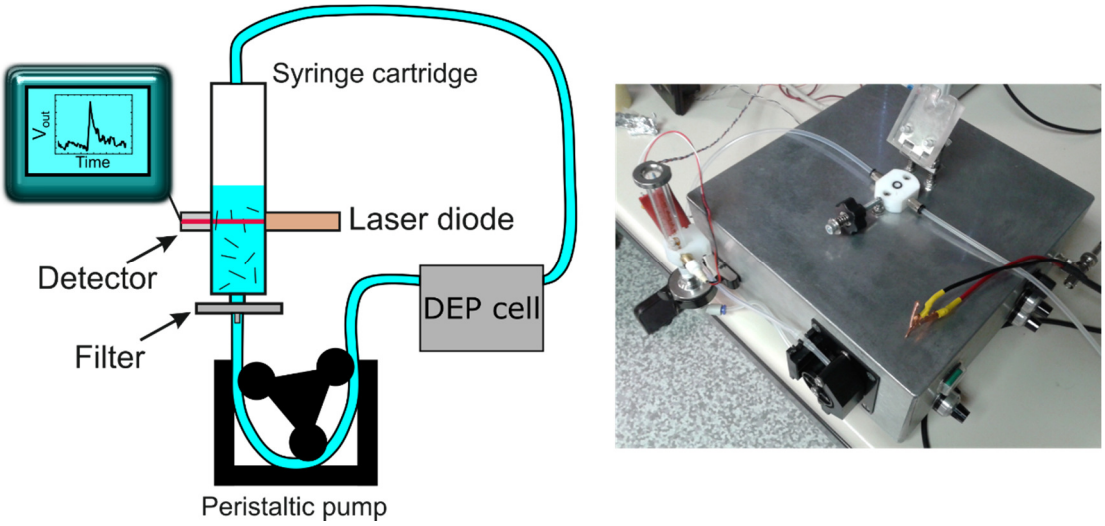

Figure 4.17. Scheme of the home-made DEP system developed in our laboratory.

A basic optical system is also developed to measure the scattered light produced by the nanostructures within the syringe cartridge to monitor changes in the NW concentration. This system consists of a red laser diode (λ_p = 650 nm) and an off-axis phototransistor assembled around the cartridge. Output analog signal is monitored by serial communication with a microcontroller board (Arduino UNO, ATmega328 microprocessor) and shown in a computer.

In comparison to the drop-casting method used for CuO NWs, the system produces a better surface quality after the process. The drop-casting method leaves NW leftovers after drying out, randomly distributed across the surface and far from the assembling sites. Those NWs are not attracted to the assembling sites because of their large distance from the site and precipitate on the surface once the droplet is fully evaporated. On the other hand, the up-side-down configuration of the substrate on the DEP cell allows the receptor chip to host only those NWs trapped under the action of the DEP force, while the rest remains in the fluid flowing underneath. Figure 4.18 shows the comparison between both methods. For both cases, the applied AC signal is the same.

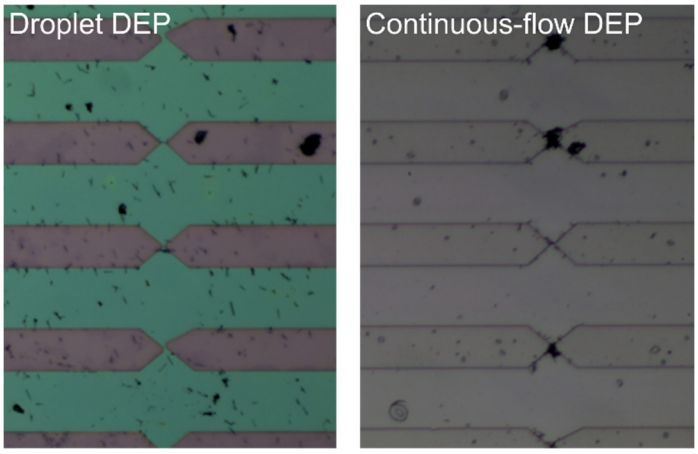

Figure 4.18. Comparison between drop-casting DEP and DEP using the home-made system.

4.2.3.1. Preliminary characterization of the system

To estimate NW losses in the whole system, the optical characteristics of the input and the output dispersions are compared in the absence of DEP bias. A 5 mL volume of a NW dispersion with a 450 NWs/µL concentration is loaded in the syringe cartridge and pumped into the system. Several aliquots of the fluid are extracted from different parts of the system and their absorbance measured in the spectrophotometer. The number of NWs is estimated from the calibration curve obtained in the previous Section. As shown in Table 4.1, there is a decrease in the number of NWs as the dispersion flows through the system. The 200-µm pore size filter placed at the output of the syringe cartridge blocks around 27 % of the NWs, obtaining a concentration of 330 NWs/µL. After the DEP cell, the concentration measured in a single run is about 220 NWs/µL, i.e. a 49% of the original concentration. For that reason, rinsing steps are introduced to clean the system after each run. A rinsing step using a 2 mL volume of pure EtOH allows extracting 16 % of the NWs. Successive rinsing steps release 2 % and 0 %, respectively. The total amount of NWs that make all the way to the output is about 67% $\left(\left(\left(220+70+10\right)/450\right)\cdot 100\right)$ of the original concentration that, along with the 27 % blocked in the filter, produced a total percentage of 94 %, leaving a remaining 6 % with an unclear location. This apparent uncertainty is believed to be caused by the accumulation of errors in the estimations of the different concentrations along the system through the absorbance measurements.

From this experiment, we conclude that three rinsing steps are at least required to remove all the remaining nanostructures from the tubing after a standard DEP process. Those steps are included in the DEP processes presented later.

Table 4.1. Summary of the absorbance measurements in the DEP system (first column) and estimation of the corresponding NW losses from calibration curve in Figure 4.16 (second column). The third column shows the percentage of NW concentration with respect to the initial dispersion. First row includes the original absorbance prior to cartridge load. Second and third rows provide data obtained before and after the DEP cell, respectively. The last three rows show values taken after successive rinsing steps (R.S.).

	Abs	Conc. (NWs/µL)	Percentage of NW conc.
Original	0.155	450	100
Before DEP cell	0.114	330	73
After DEP cell	0.078	220	49
1st R.S.	0.027	70	16
2nd R.S.	0.005	10	2
3rd R.S.	0.002	-	0

4.2.3.2. In-situ concentration control

As mentioned above, to study the concentration of the NW dispersion inside the syringe cartridge during the pumping of the NW dispersion, a basic optical system is developed to measure the scattered light (see Figure 4.17). The red laser and the detector are assembled forming an angle of 90º.

The syringe cartridge is initially filled with 4.5 mL of EtOH. The peristaltic pump is turned on to introduce and to recirculate the solvent in the system. After 2 minutes, 2 mL of EtOH are added without producing any change in the output signal. Successive 1 mL volumes of a NW dispersion (450 NWs/µL) are added every 4 minutes. Upon NW dispersion introduction, there is a fast signal increase due to the larger amount of scattered light impinging onto the detector (Figure 4.19). After reaching a peak value, the signal decreases as the NWs disperse homogeneously inside the solvent producing a plateau in the output signal after 100 s. As the experiment continues, the plateau level increases as new drops are introduced in the cartridge since the NW concentration in the system becomes larger. After 4 NW-containing droplets, the estimated NW concentration in the dispersion is about 170 NWs/µL.

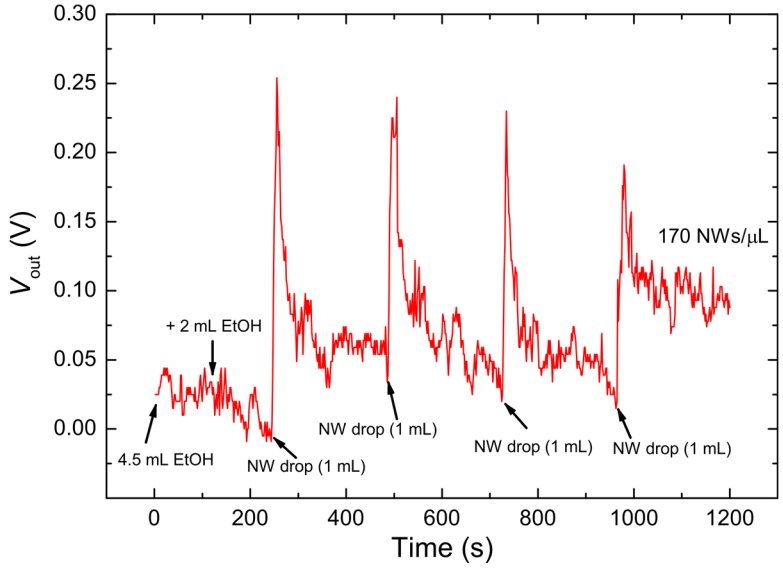

Figure 4.19. Analog signal obtained during the drop by drop increase of the ZnO NW concentration in the syringe cartridge.

4.2.4. Nanowire alignment by dielectrophoresis and real-time monitoring

Once the DEP system is characterized, we study the dielectrophoretic alignment of ZnO NWs and present an electric tool to monitor the number of NWs trapped between electrodes based on the impedance changes produced during DEP. This tool can also detect anomalies during the process.

The devices are fabricated using transparent chips with AZO electrodes prepared by optical lithography. The electrodes are built from the deposition of a 300-nm thick AZO layer by magnetron sputtering. The defined pattern includes an array of alignment sites connected to a couple of bus bars, where the AC bias is applied. The distance between electrodes varies from 4 μm to 8 μm and its shape around the assembling site can be observed in Figure 4.20. The O-ring inner volume can comprise up to 20 alignment sites with the photolithography mask used for the experiments.

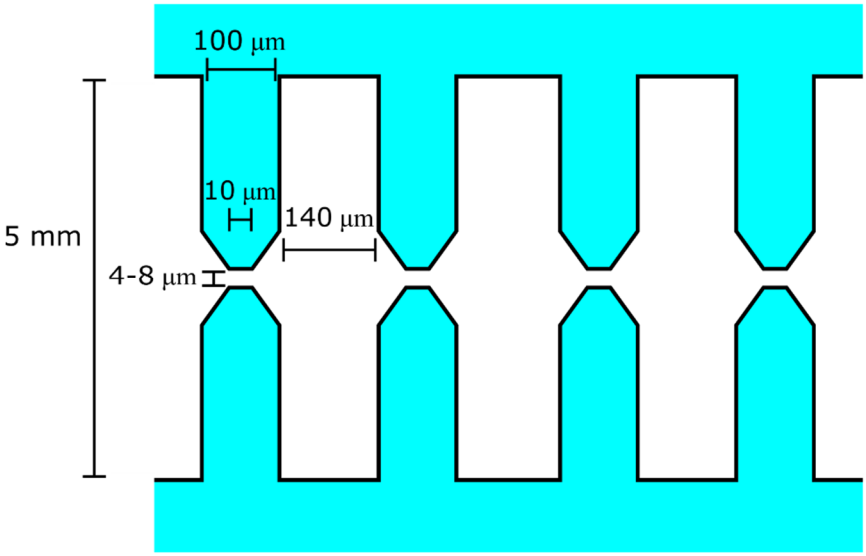

Figure 4.20. Scheme of the array of AZO electrodes.

Thanks to the high visible transparency of AZO, the electrodes present a transmittance value larger than 80 % in the full visible range and give final transparent look to the whole receptor chip.

Using the described chips, DEP processes are performed at 100 kHz frequency. The microscopic analysis of the surface reveals ZnO NWs trapped on the assembling sites. The low specific area of the assembling sites, which typically ranges from 8 to 30 μm^2, preserves the high transparency to the naked eye of the final sensors, as shown in Figure 4.21A. The number of NWs per site can be adjusted by changing the bias voltage, obtaining either a fully covered site (Figure 4.21B, left) or single NW trapping (Figure 4.21B, right).

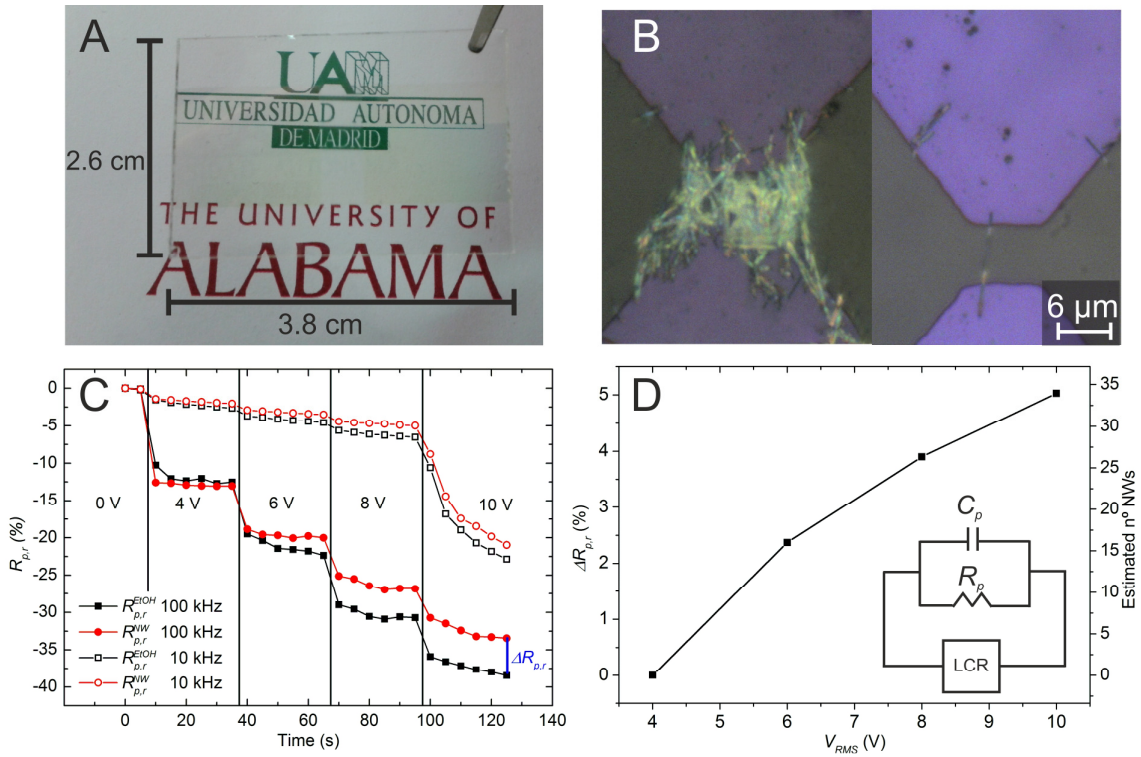

Figure 4.21. (A) Picture of one of the sensors including AZO electrodes and assembled NWs; (B) Optical microscope images of the assembling sites. Left-hand side picture shows one of the assembling sites fully covered with trapped NWs, whereas right-hand side picture exhibits a single NW trapping event in the assembly area; (C) Relative changes of the parallel resistance $(R_{p,r})$ as the bias voltage is increased from 4 to 10 V at 10 KHz (open symbols) and 100 kHz (solid symbols). The bias scan is performed in pure EtOH ($R_{p,r}^{EtOH}$, black) and in NW dispersion ($R_{p,r}^{NW}$,red) ; (D) $\Delta R_{p,r}(\%)$ difference measured at 100 kHz. The number of NWs aligned at every V_{RMS}, and estimated through independent DEP processes, is included at the right-most y axis. The inset represents a diagram of the electrical model used to assist the understanding of the monitoring process.

To investigate the use of the parallel resistance as a monitoring tool, sinusoidal waveforms with V_{RMS} ranged between 4 and 10 V and frequencies of either 10 or 100 kHz are applied between electrodes to generate the DEP signal using an LCR meter while measuring the parallel resistance (Figure 4.21C). The electrical model used in the setup is shown in the inset of Figure 4.21D. The resistance associated to the electrode is not taken into account since its value is much lower than those introduced by the NWs, as is demonstrated in Section 4.1.6. The variations of the parallel resistance dominate the variations of the total impedance, whereas parallel capacitance presents quite stable values during the experiments limited by the high parasitic capacitance of the device (~10 pF) in comparison to typical NW capacitance values at the femtofarad level, as shown in

Section 4.1.6. This limiting capacitance is the result of the large electrode area (2-3 cm^2) and it is difficult to minimize in the present setup.

The parallel resistance variations are studied during the DEP process at increasing bias voltages to find out the threshold voltage at which NW trapping occurs. Starting at 4 V, the V_{RMS} is increased 2 V every 30 s, while the relative changes of the parallel resistance are monitored. These relative changes are quantified by using:

$$R_{p,r}(\%) = \left(R_p - R_{p,o}\right)\cdot 100/R_{p,o} \tag{4.7}$$

where $R_{p,o}$ is the parallel resistance at the beginning of the scan and R_p is the parallel resistance measured in real time. The experiment is also performed in pure EtOH, allowing the extraction of another $R_{p,r}$ curve for comparison purposes. As can be seen in Figure 4.21C, $R_{p,r}$ presents a sudden downwards reduction every time V_{RMS} is increased, either in EtOH or in NW dispersions. The reduction in parallel resistance is attributed to the finite exchange current density between electrodes and solvent ruled by the electrical double-layer impedance. The super-linear relationship between the current density and the applied bias causes a reduction of the parallel resistance as the bias amplitude increases. As a result of NW trapping, the interface becomes more inhomogeneous, diminishing the charge exchange and making the changes in parallel resistance less pronounced over time. This effect produces an effective deviation of the curve taken in the DEP process compared to that found in pure EtOH. This deviation can be quantified from the difference between the relative changes $\left(\Delta R_{p,r}(\%) = R_{p,r}^{NW} - R_{p,r}^{EtOH}\right)$. Figure 4.21D presents $\Delta R_{p,r}(\%)$ as a function of the bias voltage for a DEP process at 100 kHz, along with the number of NWs trapped in the alignment sites, estimated from the microscopic analysis. The analysis of the difference at this frequency shows that the onset of the deviation begins at 6 V. A DEP process carried out at 6 V and studied under the microscopy shows evidences of NW trapping in contrast to those performed at lower bias. Furthermore, the increasing difference between both curves as the bias voltage increases suggests the assembly of a larger amount of NWs. Careful examination of the trapping sites after constant AC bias processes also confirms this point, corroborating the adequateness of the method to identify NW deposition in the DEP cell.

From the displayed results, it can be observed that the method is more sensitive to NW trapping at 100 kHz than at 10 kHz due to the larger decay rate of the parallel resistance as the bias is increased. The reason is that, at lower frequencies, the exchange current density is screened by the ion rearrangement in the electrical double layer causing smaller changes in the parallel resistance as the bias increases. In each half of the cycle of the applied potential, the double layer has enough time to be built, giving rise to a potential drop across the double layer. On the contrary, at higher frequencies, the double layer has less time to form since the mobility and diffusion of ions in the solution has a finite value. This reduction of the ion screening effect at higher frequencies produces a better scenario to measure the changes caused by the NW trapping.[25]

Despite the screening effect and the lower number of trapped NWs, the 10 kHz curves also present a parallel resistance reduction during DEP in the presence of NWs. Interestingly, an unexpected resistance drop is observed at a 10 V bias. To find out its origin, a pure EtOH droplet is drop-casted on the assembly area on one of the substrates while DEP bias is applied to the pair of electrodes. At those conditions, real-time optical microscopy reveals continuous bubble formation on those areas that leads to irreversible damage of the electrodes. Therefore, the resistance drop seems to be related to solvent electrolysis phenomena and hydrogen gas formation, which produce erosion and atom migration on the electrodes.[14, 15] This effect has been also found for CuO NWs in Section 4.1.4, when high voltages or low frequencies are applied. The strong current increase between both electrodes in that scenario gives rise to a significant reduction of the parallel resistance. Thus, the identification of this kind of anomalies during the DEP process is another practical advantage of the method.

4.2.5. Dark characteristics

At this point of the work, the last step comprises the electro-optical characterization in dark and under UV illumination of the transparent sensor chip to evaluate photocurrents, time responses and responsivities right after the DEP process. In all the electro-optic experiments, the sensor is illuminated using different light sources through an optical fiber and a lens, and a precision micropositioner to select the active area. These measurements are performed on a non-reflective surface to separate front and back contributions.

The current-voltage (*I-V*) characteristics of the devices are studied in dark by using a semiconductor parameter analyzer after a DEP alignment at a 100 kHz frequency and V_{RMS} of 6 V. The variation of the DEP time span under those conditions also leads to a different number of NWs per alignment site. The dependence of the dark current as a function of the DEP time is included in Figure 4.22. A DEP time of 30 s allows us to integrate about 3-5 NWs per site yielding low dark currents with non-linear characteristics as a function of voltage. The 1-min span produces an average number of bridging NWs per site in the range of 10-20 and a dark current value of about 1 nA at low voltages. A 3-min span produces high dark currents in the milliampere range with a linear *I-V* characteristic and a large average number of bridging NWs per site (>40). The insets of this Figure 4.22 provides SEM pictures of the NW alignment sites under those DEP times.

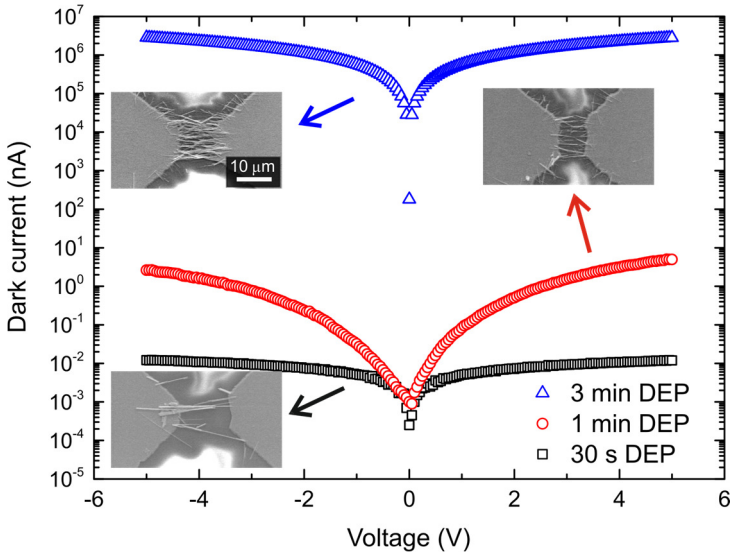

Figure 4.22. *I-V* characteristics exhibited by the samples in dark with NWs aligned under three different DEP times. Insets of this figure represents SEM images of the assembly sites. The magnification of the three images is the same. The author acknowledges the contribution of C. García Núñez in the realization of this experiment.

4.2.6. Optical response

Since for a light sensing device it is convenient to have a low dark current to obtain a strong light-to-dark current ratio, we focus our study on the optical response of the 30-s time span sample presented above.

As a first photoresponse experiment, a broadband deuterium lamp is used to produce a uniform power density over the active area of the device of about 1.4 μW/cm^2.

The curve obtained under illumination (Figure 4.23) shows a large current increase under positive and negative biases. It is important to notice that the light curves are the result of the illumination of the NWs on the assembling sites and that the selective illumination of the AZO electrodes does not produce any significant variation over the dark current. Interestingly, the light current increases super-linearly following a V^{γ} dependence where γ ranges from 2.3 to 2.8. The larger contrast between light and dark current as the bias increases is common in metal-semiconductor-metal photodiodes whose SCRs grow as the bias increases. The origin of that behavior can be found in the interface charge between the electrode surface and the NW, producing contact barriers whose lateral growth along the NW volume increases with the bias voltage. That increase leads to an enhancement of the active volume and an improvement of the collection efficiency of photogenerated charges inside the NWs. In contrast, pure photoconductors show a linear increase with bias ($\gamma = 1$) keeping the ratio between light current and dark current fairly constant.

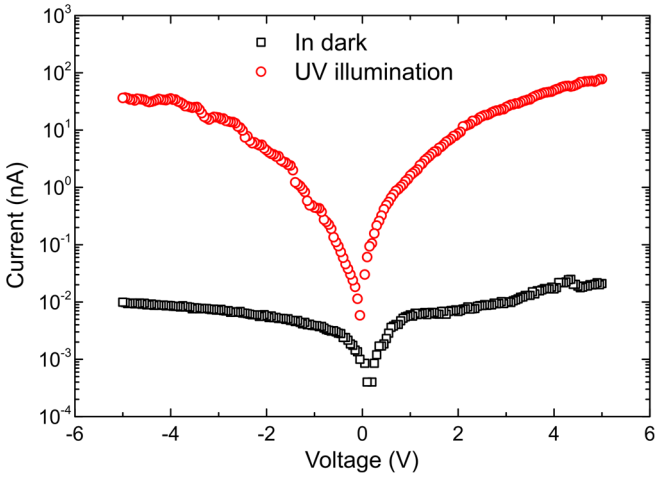

Figure 4.23. *I-V* characteristic exhibited by a sensor fabricated from a DEP process of 30 s in dark and under UV illumination.

4.2.7. Time response and response uniformity

To analyze the time response, the NW device is connected in series with a 1.5 MΩ load resistance and biased with a 5 V power supply. Light pulses from the deuterium light source are applied on the alignment sites. That resistance is chosen to be close to that exhibited by the sensor under illumination. The voltage drop across the load resistance is monitored using serial port communication with one of the 10-bit analog to digital converters in an ATmega328 microprocessor (see inset of Figure 4.24A for a scheme of

the electric circuit). The measured signal is transformed into photocurrent (I_{photo}) by subtracting the baseline to the output voltage and dividing by the load resistance. As shown in Figure 4.24A, the sensor exhibits a fast response with two characteristic time constants. The fast one is related to photo-generated charges promptly swept across the space-charge-region at the NW regions in contact with the electrodes. The long component (time constant ≈ 10 s) appears as a result of the surface electron release and the consequent oxygen desorption. This mechanism is dominant in ZnO photoconductors but becomes less important as the electric field distribution intensifies in the NW contact regions. The decay time also shows a fast response after light shutdown with a small persistent effect during a few seconds (time constant ≈ 5 s) limited by the re-adsorption of oxygen molecules.

To study the uniformity of the response across the active area, I_{photo} is also measured by scanning the assembly area using a precision micropositioner. Figure 4.24B shows a fairly symmetrical response from side to side of the assembly area. When the optical beam is centered, the whole system is illuminated and the maximum I_{photo} is obtained. The variability observed at the tails of the response curve is attributed to variations in the number of bridging NWs in the successive NW alignment sites. The inset of Figure 4.24B presents four consecutive sites covered by NWs at the center of the device.

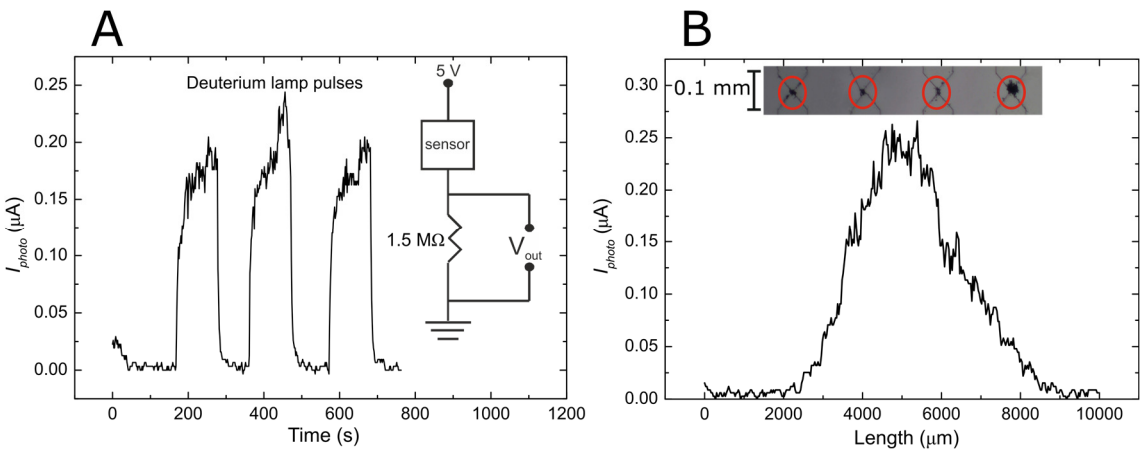

Figure 4.24. (A) Photocurrents as a function of time obtained after applying light pulses with a deuterium lamp. The inset represents a scheme of the setup used to measure the photocurrent signal. (B) Photocurrent measured at different positions along the assembly line at a bias voltage of 5 V.

4.2.8. Responsivity

Spectral responsivities (R_{photo}) of the sensor are also measured as a function of wavelength and DC bias voltage. A xenon lamp is coupled to a 1/8 m monochromator to select the wavelength (Figure 4.25). The responsivity values are obtained from:

$$R_{photo}(\lambda,V) = \frac{I_{photo}(\lambda,V)}{P(\lambda)} \tag{4.8}$$

where P is the optical power on the active area and I_{photo} is the photocurrent obtained by subtracting the baseline to the output voltage and dividing by the load resistance, 1.5 MΩ. The optical power parameter is estimated from the total power P_t using the following expression:

$$P(\lambda) = P_t(\lambda)\frac{A_{sensor}}{A_{beam}} \tag{4.9}$$

where A_{sensor} is the optical area of the sensor and A_{beam} is the area of the optical beam on the sensor surface (radius = 3.5 mm). The use of a lens at the end of the fiber produces a quite uniform power density across the entire beam, which enables the use of Equation 4.9 to estimate the power on the active areas. Indeed, studies of the uniformity of the beam at the output of the optical fiber reveal power fluctuations lower than 5 % across the beam area. Each assembling site has an area of 4×6 μm^2. Thus, the total area A_{sensor} is obtained multiplying that area by the total number of covered sites. For a device with 14 covered sites, as the one presented in the next case, the total area has a value of 336 μm^2.

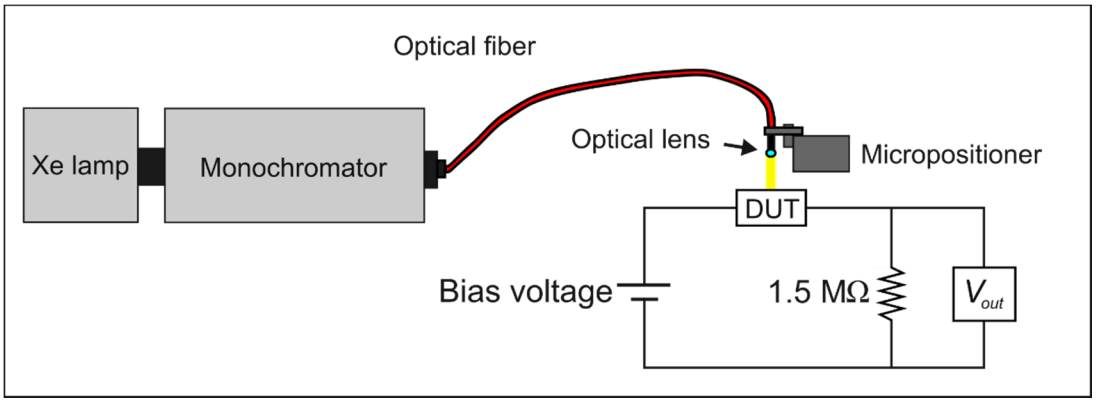

Figure 4.25. Scheme of the setup used for the spectral responsivity measurements. DUT means device under test.

Finally, $P_t(\lambda)$ is the optical power measured with a semiconductor photodiode placed in the equivalent position of the sample. The top graph of Figure 4.26 shows the spectral response curves taken at different voltages between 3 and 11 V. Responsivities between 10^4 and 10^6 A/W are obtained above the cut-off wavelength. The growing response of the device as the bias increases suggests an enlargement of the collection efficiency thanks to the broadening of the space charge regions near the contact areas. Additionally, the larger response of the device is accompanied by a relative increase of the slower component in the time response, which suggests a larger contribution of the photoconductive gain mechanism associated to the adsorption/desorption processes of oxygen molecules. Therefore, a better collection efficiency of charges and a growing impact of the internal gain mechanism are pointed out as the main reasons for the super-linear increase of the response also observed in the *I-V* characteristics.

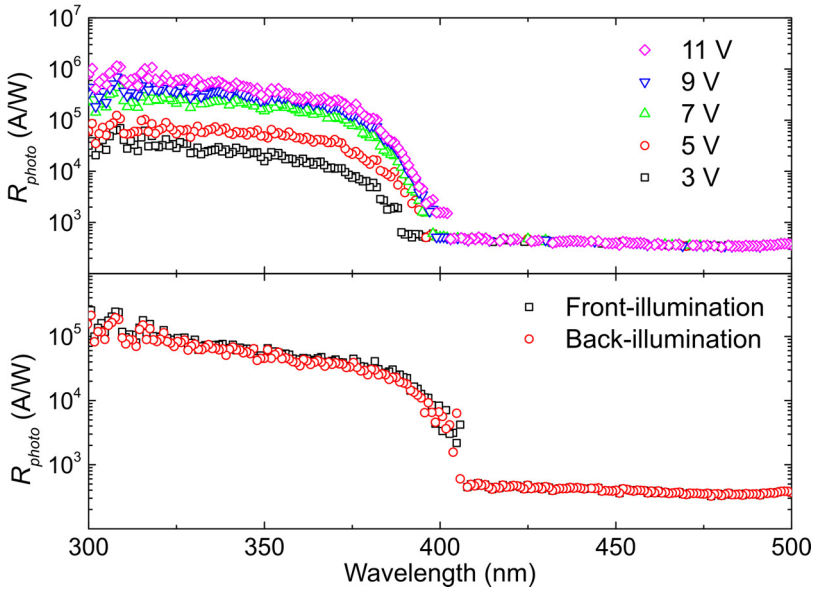

Figure 4.26. Top: estimated responsivities of the sensor at different voltages from 3 to 11 V. Bottom: spectral response at a 5 V bias under front- and back-illumination.

Taking advantage of the glassy substrate and the transparent characteristics of the electrodes, the sensor can operate under front- and back-illumination. Both device responses are compared using the same power density and bias voltage. Spectral responsivities are shown in the bottom graph of Figure 4.26, revealing negligible differences under both configurations. This indicates that there are not significant losses in the measured wavelength range when the light reaches the alignment sites through the

substrate under back-illumination. It is important to notice that bulk ZnO or nitride UV sensors rarely show this dual detection mode. Thus, the use of NWs under the described device architecture reveals another advantage over the current UV technologies.

4.3. Conclusions

4.3.1. CuO NW devices

In this work, a stepwise route has been provided for the fabrication of visible light sensing devices based on CuO, from the NW growth and processing to the electro-optical characterization.

CuO NWs have been grown by direct oxidation of Cu foils under ambient pressure in a quartz tube at different temperatures. A relationship between the growth temperature and the NW physical dimensions has been found from SEM images.

These NWs have exhibited p-type conductivity after its exposure to water vapor. This result has been compared to n-type NWs that have shown the opposite behavior.

After the growth, these NWs have been manipulated and aligned between electrodes using droplet dielectrophoresis for the fabrication of light sensors. In the alignment process by dielectrophoresis, the frequency and the effective voltage of the sinusoidal wave have been optimized to maximize the number of aligned NWs.

The final device fabricated following this procedure has been electro-optically characterized. The CuO-based sensor has been found to be sensitive to visible light, in good agreement with the absorption properties expected for CuO. Furthermore, the use of n-type AZO electrodes allows the formation of heterojunctions between AZO and CuO at both ends of the NW which speed up the response of the device in comparison to photoconductor NW devices. These results have demonstrated the effectiveness of the procedure for the development of NW-based light sensing devices.

4.3.2. ZnO NW devices

New control methods have been introduced in the fabrication of UV light sensing devices based on ZnO NWs. These methods have improved the surface quality of the

final devices and the reproducibility of the alignment process in comparison to previous works.[26]

The first goal has targeted the improvement of the dispersion quality. A simple sedimentation has been used to remove large clusters that can short-circuit electrodes after the DEP process. The quantification of the NW concentration in the dispersions has been successfully performed through absorbance measurements in a spectrophotometer.

To improve the surface quality of the resulting device and to increase the NW trapping probability, a portable and continuous-flow DEP system has been developed. This new system comprises an optical device, which includes a laser and a phototransistor, to monitor the NW dispersion. On the other hand, the alignment of NWs has been monitored in real time through parallel resistance measurements performed with a LCR, connected to the DEP system. This method allows having an estimation of the number of trapped NWs during the DEP process and, thus, to add more control mechanisms to the NW alignment works. Another advantage of monitoring the parallel resistance has been the possibility of detecting anomalies during the process, such as electrode damage induced by solvent electrolysis. Thanks to the up-side-down mounting of the substrate in the continuous-flow system, the results achieved provide higher-quality surfaces with less surface contamination produced by the solution leftovers, which are difficult to eliminate in the droplet DEP case.

The ZnO NWs have been aligned by DEP using the new system on AZO electrodes, previously defined by optical lithography on glassy substrates. Some of the advantages of this device is that it is highly transparent and that it has the capability to work under front- and back-illumination without significant performance differences between both configurations.

REFERENCES

1. T. Ito; H. Yamaguchi; T. Masumi; S. Adachi. Optical Properties of CuO Studied by Spectroscopic Ellipsometry. *J. Phys. Soc. Jpn.* **1998**, 67, 3304-3309.
2. L. Zhu; Y. Chen; Y. Zheng; N. Li; J. Zhao; Y. Sun. Ultrasound assisted template-free synthesis of Cu(OH)2 and hierarchical CuO nanowires from Cu7Cl4(OH)10·H2O. *Mater. Lett.* **2010**, 64, 976-979.
3. A.-L. Daltin; A. Addad; J.-P. Chopart. Potentiostatic deposition and characterization of cuprous oxide films and nanowires. *J. Cryst. Growth* **2005**, 282, 414-420.

4. X. Jiang; T. Herricks; Y. Xia. CuO nanowires can be synthesized by heating copper substrates in air. *Nano Lett* **2002**, 2, 1333–1338.
5. L. Yuan; Y. Wang; R. Mema; G. Zhou. Driving force and growth mechanism for spontaneous oxide nanowire formation during the thermal oxidation of metals. *Acta Mater.* **2011**, 59, 2491-2500.
6. A. M. B. Gonçalves; L. C. Campos; A. S. Ferlauto; R. G. Lacerda. On the growth and electrical characterization of CuO nanowires by thermal oxidation. *J. Appl. Phys* **2009**, 106, 034303.
7. M. Kevin; W.L. Ong; G.H. Lee; G. W. Ho. Formation of hybrid structures: copper oxide nanocrystals templated on ultralong copper nanowires for open network sensing at room temperature. *Nanotechnology* **2011**, 22, 235701 (1-10).
8. J. T. Chen; F. Zhang; J. Wang; G. A. Zhang; B. B. Miao; X. Y. Fan; D. Yan; P. X. Yan. CuO nanowires synthesized by thermal oxidation route. *J. All.Comp.* **2008**, 454.
9. C. H. Xu; C. H. Woo; S. Q. Shi. Formation of CuO nanowires on Cu foil. *Chem. Phys. Lett.* **2004**, 399, 62-66.
10. A. García Marín; C. García Núñez; E. Ruiz; J. Piqueras; J. L. Pau. Fast response ZnO:Al/CuO nanowire/ZnO:Al heterostructure light sensors fabricated by dielectrophoresis. *Appl. Phys. Lett* **2013**, 102, 232105 (1-4).
11. M. L. Zhong; D. C. Zeng; Z. W. Liu; H. Y. Yu; X. C. Zhong; W. Q. Qiu. Synthesis, growth mechanism and gas-sensing properties of large-scale CuO nanowires. *Acta Mater.* **2010**, 58, 5926-5932.
12. A. O. Musa; T. Akomolafe; M. J. Carter. Production of cuprous oxide, a solar cell material, by thermal oxidation and a study of its physical and electrical properties. *Sol. Energ. Mat. Sol. Cells* **1998**, 51, 305-316.
13. J.-W. Han; B. Kim; N. P. Kobayashi; J. Li; M. Meyyappan. A simple method for the determination of doping type in nanomaterials based on electrical response to humidity. *Appl. Phys. Lett.* **2012**, 101.
14. A. Gencoglu; A. Minerick. Chemical and morphological changes on platinum microelectrode surfaces in AC and DC fields with biological buffer solutions. *Lab. Chip.* **2009**, 9, 1866-1873.
15. H. P. Schwan. Linear and nonlinear electrode polarization and biological materials. *Annal. Biomed. Eng.* **1992**, 20, 269-288.
16. S. M. Sze; K. Kwok. *Physics of Semiconductor Devices*. 3rd ed.; Wiley: New Jersey, 2007.
17. J. L. Pau; E. Monroy; E. Muñoz; F. Calle; M. A. Sánchez-García; E. Calleja. Fast AlGaN metal-semiconductor-metal photodetectors grown on Si(111). *Electron. Lett.* **2001**, 37, 239-240.
18. R. H. Bube. *Photoconductivity of Solids*. Krieger: New York, 1978.
19. A. Othonos; M. Zervos. Ultrafast hole carrier relaxation dynamics in p-type CuO nanowires. *Nanoscale Res. Lett.* **2011**, 6, 622 (1-5).
20. L. Liao; Z. Zhang; B. Yan; Z. Zheng; Q. L. Bao; T. Wu; C. M. Li; Z. X. Shen; J. X. Zhang; H. Gong; J. C. Li; T. Yu. Multifunctional CuO nanowire devices: p-type field effect transistors and CO gas sensors. *Nanotechnology* **2009**, 20, 085203.
21. A. G. Marín; C. G. Núñez; P. Rodríguez; G. Shen; S. M. Kim; P. Kung; J. Piqueras; J. L. Pau. Continuous-flow system and monitoring tools for the dielectrophoretic integration of nanowires in light sensor arrays. *Nanotechnology* **2015**, 26, 115502.
22. K. E. v. Holde; C. Johson; P. S. Ho. *Principles of Physical Biochemistry*. 1998.
23. J. G. Solé; L. E. Bausá; D. Jaque. *An Introduction to the Optical Spectroscopy of Inorganic Solids*. 1st ed.; John Wiley & Sons: New Jersey, 2005.

24. M. Pelton; G. W. Bryant. *Introduction to Metal-Nanoparticle Plasmonics*. 1st ed.; EEUU, 2013.
25. H. Morgan; N. G. Green. *AC Electrokinetics: colloids and nanoparticles*. Research Studies Press Ltd.: Philadelphia, 2003.
26. C. García Núñez. Contribution to the Development of Electronic Devices Based on Zn_3N_2 Thin Films, and ZnO Nanowires and GaAs Nanowires. Universidad Autónoma de Madrid, Madrid (Spain), 2015.

5. A glutathione immunosensor based on total internal reflection ellipsometry

5.1. Introduction

The detection methods based on surface plasmon resonance (SPR) typically measure changes in the intensity of the reflected light.[1] The resonance energy depends on the physical properties of the metal and the refractive index of the surrounding medium, among other factors. Although SPR enables the investigation of biomolecular interactions by probing refractive index changes on the sensor surface, its coupling to ellipsometry constitutes a more sensitive and accurate method.[2] The combination of ellipsometry with the surface plasmon properties of noble metals is especially useful in total internal reflection ellipsometry (TIRE), a technique that relies on the sensitivity of the evanescent wave formed under total internal reflection conditions. The potential of this combination to study the surface recognition of specific biomolecules was shown at the beginning of this century.[2-4] Later, this approach has leaded to the fabrication of new sensors (especially extensive in the immunosensing field) for different applications, such as medical diagnosis of illnesses,[5, 6] food safety,[7-9] environmental monitoring[10, 11] or detection of explosives.[12]

It has been demonstrated that both ellipsometric functions (Ψ and Δ) present strong variations upon the excitation of SPR in Krestchmann configuration, being claimed to have 10 times larger sensitivity than regular SPR techniques.[13] Since Ψ function gives us

information on the amplitude ratio between p- and s- polarization components of the reflected beam, its reduction accounts for the absorption of the p-polarized component of the incidence light at the Au/air interface when the resonance conditions are fulfilled. On the other hand, the s-polarization component acts as a background reference of the non-resonant reflectance.

The regular thickness of the Au layer in commercial SPR sensors is around 50 nm. One important drawback of Au is that the adherence to transparent dielectrics like quartz or glass requires the use of a thin film of Cr or Ti. Due to the high absorbing properties of those layers, there is a strong reduction of the electric field intensity, broadening the reflectance dip in the Ψ function and causing the attenuation of the step in the Δ function when resonant conditions are satisfied. Recent investigations have pointed out that the use of a transparent metal oxide like Sn-doped In_2O_3 (ITO) or Al-doped ZnO as an intermediate layer can help to reduce that perturbation.[14, 15]

In common SPR, the registration of very low molecular weight molecules is still a challenge due to the small refractive change produced on the metal surface. To enhance the sensitivity to small molecules, AuNPs can be used as signal amplifiers if the molecules are conveniently bound to the NP surface.[16, 17] AuNPs exhibit a strong absorption band around 520 nm that arises from the excitation of localized surface plasmon resonance by incident light. Their surfaces can be modified in many ways to attach biomolecules following well-known modification routes.[18-20] AuNPs binding to thin Au films leads to large changes in the plasmon resonance through optical coupling between the polariton wave in the metal surface of the film and the resonant scattering in the NPs.[21-23] This property can be used to amplify low molecular weight molecule responses, improving sensors detection limit.

The detection capabilities of SPR-TIRE are studied through the development of a biosensor for glutathione (GSH), a small biomolecule present in all living organisms, but predominantly in eukaryotic cells,[24, 25] which plays a critical role in numerous biological processes.[26, 27] Among the wide number of roles, intracellular redox balance[28] detoxification, modulation of the immune response,[29] protein folding,[30] and transport of organic sulfur[31] can be highlighted. Furthermore, low levels of GSH are related to several health problems such as Crohn's disease,[32] Alzheimer,[33] cancer,[34] immune,[35] and metabolic diseases.[36, 37]

In this part of this work, the objective is to develop an immunosensor to detect GSH by combination of ellipsometry and Kretschmann configuration. The Au thin film used for SP excitation is functionalized with antiGSH to specifically recognize GSH. To improve sensitivity, AuNPs are functionalized with GSH acting as amplifiers of the antigen-antibody immunological recognition. Changes induced by the AuNP adsorption are monitored with an spectroscopic ellipsometer through the ellipsometric functions, Ψ and Δ, under the TIRE configuration. Finally, competitive immunoassays are performed using solutions containing different concentrations of free GSH and a constant amount of GSH-capped AuNPs conjugates to obtain a calibration curve between free GSH and resonance energy changes.[38]

5.2. AuNPs characterization and functionalization

The first step for the biosensor development consists of the synthesis of gold nanoparticles and the subsequent functionalization with GSH in order to obtain the conjugates used in the competitive immunoassay.

Citrate-stabilized gold nanoparticles (Cit-AuNPs) are synthesized by the aqueous citrate reduction method as explained in Section 3.3 of Chapter 3. TEM image of the NPs (inset of Figure 5.1A) shows a narrow particle size distribution. The histogram (Figure 5.1A), obtained from the TEM image, shows an average radius of 7 ± 2 nm.

The next step comprises the NPs citrate stabilizer substitution by GSH. The GSH biomolecule has a thiol group that enables the substitution of citrates through the formation of the Au-S chemisorption bond. The high affinity chemistry of the thiol groups for Au has been studied before and yields the displacement of other less stable adsorbed components from the Au surface.[39, 40]

To functionalize the NP surface, 200 μL of a free GSH aqueous solution (0.2 M) is added to 4 mL of a Cit-AuNPs solution and left overnight for stabilization. Afterwards, a purification process is carried out in order to remove the GSH excess and possible reaction byproducts by using several cycles of ultrafiltration through Amicon Ultra Centrifugal Filters with ultracel-100 K membrane at 4000 rpm, employing water as a diluent. The free GSH concentration in the NP solution after purification is lower than 5 pM.

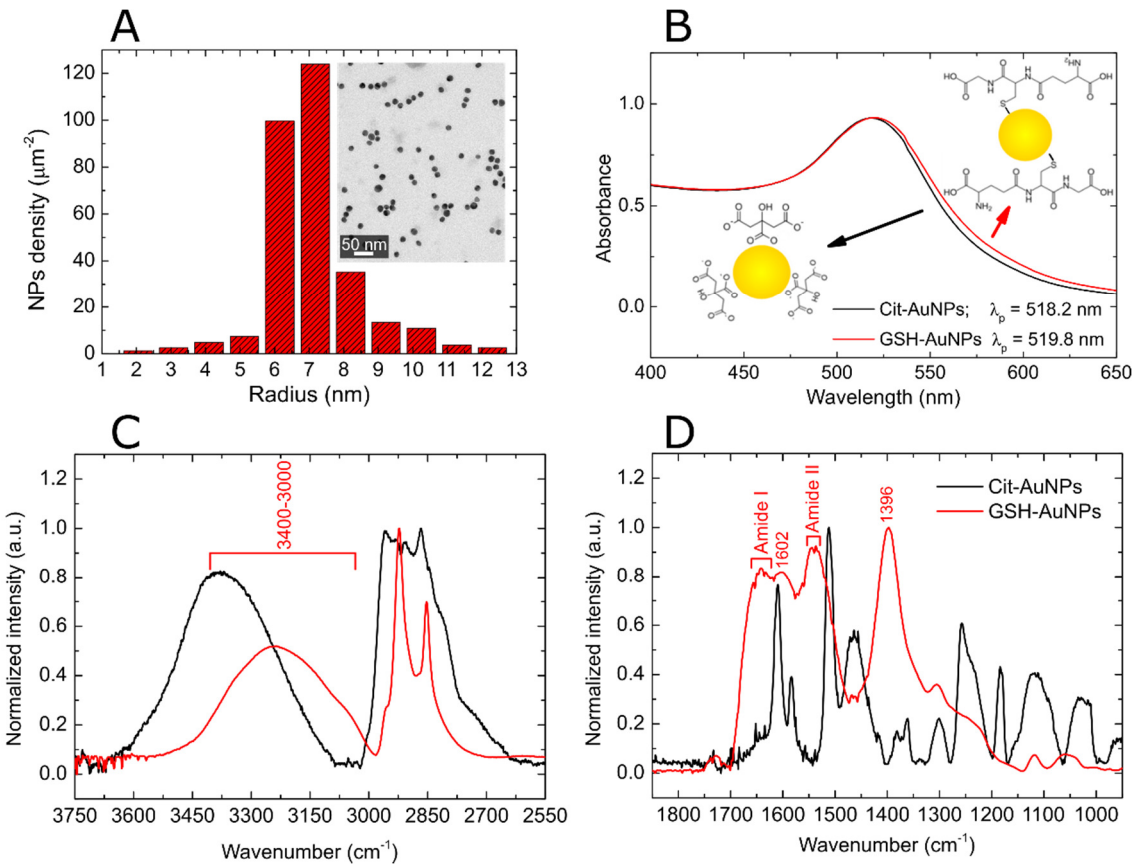

Figure 5.1. (A) Histogram of the Cit-AuNPs colloidal dispersion. Inset of Figure 5.1A shows the TEM micrograph of Cit-AuNPs; (B) Absorbance spectrum of the as-synthesized Cit-AuNPs (black curve) and GSH-AuNPs (red curve). The peak wavelengths (λ_p) for the characteristic surface plasmon bands are included. For the sake of clarity, drawings of Cit-AuNPs and GSH-AuNPs are also shown; (C,D) absorbance FTIR spectra of AuNPs before (black curve) and after (red curve) functionalization with GSH. Centered wavenumbers for the most important bands are included as labels.

Two optical techniques are used to demonstrate the effective functionalization of the NPs with the GSH biomolecule. The first technique is the UV/Visible spectrophotometry, which gives us the localized surface plasmon resonance (LSPR) characteristic band of these NPs. The position in wavelength of this band depends on their morphology, size and the molecules bonded to its surface. Taking advantage of this property, it is possible to monitor the stabilizers exchange and, also, the size of the NP. The second technique is the Fourier-transform infrared spectroscopy (FTIR), which gives us information about the molecules on the NP surface from the vibrational characteristics of their functional groups.

Before the functionalization, the UV/visible absorbance spectrum of these Cit-AuNPs exhibits the characteristic surface plasmon band with a peak wavelength (λ_p) of

518 nm (Figure 5.1B, black curve). On the other hand, FTIR absorbance spectrum (Figure 5.1C,D, black curve) shows the presence of the citrate stabilizer in the AuNPs with bands located at 2955, 2867, 1609, 1512 and 1456 cm^{-1} corresponding to the vibrational modes $\nu_{asy}(-CH_2)$, $\nu_{sym}(-CH_2)$, $\nu_{asy}(-CO_2^-)$, $\nu_{sym}(-CH_2)$, $\nu_{sym}(-CO_2^-)$, respectively.[41, 42] The broad band at approximately 3380 cm^{-1} is attributed to the ν(-OH) vibration, and the bands at 1257 and 1184 cm^{-1} are correlated with the ν(-CO) vibration. The 1110 and 1020 cm^{-1} bands correspond to ν(C-C) vibrational modes.[43]

The GSH-capped AuNPs conjugates (GSH-AuNPs) are obtained by addition of an aqueous solution of GSH immediately after preparation of Cit-AuNPs. The sulfhydryl group in GSH strongly chemisorbs to the Au surface displacing the adsorbed citrate ions. As a result, λ_p is redshifted about 1.6 nm (Figure 5.1B, red curve). This shift is in agreement with previous results about ligand exchanges in AuNPs.[44] The energy shift is characteristic of the formation of strong chemisorption bonds of thiol-containing compounds to metallic NPs, which influence more the electron density of the NP in comparison to Au-O chemical bonds. The FTIR spectrum of the GSH-AuNPs (Figure 5.1C,D, red curve) is different to that obtained for Cit-AuNPs. It exhibits characteristic bands associated with the vibrational modes of GSH in agreement with the assignments reported in the literature.[45-47] The large band at the 1660-1600 cm^{-1} range is attributed to the amide I mode, mainly associated to C=O symmetric stretching mode from amide, and NH_3^+ antisymmetric bending band that arises at 1602 cm^{-1}. The presence of the amide II mode is observed in the spectral region of 1550-1530 cm^{-1}, associated to CNH in-plane bend and CN symmetric stretching vibrations. The peak at 1396 cm^{-1} corresponds to the COO^- symmetric stretching $\nu_s(COO^-)$ and the band at 3200 cm^{-1} is assigned to the contribution of several overlapped bands, NH_3^+ antisymmetric and symmetric stretching modes $\nu_{as}(NH_3^+)$ and $\nu_s(NH_3^+)$. Additionally, CH_2 antisymmetric and symmetric stretching modes $\nu_{as}(CH_2)$ and $\nu_s(CH_2)$ are found at 2922 and 2854 cm^{-1}, respectively.

Therefore, from the spectrophotometry and FTIR results, we can conclude that the functionalization of the AuNPs with GSH has been successful thanks to the high affinity of the thiol groups for Au.

5.3. Development and characterization of the biosensing platform

Once the AuNPs are successfully functionalized, it is necessary to prepare the Au film that will be used in the TIRE setup. The Au film will be deposited by thermal evaporation on a quartz substrate. The next section discusses the advantages of using AZO as intermediate layer between the substrate and the Au film. Finally, the surface of the Au film must be modified to hold the recognition element, an antibody specific to GSH. That antibody will recognize the presence of GSH-AuNPs whose preparation was described in previous sections.

5.3.1. Suitability of the Al-doped ZnO layer

Commercial SPR sensors are typically fabricated by depositing Au on transparent substrates. A very thin intermediate layer is commonly used, such as Cr or Ti, to improve the adherence of Au to the substrate. As a substitute, an Al-doped ZnO (AZO) layer is deposited in this work between the Au thin film and the glass substrate in order to avoid absorption losses produced by those metallic materials.[14] The high transparency of AZO to visible light has been shown in the previous Chapter. This layer, besides improving the adherence of Au to the transparent substrate, helps to enhance the energy transfer from the incident radiation to the polariton wave thanks to the high transparency of the AZO at the resonance energy. Figure 5.2 shows different numerical simulations of the Δ ellipsometric function using the Fresnel equations in air. The introduction of the AZO layer (20-50 nm) only produces a slight redshift in the function in comparison to glass substrates with plain Au. On the other hand, the introduction of Cr for thicknesses in the usual nanometer range (2-4 nm) produces larger redshifts and strong attenuations, which can hinder the SPR analysis.

This result demonstrates the convenience of using material with lower absorption losses in the analyzed range, such as AZO, in order to avoid undesirable attenuation of the SPR effects on the ellipsometric functions.

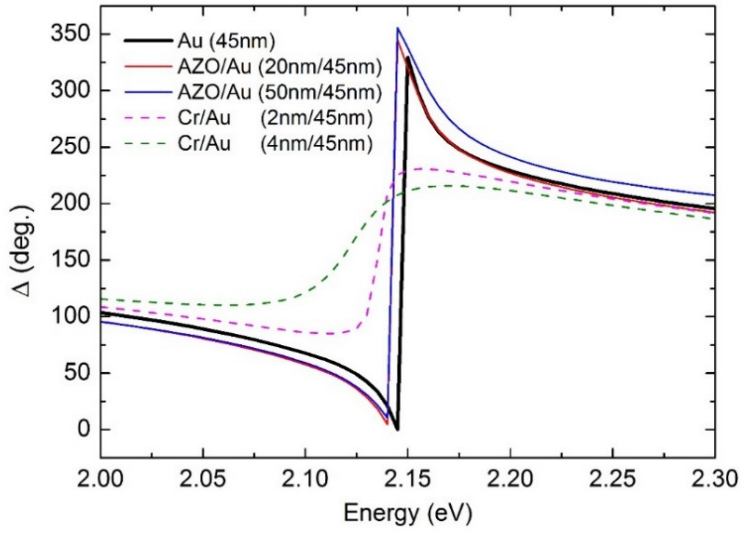

Figure 5.2. Comparison of the simulated Δ function around the resonance energy for different intermediate layers between a glass substrate and a 45 nm thick Au layer. Black solid curve represents the plain Au case. Colored solid and dash curves show the effect of AZO and Cr layers, respectively; 20 and 50 nm thick AZO intermediate layers are chosen to study the impact of these highly transparent layers on the resonance amplitude in contrast to very thin (2 and 4 nm thick) Cr layers commonly used in SPR sensors.

5.3.2. Surface modification of the biosensing platform

SPR-TIRE biosensors are fabricated for operation in a Krestchmann configuration following these steps: prior to the deposition, 2.0×2.0 cm^2 quartz substrates are cleaned by using hot trichloroethylene, acetone and ethanol; a 50-nm thick AZO layer is deposited on the substrate at 300 ºC by radio-frequency magnetron sputtering; afterwards, a 45-nm thick Au layer is thermally evaporated on the AZO thin film. The as-formed AZO/Au bilayers are functionalized step-by-step in order to obtain the final biosensing platform.

5.3.2.1. Formation of the DTSP monolayer

The first step for the AZO/Au functionalization comprises the coating of the AZO/Au bilayer with a thiol self-assembled monolayer (SAM) by dipping the bilayer in a solution of 4 mM 3,3′-Dithiodipropionic acid di(N-hydroxysuccinimide ester) (DTSP) in dimethyl sulfoxide (DMSO) overnight. This high concentration is chosen to ensure full surface coverage. The surface is rinsed with acetone and blown with dry N_2.

The modification with DTSP resulted in the adsorption of N-succinimidyl-3-thiopropionate (NTSP). This assignment is based on the fact that, on Au surfaces,

disulfides undergo dissociative chemisorption to give rise to the corresponding adsorbed thiolates.[39]

To demonstrate the successful functionalization of the AZO/Au bilayer, cyclic voltammetric measurements of the modified bilayer are carried out in 0.1 M KCl at 100 mV/s, and the results are presented in Figure 5.3. First of all, no Faradic processes are observed over the potential range of 0.0 to -0.7 V for either the unmodified or the DTSP-modified AZO/Au bilayer. Despite of the high resistance present in this bilayer, a well-defined chemically irreversible wave is observed with a peak potential of -1.1 V (versus saturated calomel reference electrode) on the first cathodic scan to -0.7 V. This is in good agreement with a report of Imabayashi et al. for the reductive desorption of a 3-mercaptopropane monolayer from a Au electrode surface.[48] Given the similarity of this molecule to NTSP, the aforementioned process is ascribed to the reductive desorption of the monolayer from the electrode surface. This is also in agreement with the general propensity of adsorbed thiolates to undergo this desorption from Au surfaces.

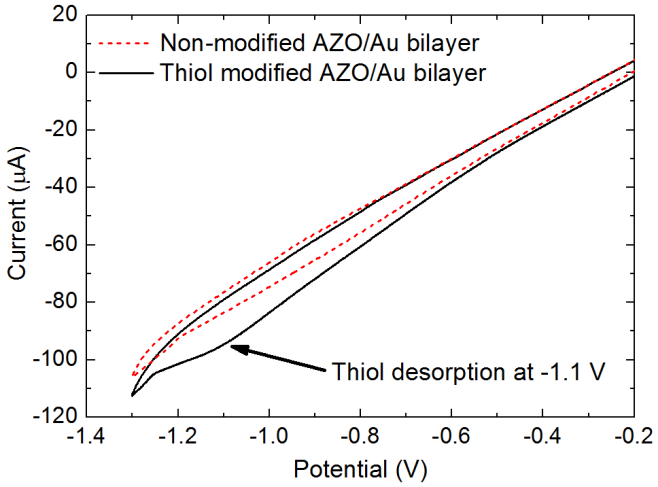

Figure 5.3. Cyclic voltammogram obtained for the thiol-modified AZO/Au bilayer (black curve) compared to the non-modified bilayer (red dashed curve). The thiol desorption peak at -1.1 V is highlighted. Measurements are carried out in nitrogen-saturated 0.1 M KCl solution at a scan rate of 100 mV/s.

A surface coverage of 9.5×10^{-10} moles/cm^2 is estimated from the charge under the reductive desorption peak assuming a value of 1 electron per sulfur atom. This value is in agreement with the typical surface density of molecules reported for the maximum thiol coverage on Au surfaces,[39] which confirms the surface modification.

The surface, now bearing an "activated ester" termination, is subsequently made to react with the antiGSH. The immobilization takes place by nucleophilic attack of primary amino groups of the antibody to the terminal N-succinimidyl esters in the monolayer.[49]

5.3.2.2. Formation of the antibody layer

The antibody immobilization on the DTSP-functionalized bilayer is optically characterized in the TIRE experimental setup in air in order to study the changes introduced in the ellipsometric functions. A schematic representation of the ellipsometric setup is shown in the Figure 3.16A. The resonance energy is determined by the position of a local minimum in the Ψ function minimum ($E_{\Psi min}$). For the AZO/Au bilayer in air, an external incidence angle of 47º has yielded the lowest value of $E_{\Psi min}$ and the strongest Δ shift, at energies of about 2.0 eV (Figure 5.4, black curve). At that incidence angle, the light spot has an elliptical shape with a 5.0×3.0 mm^2 area.

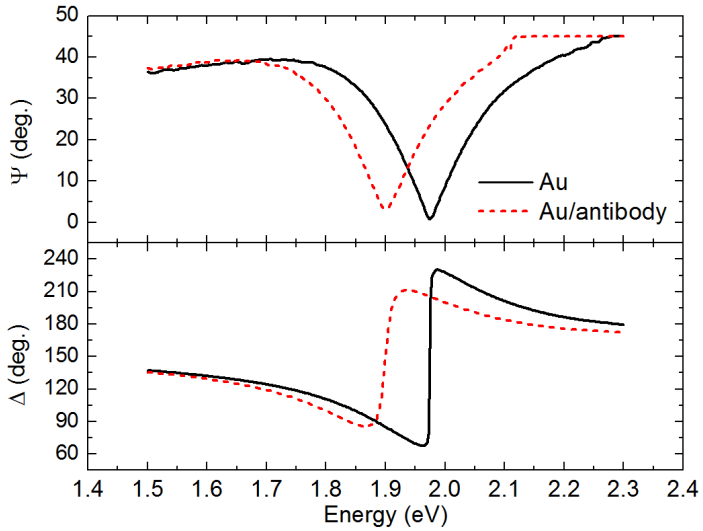

Figure 5.4. TIRE-SPR spectra measured before (black curve) and after (red curve) antibody immobilization for both ellipsometric functions (Ψ and Δ).

The antibody immobilization comprises the incubation of the DTSP-functionalized bilayer in a 150 nM antiGSH in 0.01 M KCl solution. The pH is adjusted close to the neutrality (pH ≈ 7) in order to avoid the protein denaturation. Unreacted succinimidyl moieties from the DTSP remaining on the surface are deactivated by further soaking the

bilayer into the 0.01 M KCl solution for 1 hour. Finally, the samples are rinsed a few times with deionized H_2O and blown with dry nitrogen. After immobilization, the TIRE spectrum is newly measured in air. As shown in Figure 5.4 (red curve), a significant redshift of the resonance energy is obtained due to the strong change in the refractive index caused by the adlayer. In addition, the resonance strength slightly attenuates because of the screening effect of the charges in the antibody layer, which reduces the amplitude of the polariton in the metal surface.

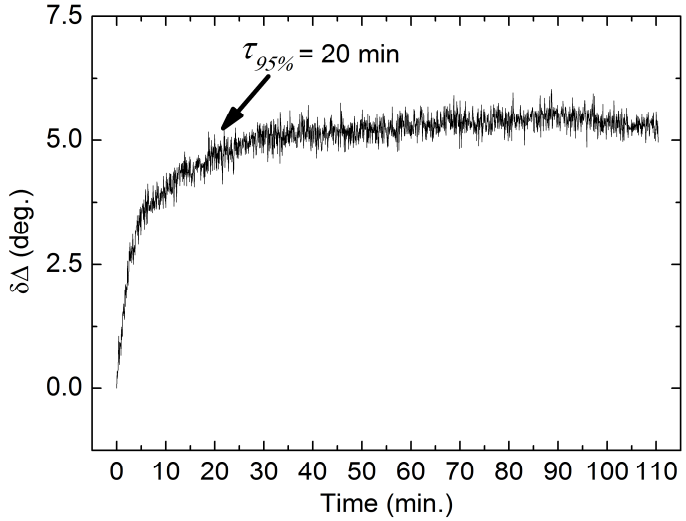

Figure 5.5. Increment of Δ function (δΔ) measured in situ during the immobilization of the antibody on the DTSP-functionalized platform

The antibody immobilization process is also studied in real-time. The ellipsometer provides this type of measurements by recording the ellipsometric functions over time at a constant energy and incidence angle. The prism, hosting the sample underneath, is directly put on a home-made flow cell, sealed with a rubber O-ring and connected to a peristaltic pump to inject the antiGSH solution. Since the refractive index of H_2O is higher, the resonance is found at larger angles and lower energies than in air. Thus, the kinetic study is performed at 1.5 eV and an external angle of 85°. The formation of the antibody layer on the DTSP-functionalized AZO/Au bilayer is monitored by studying the Δ variation over time. The use of this function is motivated by its higher sensitivity for measuring surface changes in comparison to Ψ.[50] As the antibody is immobilized on the surface, the Δ value increases monotonously up to reaching a steady level after 25 min (Figure 5.5). For the sake of clarity, Figure 5.5 represents the increment of the Δ function

(δΔ) with respect to the initial value at t = 0. Tau parameter, defined as the time needed to reach 95% of the steady level ($\tau_{95\%}$), yields a value of 20 minutes. This reaction time confirms the strong affinity of the antibody to the DTSP-functionalized Au surface.

5.3.3. Simulation of the ellipsometric response

The position of the resonance in the ellipsometric measurements is fitted using numerical simulations with the Fresnel equations. A four-layer model is used under the fused silica prism (model A, Table 5.1). From top to bottom, the model includes a 50-nm thick AZO layer whose optical constants are found by numerical inversion of ellipsometric data, independently taken on different AZO thin films on Si substrates.[15, 51] This layer is followed by a 42-nm thick Au film. Au and fused silica optical constants are taken from the literature,[52, 53] whereas air refractive index is assumed to be 1.0. The thicknesses for both layers are experimentally determined by stylus profilometry. Next, the fitting works require the introduction of a Bruggeman effective medium approximation (EMA) layer formed by Au and air to account for the surface roughness of the Au layer. The material compositions and thickness of this layer are varied to fit the energy of the final resonance, providing best fitting values of 60% for Au, 40% for air and 5.2 nm as the total thickness. Within this model, an accurate fitting of the resonance energy is obtained for the bilayer.

Table 5.1. Layer models for the AZO/Au structure that best fit the resonance energy position before (Model A) and after (Model B) antibody immobilization. The layers are ordered from bottom to top in the setup. Ambient fused silica layer accounts for the prism optical characteristics.

Model A	**Composition**	**Thickness (nm)**	**Model B**	**Composition**	**Thickness (nm)**
Ambient	Fused silica		**Ambient**	Fused silica	
	AZO	50		AZO	50
	Au	42		Au	42
EMA layer	60% Au 40% Air	5.2	**EMA layer**	60% Au 40% Antibody	5.2
Substrate	Air			Antibody	3.8
			Substrate	Air	

For the sake of simplicity, the organic layer is represented by a medium with a constant refractive index of 1.5 and a null extinction coefficient.[10] It is worth noting that DTSP-SAM effect is neglected since its presence barely modifies the spectral position of the resonance. In the new five-layer model (labeled as model B in Table 5.1), the thickness of the uniform bioorganic layer is varied to fit the resonance energy in the TIRE spectrum, yielding a best value of 3.8 ± 0.2 nm. If the thickness of the EMA Au/antibody layer is also considered by weighting the contribution of the antibody, a total layer thickness of around 5.9 nm is obtained (3.8 nm + (0.4 × 5.2 nm) = 5.9 nm). This value is within the range of 4-6 nm reported in atomic force microscopy studies for immobilized IgG antibodies.[54]

This numerical simulation demonstrates that the ellipsometric response of the AZO/Au bilayer plasmonics can be successfully described by the Fresnel equations. The introduction of the dielectric layer yields a redshift that can be explained with the refractive index increase of the surrounding medium.

5.4. Immunosensing response

In order to check the sensitivity of the TIRE resonance technique to the detection of the GSH biomolecule, the antibody-functionalized bilayer is exposed to a 100 nM GSH solution (data not shown). In this case, as expected for low molecular weight molecules, the resonance energy does not give any significant change. To enhance the sensitivity of this technique, the use of GSH-AuNPs conjugates is proposed in order to compete against free GSH for the active sites of the antibody. These conjugates are expected to produce a very strong change in the resonance of the Au thin film due to plasmonic coupling effects. As a first step to study the immunosensing response of these conjugates with the antibody-functionalized platform, the kinetics of the recognition event and the optimal concentration of these conjugates are optimized before performing the competitive assay.

5.4.1. Kinetics of GSH-AuNPs conjugates recognition by the antiGSH

The kinetic of GSH-AuNPs recognition by the antiGSH-functionalized sensor is also investigated in real-time (Figure 5.6). The configuration used is the same to that presented previously in Section 5.3.2.2. Once the sensor is functionalized by antiGSH

and any unbound antibody is removed by flowing KCl solution, a solution of 40 nM of GSH-AuNPs is injected in the flow cell. Immediately, a strong variation in Δ is observed associated to the recognition of the conjugates by the antibody molecules immobilized onto the bilayer surface. The signal reaches a steady level after around 35 min. $\tau_{95\%}$ for the recognition process yields a value of 33 minutes.

From these studies, 1 hour is set for further immunoassays to ensure that the recognition event reaches the equilibrium.

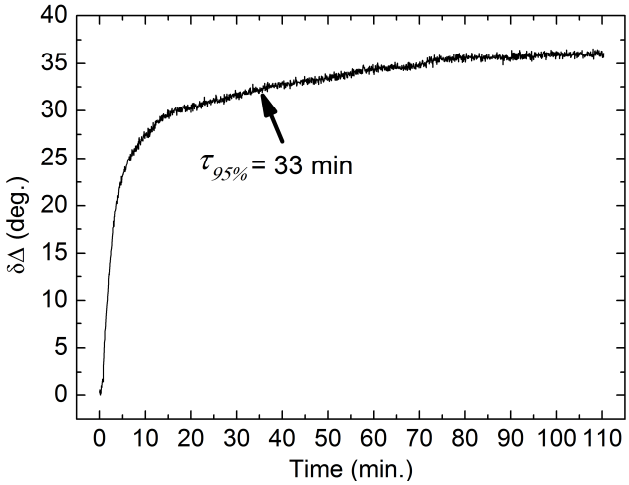

Figure 5.6. δΔ measured in situ during the recognition reaction of the GSH-AuNPs with the antibody-functionalized surface, recorded at 1.5 eV and external incidence angle of 85°.

5.4.2. Optimization of the GSH-AuNPs concentration

In order to find out the optimal NP concentration that produces a largest SPR shift after the recognition event between the antibody layer and the GSH-AuNPs, different biosensing platforms are exposed to several solutions with NP concentrations ranging from 10 to 80 nM for 1 hour by drop-casting on the biosensor surface. After washing with deionized H_2O and blowing the surface gently with dry nitrogen, the biosensor is measured again in TIRE mode. Ψ and Δ functions are recorded and the spectra represented in Figure 5.7A.

$\Delta E_{\Psi min}$ in Figure 5.7B represents the shift of the resonance energy after the GSH-AuNPs recognition on the antiGSH-functionalized surface. As can be observed, this shift shows a linear increase as the concentration increases until a 40 nM concentration and is related to the strong variation of the refractive index as GSH-AuNPs attach to the surface

and the rearrangement of the antibody layer. By contrast, the highest concentration employed (80 nM) presented a strong attenuation and broadening of the resonance, as can be observed in Figure 5.7A. This behavior is likely related to a reduction in the polariton amplitude caused by an inhomogeneous optical coupling with the AuNP resonance. Mock et al. have also observed the attenuation of the SPR band in Au films in the presence of AuNPs placed at a nanometric distance by inserting a separation dielectric layer.[55] From a practical viewpoint, a 40 nM concentration is chosen as optimal concentration for carrying out the immunosensing reaction since it provides the largest shift of the resonance energy without signal attenuation.

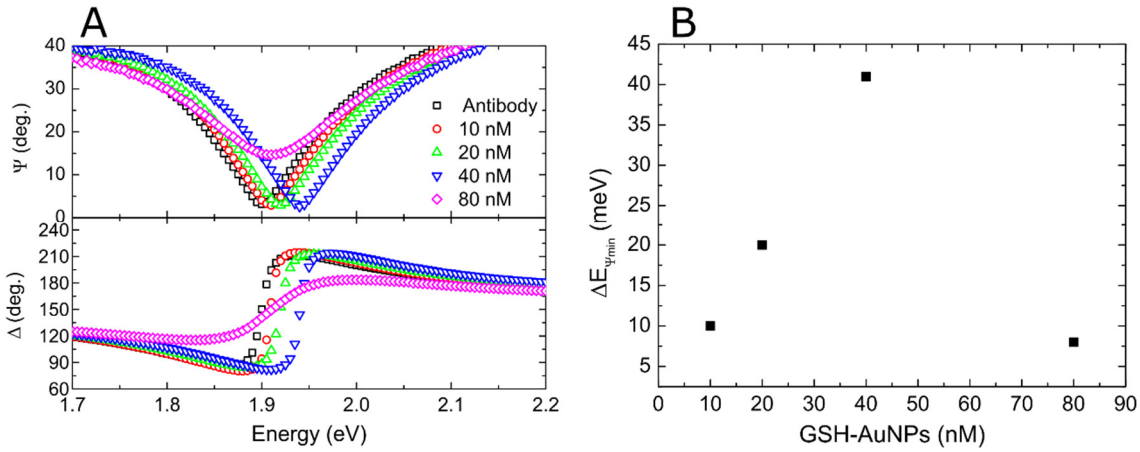

Figure 5.7. (A,B) TIRE-SPR spectra collected in air for Ψ and Δ functions, respectively. Curves represent the spectra obtained for the immobilized antibody (black squares) and for the incorporation of different concentrations of GSH-AuNPs on this antibody layer, namely 10 nM (red circles), 20 nM (green up-triangles), 40 nM (blue down triangles) and 80 nM (purple diamonds); (C) Energy shift ($\Delta E_{\Psi min}$) caused by immobilization of GSH-AuNPs at different concentrations.

The interaction between GSH-AuNPs and the antibody layer is further verified by SEM. SEM images, corresponding to the antiGSH modified sensor before (Figure 5.8A) and after (Figure 5.8B) the immunological recognition with 40 nM of GSH-AuNPs, show the presence of the GSH-AuNPs as tiny bright dots on the antibody layer. These can be more clearly observed in the image taken at higher magnification (inset of Figure 5.8B). The distribution is fairly uniform with no signs of NP aggregation, confirming their binding to the antiGSH layer. Given that NP and antibody have almost similar size, it is fair to assume that each NP binds to a single antibody molecule, giving rise to a random

NP pattern over the antibody layer. The average particle density obtained from a raster scan over an area of 330×330 nm^2 is estimated to be 160 ± 10 NPs/μm^2.

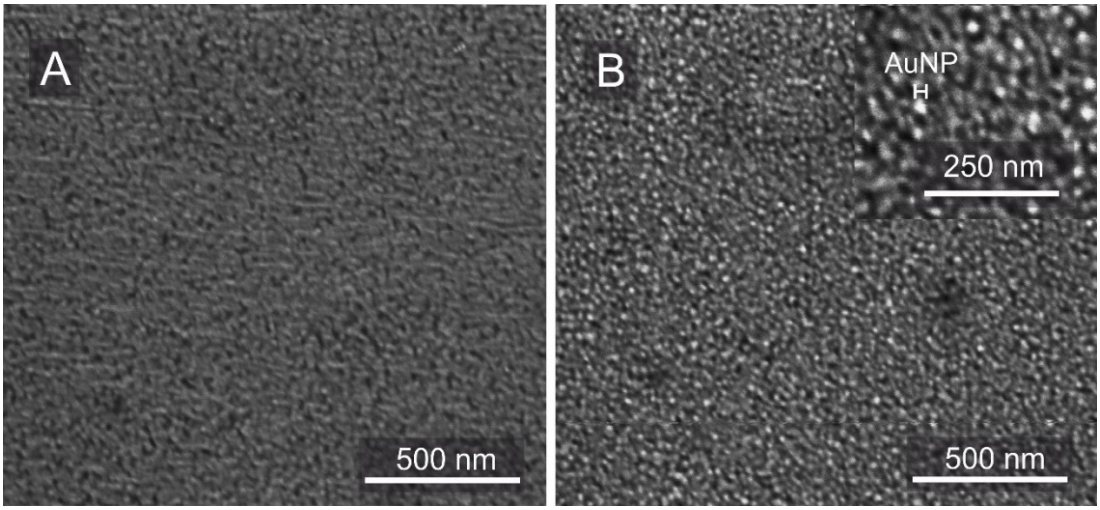

Figure 5.8. SEM images before (A) and after (B) recognition reaction of 40 nM of GSH-AuNPs on the antiGSH-functionalized biosensor (magnification 160,000x). AuNPs can be identified as bright dots. The inset of this figure is taken at a larger magnification (280,000x).

5.4.3. Competitive immunoassay

On the basis of the above results, an immunoassay for GSH detection is developed based on the competition between free GSH and GSH-AuNPs for the active sites of the antibody.

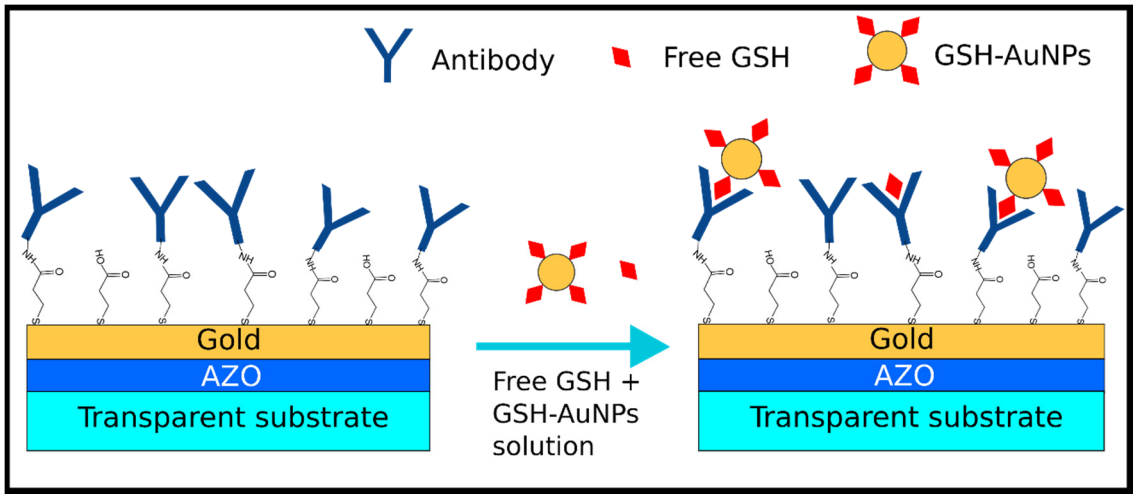

Figure 5.9. Scheme of the competitive immunoassay between free GSH and GSH-AuNPs conjugates performed on the current biosensing platform.

Different biosensing platforms are exposed for 1 hour to solutions containing a constant concentration of GSH-AuNPs (40 nM) mixed with increasing concentrations of free GSH from 10 to 100 nM. A scheme of the immunoassay concept is shown in Figure 5.9. Once the surface is rinsed with H_2O and blown with nitrogen, TIRE measurements are carried out.

Figure 5.10 shows the relative SPR shift versus the concentration of free GSH. Relative SPR shift is defined as the ratio between the energy shift caused by the mixed solution, and the shift caused by a 40 nM GSH-AuNPs control solution. Since the free GSH competes with the GSH-AuNPs for the antibody sites, the resonance shift decreases as the free GSH concentration increases. Each point is the average of three measurements whose standard deviations are represented as error bars in this Figure. Linear fitting of the experimental data yield a linear correlation in the range from 10 to 100 nM (R^2 = 0.9930). Detection and quantification limits are calculated to be 6 and 18 nM, respectively, for a standard deviation (*SD*) determined from three measurements of the blank (40 nM GSH-AuNPs).

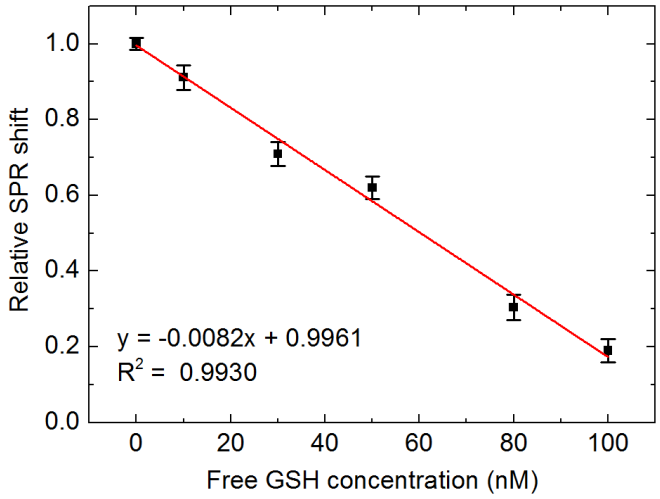

Figure 5.10. Calibration curve of the SPR shifts as a function of the free GSH concentration in mixed solutions of GSH-AuNPs conjugates and free GSH. Relative SPR shift is defined as the ratio between the energy shift caused by the mixed solution, and the shift caused by a 40 nM GSH-AuNPs control solution; error bars represent the standard deviation of three measurements.

The reproducibility of immunosensors is evaluated from the relative standard deviation (RSD) of the response obtained for 30 nM GSH concentration with 3 different sensors prepared in the same manner. A RSD value of 5.0% is obtained.

A summary of the analytical parameters of the GSH determination method is shown in Table 5.2.

Although in some cases there is no need to achieve low detection limits, because intracellular GSH concentrations in plasma are ranged from 1 to 20 μM, respectively,[56-58] in other applications a higher sensitivity is required. Standard kits usually rely on spectrofluorimetry[59] (Ellman's reagents or bimane derivates) and ELISA[60] (antigen-antibody recognition) and reach detection limits around 330 and 1660 nM. Other techniques such as electrochemistry,[61-63] high-performance liquid chromatography,[64-66] gas chromatography,[67] or quartz crystal microbalance[68] have been employed enabling the detection at lower levels. Although, all these last methods have advantages, they also present some drawbacks, such as less selectivity against other amino acids or the long times required for the analysis. Our SPR-TIRE biosensing platforms rely on the antibody-antigen immunological recognition, which confers an intrinsic specificity to GSH. Thanks to this property, this method does not require any further step, such as chromatography, to identify the attached molecule in the immunosensing layer.

Table 5.2. Summary of the GSH immunosensor analytical characteristics.

Parameter	Value
Linear range	10 -100 nM
Detection limit	6 nM
Quantification limit	18 nM
Reproducibility (30 nM GSH), n = 3	5.0 %
Repeatability, n = 3	0.4 %

5.5. Conclusions

In this work, the development of a TIRE immunosensor for GSH, a low molecular weight biomolecule, has been studied. The competitive configuration has been chosen based on the simultaneous recognition of GSH-AuNPs and free GSH. The sensor takes advantage of the amplified signal provided by AuNPs in the TIRE setup when they bind to the functionalized Au surface.

The work includes the successful functionalization of AuNPs with GSH. Infrared and UV-visible spectrophotometries have confirmed the formation of the Au-S chemisorption bond.

During the biosensing platform development, the AZO has been chosen, instead of Ti and Cr, as the intermediate layer between Au and the quartz substrate. This layer has provided comparable benefits without the absorption losses produced by the previously mentioned metals, as has been demonstrated from the numerical calculation using Fresnel equations and effective medium approximations.

The AZO/Au bilayer has been functionalized with a thiol monolayer, the DTSP, to further immobilize an antibody selective to GSH. The presence of the DTSP self-assembled monolayer has been proved through cyclic voltammetry via the thiol reductive desorption. The antibody is successfully immobilized through the nucleophilic attack of its primary amino groups to the terminal N-succinimidyl group of DTSP. The position of the SPR, defined as the minimum in Ψ, has been simulated before and after the immobilization to confirm the correlation between the experimental energy shift of the SPR and the energy shift expected from the Fresnel analysis.

The antibody immobilization and the consequent biological interaction with the GSH-AuNPs have been monitored by real-time TIRE measurements. From this experiment, it is concluded that 1 hour is enough time to ensure the equilibrium of the biological system after recognition.

The optimal concentration of GSH-AuNPs has been estimated by measuring the energy shift undergone for different GSH-AuNPs concentrations. A concentration of 40 nM has been found to be the value that caused the largest energy shift in the SPR. The presence of the GSH-AuNPs has been confirmed by SEM images.

On the basis of the above results, an immunoassay for GSH detection has been developed based on the competition between free GSH and GSH-AuNPs for the active sites of the antibody. As shown above, the present scheme has been chosen due to the amplifying role of AuNPs in the resonance shift. Thus, higher concentrations of free GSH lead to obtain lower resonance shifts. The immunosensor has shown detection limits in the nanomolar range and good reproducibility values.

REFERENCES

1. J. Homola. Present and future of surface plasmon resonance biosensors. *Anal. Bioanal. Chem.* **2003**, 377, 528-539.
2. M. Poksinski; H. Arwin. Protein monolayers monitored by internal reflection ellipsometry. *Thin Solid Films* **2004**, 455-456, 716-721.
3. P. Westphal; A. Bornmann. Biomolecular detection by surface plasmon enhanced ellipsometry. *Sensor. Actuat. B-Chem.* **2002**, 84, 278-282.
4. M. Poksinski; H. Arwin. Total internal reflection ellipsometry: ultrahigh sensitivity for protein adsorption on metal surfaces. *Opt. Lett.* **2007**, 32, 1308-1310.
5. J.-H. Lee; B.-C. Kim; B.-K. Oh; J.-W. Choi. Highly sensitive localized surface plasmon resonance immunosensor for label-free detection of HIV-1. *Nanomedicine* **2013**, 9, 1018-1026.
6. D. E. P. Souto; J. V. Silva; H. R. Martins; A. B. Reis; R. C. S. Luz; L. T. Kubota; F. S. Damos. Development of a label-free immunosensor based on surface plasmon resonance technique for the detection of anti-Leishmania infantum antibodies in canine serum. *Biosens. Bioelectron.* **2013**, 46, 22-29.
7. J. Ashley; S. F. Y. Li. An aptamer based surface plasmon resonance biosensor for the detection of bovine catalase in milk. *Biosens. Bioelectron.* **2013**, 48, 126-131.
8. V. Nanduri; A. K. Bhunia; S.-I. Tu; G. C. Paoli; J. D. Brewster. SPR biosensor for the detection of L. monocytogenes using phage-displayed antibody. *Biosens. Bioelectron.* **2007**, 23, 248-252.
9. M.-C. Estevez; J. Belenguer; S. Gomez-Montes; J. Miralles; A. M. Escuela; A. Montoyad; L. M. Lechuga. Indirect competitive immunoassay for the detection of fungicide Thiabendazole in whole orange samples by Surface Plasmon Resonance. *Analyst* **2012**, 137, 5659-5665.
10. A. Nabok; A. Tsargorodskaya; M. K. Mustafa; I. Székács; N. F. Starodub; A. Székács. Detection of low molecular weight toxins using an optical phase method of ellipsometry. *Sensor. Actuat. B-Chem.* **2011**, 154, 232–237.
11. A. Nabok; A. Tsargorodskaya; A. Hassan; N. Starodub. Total internal reflection ellipsometry and SPR detection of low molecular weight environmental toxins. *Appl. Surf. Sci.* **2005**, 246, 381-386.
12. Y. Tanaka; R. Yatabe; K. Nagatomo; T. Onodera; K. Matsumoto; K. Toko. Preparation and Characteristics of Rat Anti-1,3,5-Trinitroperhydro-1,3,5-Triazine (RDX) Monoclonal Antibody and Detection of RDX Using Surface Plasmon Resonance Immunosensor. *IEEE Sensors J.* **2013**, 13, 4452-4458.
13. H. Arwin; M. Poksinski; K. Johansen. Total internal reflection ellipsometry: principles and applications. *Appl. Optics* **2004**, 3028-3036.
14. C.-C. Chang; N.-F. Chiu; D. S. Lin; Y. Chu-Su; Y.-H. Liang; C.-W. Lin. High-sensitivity detection of carbohydrate antigen 15-3 using a gold/zinc oxide thin film surface plasmon resonance-based biosensor. *Anal. Chem.* **2010**, 82, 1207-1212.
15. J. L. Pau; J. M. Abad; M. J. Hernández; M. Cervera; E. Ruiz; C. G. Nuñez; E. Lorenzo; J. Piqueras. In *Investigation of surface plasmon resonance in Au nanoparticles deposited on ZnO:Al thin films*, Proceedings of the 8th Spanish Conference on Electron Devices, CDE'2011, 2011.
16. F. P. Zamborini; L. Bao; R. Dasari. Nanoparticles in Measurement Science. *Anal. Chem.* **2012**, 84, 541-576.
17. L. A. Lyon; M. D. Musick; M. J. Natan. Colloidal Au-Enhanced Surface Plasmon Resonance Immunosensing. *Anal. Chem.* **1998**, 70, 5177-5183.

18. M.-C. Daniel; D. Astruc. Gold Nanoparticles: Assembly, Supramolecular Chemistry, Quantum-Size-Related Properties, and Applications toward Biology, Catalysis, and Nanotechnology. *Chem. Rev.* **2004**, 104, 294-346.
19. J. Zhang; X. Xuab; X. Yang. Highly specific colorimetric recognition and sensing of sulfide with glutathione-modified gold nanoparticle probe based on an anion-for-molecule ligand exchange reaction. *Analyst* **2012**, 137, 1556-1558.
20. P. Tiwari; K. Vig; V. Dennis; S. Singh. Functionalized Gold Nanoparticles and Their Biomedical Applications. *Nanomaterials* **2011**, 1, 31.
21. X. Honga; E. A. H. Hall. Contribution of gold nanoparticles to the signal amplification in surface plasmon resonance. *Analyst* **2012**, 137, 4712-4719.
22. X. Cao; Y. Ye; S. Liu. Gold nanoparticle-based signal amplification for biosensing. *Anal. Biochem.* **2011**, 417, 1-16.
23. R. S. Moirangthem; Y.-C. Chang; P.-K. Wei. Ellipsometry study on gold-nanoparticle-coated gold thin film for biosensing application. *Biomed. Opt. Express* **2011**, 2, 2569-2576.
24. A. Meister. Selective modification of glutathione metabolism. *Science* **1983**, 220, 472-477.
25. D. W. Hedley; S. Chow. Evaluation of Methods for Measuring Cellular Glutathione Content Using Flow Cytometry. *Cytometry* **1994**, 15, 349-358.
26. H. Sies. Glutathione and its cellular functions. *Free Radic. Biol. Med.* **1999**, 27, 916-921.
27. A. Meister; M. E. Anderson. *Annu. Rev. Biochem.* **1983**, 52, 711–760.
28. M. Gutscher; A. L. Pauleau; L. Marty; T. Brach; G. H. Wabnitz; Y. Samstag; A. J. Meyer; T. P. Dick. Real-time imaging of the intracellular glutathione redox potential. *Nat. Methods* **2008**, 5, 553-559.
29. T. M. Buttke; P. A. Sandstrom. Oxidative stress as a mediator of apoptosis. *Immunol. Today* **1994**, 15, 7-10.
30. C. Appenzeller-Herzog. Glutathione- and non-glutathione-based oxidant control in the endoplasmic reticulum. *J Cell. Sci.* **2011**, 124, 847-855.
31. M. J. May; T. Vernoux; T. Leaver; M. Van Montagu; D. Inzé. *J. Exp. Bot.* **1998**, 49, 649–667.
32. E. A. Ruan; S. Rao; J. S. Burdick; S. J. Stryker; G. L. Telford; M. F. Otterson; E. C. Opara; T. R. Koch. Glutathione levels in chronic inflammatory disorders of the human colon. *Nutr. Res.* **1997**, 17, 463-473.
33. C. B. Pocernich; D. A. Butterfield. Elevation of glutathione as a therapeutic strategy in Alzheimer disease. *Biochim. Biophys. Acta* **2012**, 1822, 625-630.
34. L. Lusini; S. A. Tripodi; R. Rossi; F. Giannerini; D. Giustarini; M. T. d. Vecchio; G. Barbanti; M. Cintorino; P. Tosi; P. D. Simplicio. Altered glutathione anti-oxidant metabolism during tumor progression in human renal-cell carcinoma. *Int. J. Cancer* **2001**, 91, 55-59.
35. R. M. L. Galera; J. C. J. Giménez; J. B. M. Ronsano; R. M. S. Cardona; M. A. A. Via; C. A. Roca; J. M. T. Puigbert. *Clin. Chim. Acta* **1996**, 254, 63-72.
36. E. Mayatepek; J. Jaeken. Disorders in the Metabolism of Glutathione and Imidazole Dipeptides. In *Inborn Metabolic Diseases*, Saudubray, J.-M.; van den Berghe, G.; Walter, J., Eds. Springer Berlin Heidelberg: 2012; pp 423-430.
37. A. Meister. Glutathione Metabolism and Its Selective Modification *J. Biol. Chem.* **1988**, 263, 17205-17208.
38. A. García-Marín; J. M. Abad; E. Ruiz; E. Lorenzo; J. Piqueras; J. L. Pau. Glutathione Immunosensing Platform Based on Total Internal Reflection Ellipsometry Enhanced by Functionalized Gold Nanoparticles. *Anal. Chem.* **2014**, 86, 4969-4976.

39. J. C. Love; L. A. Estroff; J. K. Kriebel; R. G. Nuzzo; G. M. Whitesides. Self-assembled monolayers of thiolates on metals as a form of nanotechnology. *Chem. Rev.* **2005**, 105, 1103-1169.
40. R. G. Nuzzo; D. L. Allara. Adsorption of bifunctional organic disulfides on gold surfaces. *J. Am. Chem. Soc.* **1983**, 105, 4481-4483.
41. J.-W. Park; J. S. Shumaker-Parry. Structural Study of Citrate Layers on Gold Nanoparticles: Role of Intermolecular Interactions in Stabilizing Nanoparticles. *J. Am. Chem. Soc.* **2014**, 136, 1907-1921.
42. B. H. Stuart. *Infrared Spectroscopy: Fundamentals and Applications*. Wiley: 2004.
43. E. J. Baran; I. Viera; M. H. Torre. Vibrational spectra of the Cu(II) complexes of l-asparagine and l-glutamine. *Spectrochim. Acta, Part A* **2007**, 66, 114-117.
44. S. K. Ghosh; S. Nath; S. Kundu; K. Esumi; T. Pal. Solvent and Ligand Effects on the Localized Surface Plasmon Resonance (LSPR) of Gold Colloids. *J. Phys. Chem. B* **2004**, 108, 13963-13971.
45. W. Qian; S. Krimm. Vibrational analysis of glutathione. *Biopolymers* **1994**, 34, 1377-1394.
46. M. Picquart; L. Grajcar; M. H. Baron; Z. Abedinzadeh. Vibrational Spectroscopic Study of Glutathione Complexation in Aqueous Solutions. *Biospectroscopy* **1999**, 5, 328-337.
47. A. Barth; P. I. Haris. *Biological and biomedical infrared spectroscopy*. IOS Press: 2009.
48. S.-i. Imabayashi; D. Hobara; T. Kakiuchi; W. Knoll. Selective Replacement of Adsorbed Alkanethiols in Phase-Separated Binary Self-Assembled Monolayers by Electrochemical Partial Desorption. *Langmuir* **1997**, 13, 4502-4504.
49. M. Darder; K. Takada; F. Pariente; E. Lorenzo; H. D. Abruña. Dithiobissuccinimidyl propionate as an anchor for assembling peroxidases at electrodes surfaces and its application in a H_2O_2 biosensor. *Anal. Chem* **1999**, 71, 5530-5537.
50. R. S. Moirangthem; Y.-C. Chang; S.-H. Hsu; P.-K. Wei. Surface plasmon resonance ellipsometry based sensor for studying biomolecular interaction. *Biosens. Bioelectron.* **2010**, 25, 2633-2638.
51. M. J. Hernandez; J. Garrido; J. Piqueras. Silicon dioxide deposition by electron cyclotron resonance plasma: Kinetic and ellipsometric studies. *J. Vac. Sci. Technol. B* **1994**, 12, 581-584.
52. D. E. Aspnes; E. Kinsbron; D. D. Bacon. Optical properties of Au: sample effects. *Phys. Rev. B* **1980**, 21, 3290-3299.
53. I. H. Malitson. Interspecimen Comparison of the Refractive Index of Fused Silica. *J. Opt. Soc. Am.* **1965**, 55, 1205-1208.
54. M. E. Browning-Kelley; K. Wadu-Mesthrige; V. Hari; G. Y. Liu. Atomic Force Microscopic Study of Specific Antigen/Antibody Binding. *Langmuir* **1997**, 13, 343-350.
55. J. J. Mock; R. T. Hill; A. Degiron; S. Zauscher; A. Chilkoti; D. R. Smith. Distance-Dependent Plasmon Resonant Coupling between a Gold Nanoparticle and Gold Film. *Nano Lett.* **2008**, 8, 2245-2252.
56. J. D. Adams; J. N. Johannessen; J. P. Bacon. Quantification of glutathione and glutathione disulfide in human plasma. *Clin. Chem.* **1987**, 33, 1675-1676.
57. S. Curello; C. Ceconi; A. Cargnoni; A. Cornacchiari; R. Ferrari; A. Albertini. Improved procedure for determining glutathione in plasma as an index of myocardial oxidative stress. *Clin. Chem.* **1987**, 33, 1448-1449.
58. G. Wu; Y.-Z. Fang; S. Yang; J. R. Lupton; N. D. Turner. Glutathione Metabolism and Its Implications for Health. *J. Nutr.* **2004**, 134, 489-492.

59. A. J. Meyer; M. J. May; M. Fricker. Quantitative in vivo measurement of glutathione in Arabidopsis cells. *The Plant Journal.* **2001**, 27, 67-78.
60. ELISA commercial kits for glutathione. http://www.biomatik.com/products/productDetail/ELISA-Kit-for-Glutathione--GSH---General--competitive-type.aspx, http://www.uscnk.com/uscn/ELISA-Kit-for-Glutathione-GSH-1197.htm (accessed May, 2016).
61. P. Miao; L. Liu; Y. Nie; G. Li. An electrochemical sensing strategy for ultrasensitive detection of glutathione by using two gold electrodes and two complementary oligonucleotides. *Biosens. Bioelectron.* **2009**, 24, 3347-3351.
62. P. C. White; N. S. Lawrence; J. Davis; R. G. Compton. Electrochemical determination of thiols: A perspective. *Electroanal.* **2002**, 14, 89-98.
63. J. C. Ndamanisha; J. Bai; B. Qi; L. Guo. Application of electrochemical properties of ordered mesoporous carbon to the determination of glutathione and cysteine. *Anal. Biochem.* **2009**, 386, 79-84.
64. C. Lu; Y. Zu; V. W. W. Yam. Nonionic surfactant-capped gold nanoparticles as postcolumn reagents for high-performance liquid chromatography assay of low-molecular-mass biothiols. *J. Chromatogr. A* **2007**, 1163, 328-332.
65. W. Zhang; F. Wan; W. Zhu; H. Xu; X. Ye; R. Cheng; L.-T. Jin. Determination of glutathione and glutathione disulfide in hepatocytes by liquid chromatography with an electrode modified with functionalized carbon nanotubes. *J. Chromatogr. B* **2005**, 818, 227-232.
66. J. Vacek; B. Klejdus; J. Petrlová; L. Lojková; V. Kubá. A hydrophilic interaction chromatography coupled to a mass spectrometry for the determination of glutathione in plant somatic embryos *Analyst* **2006**, 131, 1167-1174.
67. H. Kataoka; K. Takagi; M. Makita. Determination of glutathione and related aminothiols by gas chromatography with flame photometric detection. *Biomed. Chromatogr.* **1995**, 9, 85-89.
68. A. E. Gerdon; D. W. Wright; D. E. Cliffel. Quartz crystal microbalance detection of glutathione-protected nanoclusters using antibody recognition. *Anal. Chem.* **2005**, 77, 304-310.

6. Ellipsometric biosensing platforms based on gallium nanostructures

6.1. Introduction

The surface plasmon can be confined in a nanostructure, if the size is smaller than the wavelength of light used to excite it. This phenomenon is known as localized surface plasmon resonance (LSPR). Unlike the SPR in thin films, the finiteness of the nanostructure geometry relaxes the requirements to excite its resonance. Nanostructures exhibit a dispersion relation in the form of a rather flat horizontal line, enabling the direct coupling of the light with the right photon energy and polarization.

The most common nanostructures for producing LSPR are those of Au and Ag, which have attracted considerable attention.[1-4] In air, they present plasmonic effects in the visible range. In particular, spherical-shaped nanoparticles (NPs) show the LSPR when the real part of the dielectric function takes the value of -2 in air (Fröhlich's condition in the quasi-static approximation).[5] Table 6.1 includes the wavelength at which this condition occurs for different metals: Ga, In, Au, Ag, Pt and Cu. Optical constants have been taken from the literature, whereas Pt has been found in the database of the WVASE software.[6-10] The resonance is found at wavelengths larger than 350 nm for Au, Ag and Cu. However, spherical Ga, In and Pt nanoparticles present the LSPR phenomenon deeper in the UV.

The resonant condition of these nanostructures is influenced by different factors, such as the nanostructure geometry, refractive index of the surrounding medium, presence of the substrate, etc. An increase of the refractive index of surrounding medium produces an energy shift towards lower energies, that is, higher wavelengths. A similar behavior is observed when the nanostructures are placed in direct contact with a dielectric substrate. On the other hand, the geometry can yield the splitting of the resonance into two or more oscillatory modes, depending on the geometry acquired.

Table 6.1. LSPR position for different metals in the Fröhlich's condition in air.

Material	Resonance (nm)
Au	490
Ag	370
Cu	365
Ga	305
Pt	230
In	170

Ga is a low-melting point metal (~30 ºC) that, in the form of a nanostructure, presents strong supercooling effects yielding freezing temperatures (< -50 ºC) well below the melting point of the bulk material. Ga nanoparticles (GaNPs) have become an attractive solution for LSPR applications due to their interesting properties. One of the most relevant properties is the wide tunability of the resonance energy. Previous ellipsometric analysis carried out by other authors have shown the large shift of the optical extinction based on these NPs as a function of size when they are deposited on dielectric substrates.[11-13] Other advantages reported for GaNPs are the resilience of the plasmon energy to the metal surface oxidation and the simplicity of the preparation methods.[9, 13] Several techniques have been used to obtain these NPs such as molecular beam epitaxy (MBE),[12, 13] thermal evaporation[14, 15] and colloidal synthesis.[16] The first two approaches are the most common in the bibliography and involve the NP growth on a substrate. Due to coalescence processes, bimodal distributions with large NPs surrounded by smaller ones are mainly obtained. During the growth, these NPs are in liquid phase and typically take a hemispherical morphology due to the large surface tension of Ga.[17] After their exposure to ambient conditions, these NPs are surrounded by a very thin oxide shell,

lower than 3.0 nm, which preserves the hemispherical shape of the liquid Ga core on the substrate.[16, 18, 19]

The effective use of GaNPs has been demonstrated in different applications, such as Surface-Enhanced Raman Spectroscopy (SERS), fluorescence spectroscopy, and photo-induced degradation studies of biomolecules, showing large UV local enhancement factors compared to Au or Ag NPs.[20-22] Recently, their potential applicability for biomedical applications through the inhibition of microorganism growth has been demonstrated.[23] In ellipsometric analysis under external reflection, GaNPs have been also studied, presenting two bands in the pseudodielectric function, attributed to in-plane and out-of-plane oscillatory modes.[11, 13] Their energies are determined by the NP size, the dielectric properties of the substrate and the incidence angle. These bands shift in energy as a function of the NP size, covering a wide range from the UV to the IR, for NP radii in the 10-150 nm range.

This part of this work describes the development of biosensing platforms based on GaNPs. These NPs are deposited on Si substrates by Joule-effect thermal evaporation of metallic Ga. The plasmonic behavior of GaNPs is investigated by means of the Mie theory and discrete dipole approximation (DDA). Their optical properties are analyzed using spectroscopic ellipsometry under external reflection mode at different incidence angles. The study shows evidence of a characteristic behavior of the pseudodielectric function when the p-component of the reflected beam retards with respect to the s-component. This effect leads to a reversal of polarization handedness (RPH), when Δ becomes 180º, a condition that has been proved to be sensitive to the modification of the GaNP surface.[24, 25] To demonstrate the sensing capabilities of GaNPs, an immunosensor for the glutathione (GSH) biomolecule and a biosensor for DNA sequences are developed. For the fabrication of the biosensing platform, the GaNPs/Si surfaces are functionalized with the corresponding recognition element: an antibody for the GSH and a capture probe chain for the DNA sequence.

The detection of specific DNA sequences provides the fundamental basis for monitoring a wide variety of viral infection, as well as, genetic and infectious diseases. SPR has shown very good results for label-free DNA and single nucleotide polymorphism (SNP) detection. However, the excitation of plasmons has usually been done in thin films of noble metals[26-28] requiring complex optical coupling systems to excite plasmon waves. In these methods, detection limits have been estimated in the micromolar range,[29, 30] in

particular concerning the detection of SNPs. Only few works reporting detection limits in the nanomolar range can be found in the literature.[31] The use of nanostructures, such as those of Ga, can enable the detection of DNA sequences without the use of coupling systems. In order to assess the great potential of deposited GaNPs, a specific synthetic DNA sequence of *Helicobacter pylori (H. pylori)*, a bacterium that can cause digestive illness and even stomach cancer, has been chosen as a case of study within the framework of developing approaches of broad applicability. These studies have revealed the great potential of deposited GaNPs as a biosensing platform. However, analysis in real samples comprises a more difficult objective.

For this reason, after the quantification of these synthetic oligonucleotides, the applicability of this platform to real genomic DNA samples from patients with Cystic Fibrosis is studied. Cystic Fibrosis is a genetic disease with autosomal recessive inheritance and a high global prevalence, which causes obstruction and recurrent infections of the respiratory tract associated with pancreatic insufficiency, often leading to a fatal outcome. The origin of this disease is the mutation in the Cystic Fibrosis transmembrane conductance regulator gene (CFTR) that codifies the protein with the same name. The role of the CFTR protein is to act as an ion channel for negatively charge ions, such as Cl^-, in the cell membrane of different organs.[32] A malfunction of this protein affects the production of fluids, such as mucus, sweat, etc. A larger number of mutations has been described in this gene, being the F508del the most common,[33] which comprises a three-nucleotide deletion causing the loss of a phenylalanine residue at the position 508 of the CFTR protein. The biosensing platform developed will be able to detect the mutations in the DNA through the comparison to healthy volunteers.

The detection method in these developed biosensors relies on the monitoring of changes induced by the analyte recognition in the pseudodielectric function at the RPH condition. The main differences in this new setup with respect to the previous Chapter are the absence of signal amplifiers and optical coupling systems (such as the prism). Both differences involve an evident simplification of the entire procedure.

6.2. Plasmonic behavior of gallium nanoparticles: Mie theory and discrete dipole approximation

6.2.1. Mie theory calculations

The easiest approach to understand the oscillatory properties of nanostructures is the Mie theory. This theory is the exact solution of Maxwell's equations for an isotropic sphere. MiePlot v4.3.05, a freely available program, is chosen for the purpose of giving an insight on the properties of GaNPs.[34]

The calculations are performed for Ga spheres surrounded by air (n = 1) and compared with the results obtained for Au spheres. Experimental dielectric functions of Ga and Au are taken from the literature and represented in the insets of Figure 6.1.[6, 9] As pointed out in the Introduction, the oxide shell is not considered due to its negligible effect in the LSPR. Figure 6.1 shows the extinction efficiency (Q_{ext}) spectra, defined as the extinction cross-section divided by the geometrical cross-sectional area of the sphere. A strong band is clearly located at around 2.50 eV (496 nm) for the smallest AuNPs (radius ≤ 40 nm, corresponding to the dipolar oscillations of the AuNP, which confers strong red-violet colors to Au colloids. On the other hand, the dipolar oscillations for equivalent GaNPs appear in the UV region, located at 3.50-4.25 eV.

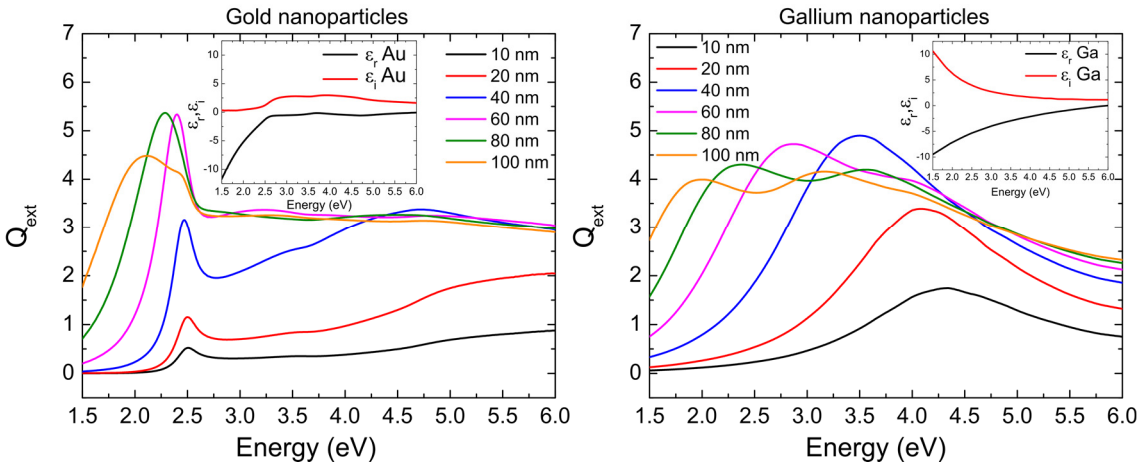

Figure 6.1. Extinction efficiency for spheres of different radii from 10 to 100 nm surrounded by air (n = 1). Inset of this Figure represent the dielectric functions of Ga and Au taken from the bibliography.

If the NP size is increased, the LSPR undergoes a redshift for both materials. The maximum efficiency is obtained for NPs for radius equal to 80 nm, for Au, and 40 nm, for Ga. (Figure 6.1). For very large NPs, another band can be observed at higher photon energies compared to the dipole mode. This high energy band typically corresponds to multipolar oscillations.

It is noteworthy that the word "efficiency" can lead us to believe that this parameter cannot be larger than the unity in the overall spectra. Nevertheless, small particles (sizes somewhat below the wavelength) are well-known to exhibit this behavior and can be interpreted as if they are perturbing the electromagnetic field of an area larger than its cross-section.[35, 36]

The peak energy is estimated and represented in Figure 6.2 as a function of the sphere radii. The resonance energy shift with the NP size is caused by the retardation effects. The interpretation of this phenomenon is that the electron oscillation between one end of the particle and the other one has to accommodate the incident electromagnetic phase. In other words, a particle with a long dimension along the direction of electron oscillation will have a lower LSPR energy (longer wavelength) than the short one.[37, 38]

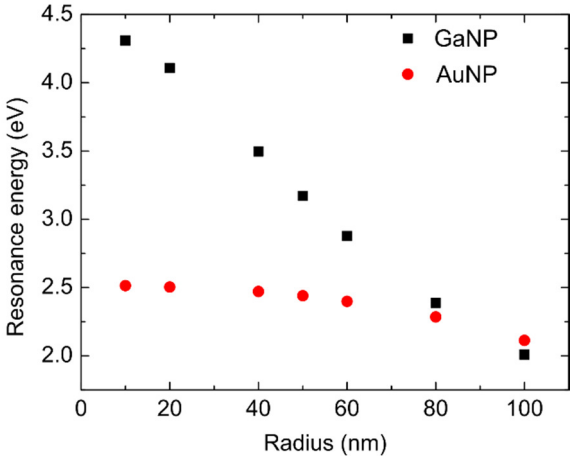

Figure 6.2. Photon energies at the LSPR peak maxima as a function of the sphere radii for Ga and Au materials.

As can be seen in Figure 6.2, the redshift is more significant for Ga than for Au due to its larger dielectric function in the analyzed wavelength region (see insets of Figure

6.1). This is an advantage of Ga over Au because this strong size-sensitive resonance allows the tuning of the optical properties by controlling the NP size.

Mie theory is limited to the study of spherical-shaped nanostructures. Hemispherical-shaped NPs, such as those obtained after Ga evaporation processes, require the use of numerical approaches to deepen into the understanding of the Ga plasmonics.

6.2.2. Discrete dipole approximation calculations

For arbitrary-shape nanostructures, simulations are performed using discrete dipole approximation (DDA), with the software DDSCAT 7.30, freely available online. Hemispheres with radius between 10 and 100 nm are modeled keeping a constant interdipole distance of 2 nm in all experiments. Lower distances have not shown remarkable differences and lead to very long computational times that make the problem unaffordable for a common desktop computer.

In the simulations, the hemispheres are illuminated with linearly polarized light beams in two different configurations to selectively excite in-plane or out-of-plane oscillatory modes. Normal incidence is chosen in Configuration 1, whereas grazing incidence (incidence angle = 90°) is chosen in Configuration 2, being the electric field perpendicular to the wavevector $\vec{k}$ in both cases (transverse wave). Figure 6.3A illustrates the vector directions associated to both configurations. The incidence plane is taken as the plane that divides the hemispherical NP in two halves. Thus, Configuration 1 probes the NP response under s-polarized light, for which the electric field vector $(\vec{E}_S)$ is perpendicular to the incidence plane. In contrast, Configuration 2 probes the response under p-polarized light, for which the electric field $(\vec{E}_P)$ is parallel to the incidence plane. The refractive index of the surrounding medium is 1 and the substrate is not introduced, for the sake of clarity. Each configuration gives rise to an extinction band whose maximum is found at decreasing energies as the NP size increases (Figure 6.3B,C). Figure 6.3D shows the estimated peak energy for both configurations as a function of the hemisphere radii.

The results obtained from the Mie theory for a sphere are located in an energy value between both oscillations modes in the hemisphere. Thus, the symmetry reduction in the hemisphere yields the splitting of the spherical dipolar mode (from 4.25 to 2.00 eV) into two dipolar modes, one at higher photon energies (4.75 to 4.00 eV) and the other one at lower energies (3.50 to 2.00 eV). As shown in the sphere case, the redshift of the peak energy is related to retardation effects.

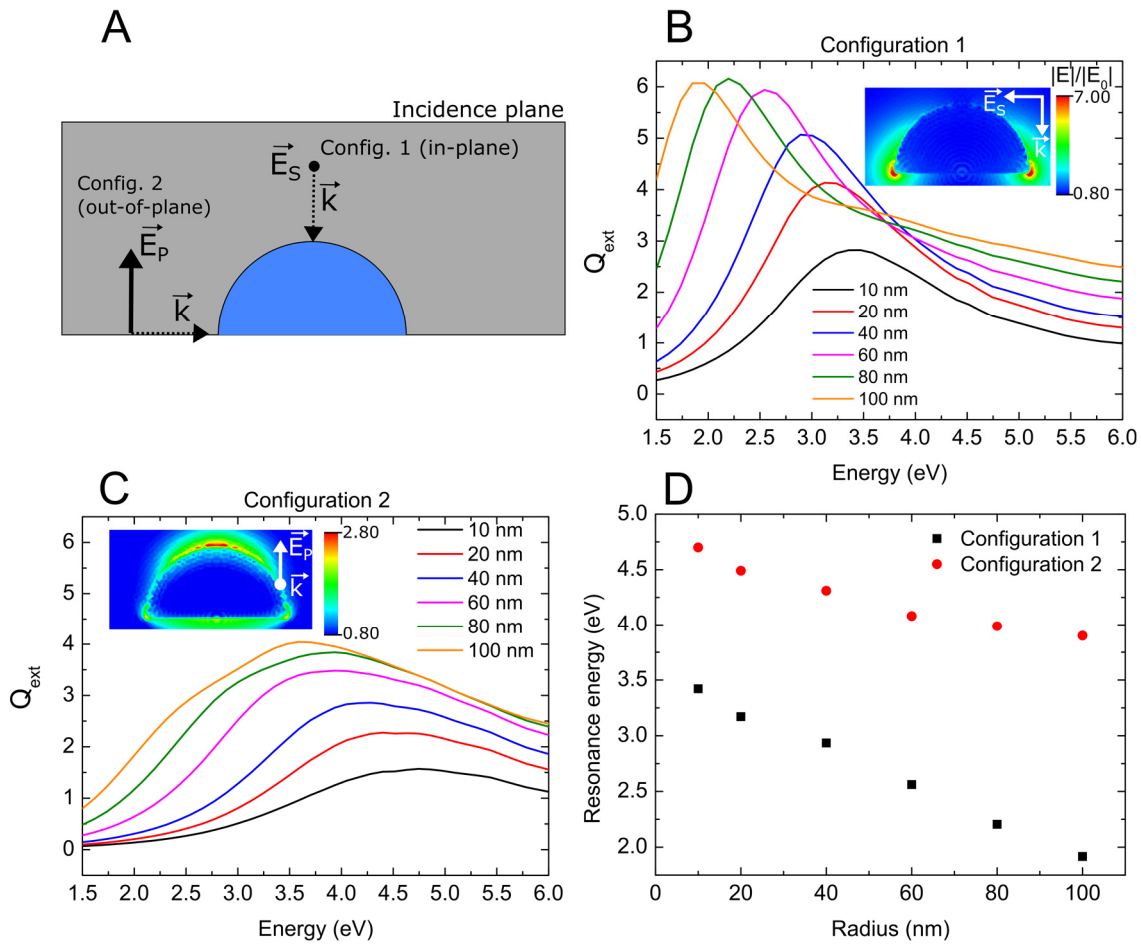

Figure 6.3. (A) Electric field vector and wavevector for Configuration 1 $(\vec{E}_S, \vec{k})$, used for exciting in-plane oscillatory modes, and Configuration 2 $(\vec{E}_P, \vec{k})$, used for the out-of-plane oscillatory modes. The NP has a hemispherical geometry and it is surrounded by a medium with a refractive index of 1; (B,C) extinction efficiency for a single hemisphere of different radii, for Configuration 1 and Configuration 2. Insets of Figure 6.3B,C represent near-field calculations for a hemisphere of radius 60 nm; (D) photon energies at the LSPR peak maxima as a function of the hemisphere radii for Ga and Au materials.

A near-field calculation of normalized electric field intensity $|E|/|E_0|$ inside and in the vicinity of a GaNP is performed for sites defined on a regular rectangular grid that includes the original target.[39] The insets of Figure 6.3B,C represent the electric field distribution in the middle plane perpendicular to the incidence plane for both Configurations. The selected photon energy corresponds, in each case, to the peak energy in the Q_{ext} spectra. As can be observed, the high intensity lobes, also known as *hot spots*, are aligned with the light polarization direction and located near the NP edges. For Configuration 1, the highest field is found at the bottom edge of the NP, whereas, in Configuration 2, the field is essentially enhanced at the upper region of the NP. Although both types of polarizations produce local enhancements of the electric field, the *hot spots* are more intense under s-polarized light beams (see scales on the inset) mainly due to the sharper geometry of the NP edge. This geometrical property also makes that the extinction band in the in-plane mode is narrower and more intense than the same band in the out-of-plane mode.

The addition of a substrate is studied by introducing a rectangular block of 82810 dipoles (180 nm × 18 nm × 180 nm for x, y and z dimensions) in direct contact to a hemisphere of 60411 dipoles (120 nm × 60 nm × 120 nm). These numbers of dipoles result from the use of an interdipole distance of 2 nm. Although a few studies have been performed using a larger substrate, it has been determined that the increase of the volume does not change significantly the resonance energy maximum and introduces a much higher computational cost. Real and imaginary parts of the dielectric functions for the substrate are varied independently. The values introduced helps to give insight into the effect of dielectric substrates, such as glass, silicon or sapphire. As will be shown in the next Section, GaNPs are deposited on Si substrates.

In general, the addition of the substrate results in an attenuation of the extinction efficiency and a shift of the maxima towards lower energies due to the increase of the dielectric function environment below the hemisphere (see Figure 6.4).[9] The increasing value of ε_i also shows a slightly broadening effect. We believe that this is caused by the dampening effect of this parameter, associated to the decay of the electric field amplitude in the SPR wave.[26]

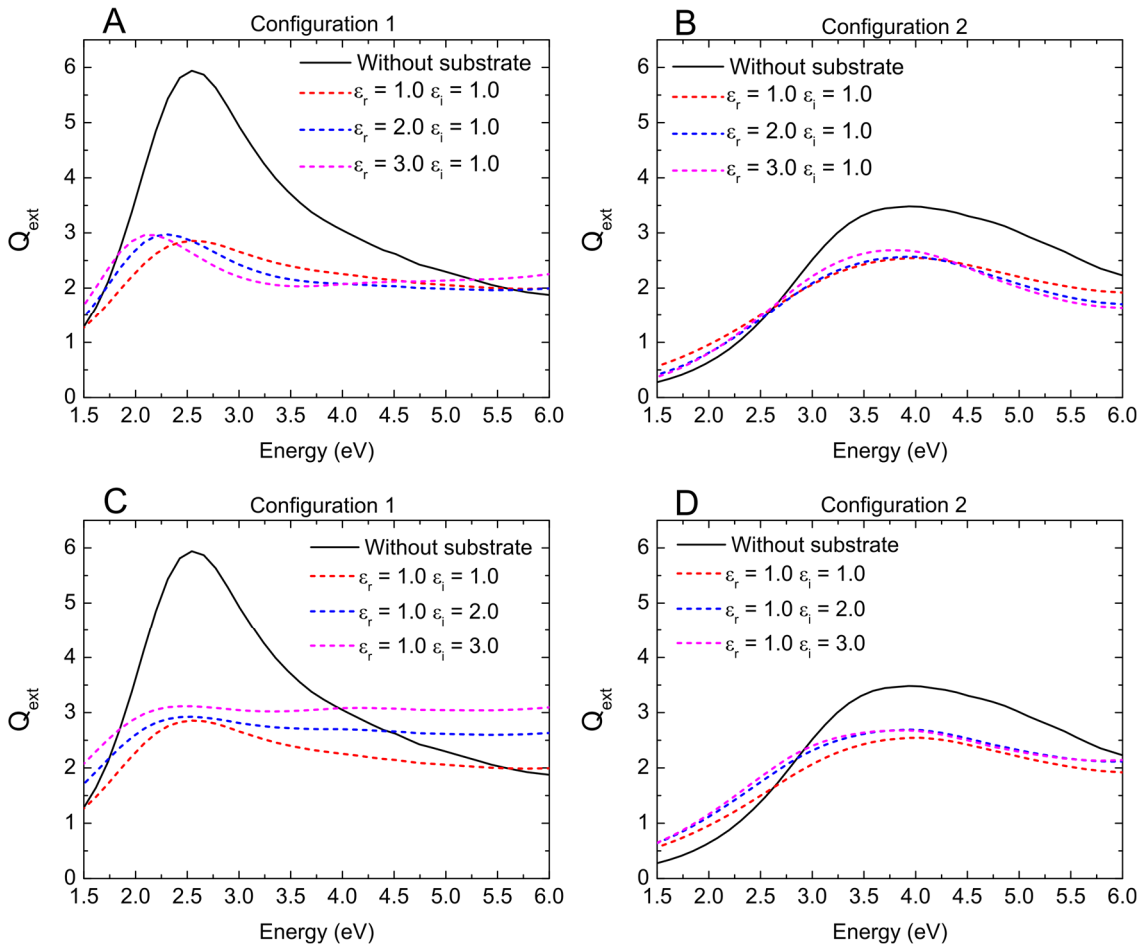

Figure 6.4. Extinction efficiency spectra for a single hemisphere resting on substrates with different dielectric functions under Configuration 1 (A,C) and Configuration 2 (B,D). Results are compared with those obtained for a free-standing hemisphere in air (black curves).

6.3. Characterization of the nanostructured surface

6.3.1. GaNP deposition and characterization of size distribution

GaNPs/Si platforms are formed by deposition of Ga on Si(100) wafers in a Joule-effect thermal evaporator under a constant electrical current for different times ranged between 0.25 and 3 minutes. Prior to Ga deposition, Si substrates are cleaned with an aqueous solution of hydrofluoric acid to etch the native oxide.

After evaporation, the surface is analyzed using SEM in order to study the morphology and the size distribution of the GaNPs. As can be seen in the insets of Figure 6.5, the surface is fully covered by NPs. All evaporations present a large number of particles with radius lower than 75 nm (Figures 6.5A,B correspond to evaporation times of 0.5 and 2 minutes, respectively). As the evaporation time increases, the coalescence of

the smaller particles provokes the appearance of particles with larger radius. As an example, the 2-min evaporation time (Figure 6.5B) produces a group of NPs with radii between 75 and 160 nm and an average value of 120 ± 10 nm. Thus, the final morphology for evaporation times longer than 1.3 min consists of a distribution of large NPs surrounded by a halo of smaller ones, giving rise to bimodal NP distributions, as the one shown in Figure 6.5B.

From cross-sectional images (inset of Figure 6.5A,B), we observe that the NP contact angle on the substrate plane is closed to 90º, giving rise to hemispherical shapes. This morphology results from the surface tension of liquid Ga on the silicon substrate, and it is preserved due to a slight oxidation of the NP surface formed after exposing the NPs to air.[40]

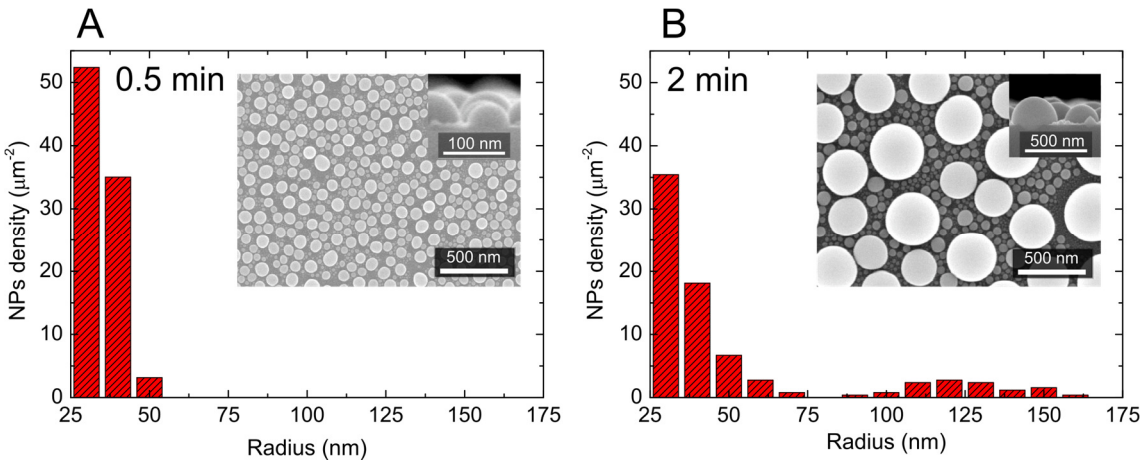

Figure 6.5. Histograms of the NPs for two evaporation times: (A) 0.5 min and (B) 2 min. Insets of Figures 6.5A,B are aerial and cross-sectional SEM images of the as-deposited GaNPs.

6.3.2. X-ray diffractometry

X-ray diffraction analysis of the as-deposited GaNPs/Si platforms are performed in grazing incidence diffraction geometry. In that geometry, the diffraction is surface sensitive due to the low penetration depth of the beam. The data is acquired at an incidence angle of 0.5º (Figure 6.6). The spectra show the appearance of a significant broad band between 30 and 50 degrees, only when GaNPs are present. This type of band is typical of low-crystallinity materials[41] and overlaps with the strongest diffraction lines in orthorhombic α-Ga (dashed vertical lines) and monoclinic β-Ga_2O_3 (dotted vertical

lines), which are the most common phases in ambient conditions for gallium and gallium oxide materials. The diffraction angles are identified from the diffraction files (#00-005-0601 and #01-087-1901) of the International Centre for Diffraction Data (ICDD).

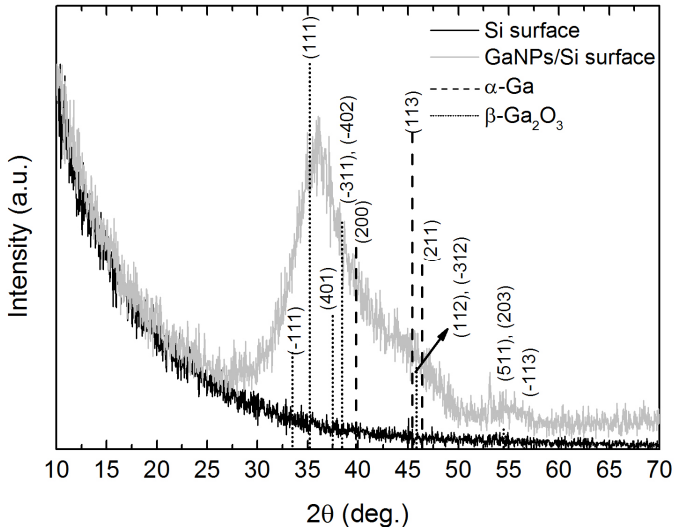

Figure 6.6. X-ray diffractograms of a GaNPs/Si sample (grey curve) and a plain Si wafer (black curve) at an incidence angle of 0.5°. The strongest theoretical diffraction peaks are represented as dashed lines (α-Ga) and dots (β-Ga_2O_3).

6.3.3. X-ray photoelectron spectroscopy

The chemical structure of as-deposited GaNPs/Si platforms is analyzed through XPS. The survey scan (Figure 6.7A) reveals the typical bands associated to Ga ($2p_{1/2}$, $2p_{3/2}$, 3s, $3p_{3/2}$ and $3d_{5/2}$). All bands have been identified by using the LaSurface and the National Institute of Standards and Technology (NIST) databases.[42] Ga $2p_{1/2}$, $2p_{3/2}$ and $3d_{5/2}$ comprise dual bands, similar to the one shown in Figure 6.7B. The high energy band (leftmost) is attributed to the native oxide, whereas the low energy band corresponds to the Ga element. The C1s photoemission band is also present due to unintentional carbon contamination of the surface after exposure to the ambient.[43]

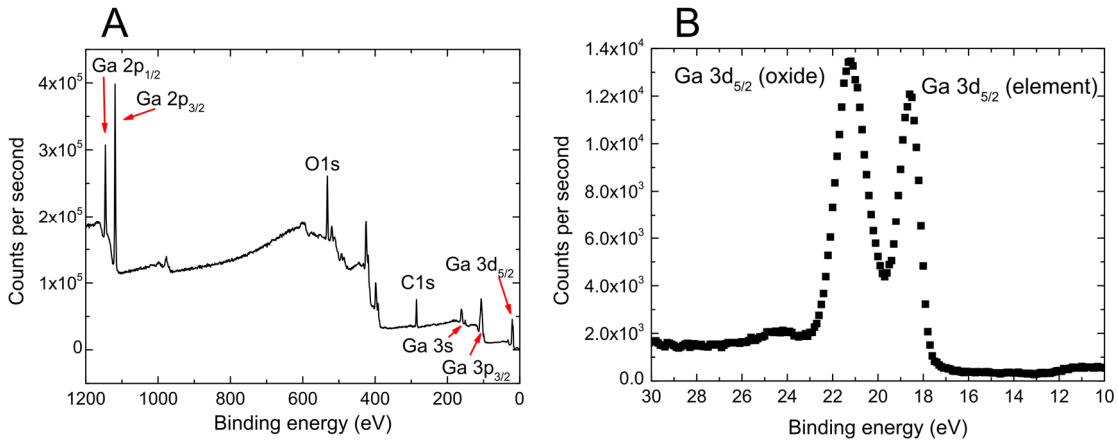

Figure 6.7. (A) XPS survey of a GaNPs/Si sample; Ga $3d_{5/2}$ core level signal.

6.3.4. Ellipsometric characterization of GaNPs/Si platforms

6.3.4.1. Influence of evaporation time

The optical response of the whole GaNPs/Si platform is studied by analyzing the pseudodielectric function in the spectroscopic ellipsometry measurements. The experimental setup is represented in Figure 3.15 of the Chapter 3. The imaginary part of the pseudodielectric function ($<\varepsilon_i>$) accounts for the light extinction upon reflection on the sample surface.[11] It is worth noticing that this function accounts for the optical properties of the whole system, the resonance of the NPs and the Si absorption.

The spectra in Figure 6.8A show $<\varepsilon_i>$ as a function of energy for different evaporation times, recorded at an incidence angle of 70º. Two bands arise in different parts of the spectral range under analysis. The peak energy for both bands is clearly dependent on the NP evaporation time. The low energy band comes out between 1.5 and 2.5 eV for times lower than 1.0 min. Those times yield unimodal distributions of NPs due to the absence of NP coalescence processes. On the other hand, the high energy band in Figure 6.8A is found between 3-5 eV for deposition times larger than 1.3 min. Those evaporation times give rise to bimodal distributions of NPs due to the coalescence process.

Figure 6.8B represents the peak energy for both bands (as open squares and circles). The energies of the low energy band match the energies found for the in-plane resonant mode in the DDA studies of NPs with radii between 30 and 50 nm on a silicon substrate (black dashed curve in Figure 6.8B). It is unlikely that this band is related to

out-of-plane modes because the energies for those resonant modes are found at much larger energies for the NP sizes present in the sample histograms.

As shown above, the high energy band starts to appear in the spectral range under analysis for evaporation times larger than 1.3 min. The DDA studies show that those energies would be preferentially associated with out-of-plane resonant modes although the match between the experimental datapoints and the simulation (red dashed curve in Figure 6.8B) is not perfect. It is hypothesized that the interaction between the small and large NPs in the bimodal distribution found for those deposition times may modify the energy of the resonant mode, shifting it towards higher energies. Thus, slight differences can arise between the $< \varepsilon_i >$ peak energies and the DDA simulations due to the lack of uniformity in the NP distribution induced by the coalescence processes for long evaporation times.

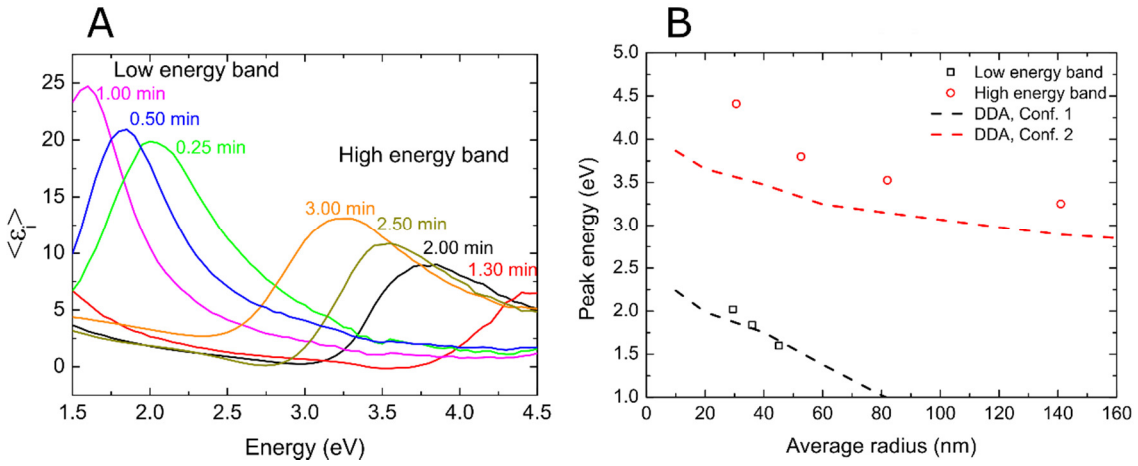

Figure 6.8. (A) $< \varepsilon_i >$ obtained under illumination with an incidence angle of 70º for different evaporation times; (B) peak energies for both absorption bands, as obtained from Figure 6.8A, and compared with DDA simulation results for single hemispheres on a Si substrate (dashed curves).

6.3.4.2. Reversal of polarization handedness (RPH)

Up to now, the ellipsometric response of these NPs has been studied at an incidence angle of 70º. In the following experiments, the influence of the incidence angle is studied for a sample with a deposition time of 2.0 min. As this angle is reduced in the

spectroscopic ellipsometer, $< \varepsilon_i >$ becomes negative in a narrow spectral window below the high energy band producing a characteristic line-shape in $< \varepsilon_i >$ (Figure 6.9A).

To deepen into the understanding of the line-shape origin, the corresponding Ψ and Δ for these incidence angles are also shown in Figure 6.9B. As the photon energy increases from 1.5 eV, Ψ value decreases and a large phase variation in Δ can be observed associated to the retardation of the p-polarized component with respect to the s-polarized one. This variation yields a phase shift difference of $\Delta = 180^{o}$ between both polarization components at high energies (around 3.00 and 3.25 eV in this sample, depending on the incidence angle). This phase shift indicates that there is a reversal of the polarization handedness (RPH) upon reflection on the sample surface. Thus, under those conditions, a reflected beam has a polarization vector that rotates in the opposite direction, compared to the rotation direction of the polarization vector in the incident beam. Between the energy of the Ψ dip and the RPH ($\Delta = 180^{o}$), $< \varepsilon_i >$ takes negative values producing the characteristic line-shape (Figure 6.9A). The maximum peak-to-peak amplitude is achieved when the incidence angle is set at 55°.

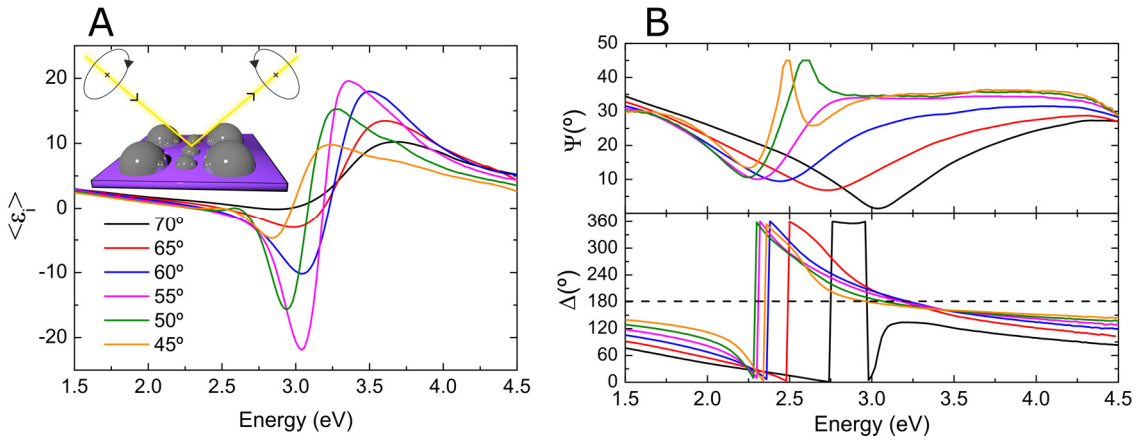

Figure 6.9. (A) $< \varepsilon_i >$ obtained at incidence angles between 45 and 70° for a GaNPs/Si platform with an evaporation time of 2 min. Inset shows a scheme of the RPH condition, where the polarization vector of the reflected beam rotates in the opposite direction respect to the incident beam. (B) Ψ and Δ for the same set of measurements. The RPH condition is highlighted with a horizontal dashed line ($\Delta = 180^{o}$).

From the mathematical viewpoint, $< \varepsilon_i >$ becomes negative when Δ takes values between 360° and 180°, yielding negative values of the numerator in Equation 2.20. The

closer to zero the denominator is in Equation 2.20 in Chapter 2, the larger the peak-to-peak amplitude becomes around the RPH condition (Δ = 180º). This happens when Ψ approaches 45º and $\sin(2\Psi)\cdot\cos(\Delta)$ becomes -1, giving rise to a singularity in $<\varepsilon_i>$. If the incident beam was circularly polarized, this result would yield a reflected beam whose polarization vector would rotate circularly in the opposite direction. The inset of Figure 6.9A shows a representation of this effect.

To study the influence of Ψ and Δ functions over $<\varepsilon_i>$ at the RPH condition, Equation 2.20 in Chapter 2 is differentiated with respect to energy (*E*):

$$\left.\frac{\partial <\varepsilon_i>}{\partial E}\right|_{\Delta=180^\circ} = \frac{\partial <\varepsilon_i>}{\partial \Psi}\cdot\frac{\partial \Psi}{\partial E} + \frac{\partial <\varepsilon_i>}{\partial \Delta}\cdot\frac{\partial \Delta}{\partial E} = -\Lambda\cdot\Theta\cdot\frac{\partial \Delta}{\partial E}, \qquad (6.1)$$

where $\Lambda = \left(\sin(\varphi)\tan(\varphi)\right)^2$ and $\Theta = \sin(4\Psi)/\left(1-\sin(2\Psi)\right)^2$. A representation of Equation 6.1 versus the incidence angle is shown in Figure 6.10A. Ψ data are obtained at the energy where Δ = 180º, whereas $\partial\Delta/\partial E$ values are obtained after differentiating Δ curves around the RPH condition in Figure 6.9B. As can be seen, the maximum value is obtained at 55º, following the similar trend observed in Figure 6.10A, in which the largest variation of $<\varepsilon_i>$ with respect to the energy is observed at the same incidence angle.

Figure 6.10B shows the values of these parameters as a function of the incidence angle for the sample under study. $\partial\Delta/\partial E$ takes negative values, whereas Λ and Θ are both positive. Therefore, $\partial <\varepsilon_i>/\partial E$ remains positive in the spectral region surrounding the RPH condition and enables the quantification of the steep slope.

The behavior of each parameter as a function of the incidence angle is quite different. Thus, for instance, as the incidence angle increases, $\partial\Delta/\partial E$ only experiments slight variations. On the other hand, Λ increases significantly with the incidence angle, whereas Θ undergoes a strong reduction at 55º. The product between the latter parameters is maximized near 55º, justifying the behavior observed for $\partial <\varepsilon_i>/\partial E$.

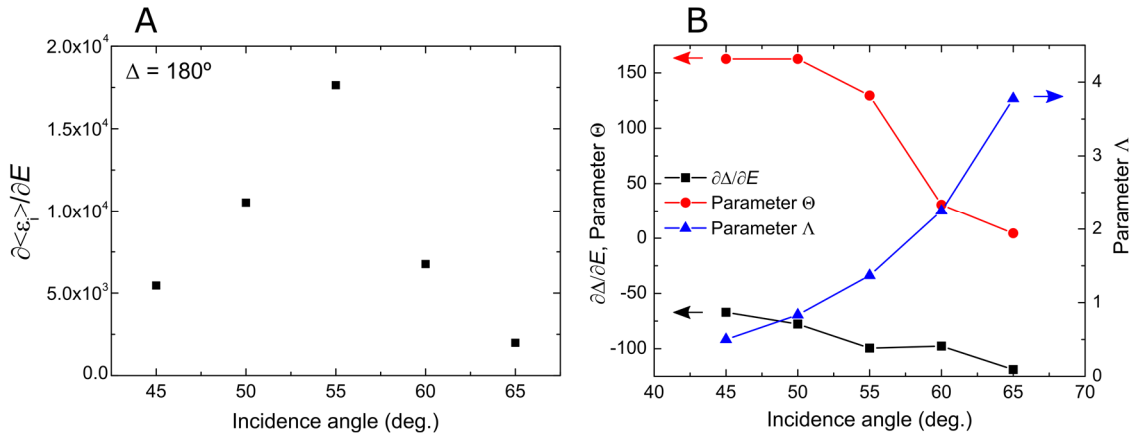

Figure 6.10. (A) $\partial < \varepsilon_i > / \partial E$ as a function of the incidence angle. (B) Representation of the different parameters of Equation 6.1.

The analysis suggests that incidence angles around 55º are optimal to obtain the largest slope of $< \varepsilon_i >$ in the RPH condition for a sample with a deposition time of 2 min.

Figure 6.11 shows $< \varepsilon_i >$ for different deposition times (1.30, 1.50, 2.00, 2.5 and 3 min) taken at 55º. The RPH condition shifts towards lower energies as evaporation time increases. The inset of this Figure shows SEM images of two GaNPs/Si platforms along the study for different evaporation times. It is worth noticing that long evaporation times lead to very large GaNPs, which do not show the RPH condition. Those samples optically behave as a thick Ga film due to the advanced state of coalescence.

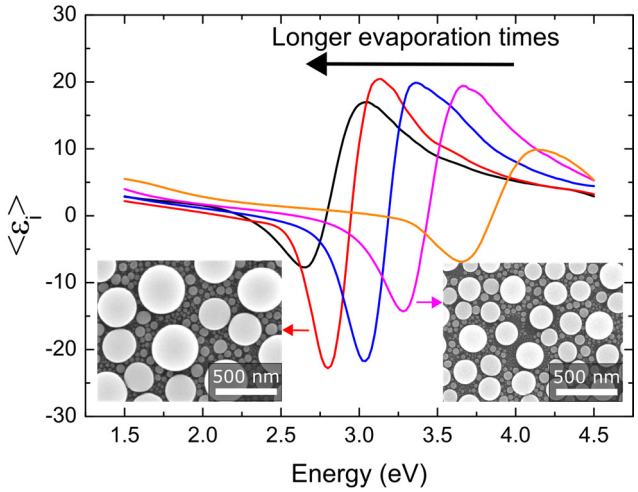

Figure 6.11. $< \varepsilon_i >$ for GaNPs/Si samples obtained from evaporation times of 1.30, 1.50, 2.00, 2.5 and 3 min, measured at a 55º incidence angle. Insets of this Figure show SEM images for two different deposition times.

Hereinafter, the GaNPs/Si samples used for the development of sensors will be obtained from evaporation times of 2 min and they will be interrogated at an incidence angle of 55º to take advantage of the high peak-to-peak amplitude around the RPH condition. Typically, those samples exhibit a similar peak-to-peak amplitude (around 40) and a RPH energy in the 2.8-3.6 eV range. In further experiments, two relevant parameters are quantified for monitoring surface changes induced by chemical modifications: the variation of the slope at the RPH condition ($\delta\theta = \delta\theta_2 - \delta\theta_1$) and the energy shift ($\delta E = \delta E_2 - \delta E_1$) of the inflection point. Both of them can be extracted from $< \varepsilon_i >$ spectra after its differentiation with respect to energy ($\partial < \varepsilon_i > / \partial E$).

6.4. An immunosensor for glutathione

6.4.1. Development of the sensing platform

GaNPs/Si platforms, obtained from an evaporation time of 2 min on Si substrates, are used for the detection of GSH in aqueous solution through immunosensing assays. As represented in the Figure 6.12, the first step for immunosensor development involves the immobilization of the recognition element to construct the biorecognition layer. For this purpose, the GaNPs/Si platforms are functionalized with a monolayer of 3,3′-Dithiodipropionic acid di(N-hydroxysuccinimide ester) (DTSP) by immersion in a 4 mM solution of DTSP in dimethyl sulfoxide (DMSO) and left overnight. Modification with DTSP results in the adsorption of N-succinimidyl-3-thiopropionate (NTSP). We believe that, similar to Au surfaces, disulfides undergo dissociative chemisorption to give rise to the corresponding adsorbed thiolates. An estimation of the NTSP molecule size based on the chemical bonds characteristic length is around 1 nm.

The DTSP-modified GaNPs/Si platform (DTSP-GaNPs) is rinsed with acetone and blown with dry N_2. The next step comprises the immobilization of an antibody specific to GSH (antiGSH) on the DTSP-GaNPs platform by its incubation in 0.01 M KCl solution (pH ≈ 7) containing 150 nM of the antibody for 2 hours. Unreacted succinimidyl moieties from the DTSP remaining on the surface are deactivated by further soaking the platform into the 0.01 M KCl solution for 1 hour. Finally, the developed immunosensor (antiGSH-DTSP-GaNPs) is rinsed with deionized water and blown with dry N_2. Typically, the width and height of IgG antibodies are in the order of 14.5 and 8.5 nm, respectively.[44]

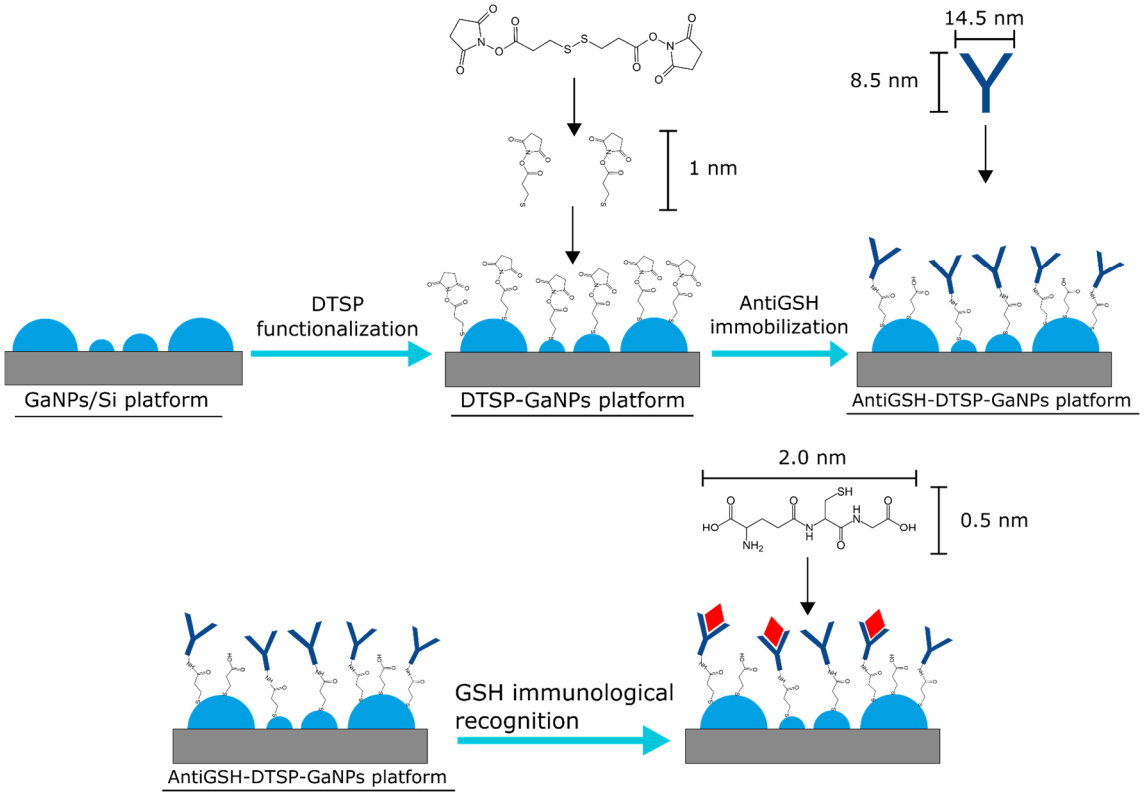

Figure 6.12. Schematic representation of the biosensing platform development and the GSH biological recognition. An estimation of the size of used biomolecules, based on the chemical bonds length, is also represented in that Figure. Information about the length of the bonds has been found in the literature.[45]

6.4.1.1. FTIR characterization

In order to assess the success of the GaNPs/Si platform functionalization with DTSP and the subsequent immobilization of the antiGSH on the DTSP-functionalized platform, FTIR measurements are performed under diffuse reflectance configuration. All the FTIR spectra in Figure 6.13 are shown referenced to the spectrum obtained from as-evaporated GaNPs on the Si substrate.

After the functionalization with DTSP (black curve in Figure 6.13), the C=O symmetric stretching mode, ν_s(CO), at 1747 cm^{-1} can be identified. The broad band observed in the 3100-3400 cm^{-1} range can be attributed to ν(-OH) vibrations, likely caused by adsorbed water molecules. On the other hand, the FTIR spectrum after antibody immobilization is represented as a red curve in Figure 6.13. The typical amide bands are evident after the antibody immobilization: the amide I band, centered at 1684 cm^{-1}, (mainly C=O symmetric stretching mode, ν_s(CO)) and the amide II band, centered at 1546 cm^{-1}, (CNH in-plane bending and C-N symmetric stretching modes, δ(CNH) and

ν_s(CN)).[46] Additionally, the 3100-3400 cm^{-1} broad band, attributed before to ν(-OH) vibrations, can overlap with those modes found for amine groups [ν_s(NH) and ν_{as}(NH)].

From this analysis, we can conclude that the GaNPs/Si platform has been successfully functionalized. It is worth noticing that the bands are weak because the DTSP and the antibody typically form very thin layers with thicknesses of several nanometers.

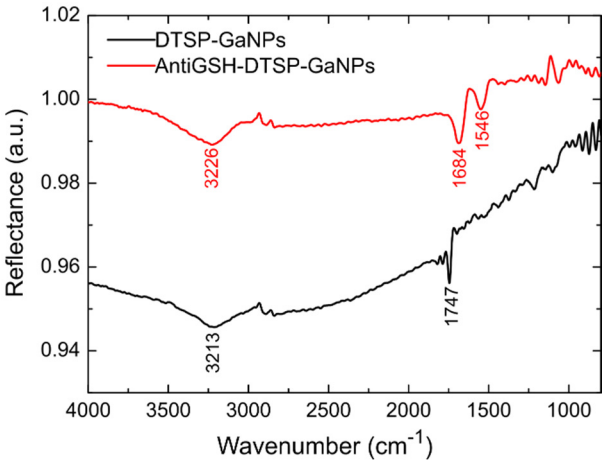

Figure 6.13. FTIR spectra of DTSP-GaNPs (black curve) and antiGSH-DTSP-GaNPs (red curve) surfaces. All spectra are referenced to the spectrum obtained from the as-evaporated GaNPs/Si platform (non-functionalized)

6.4.1.2. Ellipsometric characterization

The successive steps followed for GaNPs/Si sensor development are characterized by ellipsometry. For this purpose, $<\varepsilon_i>$ is recorded at 55º under external reflection configuration for each functionalization step and shown in Figure 6.14A. For the sake of clarity, these spectra are differentiated with respect to the energy, denoted as $\partial <\varepsilon_i> / \partial E$, to obtain the inflexion point (Figure 6.14B). This Figure reveals changes in both $\delta\theta$ and δE parameters, related to the chemical modification of the NPs surface. The bonding of the antiGSH to the DTSP layer produces the most pronounced energy shift in the inflection point (δE = 110 meV), as this biomolecule is considerably larger in size than the DTSP (δE = 3 meV). The DTSP is a low molecular weight molecule, whose size is estimated in the nanometer level, giving rise to a weaker energy shift compared to an antibody (see Figure 6.12 to compare the estimated sizes).

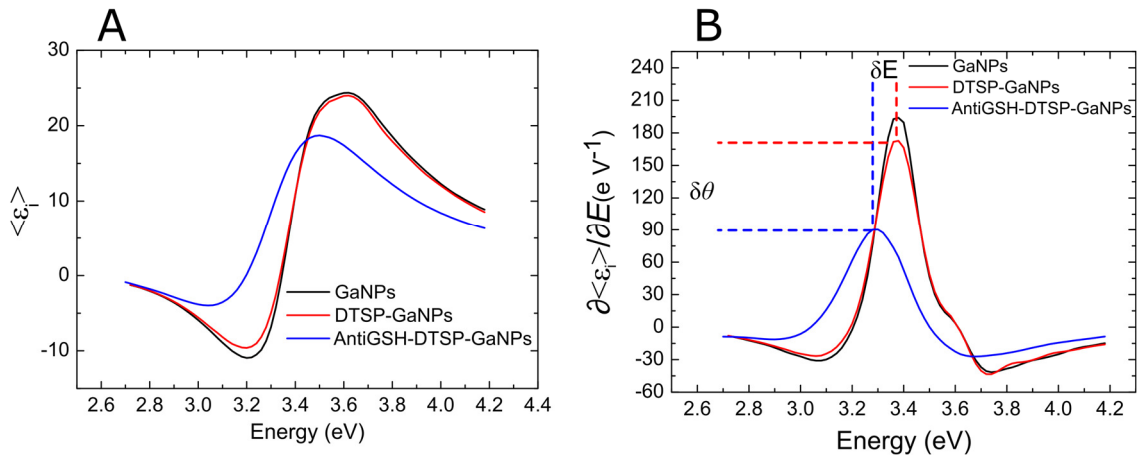

Figure 6.14. (A) $< \varepsilon_i >$ measured after each functionalization step: as-deposited GaNPs, after forming the DTSP layer and after antibody immobilization (black, red and blue curves respectively); (B) $\partial < \varepsilon_i > / \partial E$ spectra obtained after differentiation of $< \varepsilon_i >$ with respect to the energy.

The optimal amount of the antibody to cover the surface of the GaNPs/Si platforms through the bonding to DTSP is determined by immobilizing antiGSH with concentrations ranging from 25 to 600 nM. The results of this experiment are represented in Figure 6.15. As the antiGSH concentration increases, δE undergoes a larger redshift that is proportional to the surface coverage. Finally, δE reaches a plateau, which reveals the saturation of the DTSP binding sites on the GaNPs. The data is optimally fitted to a Langmuir isotherm (Equation 6.2), which accounts for the formation of a monolayer:

$$\delta E = \delta E_{\max} \cdot K_L \cdot c \,/\, 1 + K_L \cdot c \,, \qquad (6.2)$$

where K_L and c are the Langmuir constant and the antibody concentration, respectively. The fitting is included in this Figure as a red curve. A δE_{max} of 146 meV results from the fitting. To prevent unnecessary reactive consumption, an antibody concentration of 150 nM is an optimal choice since it is found in the plateau. Much higher antiGSH concentrations only may lead to slightly higher responses, whereas lower concentrations can reduce GSH recognition sites and, thus, sensor sensitivity.

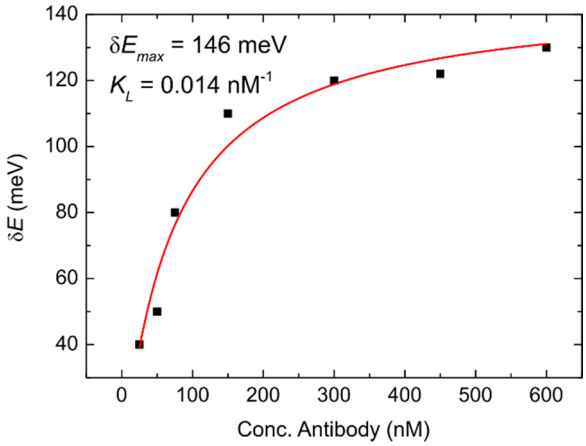

Figure 6.15. Saturation curve for antibody concentrations ranged between 25-600 nM.

6.4.2. Biosensor response and quantification of glutathione

To evaluate the immunosensing response of the developed platform to the GSH biomolecule, an antiGSH-DTSP-GaNPs platform is incubated for 1 hour with the aqueous solution of 100 nM of GSH, followed by a rinsing stage with deionized water and blowing with N_2. The incubation time is chosen according to the results obtained from the kinetic study between the same antibody and analyte, as shown in the previous Chapter. In that experiment, it was concluded that 35 min are enough to ensure that the binding process reaches the equilibrium.[47] Although no significant changes in δE are observed (see Figure 6.16A,B), an attenuation of the peak-to-peak amplitude in $< \varepsilon_i >$ is clear. The negligible energy shift is attributed to the fact that specific binding of GSH to the immunosensor surface does not contribute significantly to the total refractive index of the system in comparison to the contribution of the antiGSH binding before the recognition event. However, an attenuation in the spectra is observed, somewhat caused by the antigen-antibody recognition. Thanks to this attenuation, the slope at the inflection point ($\delta\theta$) is measured, instead of using δE.

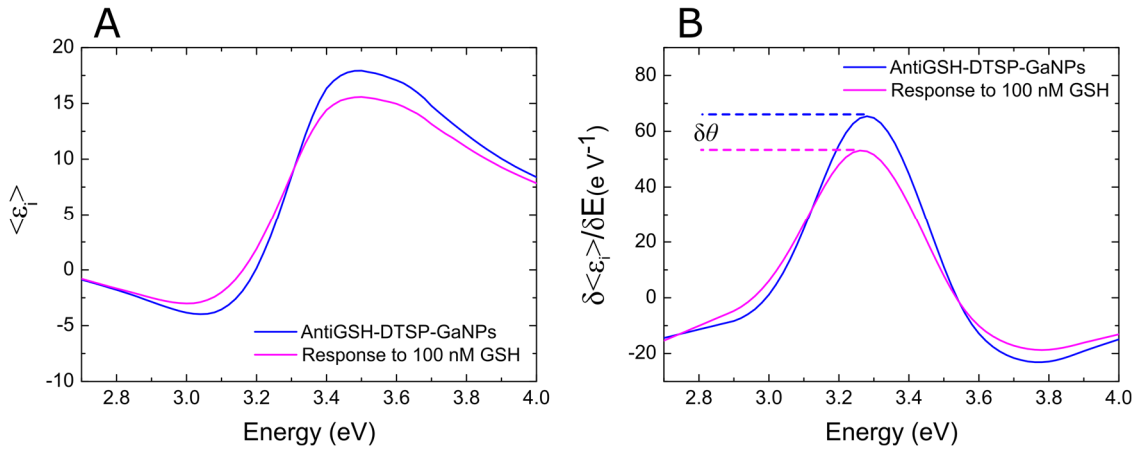

Figure 6.16. (A) $< \varepsilon_i >$ measured before and after the recognition event of the GSH with the antiGSH-DTSP-GaNPs platform; (B) $\partial < \varepsilon_i > / \partial E$ spectra obtained after differentiation of $< \varepsilon_i >$ with respect to the energy.

On the basis of the above results, an immunoassay for GSH detection is developed following the $\delta\theta$ changes caused by the GSH recognition in the antibody active sites of the immunosensing platform. Different immunosensors, prepared in the same manner, are incubated for 1 hour with increasing concentrations of aqueous solutions of GSH from 50 to 800 nM.

Figure 6.17 shows the calibration curve obtained by plotting $\delta\theta$ versus GSH, with $\delta\theta$ and [GSH] expressed in eV^{-1} and nM units, respectively. In this figure, the $\delta\theta$ changes are obtained by subtracting the slope change caused by the blank (deionized H_2O) to that one obtained for each concentration of GSH in the $< \varepsilon_i >$ spectra. Each point in the curve represents the average value of measurements from three different immunosensors. A good linear correlation between the signal and the GSH concentration is observed in the concentration range studied (R^2 = 0.985). The detection and quantification limits, calculated as the ratio between three and ten times the standard deviation of background signal and the curve slope, are 10 nM and 50 nM, respectively. These values represent an improvement compared to the sensitivity of standard ELISA kits available in the market, whose detection limit ranges between 330 and 1660 nM.[48]

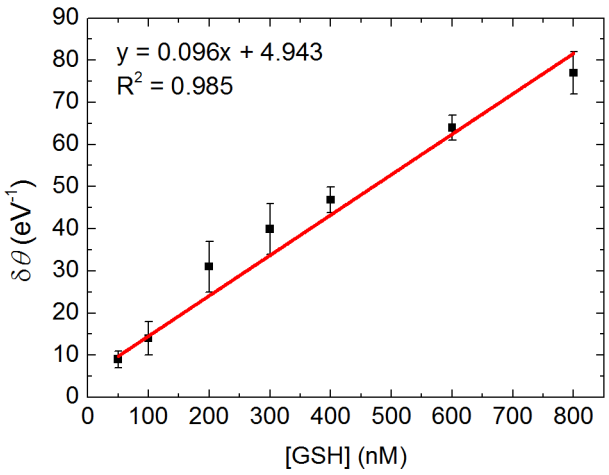

Figure 6.17. Calibration curve for GSH; error bars represent the standard deviation of measurements from three different immunosensors

The repeatability is evaluated from the relative standard deviation (RSD) of three successive determinations with the same immunosensor. A RSD value of 0.4 % is obtained. The reproducibility of the antiGSH-DTSP-GaNPs platform response to 400 nM GSH using three different immunosensors is found to be 6.0 %. A summary of the analytical characteristics of the developed GSH immunosensor is shown in Table 6.2.

Table 6.2. Summary of the GSH immunosensor analytical characteristics.

Parameter	Value
Linear range	50 - 800 nM
Detection limit	10 nM
Quantification limit	50 nM
Reproducibility (400 nM), n = 3	6.0 %
Repeatability, n = 3	0.4 %

From these results, it can be concluded that the employment of GaNPs as a nanomaterial for GSH immunosensor development allows obtaining an analytical response, which compares well with those previously developed in our laboratory that also include nanomaterials such as AuNPs.[47] However, the immunosensor developed in the present work presents several advantages such as an easier fabrication procedure, the employment of a less expensive nanomaterial, and obtaining large arrays of GaNP platforms in a single evaporation.

6.5. A DNA biosensor

6.5.1. Development of the sensing platform

The biosensing capabilities of the GaNPs/Si platform have been demonstrated in the previous Section. However, one question arises about its applicability and it is if it can be extended to other analytes through the immobilization of other recognition elements. To test the potential of the platform to sense other analytes, a DNA biosensor is also developed using GaNPs on a Si substrate with an evaporation time of 2 min.

As represented in the Figure 6.18, the first step is the immobilization of the 5'-end hexamethylthiol DNA capture probe (12 nucleotide bases, being the complete sequence in Table 3.1 in Chapter 3) from the *H. Pylori* (HP1-SH) on the GaNPs/Si platform. For this aim, 20 μL of a 2.0 μM HP1-SH solution is transferred onto the clean GaNPs/Si platform and it is kept standing for 1 hour at 4 ºC. Afterwards, the oligonucleotide-functionalized GaNPs platform (HP1-SH–GaNPs) is immersed in a 1.0 mM 6-mercapto-1-hexanol (MCH) solution during 1 hour. After each functionalization step, the resulting platform is thoroughly washed with sterile water for 30 min and dried with N_2 in order to remove unspecific reagents. The MCH is a short thiol chain that acts as lateral spacer in order to avoid unspecific interactions between the HP1-SH and the platform surface, and keep the probe standing up with the bases available for the hybridization with the corresponding target DNA sequence.

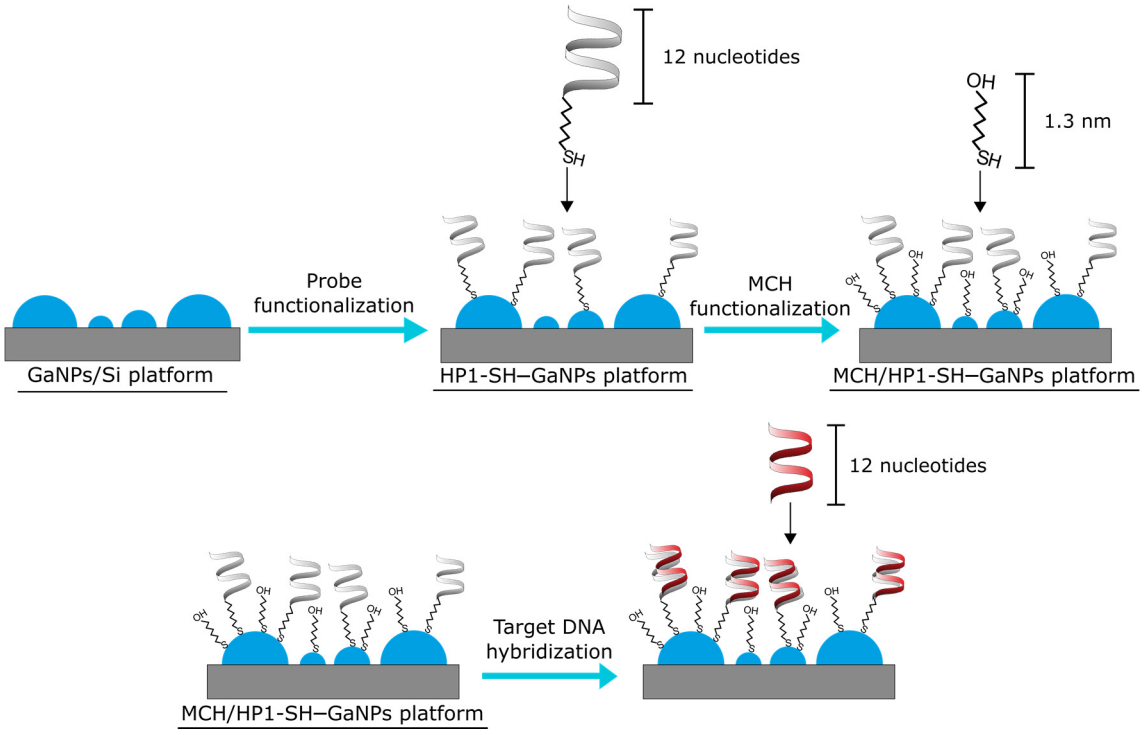

Figure 6.18. Schematic representation of the biosensing platform development and analyte hybridization. An estimation of the MCH size, based on the chemical bonds length, is also represented in that Figure. Information about the length of the bonds has been found in the literature.[45]

6.5.1.1. X-ray photoelectron spectroscopy characterization

The presence of thiolated species on the GaNPs/Si platform is evidenced by XPS analysis. The XPS spectra of the platform is obtained before and after modification with HP1-SH and MCH, and is shown in Figure 6.19.

The XPS spectra of the modified platform show a S2s core level at 227 eV, whereas no evidence of the S2s core level appears in the reference substrate. Only one chemical state of the S2s level is observed, which suggests the existence of an only type of bond between the S (from the thiol) and the GaNPs. The S2p photoemission signal overlaps with part of the Ga3s band (data not shown).

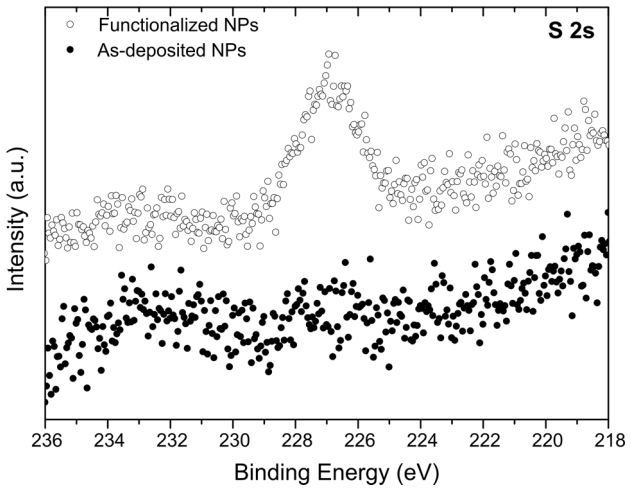

Figure 6.19. S2s core level signal of the GaNPs/Si sample before (black circles) and after the modification with the HP1-SH probe and the MCH (open circles).

6.5.1.2. Ellipsometric characterization

The whole functionalization process of the GaNPs/Si platform is monitored using ellipsometry. Figure 6.20A shows the $<\varepsilon_i>$ spectra of a GaNPs/Si platform before and after modification with the HP1-SH probe and the MCH, acquired under external reflection configuration at 55º incidence angle. These spectra are differentiated with respect to the energy to obtain the inflexion point (Figure 6.20B). As can be seen, there is an energy shift in the spectra before and after successive modifications due to the increasing refractive index around the NP, coming from the large biomolecule immobilization. From Figure 6.20B, δE values are estimated to be 30 ± 5 and 20 ± 10 meV after the modification with the HP1-SH probe and the further modification with the MCH, respectively.

In order to assess that the δE changes are strictly caused by the chemical modification of the NP surface and not related to other factors, such as thermal effects induced by the changes in temperature, the $<\varepsilon_i>$ spectra of an as-fabricated GaNPs/Si platform is measured before and after storing it at temperatures of 4 ºC and 40 ºC for 1 hour. NPs functionalization and the subsequent hybridization are performed at those temperatures (4 ºC for NP functionalization with the HP1-SH and 40 ºC for the hybridization, respectively). Since no significant changes are observed in the spectra, one can conclude that δE is strictly caused by the chemical modification of the NPs.

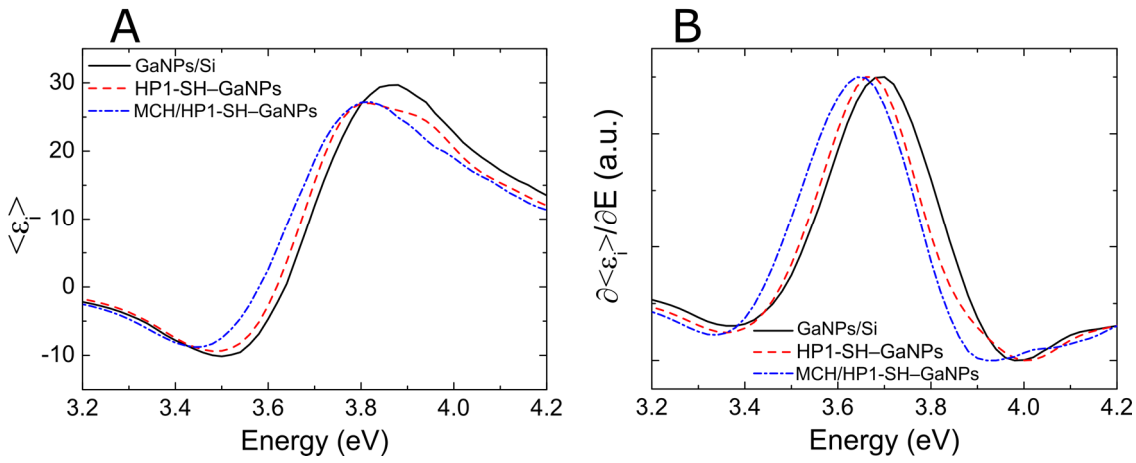

Figure 6.20. (A) $< \varepsilon_i >$ spectra of a GaNPs/Si platform before (black line) and after the modification with: the HP1-SH (red dashed line) and the MCH (blue dashed-dotted line); (B) The corresponding normalized $\partial < \varepsilon_i > / \partial E$ spectra of the same sample.

The optimal amount of the thiolated probe is determined through the immobilization of different concentrations of HP1-SH ranged from 0.010 to 20 μM. Figure 6.21 shows the δE values versus HP1-SH concentration. For low HP1-SH concentrations, δE increases with the increasing amount of the HP1-SH up to 2.0 μM. For larger concentrations, δE levels off due to the surface saturation. The data is optimally fitted to a Langmuir isotherm equation (Equation 6.2). The curve fitting gives rise to a K_L of 9.44 μM and a δE_{max} of 50 meV.

From the above results, it is concluded that a HP1-SH concentration of 2.0 μM can be optimal for the biosensor preparation, since this value was in the plateau where higher concentrations would hardly improve the response, whereas lower concentrations could reduce DNA hybridization sites and, thus, sensor sensitivity. Moreover, the isotherm seems to indicate that the immobilization of HP1-SH onto GaNPs platform takes place through the formation of a single monolayer, like thiolated DNA strands on Au surfaces.[49]

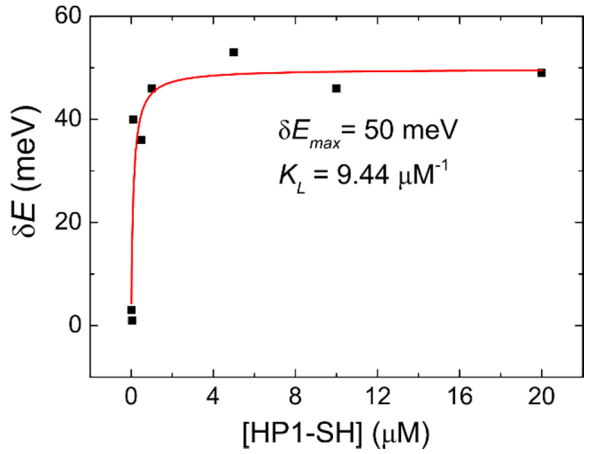

Figure 6.21. Representation of δE as a function of the DNA probe concentration. The red line represents the fitting curve obtained from the Langmuir isotherm equation.

6.5.2. Biosensor response and quantification of DNA

The potential use of MCH/HP1-SH–GaNPs sensing platforms as nucleic acid biosensors is evaluated through hybridization assays. These assays comprise the hybridization of MCH/HP1-SH–GaNPs sensing platforms with 20 µL of a 0.4 M NaCl hybridization solution containing the complementary ($HP2_C$) or non-complementary ($HP2_{NC}$) sequences, corresponding to the *H. Pylori*, for 1 hour at 40 ºC (see Figure 6.18). The complete sequences is shown in Table 3.2. After the hybridization event, the sensing platforms are immersed in nuclease-free sterile water for 30 min, and dried with N_2 before recording the ellipsometric measurements.

In the first hybridization test, 0.50 nM of $HP2_C$ and $HP2_{NC}$ sequences are used as DNA targets. The corresponding signals before and after hybridization are shown in Figure 6.20A. As can be seen, the hybridization of the probe chain with the $HP2_C$ in the biosensor recognition layer resulted in a considerably shift in δE of around 70 meV (from black curve to red-dashed curve), whereas virtually no changes ($\leq$ 10 meV) are observed for the $HP2_{NC}$ (blue-dotted curve). This difference in magnitude of δE indicates that a target sequence of the *H. Pylori* DNA fragment can be specifically detected using the developed biosensing platforms.

Different MCH/HP1-SH–GaNPs sensing platforms, prepared by the same manner, are incubated with increasing concentrations of $HP2_C$ from 10 pM to 3.0 nM. As can be seen in Figure 6.20B, there is a fairly linear correlation between δE and the increasing amount of $HP2_C$ over all the range studied, with a linear correlation coefficient of R^2 =

0.990. The detection and quantification limits are estimated to be 6.0 and 20 pM, respectively. The reproducibility of the biosensor is determined by measuring the response of five different biosensing platforms prepared using the same protocol and exposed to 0.5 nM $HP2_C$. A final RSD is found to be 3.4 %. On the other hand, the repeatability is evaluated from five successive determinations with the same biosensor, being 0.4 %. A summary of the analytical parameters obtained for this biosensor are shown in Table 6.3.

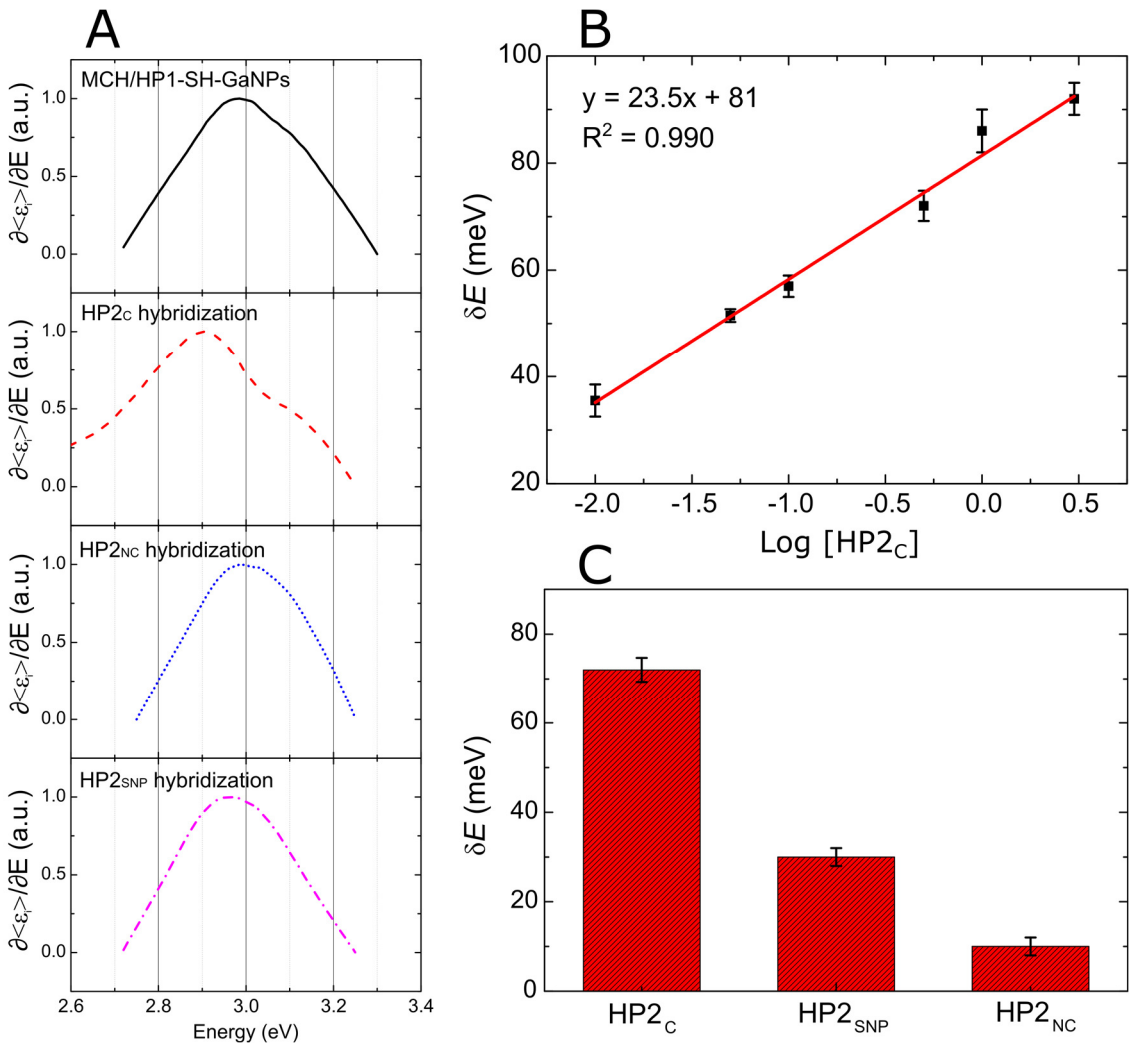

Figure 6.20. (A) Normalized $\partial < \varepsilon_i > / \partial E$ spectra of a GaNPs/Si platform modified with the HP1-SH capture probe and MCH, before (black curve) and after the hybridization event in the presence of a complementary, $HP2_C$ (red dashed curve), non-complementary, $HP2_{NC}$ (blue dotted curve) and single nucleotide polymorphism sequence, $HP2_{SNP}$ (magenta dashed-dotted curve); (B) Representation of δE versus $HP2_C$ concentration. The fitting curve and equation are also included; (C) Bar diagram of the δE undergone after hybridization with the $HP2_C$, $HP2_{SNP}$ and $HP2_{NC}$ sequences. The data are the average of five determinations and the error bars represent the standard deviation.

Table 6.3. Summary of the DNA biosensor analytical characteristics.

Parameter	Value
Linear range	10 pM – 3.0 nM
Detection limit	6.0 pM
Quantification limit	20 pM
Reproducibility (0.5 nM), n = 5	3.4 %
Repeatability, n = 5	0.4 %

6.5.3. Detection of single nucleotide polymorphisms

The selectivity of the biosensor is evaluated by using a sequence containing a Single Nucleotide Polymorphism ($HP2_{SNP}$) as target under the same hybridization conditions employed above (the complete sequence is in Table 3.1). The hybridization with the $HP2_{SNP}$ sequence would give a distorted double helix, which can be detected by the changes on the optical properties of the sensing layer. Based on this, one would anticipate a different biosensor response when comparing to the hybridization with the perfect matched sequence, $HP2_C$.

Figure 6.20A shows the $< \varepsilon_i >$ spectrum of a platform modified with the probe before and after hybridization with 0.50 nM $HP2_{SNP}$ (from black curve to dashed-dotted magenta curve). As can be seen, the presence of the mutation in the DNA sequence causes a redshift of the inflexion point. From the response of five biosensors an average value in δE of 30 meV is observed, which is less than a half of the energy shift of around 70 meV observed when the biosensors respond to 0.50 nM of a perfect matched sequence $HP2_C$ (see Figure 6.20C to compare between the different DNA sequences). Since the error associated to each measurement is less than 5 %, it can be concluded that the developed sensing system is able to unambiguously detect the presence of a SNP in a given sequence at the nanomolar concentration, without the need of stringent conditions (i.e. formamide) usually employed for such purpose.

6.5.4. Study of interferences

Concerning selectivity, other important aspect to take into account for analytical application of DNA biosensing platforms is the effect on the response of other sequences present in the sample that can act as potential interferents. The following experiment is

performed in order to assess if the developed biosensing platform can detect a specific DNA sequence in a sample containing other sequences besides the analyte. For this aim, the response to samples containing both *H. Pylori* and *Escherichia Coli* (*E. Coli*) sequences, at different concentrations, is evaluated. Figure 6.21 shows the bar diagram of the results. As can be seen, the presence of *E. Coli* at lower concentration (from 0.05 nM to 0.25 nM) than the *H. Pylori* sequence (0.5 nM) does not affect the biosensor response. When the *E. Coli* sequence is present at high concentrations (0.5 nM and 1.0 nM), the biosensor response decreases about 30 %. From these results, it can be concluded that it is possible to detect the target sequence in the presence of other pathogen in the sample as long as the interferent concentration is at least similar or below the target.

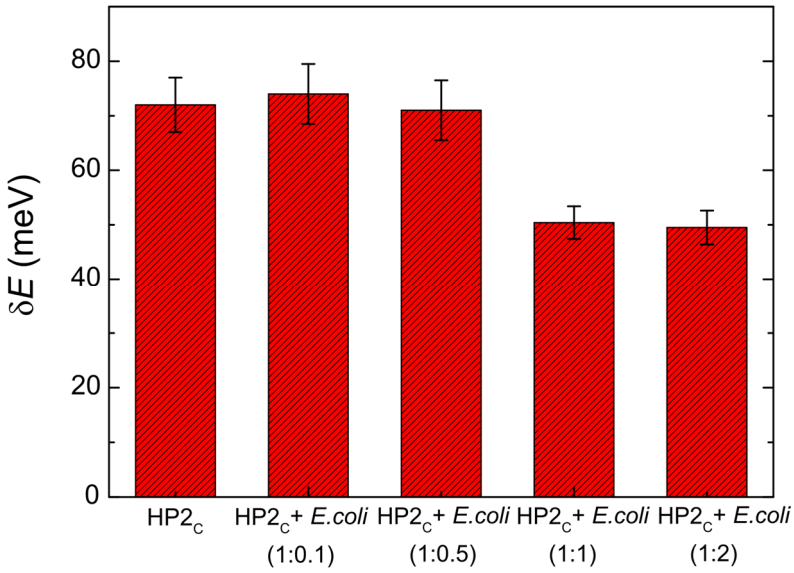

Figure 6.21. Bar diagram of the δ*E* undergone after hybridization with 0.5 nM of *H. Pylori* (first red bar, represented as $HP2_C$), compared to hybridization assays with 0.5 nM of *H. Pylori* and increasing concentrations of an *E. Coli* sequence (second to fourth bar, represented as $HP2_C$ + *E. Coli*): 0.05 nM, 0.25 nM, 0.5 nM and 1.0 nM. The data are the average of five determinations and the error bars represent the standard deviation

6.5.5. Detection of gene mutation in real genomic DNA

Up to now, the applicability of the GaNPs/Si platform has been demonstrated for the detection of synthetic DNA sequences, as well as, their possible mutations. The detection of DNA mutations is of great interest for biomedical applications, since these mutations are the origin of a wide range of diseases and cancers. These applications require the use of real genomic DNA samples. In the following Section, the potential use

of this biosensing platform to work with this genomic DNA is studied. This is an important and essential step further in the development of commercial platforms.

The analysis of real samples requires additional procedures in order to obtain the genomic DNA. This procedure includes the extraction, purification and amplification of the DNA by Polymerase Chain Reaction (PCR), being performed in the Medical and Molecular Genetics Institute (INGEMM) of Madrid (Spain). As a case of study, the F508del mutation associated with Cystic Fibrosis disease is chosen. Mutation detection is directly accomplished in a 373 base pairs sequence from exon 11 in the CFTR gene. The genomic DNA was isolated by the INGEMM from peripheral blood leukocytes and amplified by PCR (the complete sequence is in Table 3.2).

The first step of the biosensing platform fabrication comprises the immobilization of a thiolated synthetic probe, denoted as CF1-SH, (100 base pairs, sequence in Table 3.2) onto the GaNPs/Si platform. As demonstrated in the previous Section from the XPS analysis in the *H. Pylori* case, thiolated molecules will anchor the GaNP surface. Thus, the functionalization procedure of the GaNPs/Si platform will be similar to that used in that Section. For this aim, 20 μL of a 2.0 μM CF1-SH solution is transferred onto the clean GaNPs/Si platform and it is kept standing for 1 hour at 4 ºC. Afterwards, the oligonucleotide functionalized GaNPs/Si platform (CF1-SH–GaNPs) is immersed in a 1.0 mM MCH solution during 1 hour and the resulting MCH/CF1-SH–GaNPs platform is thoroughly washed with sterile water for 30 min and dried with N_2.

The modification of GaNPs/Si platform with the CF1-SH probe and the MCH causes a δE of 105 ± 5 meV. Figure 6.22 shows the normalized $\partial < \varepsilon_i > / \partial E$ spectra before (black line) and after (red dotted line) this modification. This shift is stronger than that observed in the case of *H. Pylori* probe immobilization (around 50 meV, with 12 nucleotide bases), accounting for the larger number of base pairs and, thus, a higher increase in the refractive index of the GaNPs surrounding medium.

The hybridization response of the functionalized platform to the wild type or total complementary DNA sequence ($CF2_{WT}$), is studied. For this aim, several MCH/CF1-SH–GaNPs platforms are hybridized with 5 μL of 50 pg/μL solution of $CF2_{WT}$ for 1 h at 40 ºC, followed by the immersion of the platform in nuclease-free sterile water for 30 min. Prior to the hybridization, the amplicon is denatured by immersing the solution in boiling water (100 ºC) for 30 minutes followed by rapid cooling in an ice bath.

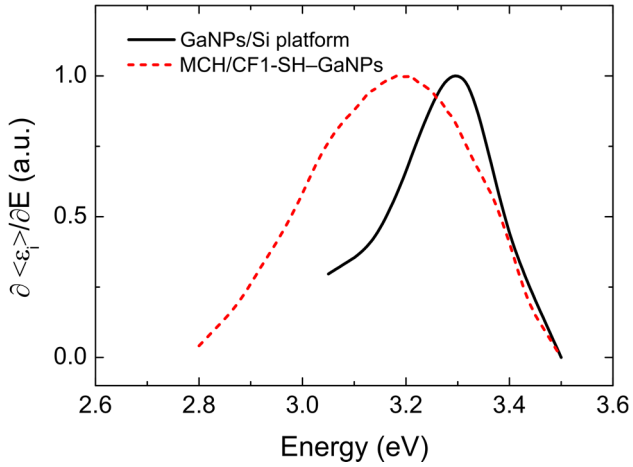

Figure 6.22. Normalized $\partial < \varepsilon_i > / \partial E$ spectra of a GaNPs/Si platform, before (black line) and after (dotted line) the modification with the CF1-SH capture probe and MCH.

Figure 6.23A shows the $\partial < \varepsilon_i > / \partial E$ spectra of the probe-functionalized platform before (black line) and after (red dotted line) the hybridization with the $CF2_{WT}$ sequence. This step gives rise to an additional energy shift of around 150 meV.

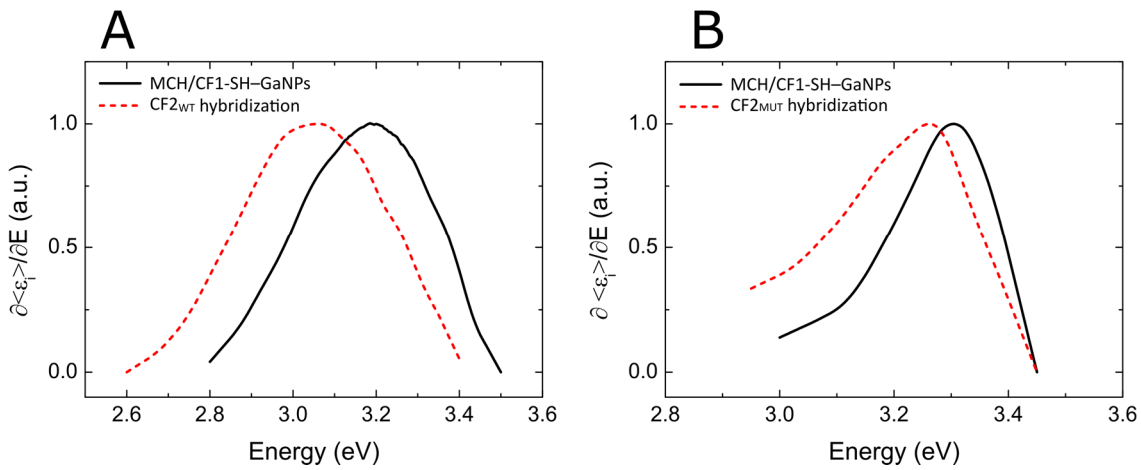

Figure 6.23. Normalized $\partial < \varepsilon_i > / \partial E$ spectra of a GaNPs/Si platform modified with the CF1-SH capture probe and MCH, before (black line) and after (dotted line) the hybridization with the wild (A) and mutated (B) type sequences.

A similar experiment is performed with the mutated sequence ($CF2_{MUT}$) to evaluate the discrimination between both forms of the gene under study. The hybridization of this sequence with the functionalized platform is carried out with the same procedure and concentration, compared to that used with the wild type sequence. The resulting

normalized spectra, before and after the hybridization process, are shown in Figure 6.23B. The $CF2_{MUT}$ hybridization also yields a redshift of around 30 meV. It is worth noting that the mutated form interacts with the capture probe in a different extension due to the deletion of some bases in its sequence. Consequently, this effect produces a distorted double helix on the functionalized platform and, thus, weaker δE.

Figure 6.24 shows a bar diagram of δE for both sequences, averaged for five measurements. The standard deviation is also calculated and represented as error bars. The 5-time higher signal in the case of the $CF2_{WT}$ sequence allows a perfect discrimination between the wild type and the mutated form of the gene.

The reproducibility of the developed methodology is evaluated from the response of five different biosensors prepared in the same manner. Reproducible signals with a RSD less than 5.0 % are obtained. These results demonstrates that the developed system can be applied to detect gene mutations in DNA real samples. The developed method can be competitive to conventional SPR concerning sensitivity and selectivity, and can be an alternative screening method to detect gene mutations.

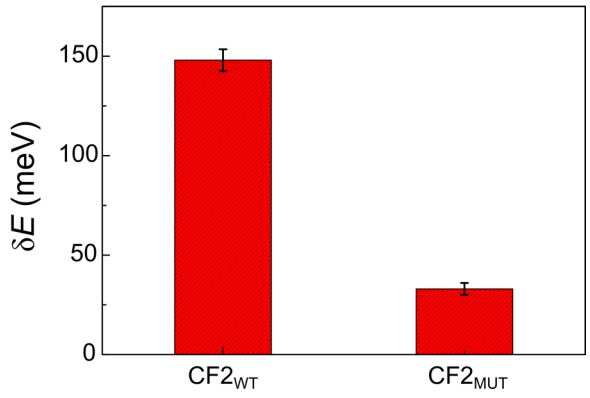

Figure 6.24. Bar diagram of δE undergone after hybridization with the $CF2_{WT}$ and the $CF2_{MUT}$ sequences. The data are the average of five assays and the error bars represent the standard deviation.

6.6. Conclusions

In this work, the development of GaNP-based biosensing platforms has been presented. Calculations based on the Mie theory have been performed to study the plasmonics of homogeneous spheres. The analysis of GaNPs with different radii has revealed that, in comparison to AuNPs, the resonances associated to dipolar oscillations

inside the GaNPs cover a wider range, from UV to infrared, whereas Au is mainly located in the visible range. On the other hand, numerical simulations performed with the DDA approach have been carried out to study the plasmonics of a hemisphere. In particular, the study focused on the splitting of the resonant modes in GaNPs for in-plane and out-of-plane dipolar oscillations due to the hemispherical geometry of NPs. These modes have been found to be sensitive to the polarization of the incident light. The addition of a substrate in direct contact with the NP has been included in the simulations, yielding a redshift in the oscillatory modes, due to the refractive index increase of the surrounding medium.

GaNPs have been successfully deposited on Si substrates by Joule-effect thermal evaporation of metallic Ga. For the evaporation time (2 min) used to fabricate the GaNPs/Si platforms in the biosensing experiments, the histogram obtained from SEM aerial images has revealed the presence of bimodal distributions of NPs due to the coalescence process during evaporation.

Surface characterization techniques, such as XPS and XRD have provided structural and composition information about the NPs. The data show the presence of a gallium oxide shell surrounding an amorphous- or liquid-phase inner core.

Ellipsometric measurements under external reflection configuration at 70º incidence angle have shown evidence of two bands separated by several electronvolts, whose energy position depends on the NP size. Longer evaporation times have yielded more prominent redshifts. Thanks to the calculations performed with the DDA, these bands have been attributed to in-plane and out-of-plane resonance modes of the small NPs deposited on a Si substrate.

Additionally, an interesting behavior of these GaNPs/Si platforms has been observed under certain conditions of energy and incidence angle. When the phase shift difference, Δ, reaches a value of 180º, and the RPH condition occurs. Under this condition, the $< \varepsilon_i >$ function takes a sigmoidal lineshape close to the high energy resonant band. The analysis of the data has revealed that the optimal incidence angle with the largest peak-to-peak value has been located around 55º. At that incidence angle, the optimal photon energies have been found in the 2.8-3.6 eV range.

The $< \varepsilon_i >$ curve under the RPH condition have shown a great sensitivity to the NP surface modification. XPS analysis has demonstrated the chemical modification of these NPs by using thiols compounds.

Finally, GaNPs/Si systems have been studied as potential biosensing platforms. The first approach has been the development of an immunosensor for GSH. The procedure begins with the NP functionalization by surface thiolation and the subsequent antibody immobilization. The NP surface modification has been also confirmed through FTIR measurements. GSH has been detected in the submicromolar range with a limit of detection of 10 nM. Additionally, their biosensing capabilities have been demonstrated through the fabrication of a DNA biosensor. In this case, the NP surface has been modified with a thiol probe chain from the *H. pylori* pathogen. A successful detection of the complementary sequence has been achieved in the pico and nanomolar range, estimating a very low limit of detection of 6.0 pM. Concerning selectivity, this biosensing platform is able to discriminate between complementary and mutated, with only a single nucleotide polymorphism and sequences at equal concentrations. Furthermore, the influence of possible interferences due to the presence of common pathogens, such as *E. Coli*, has been studied. The conclusion arising from this study is that other pathogens do not interfere in the response as long as their concentrations are, at least, below the target sequence. For both approaches, the use of signal amplifiers has not been required, which has simplified the whole procedure.

A step forward to demonstrate the wide applicability of this biosensing platform is its use in more complex media or real samples. In this respect, the detection of a specific gene mutation in the CFTR protein in PCR amplicons extracted from leukocyte cells has been studied. The promising results obtained have demonstrated that the developed biosensor can be used for the direct detection of mutations in PCR amplified products without complicated sample treatment procedures.

REFERENCES

1. K. A. Willets; R. P. V. Duyne. Localized surface plasmon resonance spectroscopy and sensing. *Annu. Rev. Phys. Chem.* **2007**, 58, 267-297.
2. S. Eustis; M. A. El-Sayed. Why gold nanoparticles are more precious than pretty gold: Noble metal surface plasmon resonance and its enhancement of the radiative and

nonradiative properties of nanocrystals of different shapes. *Chem. Soc. Rev.* **2006**, 35, 209-217.
3. R. Viswambari Devi; M. Doble; R. S. Verma. Nanomaterials for early detection of cancer biomarker with special emphasis on gold nanoparticles in immunoassays/sensors. *Biosens. Bioelectron.* **2015**, 68, 688-698.
4. M.-C. Daniel; D. Astruc. Gold Nanoparticles: Assembly, Supramolecular Chemistry, Quantum-Size-Related Properties, and Applications toward Biology, Catalysis, and Nanotechnology. *Chem. Rev.* **2004**, 104, 294-346.
5. S. A. Maier. *Plasmonics: Fundamentals and Applications*. Springer: 2007.
6. D. E. Aspnes; E. Kinsbron; D. D. Bacon. Optical properties of Au: sample effects. *Phys. Rev. B* **1980**, 21, 3290-3299.
7. E. A. Taft; H. R. Philipp. Optical Constants of Silver. *Phys. Rev.* **1961**, 121, 1100-1103.
8. E. D. Palik. *Handbook of Optical Constants of Solids*. Academic Press: 1998.
9. P. Albella; B. Garcia-Cueto; F. González; F. Moreno; P. C. Wu; T.-H. Kim; A. Brown; Y. Yang; H. O. Everitt; G. Videen. Shape Matters: Plasmonic Nanoparticle Shape Enhances Interaction with Dielectric Substrate. *Nano Lett.* **2011**, 11, 3531–3537.
10. R. Y. Koyama; N. V. Smith; W. E. Spicer. Optical Properties of Indium. *Phys. Rev. B* **1973**, 8, 2426-2432.
11. D. Tonova; M. Patrini; P. Tognini; A. Stella; P. Cheyssac; R. Kofman. Ellipsometric study of optical properties of liquid Ga nanoparticles. *J. Phys.: Condens. Matter* **1999**, 11, 2211-2222.
12. M. W. Knight; T. Coenen; Y. Yang; B. J. M. Brenny; M. Losurdo; A. S. Brown; H. O. Everitt; A. Polman. Gallium plasmonics: deep subwavelength spectroscopic imaging of single and interacting gallium nanoparticles. *ACS Nano* **2015**, 9, 2049-2060.
13. P. C. Wu; T.-H. Kim; A. S. Brown; M. Losurdo; G. Bruno; H. O. Everitt. Real-time plasmon resonance tuning of liquid Ga nanoparticles by in situ spectroscopic ellipsometry. *Appl. Phys. Lett.* **2007**, 90, 103119.
14. M. J. Hernández; M. Cervera; E. Ruiz; J. L. Pau; J. Piqueras; M. Avella; J. Jiménez. Gallium-assisted growth of silicon nanowires by electron cyclotron resonance plasmas. *Nanotechnology* **2010**, 21, 455602.
15. P. Ghigna; G. Spinolo; G. B. Parravicini; A. Stella; A. Migliori; R. Kofman. Metallic versus Covalent Bonding: Ga Nanoparticles as a Case Study. *J. Am. Chem. Soc.* **2007**, 129, 8026-8033.
16. M. Yarema; M. Wörle; M. D. Rossell; R. Erni; R. Caputo; L. Protesescu; K. V. Kravchyk; D. N. Dirin; K. Lienau; F. von Rohr; A. Schilling; M. Nachtegaal; M. V. Kovalenko. Monodisperse Colloidal Gallium Nanoparticles: Synthesis, Low Temperature Crystallization, Surface Plasmon Resonance and Li-Ion Storage. *J. Am. Chem. Soc.* **2014**, 136, 12422-12430.
17. S. C. Hardy. The surface tension of liquid gallium. *J. Cryst. Growth* **1985**, 71, 602-606.
18. M. J. Regan; H. Tostmann; P. S. Pershan; O. M. Magnussen; E. DiMasi; B. M. Ocko; M. Deutsch. X-ray study of the oxidation of liquid-gallium surfaces. *Phys. Rev. B* **1997**, 55, 10786-10790.
19. G. Schön. Auger and direct electron spectra in X-ray photoelectron studies of zinc, zinc oxide, gallium and gallium oxide. *J. Electron. Spectrosc. Relat. Phenom.* **1973**, 2, 75-86.
20. Y. Yang; J. M. Callahan; T.-H. Kim; A. S. Brown; H. O. Everitt. Ultraviolet Nanoplasmonics: A Demonstration of Surface-Enhanced Raman Spectroscopy,

Fluorescence, and Photodegradation Using Gallium Nanoparticles. *Nano Lett.* **2013**, 13, 2837−2841.
21. J. L. Pau; A. García-Marín; M. J. Hernández; E. Lorenzo; J. Piqueras. Optical biosensing platforms based on Ga–graphene plasmonic structures on Cu, quartz and SiO_2/Si substrates. *Phys. Status Solidi (b)* **2016**, 253, 664-670.
22. P. C. Wu; C. G. Khoury; T.-H. Kim; Y. Yang; M. Losurdo; G. V. Bianco; T. Vo-Dinh; A. S. Brown; H. O. Everitt. Demonstration of surface-enhanced Raman scattering by tunable, plasmonic gallium nanoparticles. *J. Am. Chem. Soc.* **2009**, 131, 12032–12033.
23. P. Narayanasamy; B. L. Switzer; B. E. Britigan. Prolonged-acting, Multi-targeting Gallium Nanoparticles Potently Inhibit Growth of Both HIV and Mycobacteria in Co-Infected Human Macrophages. *Sci. Rep.* **2015**, 5, 8824 (1-7).
24. A. García Marín; M. J. Hernández; E. Ruiz; J. M. Abad; E. Lorenzo; J. Piqueras; J. L. Pau. Immunosensing platform based on gallium nanoparticle arrays on silicon substrates. *Biosens. Bioelectron.* **2015**, 74, 1069-1075.
25. A. G. Marín; T. Garcia-Mendiola; C. N. Bernabeu; M. J. Hernández; J. Piqueras; J. L. Pau; F. Pariente; E. Lorenzo. Gallium plasmonic nanoparticles for label-free DNA and single nucleotide polymorphism sensing. *Nanoscale* **2016**, 8, 9842-9851.
26. R. B. M. Schasfoort; A. J. Tudos. *Handbook of surface plasmon resonance*. RSC Publishing, Cambridge: 2008.
27. W. A. Murray; W. L. Barnes. Plasmonic materials. *Adv. Mater.* **2007**, 19, 3771-3782.
28. J. Homola; S. S. Yee; G. Gauglitz. Surface plasmon resonance sensors: review. *Sens. Actuators B Chem.* **1999**, 54, 3-15.
29. P. K. Wilson; T. Jiang; M. E. Minunni; A. P. F. Turner; M. Mascini. A novel optical biosensor format for the detection of clinically relevant TP53 mutations. *Biosens. Bioelectron.* **2005**, 20, 2310-2313.
30. S.-i. Nakano; T. Kanzaki; M. Nakano; D. Miyoshi; N. Sugimoto. Measurements of the Binding of a Large Protein Using a Substrate Density-Controlled DNA Chip. *Anal. Chem.* **2011**, 83, 6368-6372.
31. L. G. Carrascosa; A. Calle; L. M. Lechuga. Label-free detection of DNA mutations by SPR: application to the early detection of inherited breast cancer. *Anal. Bioanal. Chem.* **2009**, 393, 1173-1182.
32. S. M. Rowe ; S. Miller ; E. J. Sorscher Cystic Fibrosis. *N. Eng. J. Med.* **2005**, 352, 1992-2001.
33. B. Kerem; J. M. Rommens; J. A. Buchanan; D. Markiewicz; T. K. Cox; A. Chakravarti; M. Buchwald; L. C. Tsui. Identification of the cystic fibrosis gene: genetic analysis. *Science* **1989**, 245, 1073-1080.
34. MiePlot webpage. http://www.philiplaven.com/mieplot.htm (accessed March, 2016).
35. C. F. Bohren; D. R. Huffman. *Absorption and scattering of light by small particles*. Wiley: 1983.
36. M. Kerker; E. M. Loebl. *The Scattering of Light and Other Electromagnetic Radiation: Physical Chemistry: A Series of Monographs*. Elsevier Science: 2013.
37. F. D. Sala; S. D'Agostino. *Handbook of Molecular Plasmonics*. Taylor & Francis: 2013.
38. R. Emilie; Z. Jian; R. L. Mark; A. M. Chad; D. M. Laurence; P. V. D. Richard. Correlating the structure and localized surface plasmon resonance of single silver right bipyramids. *Nanotechnology* **2012**, 23, 444005.
39. P. J. Flatau; B. T. Draine. Fast near field calculations in the discrete dipole approximation for regular rectilinear grids. *Opt. Express* **2012**, 20, 1247-1252.

40. P. C. Wu; M. Losurdo; T.-H. Kim; M. Giangregorio; G. Bruno; H. O. Everitt; A. S. Brown. Plasmonic Gallium Nanoparticles on Polar Semiconductors: Interplay between Nanoparticle Wetting, Localized Surface Plasmon Dynamics, and Interface Charge. *Langmuir* **2009**, 25, 924-930.
41. A. Di Cicco. Phase Transitions in Confined Gallium Droplets. *Phys. Rev. Lett.* **1998**, 81, 2942-2945.
42. XPS databases. http://www.lasurface.com/accueil/index.php; http://srdata.nist.gov/xps/ (accessed March, 2016).
43. H. Rauscher; M. Perucca; G. Buyle. *Plasma Technology for Hyperfunctional Surfaces: Food, Biomedical and Textile Applications*. Wiley: 2010.
44. M. E. Browning-Kelley; K. Wadu-Mesthrige; V. Hari; G. Y. Liu. Atomic Force Microscopic Study of Specific Antigen/Antibody Binding. *Langmuir* **1997**, 13, 343-350.
45. D. R. Lide. *CRC Handbook of Chemistry and Physics, 85th Edition*. Taylor & Francis: 2004.
46. F. Parker. *Applications of Infrared Spectroscopy in Biochemistry, Biology, and Medicine*. Springer: 2012.
47. A. García-Marín; J. M. Abad; E. Ruiz; E. Lorenzo; J. Piqueras; J. L. Pau. Glutathione Immunosensing Platform Based on Total Internal Reflection Ellipsometry Enhanced by Functionalized Gold Nanoparticles. *Anal. Chem.* **2014**, 86, 4969-4976.
48. ELISA commercial kits for glutathione. http://www.biomatik.com/products/productDetail/ELISA-Kit-for-Glutathione--GSH---General--competitive-type.aspx, http://www.uscnk.com/uscn/ELISA-Kit-for-Glutathione-GSH-1197.htm (accessed May, 2016).
49. T. M. Herne; M. J. Tarlov. Characterization of DNA Probes Immobilized on Gold Surfaces. *Journal of the American Chemical Society* **1997**, 119, 8916-8920.

7. Conclusions and future work

In the following Sections, the conclusions from the different Chapters are presented along with new ideas to continue or to open new research lines related to the work presented in this thesis. Hopefully, it will help future researchers to progress faster in the knowledge and fabrication of novel sensors.

7.1. Nanowire-based light sensors

7.1.1. Conclusions

7.1.1.1. CuO-based light sensors

In this work, a stepwise route has been provided for the fabrication of visible light sensing devices based on CuO, from the NW growth and processing to the electro-optical characterization.

- CuO NWs have been grown by direct oxidation of Cu foils under ambient pressure at different temperatures. The effect of the growth temperature has been studied from aerial and cross-sectional SEM images, revealing the effects of oxidation temperature on the NW physical dimensions.
- These NWs have been manipulated and aligned between electrodes using droplet dielectrophoresis for the fabrication of light sensors. The frequency and the

effective voltage of the sinusoidal wave have been optimized to maximize the number of aligned NWs.

- P-type conductivity has been found in CuO NWs, previously aligned between electrodes, after exposure to water vapor. The opposite behavior has been exhibited by ZnO NWs, as corresponds to an n-type semiconductor.

- A light sensor, comprising CuO NWs aligned between AZO electrodes, has been built and electro-optically characterized. The sensor has shown sensitivity to visible light, in good agreement with the absorption properties expected for CuO. Furthermore, the use of n-type AZO electrodes has allowed the formation of heterojunctions between AZO and CuO at both ends of the NW, which speeds up the response of the device in comparison to photoconductor NW devices. These results have demonstrated the effectiveness of DEP for the fast and cost-effective development of NW-based light sensing devices.

7.1.1.2. ZnO-based light sensors

New control methods have been introduced in the fabrication of UV light sensing devices based on ZnO NWs. These methods have improved the surface quality of the final devices and the reproducibility of the alignment process.

- The first goal has targeted the improvement of the dispersion quality. Simple sedimentation has been used to get rid of large clusters in the solution that can short-circuit electrodes after the DEP process. The quantification of the NW concentration in the dispersions has been successfully performed through absorbance measurements in a spectrophotometer.

- A portable and continuous-flow DEP system has been developed in order to improve the surface quality of the resulting device and to increase the NW trapping probability. This new system comprises an optical tool, which includes a laser and a phototransistor, to monitor the NW dispersion. On the other hand, the alignment of NWs has been monitored in real time through parallel resistance measurements performed with a LCR, connected to the DEP system. This method has allowed estimating the number of trapped NWs during the DEP process and, thus, to add more control mechanisms to the NW alignment works. Another advantage of

monitoring the parallel resistance has been the possibility of detecting anomalies during the process, such as electrode damage induced by solvent electrolysis. Thanks to the up-side-down mounting of the substrate in the continuous-flow system, higher-quality surfaces have been achieved with less surface contamination produced by the solution leftovers which are difficult to eliminate in the droplet DEP case.

- The ZnO NWs have been aligned by DEP using the new system on AZO electrodes. Some advantages of this device are its high transparency and its capability to work under front- and back-illumination, without significant performance differences between both configurations.

7.1.2. Future work

- Currently, the developed DEP system is relatively heavy and extensive in size. An upgraded and more miniaturized system could be designed to host the electronics inside smaller housings. Commercially available integrated circuits have been specifically designed to work as function generators, which could help to reduce the electronics inside and, thus, the dimensions of the system.

- DEP is not only restricted to NWs, but it can be also used to manipulate 2D materials. Graphene and MoS_2 sheets has arisen as promising materials due to their electro-optical properties. These materials have a vast functionalization chemistry, which can be interesting to anchor different molecules in order to develop novel sensors. The alignment of flakes of these materials, obtained by mechanical exfoliation, can become the base for the mass production of biological and gas sensing devices.

- CuO-based sensors have presented a rather low responsivity compared to other nanostructures, such as ZnO NWs. The electro-optical characteristics of the CuO NWs can be improved through the decoration of the NW with NPs. These NPs can be attached to the NW sidewalls through the formation covalent bonds or other linkages, giving rise to the formation of Schottky barriers or rectifying junctions that can modify the electronic properties of the NW. This approach has shown promising results for AuNP-decorated ZnO NWs.

- Another approach is the chemical functionalization of the NW surface with different molecules. Preliminary results have been performed in our laboratory based on the silanization of ZnO NWs. These experiments have suggested an improvement of the linearity of the I-V characteristics.

- Nowadays, the fabrication of electronic devices on plastic substrates is attracting a great deal of attention in the scientific community. The NWs can be aligned between electrodes defined in transparent plastic substrates, such as 4,4'-oxydiphenylene-pyromellitimide (Kapton) or cellulose acetate. The advantage of plastics is evident since they are much lighter in weight than glass, silicon or quartz. In addition, they can be adjusted to the shape of any irregular surface or holder. This property can open the possibility to integrate flexible sensors on skin or fabricate electronic skins.

7.2. An immunosensor for glutathione under total internal reflection ellipsometry

7.2.1. Conclusions

In this work, the development of a TIRE immunosensor for GSH, a low molecular weight biomolecule, has been studied. The competitive configuration has been chosen based on the simultaneous recognition of GSH-AuNPs conjugates and free GSH. The sensor takes advantage of the amplified signal provided by AuNPs in the TIRE setup when they bind to the functionalized Au surface.

- The successful functionalization of AuNPs with GSH has been obtained. Infrared and UV-visible spectrophotometries have confirmed the chemisorption of GSH on the Au surface.

- The biosensing platform (AZO/Au bilayer) has been developed in two steps: deposition of AZO by rf-magnetron sputtering on quartz substrates, and the subsequent evaporation of Au by Joule-effect thermal evaporation. AZO has demonstrated benefits over Ti and Cr, as the intermediate layer between Au and the quartz substrate. In this respect, AZO has provided lower absorption losses, as has been shown from the numerical calculation using Fresnel equations and effective medium approximations.

- The AZO/Au bilayer has been functionalized with a thiol monolayer, the DTSP, to further immobilize an antibody selective to GSH. The presence of the DTSP self-assembled monolayer has been proved through cyclic voltammetry via the thiol reductive desorption. The antibody is successfully immobilized through the nucleophilic attack of its primary amino groups to the terminal N-succinimidyl group of DTSP. The position of the SPR, defined as the minimum in Ψ, has been simulated before and after the immobilization to confirm the correlation between the experimental energy shift of the SPR and the energy shift expected from the Fresnel analysis.

- The antibody immobilization on the DTSP-functionalized bilayer and the consequent immunological recognition of the antibody with the GSH-AuNPs conjugates have been monitored by real-time TIRE measurements.

- The optimal concentration of the GSH-AuNPs conjugates has been estimated by measuring the resonance energy shift in ellipsometry undergone for different GSH-AuNPs concentrations. A concentration of 40 nM has been found to be the value that caused the largest energy shift in the SPR. The presence of the conjugates has been confirmed by SEM images.

- Finally, an immunoassay for GSH detection has been developed based on the competition between free GSH and GSH-AuNPs for the active sites of the antibody. The immunosensor has shown detection limits in the nanomolar range and good reproducibility values.

7.2.2. Future work

- Concerning the plasmonic technology, Ag presents a stronger and sharper SPR band and, thus, higher theoretical sensitivity compared to Au. Despite the functionalization chemistry of Au is more extended, the use of Ag could be interesting if higher sensitivities are required. The main drawback of Ag is its rapid oxidation and passivation, which can attenuate its plasmonic properties. However, if necessary, this issue could be avoided through additional surface functionalization steps.

- In this work, AuNPs have been used as signal amplifiers. Ag colloids are also easy to synthetize through the citrate reduction method. As shown above, this material presents stronger SPR effects being suitable to act as amplifiers.

- Some of the drawbacks of ellipsometry is the lack of portability and the high cost of the ellipsometer. The development of a portable ellipsometer can help to overcome these drawbacks and provide a way to perform in-situ measurements without taking the samples to a laboratory. Furthermore, the portable ellipsometer can be also combined with a microfluidic system to automatize the sensing process. Although these approaches may require a large amount of time, they will involve a huge step forward to a future technology transfer to the Industry.

7.3. Biosensing platforms based on gallium nanostructures

7.3.1. Conclusions

In this work, the development of GaNP-based biosensing platforms has been presented. Their applicability to detect GSH and DNA sequences has been demonstrated. Before the fabrication of the biosensing platforms, the plasmonic properties of GaNPs and their response under external reflection ellipsometry have been deeply studied.

- Calculations based on the Mie theory have been performed to study the plasmonics of homogeneous spheres. The analysis of GaNPs with different radii has revealed that the resonances associated to dipolar oscillations of the NPs cover a wide range, from UV to infrared, whereas the resonances of AuNPs are mainly located in the visible range. On the other hand, numerical simulations performed with the DDA approach have been carried out to study the plasmonics of a hemisphere. In particular, the study has focused on the splitting of the resonant modes in spherical GaNPs into in-plane and out-of-plane dipolar oscillations due to the hemispherical geometry of the NPs. These modes have been found to be sensitive to the polarization of the incident light. The addition of a substrate in direct contact with the NP has been included in the simulations, yielding a redshift in the oscillatory modes, due to the refractive index increase of the surrounding medium.

- Large arrays of GaNPs have been successfully deposited on Si substrates by Joule-effect thermal evaporation of metallic Ga. For the evaporation times (2 min) used

to fabricate the GaNPs/Si platforms in the biosensing experiments, the histogram obtained from SEM aerial images has revealed the presence of bimodal distributions of NPs due to the coalescence process during evaporation.

- Surface characterization techniques, such as XPS and XRD have provided structural and compositional information about the NPs. The data has shown the presence of a gallium oxide shell surrounding an amorphous- or liquid-phase inner core.

- Ellipsometric measurements under external reflection configuration at 70º incidence angle have shown evidence of two bands separated by several electronvolts, whose energy position depends on the NP size. The energy position redshifts as the evaporation time increases and, thus, the particles are larger. Thanks to the calculations performed with the DDA, those bands have been attributed to in-plane and out-of-plane resonant modes of hemispherical GaNPs deposited on Si substrates.

- Additionally, an interesting behavior of these GaNPs/Si platforms has been observed under certain conditions of energy and incidence angle. When the phase shift difference, Δ, has reached a value of 180º, the RPH condition has occurred. Under this condition, the $< \varepsilon_i >$ function has taken a sigmoidal lineshape close to the high energy resonant band.

- The $< \varepsilon_i >$ function under the RPH condition have shown a great sensitivity to the NP surface modification. Taking advantage of this property, GaNPs/Si platforms have been studied as potential biosensing platforms. The first approach has been the development of an immunosensor for GSH. The procedure has begun with the NP functionalization by surface thiolation with the DTSP and the subsequent antibody immobilization. The NP surface modification has been confirmed through FTIR measurements. Finally, GSH has been detected in the submicromolar range with a detection limit of 10 nM.

- The use of GaNPs/Si platforms have been extended to other analytes, such as DNA sequences. In this case, the NP surface has been modified with a thiol-modified probe chain, selective to a complementary sequence of the *H. Pylori* pathogen. The functionalization of the NP surface has been demonstrated through XPS

measurements. A successful detection of this sequence has been achieved in the pico and nanomolar range. A very low detection limit of 6.0 pM has been found. For both biosensors, the use of signal amplifiers has not been required, which has simplified the whole procedure.

- The selectivity of this DNA biosensor has been studied. The current platform has been able to discriminate between complementary and mutated sequences from the same pathogen. The experiments have been carried out using mutated sequences, with only a single nucleotide polymorphism, at the same concentration than the complementary sequence. Furthermore, the influence of possible interferences due to the presence of other pathogens, such as *E. Coli*, has been studied. The conclusion arising from this study is that other pathogens do not interfere in the response as long as their concentrations are below the concentration of the target sequence.

- The applicability of this biosensing platform in real genomic samples has been demonstrated. In this respect, the detection of a specific mutation in the CFTR gene, which causes the Cystic Fibrosis disease has been studied. The corresponding wild and mutated sequences have been extracted from peripheral blood leukocytes by the Medical and Molecular Genetics Institute (INGEMM) of Madrid. The promising results obtained have demonstrated that the developed biosensor can be used for the direct detection of mutations in PCR amplified products without complicated sample treatment procedures.

7.3.2. Future work

- The biosensing capabilities of the GaNPs/Si platforms have been demonstrated after the biological recognition of different analytes. Due to the operation in external reflection mode, it is possible to use the ellipsometric GaNPs/Si platforms in continuous-flow systems to monitor the recognition process in real-time. This would allow optimizing the incubation time, analyzing the recognition kinetics or studying the stability of the chemical bonds over time. In more complex samples, it might also help to identify the reaction times of different species, contributing to improve the cross-sensitivity.

- Up to now, the evaporation of Ga forms a randomly ordered array of NPs on the substrate. An improvement of the NPs arrangement may increase the sensor sensitivity. For this aim, the definition of an ordered pattern of holes in thin films of materials with high Ga surface diffusivity can yield arrays where the interparticle distance is better controlled. The size of the hole would determine the diameter and number of GaNPs that can host inside. The use of nanolithography to produce holes with sizes ≤ 100 nm would help to obtain distributions of simple NPs with diameters ruled by the hole size.

- Previous studies have reported the possibility of enhancing the Raman signal of biomolecules and 2D materials due to the SERS effects of GaNPs. Those SERS capabilities can be combined with the action of other metal NPs, such as Au or Ag, to develop more sensitive platforms. As a carbon-based material, graphene has a well-known chemical functionalization procedure, being a good candidate for the development of a wide variety of sensors based on the SERS effect.

- The NP geometry on Si substrates is found to be quite hemispherical (contact angle around 90º). The contact angle can be modified by using self-assembled monolayers or 2D materials on substrate surface. Thus, the geometry can be optimized in order to enhance the localized electric fields on the NP edges. This is a critical issue for sensing purposes, especially when the transduction method relies on the electric field intensity formed around the nanostructure. Carbon-based materials, for instance, can help to obtain a larger contact angle, whereas the evaporation on rough substrates tends to produce smaller contact angles.

- The detection of glutathione can be extended to real samples. There are several inflammatory conditions, such as Crohn's disease, related to low levels of this biomolecule. This biomolecule is found inside cells, being required the analyte extraction before the analysis. The extraction procedure typically includes the cell lysis by chemical or physical procedures. The idea is to use the cell lysates without further purification. One of the arising problems is that these kind of matrices consist of a large number of compounds, which can hinder the analyte detection. In this respect, the selectivity of the recognition element is crucial. However, antibodies are very selective and can deal with this issue. Another related problem of these matrices is that they can have a strong acidic or basic nature, which might

damage the biosensing platform. Therefore, the stability of the platform to these more aggressive media should be studied. As mentioned in the first point, real-time measurements may be useful for providing information about the current platform stability to these kind of media.

7. Conclusiones y trabajo futuro

En las siguientes Secciones se presentan las conclusiones de los diferentes Capítulos, junto con nuevas ideas para continuar y abrir nuevas líneas de investigación relacionadas con el trabajo presentado en esta tesis. Espero que ayude a futuros investigadores a progresar más rápido en el conocimiento y la fabricación de nuevos sensores.

7.1. Sensores de luz basados en nanohilos

7.1.1. Conclusiones

7.1.1.1. Sensores de luz basados en CuO

En este trabajo, se ha propuesto una ruta paso a paso para la fabricación de dispositivos sensores de luz basados en CuO, desde el crecimiento y el procesado de sus nanohilos (NWs) hasta su caracterización electroóptica.

- Los CuO NWs se han crecido por oxidación directa de láminas de Cu bajo presión atmosférica a diferentes temperaturas. Se ha estudiado la influencia de la temperatura por SEM, revelando su efecto en la oxidación sobre las dimensiones físicas del NW.
- Estos NWs se han manipulado y alineado entre electrodos mediante dielectroforesis (DEP) por drop-casting con el objetivo de fabricar sensores de luz. La frecuencia y

el voltaje efectivo de la onda sinusoidal aplicada se ha optimizado para maximizar el número de NWs alineados.

- Se ha encontrado que los CuO NWs poseen una conductividad tipo p, tras su exposición al vapor de agua. En cambio, los ZnO NWs han exhibido el comportamiento opuesto, como corresponde a un semiconductor tipo n.

- Se ha fabricado y caracterizado electroópticamente un sensor de luz, basado en CuO NWs alineados entre electrodos de AZO. Este sensor ha mostrado ser sensible a la luz, en el rango espectral visible, de acuerdo con las propiedades ópticas esperadas por el CuO. Además, el uso del AZO, un material tipo n, como electrodo ha permitido la formación de heterouniones entre el AZO y el CuO a ambos extremos del NW, lo que ha acelerado la respuesta del dispositivo en comparación con otros fotoconductores basados en NWs. Estos resultados han demostrado la efectividad de la DEP para un desarrollo rápido y barato de dispositivos sensores de luz basados en NWs.

7.1.1.2. Sensores de luz basados en ZnO

Se han establecido nuevos métodos de control para la fabricación de dispositivos sensores de ultravioleta (UV) basados en NWs de ZnO. Estos métodos han mejorado la calidad superficial de los dispositivos fabricados y la reproducibilidad del proceso de alineamiento.

- El primer objetivo se ha enfocado en la mejora de la dispersión de NWs. Se ha llevado a cabo un paso previo de sedimentación para eliminar los clusters de gran tamaño en la dispersión, los cuales pueden cortocircuitar los electrodos tras el proceso de DEP. La estimación de la concentración de NWs en la dispersión se ha llevado a cabo con éxito mediante espectrofotometría de absorción.

- Se ha desarrollado un sistema de DEP portable y de flujo continuo para mejorar la calidad superficial de dispositivo final e incrementar la probabilidad de atrapado de NWs. Este nuevo sistema contiene un dispositivo óptico, que incluye un láser y un fototransistor, para monitorizar la dispersión. Por otra parte, el alineamiento de NWs se ha monitorizado en tiempo real a través de medidas de la resistencia paralela mediante el uso de un LCR conectado al sistema DEP. Este método ha

permitido estimar el número de NWs atrapados durante el proceso de DEP y, por tanto, añadir más mecanismos de control al proceso de atrapamiento. Otra ventaja de la monitorización de la resistencia paralela ha sido la posibilidad de detectar anomalías durante el atrapamiento, por ejemplo el daño de los electrodos causado por la electrólisis del disolvente. Gracias al montaje boca abajo del sustrato en el sistema DEP de flujo continuo, se han obtenido superficies de mayor calidad y con menor contaminación producida por las estructuras no atrapadas en los electrodos, las cuales son difíciles de eliminar mediante DEP por drop-casting.

- Los ZnO NWs han sido alineados entre electrodos de AZO por este nuevo sistema de DEP para la fabricación de sensores de luz en el rango UV. Algunas de las ventajas de este nuevo dispositivo son su alta transparencia y su capacidad para funcionar bajo iluminación a ambos lados del dispositivo, sin pérdidas significativas entre ambas configuraciones.

7.1.2. Trabajo futuro

- Actualmente el sistema desarrollado para DEP es relativamente pesado y grande. Se podría diseñar una nueva versión miniaturizada, con toda su electrónica contenida en pequeñas cajas. Ciertos circuitos integrados, creados específicamente para funcionar como generadores de funciones, se han encontrado a la venta, lo cual podría ayudar a reducir de tamaño toda la electrónica y, por tanto, las dimensiones del sistema DEP.

- El sistema de DEP no está restringido al alineamiento de NWs, sino que se puede utilizar también para manipular materiales bidimensionales. Las láminas de grafeno y de MoS_2 han mostrado tener propiedades electróopticas interesantes, además de una extensa funcionalización química que podría ser útil para anclar diferentes moléculas y, así, fabricar nuevos sensores. El alineamiento de estos materiales, obtenidos por exfoliación mecánica, puede convertirse en la base para la producción en masa de sensores biológicos y de gases.

- Los sensores de CuO han presentado una baja responsividad comparada con otras nanoestructuras, como los NWs de ZnO. Estas propiedades electróopticas se podrían mejorar mediante la decoración del NW con nanopartículas. Estas

nanopartículas se pueden anclar a las paredes del NW mediante enlaces covalente u otros medios, dando lugar a la formación de barreras Schottky o uniones rectificantes que pueden modificar las propiedades electrónicas del NW. Esta estrategia ha mostrado resultados prometedores en la literatura para NWs de ZnO decorados con nanopartículas de Au.

- Otra estrategia es la funcionalización química del NW con diferentes moléculas. Estudios preliminares han sido llevados a cabo en nuestro laboratorio, basados en la silanización de los NWs de ZnO, mostrando una mejora en la linealidad de las características I-V.

- Hoy en día, la fabricación de dispositivos electrónicos en sustratos plásticos está atrayendo mucha atención en la comunidad científica. Los NWs se pueden alinear entre electrodos definidos en sustratos transparentes plásticos, como el Kapton o el acetato de celulosa. La ventaja de los plásticos es evidente puesto que son mucho más ligeros que el vidrio, el silicio o el cuarzo. Además, se pueden ajustar a cualquier superficie irregular, abriendo la posibilidad de integrar sensores flexibles en la piel o, incluso, fabricar pieles electrónicas.

7.2. Inmunosensor para glutatión mediante elipsometría por reflexión total interna

7.2.1. Conclusiones

En este trabajo se ha estudiado el desarrollo de un inmunosensor TIRE para el GSH, una biomolécula de bajo peso molecular. Se ha escogido la configuración competitiva basada en el reconocimiento simultáneo de los conjugados GSH-AuNPs y del GSH libre. Este sensor se aprovecha de la amplificación de la señal producida por las AuNPs en el modo TIRE, al enlazarse con la superficie funcionalizada de oro.

- Se ha funcionalizado con éxito las AuNPs con GSH. Las medidas realizadas por espectrofotometría de UV-visible e infrarrojo han confirmado su correcta funcionalización.

- La plataforma biosensora (bicapa AZO/Au) se ha desarrollado en dos pasos: depósito de AZO por sputtering en sustratos de cuarzo, y el posterior depósito de Au por evaporación térmica de efecto Joule. El AZO ha mostrado tener ventajas

sobre el Ti y el Cr, como capa intermedia entre el Au y el sustrato de cuarzo. A este respecto el AZO ha reducido las pérdidas por absorción, como se ha demostrado en los cálculos numéricos realizado con las ecuaciones de Fresnel y con el uso de la aproximación por medios efectivos.

- La bicapa AZO/Au se ha funcionalizado con una monocapa tiólica, el DTSP, para después inmovilizar un anticuerpo selectivo al GSH. Se ha demostrado la presencia del DTSP mediante voltamperometría cíclica, vía desorción reductora del tiol. El anticuerpo se ha inmovilizado mediante ataque nucleófilo de sus grupos aminos primarios al grupo N-succinimidil del DTSP. Se ha simulado con las ecuaciones de Fresnel la posición del SPR, definida como el mínimo en Ψ, antes y después de la inmovilización para confirmar la correlación entre el desplazamiento en energía del SPR y el desplazamiento esperado.

- Se ha monitorizado con éxito, mediante medidas TIRE en tiempo real, la inmovilización del anticuerpo en la bicapa funcionalizada con DTSP y el reconocimiento inmunológico del anticuerpo con los conjugados GSH-AuNPs.

- Se ha estimado la concentración óptima de los conjugados GSH-AuNPs mediante la medida del desplazamiento en energía de la resonancia en elipsometría, para diferentes concentraciones del conjugado. Se ha visto que una concentración de 40 nM es óptima ya que ha producido el mayor desplazamiento en energía. La presencia de estos conjugados se ha confirmado mediante SEM.

- Finalmente, se ha desarrollado un inmunoensayo para la detección del GSH basado en la competición entre los conjugados GSH-AuNPs y el GSH libre por los sitios activos del anticuerpo. El inmunosensor ha mostrado un límite de detección estimado de 6 nM, con buenos valores de reproducibilidad.

7.2.2. Trabajo futuro

- Con respecto a la tecnología plasmónica, el Ag presenta una banda SPR más fuerte y estrecha y, por tanto, una sensibilidad teórica mayor que la del Au. A pesar de que la química de funcionalización del Au es más extensa, el uso del Ag podría ser interesante si se requieren mayores sensibilidades. La principal desventaja del Ag es su rápida oxidación y pasivación, lo cual puede atenuar sus propiedades

plasmónicas. Sin embargo, si fuese necesario, este problema se podría evitar mediante tratamientos previos de su superficie.

- En este trabajo, las AuNPs se han utilizado como amplificadores de la señal. Los coloides de Ag también son fáciles de sintetizar mediante el método de reducción con citrato. Como se ha mostrado más arriba, este material presenta efectos SPR más fuerte, siendo también adecuado su uso como amplificadores.

- Algunas de las desventajas de la elipsometría es la baja portabilidad del sistema y su alto coste. El desarrollo de un elipsómetro portable puede ayudar a solucionar estas contrapartidas y proveer una manera de realizar medidas in-situ sin necesidad de trasladar las muestras al laboratorio. Además, un elipsómetro portable se puede combinar con un sistema microfluídico para automatizar completamente el proceso de sensado. Aunque dichas estrategias puedan requerir una gran cantidad de tiempo, éstas pueden suponer un gran paso adelante a una posible transferencia de tecnología a la Industria.

7.3. Plataformas biosensoras basadas en nanoestructuras de galio

7.3.1. Conclusiones

En este trabajo se presenta el desarrollo de plataformas biosensoras basadas en GaNPs. Se ha demostrado su potencial aplicabilidad para detectar GSH y cadenas de ADN. Previa a la fabricación de plataformas biosensoras, se han estudiado en profundidad las propiedades plasmónicas de las GaNPs y su respuesta a las medidas elipsométricas bajo la configuración de reflexión externa.

- Se han llevado a cabo cálculos basados en la teoría de Mie para estudiar la plasmónica de esferas homogéneas. El análisis de GaNPs con diferentes radios ha revelado que, las resonancias asociadas a oscilaciones dipolares por parte de las NPs cubren un amplio rango espectral, desde el UV al infrarrojo, mientras que las resonancias de las AuNPs está principalmente localizadas en el visible. Por otra parte, se han llevado a cabo simulaciones con el DDA para estudiar la plasmónica de las partículas semiesféricas. En particular, el estudio se ha focalizado en la separación de los modos de resonancia de las GaNPs esféricas en oscilaciones dipolares “en el plano” y “fuera del plano” debido a la geometría semiesférica. Se

ha observado que estos modos son sensibles a la polarización de la luz incidente. La adición de un sustrato en contacto directo con la NP ha sido incluida en las simulaciones, dando lugar a un desplazamiento hacia el rojo de los modos oscilatorios debido a un aumento del índice de refracción del medio.

- Se han depositado grandes áreas de GaNPs con éxito sobre sustratos de Si mediante evaporación térmica de Ga. Para una evaporación de 2 minutos, tiempo que se ha utilizado para la fabricación de plataformas GaNPs/Si en los experimentos de biosensado, el histograma obtenido por SEM ha mostrado la presencia de distribuciones bimodales de NPs debido al proceso de coalescencia durante la evaporación.

- Se ha obtenido información sobre la estructura y composición de las NPs mediante las técnicas XPS y XRD de caracterización superficial. Los datos han mostrado la presencia de una capa de óxido de Ga rodeando el interior líquido o amorfo hecho de Ga.

- Las medidas elipsométricas realizadas en el modo de reflexión external a un ángulo de incidencia de 70º han mostrado evidencias de dos bandas separadas varios electronvoltios, cuya posición en energía depende del tamaño de la NP. Esta posición se ha desplazado hacia el rojo a medida que el tiempo de evaporación aumentaba y, por tanto, a medida que las GaNPs eran más grandes. Gracias a los cálculos llevados a cabo mediante DDA, estas bandas se han atribuido a los modos resonantes "en el plano" y "fuera del plano" de las GaNPs semiesféricas depositadas sobre sustratos de Si.

- Además, se ha observado un comportamiento interesante en estas plataformas GaNPs/Si bajo ciertas condiciones de energía y ángulo de incidencia. Cuando la diferencia de desfases, Δ, ha alcanzado el valor de 180º, se ha producido la condición RPH. Bajo esta condición, la función $< \varepsilon_i >$ ha adquirido una forma sigmoidal cerca de la banda de la resonancia de alta energía.

- La función $< \varepsilon_i >$, bajo la condición RPH, ha mostrado una gran sensibilidad a la modificación superficial de la NP. Aprovechando esta propiedad, se han estudiado las GaNPs/Si como potenciales plataformas biosensoras. La primera plataforma biosensora desarrollada ha sido un inmunosensor para el GSH. El procedimiento ha

comenzado con la funcionalización de la superficie de la NP con DTSP y la posterior inmovilización del anticuerpo sobre la superficie funcionalizada con DTSP. Estas modificaciones se han confirmado mediante medidas FTIR. Finalmente, el GSH se ha detectado en el rango submicromolar, estimando un límite de detección de 10 nM.

- El uso de estas plataformas se ha extendido a otros analitos, como las cadenas de ADN. En este caso, la superficie de la NP se ha modificado con una sonda sintética tiolada, selectiva a una secuencia complementaria presente en el patógeno *H. Pylori*. La funcionalización se ha demostrado mediante medidas XPS. Se ha logrado detectar con éxito estas secuencias complementarias en el rango pico y nanomolar, estimando un límite de detección de 6.0 pM. En ambos biosensores no se ha requerido el uso de amplificadores de señal, lo cual ha simplificado considerablemente el proceso de biosensado.

- Se ha estudiado la selectividad de este biosensor de ADN. La plataforma ha sido capaz de discriminar entre secuencias complementarias y mutadas provenientes del mismo patógeno. Los experimentos se han llevado a cabo utilizando secuencias mutadas con un polimorfismo de nucleótido único a concentraciones similares para ambas cadenas. Por otra parte, se ha estudiado la influencia de posibles interferentes debido a la presencia de otros patógenos, como la *E. Coli*. La conclusión derivada de este estudio es que el patógeno *E. Coli* no interfiere en la respuesta, siempre y cuando su concentración esté por debajo de la concentración del analito.

- Se ha estudiado la aplicabilidad de estas plataformas para el biosensado de muestras reales. Para ello, se ha estudiado la detección de una mutación específica presente en el gen CFTR, causante de la enfermedad denominada Fibrosis Quística. Las secuencias salvaje y mutada han sido extraídas de leucocitos periféricos por parte del Instituto de Genética Médica y Molecular de Madrid. Los resultados obtenidos han sido prometedores y han demostrado que el biosensor desarrollado puede ser utilizado para la detección directa de mutaciones en productos amplificados por PCR sin necesidad de pretratamientos de la muestra.

7.3.2. Trabajo futuro

- Las capacidades biosensoras de las plataformas GaNPs/Si se han demostrado tras el reconocimiento de diferentes analitos. Debido a que las medidas se llevan a cabo en modo reflexión externa, es posible utilizar estas plataformas en sistemas de flujo continuo para monitorizar los procesos de reconocimiento en tiempo real. Esto permitiría optimizar el tiempo de incubación, estudiar la cinética de reconocimiento o estudiar la estabilidad de los enlaces en función del tiempo. En muestras más complejas, podría ayudar a identificar los tiempos de reacción de diferentes especies, contribuyendo a mejorar la sensibilidad cruzada.

- Hasta ahora, las evaporaciones de Ga forman arrays de NPs ordenados de forma aleatoria sobre el sustrato. Una mejora en el ordenamiento de las NPs puede mejorar la sensibilidad del sensor. Por ello, la definición de un patrón de huecos en capas finas de materiales, para las cuales el Ga presente una alta difusión superficial, puede dar lugar a arrays donde la distancia entre partículas pueda ser controlada. El tamaño del hueco determinaría el diámetro y el número de GaNPs que pueda contener dentro. Por ejemplo, el uso de la nanolitografía para producir huecos menores de 100 nm ayudaría a obtener distribuciones de NPs con diámetros gobernados por el tamaño del hueco.

- Estudios previos han demostrado la posibilidad de incrementar la señal Raman de biomoléculas y materiales 2D debido al efecto SERS de las GaNPs. Este efecto se puede combinar con la acción de NPs de otros metales, como el Au o el Ag, para desarrollar plataformas más sensibles. Como material basado en carbono se puede utilizar el grafeno, el cual tiene una química de funcionalización ampliamente conocida, siendo un candidato ideal para el desarrollo de este tipo de sensores basados en SERS.

- La geometría de las NPs sobre sustratos de Si ha mostrado ser semiesférica (ángulo de contacto alrededor de 90º). El ángulo de contacto se puede modificar usando monocapas autoensambladas o materiales 2D sobre las NPs. Por lo tanto, la geometría de la NP se puede optimizar para incrementar el campo eléctrico localizado en sus bordes. Éste es un tema crítico para el sensado, especialmente cuando el método de transducción confía en la intensidad del campo eléctrico formado alrededor de la nanoestructura. Los materiales basados en carbono, por

ejemplo, permiten obtener ángulos de contacto elevados, mientras que la evaporación sobre sustratos rugosos tiende a producir ángulos de contacto más pequeños.

- La detección de GSH se puede extender al análisis de muestras reales. Existen varias enfermedades inflamatorias, como la enfermedad de Crohn, relacionadas con la disminución en la concentración de esta biomolécula. El GSH se encuentra generalmente dentro de las células, siendo requerida la extracción previa de la misma antes del análisis. El procedimiento de extracción incluye típicamente la lisis de la célula por medios físicos o químicos. La idea es usar estos lisados sin requerir pretratamientos de la muestra. Uno de los problemas que surgen en el uso de estas matrices es la alta cantidad de compuestos que contienen, los cuales pueden dificultar la detección del analito. A este respecto, la selectividad del elemento de reconocimiento es crucial. No obstante, los anticuerpos son altamente selectivos y pueden tratar con este problema. Otro problema relacionado con estas matrices es que pueden exhibir un comportamiento fuertemente ácido o básico, el cual podría dañar la plataforma sensora. Por lo tanto, la estabilidad de la plataforma a estos medios debería ser estudiada. Como se ha mencionado en el primer punto, las medidas en tiempo real podrían ser útiles para proveer información a este respecto.

Appendix A

This appendix includes all the contributions resulting from this research.

Journal papers and proceedings

1. **Antonio García Marín**, Tania García-Mendiola, Cristina Navio Bernabeu, María Jesús Hernández, Juan Piqueras, and Jose Luis Pau, Félix Pariente, Encarnación Lorenzo, "Gallium Plasmonic Nanoparticles for Label Free DNA and Single Nucleotide Polymorphism Sensing", Nanoscale 8 (2016) 9842-9851.

2. Jose Luis Pau, **Antonio García Marín**, María Jesús Hernández, Encarnación Lorenzo, and Juan Piqueras, "Plasmonic coupling and chemical modification of Ga-graphene heterogenous surfaces supported on Cu, quartz and SiO_2/Si substrates", Physica Status Solidi B 253 (2016) 664-670.

3. **Antonio García Marín**, María Jesús Hernández, Eduardo Ruiz, Jose María Abad, Encarnación Lorenzo, Juan Piqueras, Jose Luis Pau, "Immunosensing platform based on gallium nanoparticle arrays on silicon substrates", Biosensors and Bioelectronics 74 (2015) 1069-1075.

4. **A García Marín**, C García Núñez, P Rodríguez, G Shen, S M Kim, P Kung, J Piqueras and J L Pau, "Continuous-flow system and monitoring tools for the dielectrophoretic integration of nanowires in light sensor arrays", Nanotechnology 26 (2015) 115502.

5. C. García Núñez, M. Sachsenhauser, B. Blashcke, **A. García Marín**, Jose A. Garrido, and Jose L. Pau. "Effects of Hydroxylation and Silanization on the Surface Properties of ZnO Nanowires" ACS Applied Materials & Interfaces 7 (2015) 5331−5337.

6. **Antonio García-Marín**, José M. Abad, Eduardo Ruiz, Encarnación Lorenzo, Juan Piqueras, and José L. Pau. "Glutathione Immunosensing Platform Based on Total Internal Reflection Ellipsometry Enhanced by Functionalized Gold Nanoparticles", Analytical Chemistry 86 (2014) 4969-4976.

7. J. L. Pau, C. García Núñez, **A García Marín**, C. Guerrero, P. Rodríguez, S. Borromeo, J. Piqueras. "Contact properties and surface reaction kinetics of single ZnO nanowire devices fabricated by dielectrophoresis" SPIE 8987 (2014), Oxide-based Materials and Devices V, 89871Q.

8. M. Revenga-Parra, T. García-Mendiola, J. González-Costas, E. González-Romero, **A. García Marín**, J.L. Pau, F. Pariente, E. Lorenzo. "Simple

diazonium chemistry to develop specific genesensing platforms", Analytica Chimica Acta 813 (2014) 41-47.

9. C. Gómez-Anquela, M. Revenga-Parra, J.M. Abad, **A. García Marín**, J.L. Pau, F. Pariente, J. Piqueras, E. Lorenzo. "Electrografting of N',N'-dimethylphenothiazin-5-ium-3,7-diamine (Azure A) diazonium salt forming electrocatalytic organic films on gold or graphene oxide gold hybrid electrodes", Electrochimica Acta 116 (2014) 59-68.
10. C. G. Núñez, J. L. Pau, E. Ruíz, **A. G. Marín**, B. J. García, J. Piqueras, G. Shen, D. S. Wilbert, S. M. Kim and P. Kung, "Enhanced fabrication process of zinc oxide nanowires for optoelectronics" Thin Solid Films 555 (2014) 42-47.
11. C García Núñez, **A García Marín**, P Nanterne, J Piqueras, P Kung and J L Pau, "Conducting properties of nearly depleted ZnO nanowire UV sensors fabricated by dielectrophoresis" Nanotechnology 24 (2013) 415702.
12. Jose Luis Pau Vizcaíno, Carlos García Nuñez, **Antonio García Marín**, Eduardo Ruiz, Juan Piqueras, "Optical sensors based on metal oxide nanowires for UV/IR detection" SPIE 8774 (2013), Optical Sensors, 87740L.
13. **A. García Marín**, C. García Núñez, E. Ruiz, J. Piqueras, J. L. Pau, "Fast response ZnO:Al/CuO nanowire/ZnO:Al heterostructure light sensor" Applied Physics Letters 102 (2013) 232105.
14. J. L. Pau, C. García Núñez, **A. García Marín**, E. Ruiz, J. Piqueras, "Metal oxide nanowires as building blocks for light detectors, gas sensors and biosensors", IEEE Xplore (2013) 171-174.

Patents

1. Jose Luis Pau Vizcaíno, **Antonio García Marín**, and Juan Piqueras, "Condensation sensor and method for manufacturing said sensor", 6 Feb 2014, International Application No: PCT/ES2013/070546.

Book chapters

1. J. L. Pau, **A. García Marín**, M. J. Hernández, M. Cervera, J. Piqueras, "Analysis of plasmonic structures by spectroscopic ellipsometry", *Research Perspectives on Functional Micro- and Nanoscale Coatings*, Idea Group Publishing (IGI-Global), Chapter 8, 208-239. May 2016. ISBN 9781522500674

Conference contributions

Invited talks

1. J. L. Pau, C. García Núñez, **A. García Marín**, J. Piqueras. "Nanowire photodetectors and imagers fabricated by dielectrophoretic assembly: review and prospects" 4th Early Stage Researchers Workshop. IMDEA, Madrid (Spain), 25-26 Jun 2014.

Oral presentations

1. **A. García Marín**, M. J. Hernández, E. Ruiz, Jose M. Abad, E. Lorenzo, J. Piqueras, M. Cervera, J. L. Pau "Ellipsometric biosensing platforms based on the plasmonic resonance of gallium nanoparticles" VII Workshop NyNA, Salamanca (Spain). 6-8 Jul 2015.

2. E. Lorenzo, **A. García Marín**, T. García, M. J. Hernández, E. Ruiz, J. M. Abad, J. Piqueras, J. L. Pau "Biosensor Platforms Based on Ga Nanoparticle Arrays" VII Workshop NyNA, Salamanca (Spain). 6-8 Jul 2015.

3. **A. García Marín**, M. J. Hernández, E. Ruiz, José M. Abad, E. Lorenzo, J. Piqueras, J. L. Pau. "Biosensing platforms based on the plasmon resonance of gallium nanodroplets" XVII Young researchers meeting. Institute Nicolás Cabrera, Madrid (Spain), 19 Dec 2014.

4. J. L. Pau, C. García Núñez, **A. García Marín**, C. Guerrero, P. Rodríguez, S. Borromeo, J. Piqueras. "Contact properties and surface reaction kinetics of single ZnO nanowire devices fabricated by dielectrophoresis" SPIE Photonics West 2014, San Francisco (USA), 1-6 Feb 2014.

5. **A. García Marín**, C. García Núñez, C. Guerrero, J.M. Abad, E. Lorenzo, J. Piqueras, J.L. Pau. "Dielectrophoresis as a fabrication tool for single nanowire electronic devices". 3rd Early Stage Researchers Workshop. IMDEA, Madrid (Spain), 27-28 Jun 2013.

6. Jose Luis Pau Vizcaíno, Carlos García Nuñez, **Antonio García Marín**, Eduardo Ruiz, Juan Piqueras. "Optical sensors based on metal oxide nanowires for UV/IR detection". SPIE Optics + Optoelectronics 2013, Prague (Czech Republic), 15-18 Apr 2013, oral presentation.

7. J. L. Pau, C. García Nuñez, **A. García Marín**, E. Ruiz, J. Piqueras. "Metal oxide nanowires as building blocks for light detectors, gas sensors and biosensors". 9th Spanish Conference on Electron Devices (CDE), Valladolid (Spain), 12-14 Feb 2013.

8. C. García Núñez, J. L Pau, E. Ruíz, **A. García Marín**, B. J García, J. Piqueras, G. Shen, D. S Wilbert, S. M Kim, P. Kung. "Enhanced fabrication process of

zinc oxide nanowire for optoelectronics" 4th International Symposium on Transparent Conductive Materials (TCM), Crete (Greece), 21-26 Oct 2012.

Poster presentations

1. **A. García Marín**, T. García, M. J. Hernández, E. Ruiz, E. Lorenzo, J. Piqueras, J. L. Pau "Ellipsometric biosensing platforms based on the plasmonic resonance of gallium nanoparticles". Europtrode XIII, Graz (Austria), 20-23 Mar 2016.
2. **A. García Marín**, M. J. Hernández, E. Ruiz, Jose M. Abad, E. Lorenzo, J. Piqueras, M. Cervera, J. L. Pau "Ellipsometric biosensing platforms based on the plasmonic resonance of gallium nanoparticles" VII Workshop NyNA, Salamanca (Spain). 6-8 Jul 2015.
3. **A. García Marín**, C. García Núñez, E. Ruiz, J. Piqueras, J.L. Pau. "p-type CuO nanowire photodetectors". Nanoportugal 2013, Oporto (Portugal), 13-15 Feb 2013.
4. **A. García Marín**, J. M. Abad, J. L. Pau, E. Lorenzo, J. Piqueras, "Advanced ellipsometric immunosensor based on Al-doped ZnO surfaces" Europtrode XI, Barcelona (Spain), 1-4 Apr 2012.
5. **A. García Marín**, J. M. Abad, J. L. Pau, E. Ruiz, E. Lorenzo, J. Piqueras, "High-sensivity ellipsometric immunosensors based on Au nanoparticle plasmon resonance in Al-doped zinc oxide thin films" NanoSpain 2012, Santander (Spain), 27 Feb-1 Mar 2012.
6. J. L. Pau, **A. García Marín**, C. García Nuñez, E. Ruiz, J. Piqueras "NO sensors for disease control and medication monitoring in asthmatic patients" Nanoportugal 2013, Oporto (Portugal), 13-15 Feb 2013.
7. J. L. Pau, **A. García Marín**, J. M. Abad, M. J. Hernández, M. Cervera, E. Lorenzo, J. Piqueras "Total internal reflection ellipsometry for biosensing applications". Europtrode XI, Barcelona (Spain), 1-4 Apr 2012.

Press releases

1. Nanopartículas de galio sobre silicio: una nueva plataforma para el desarrollo de (bio)sensores (published on November 25, 2015)
   http://www.madrimasd.org/informacionidi/noticias/noticia.asp?id=65122